

Development of a chemical kinetics reaction mechanism for tetramethylsilane-doped flames and comprehensive thermochemistry of silanes and siloxanes

Von der Fakultät für Ingenieurwissenschaften, Abteilung Maschinenbau und
Verfahrenstechnik der

Universität Duisburg-Essen

zur Erlangung des akademischen Grades

eines

Doktors der Ingenieurwissenschaften

Dr.-Ing.

genehmigte Dissertation

von

Hossein Janbazi

aus

Ghaemshahr, Iran

Gutachter: Univ.-Prof. Dr.-Ing. Prof. Andreas Kempf

Univ.-Prof. Dr. rer. nat. Tina Kasper

Tag der mündlichen Prüfung: 27.09.2021

Acknowledgements

The present work was conducted during my PhD studies at the chair of Fluid Dynamics, Institute for Combustion and Gas Dynamics at the University of Duisburg-Essen. In the framework of a DFG-project "FOR2284", I have carried out the research project 'TP8': 'Modeling of precursor chemistry - Development, reduction, and optimization of reaction mechanisms of decomposition and of the combustion of organometallic compounds'.

Undertaking this PhD has been a truly life-changing experience for me and it would not have been possible to do without the support and guidance that I received from many people.

First of all, I would like to thank Prof. Dr.-Ing. Andreas Kempf, for offering me the opportunity of a PhD at the chair of Fluid Dynamics. I thank him for giving me the freedom to follow my research interests and for his encouragement to publish my work.

I wish to thank my group leader Dr.-Ing. Irenaeus Wlokas for his encouragement and thoughtful support with his knowledge and ideas from the beginning of PhD at the chair of Fluid Dynamics.

I would like to say a special thank you to Priv.-Doz. Dr. Sebastian Peukert. His support, guidance, passion, and cooperativeness helped me a lot to make this work possible. His overall insights and knowledge in quantum chemistry and reaction kinetic fields have made this an inspiring experience for me.

My special gratitude goes to my co-examiner Prof. Dr. rer. nat. Tina Kasper for her interest in evaluating my thesis. I wish to thank Prof. Dr. rer. nat. Christof Schulz for his support and scientific feedback in publishing my work.

I would like to thank all my colleagues, with whom I have shared moments of happiness. It was my honor to work with them in such an open, friendly, and pleasant environment.

At last but not least, I wish to thank my parents and my two sisters who encouraged me to pursue my education in Germany and provided me with their love and support throughout my whole life.

Abstract

In this work, a comprehensive database for the thermodynamic properties of a large group of silicon-organic compounds is provided. A reaction mechanism is also developed for tetramethylsilane (TMS) as a precursor in the flame synthesis of silica nanoparticles.

In the first part of this work, a combinatorial consideration is applied to derive group additivity values (GAVs) required to describe the thermochemistry of a large group of silicon-organic compounds. Due to a lack of experimental data for Si–C–H–O species, the thermochemistry of species is calculated by quantum chemical calculations. The theoretically calculated compounds are considered as a training set for the regression of GAVs. Based on the group additivity method, a multivariate linear regression analysis is performed. The regressed group additivity values serve as an alternative for the estimation of thermodynamic data of new silicon-organic compounds. The uncertainty of quantum chemical calculations, as well as the uncertainty of GAVs are discussed in this work. The final results are provided as databases.

For the second part of this work, a kinetics model is developed for the decomposition and oxidation of TMS as a promising precursor for the flame synthesis of silica nanoparticles. The reaction mechanism is developed and validated based on the experimental data. The reaction pathways analysis and the sensitivity analysis are performed to the developed kinetics model. The sources of uncertainty and the possibility to improve the kinetics model are discussed. In this mechanism, reaction rate coefficients are either estimated via an algorithmic optimization procedure or are assumed based on analogies to similar reactions in the literature or calculated using Rice–Ramsperger–Kassel–Marcus theory (RRKM) theory. The genetic algorithm-based optimizer is also extended in this work.

Zusammenfassung

In dieser Arbeit wird eine umfassende Datenbank für die thermodynamischen Eigenschaften einer großen Gruppe von siliziumorganischen Verbindungen bereitgestellt. Außerdem wird ein Reaktionsmechanismus für Tetramethylsilan (TMS) als Vorläufer für die Flammensynthese von Siliziumdioxid-Nanopartikeln entwickelt.

Im ersten Teil dieser Arbeit wird eine kombinatorische Betrachtung angewandt, um Gruppenadditivitätswerte (GAVs) abzuleiten, die zur Beschreibung der Thermochemie einer großen Gruppe von siliziumorganischen Verbindungen erforderlich sind. Da es an experimentellen Daten für Si-C-H-O-Spezies mangelt, wird die Thermochemie der Spezies durch quantenchemische Berechnungen ermittelt. Die theoretisch berechneten Verbindungen werden als Trainingsmenge für die Regression von GAVs betrachtet. Auf der Grundlage der Methode der Gruppenadditivität wird eine multivariate lineare Regressionsanalyse durchgeführt. Die regressierten Werte der Gruppenadditivität dienen als Alternative für die Schätzung der thermodynamischen Daten neuer siliziumorganischer Verbindungen. Die Unsicherheit von quantenchemischen Berechnungen sowie die Unsicherheit von GAVs werden in dieser Arbeit diskutiert. Die Endergebnisse werden als Datenbanken zur Verfügung gestellt.

Im zweiten Teil dieser Arbeit wird ein kinetisches Modell für die Zersetzung und Oxidation von TMS als vielversprechendes Ausgangsmaterial für die Flammensynthese von Siliziumdioxid-Nanopartikeln entwickelt. Der Reaktionsmechanismus wird auf der Grundlage der experimentellen Daten entwickelt und validiert. Die Analyse der Reaktionswege und die Sensitivitätsanalyse werden für das entwickelte kinetische Modell durchgeführt. Die Quellen der Unsicherheit und die Möglichkeiten zur Verbesserung des kinetischen Modells werden diskutiert. Bei diesem Mechanismus werden die Reaktionsgeschwindigkeitskoeffizienten entweder über ein algorithmisches Optimierungsverfahren geschätzt oder auf der Grundlage von Analogien zu ähnlichen Reaktionen in der Literatur angenommen oder anhand der Rice-Ramsperger-Kassel-Marcus-Theorie (RRKM) berechnet. Der auf einem genetischen Algorithmus basierende Optimierer wird in dieser Arbeit ebenfalls erweitert.

Table of contents

List of figures	viii
List of tables	xi
Nomenclature	xiv
1 Introduction	1
1.1 Motivation	1
1.2 Novelty of the work	3
1.3 Structure of this thesis	4
2 Gas-phase synthesis of Silica nanoparticles	5
2.1 Commercial significance of silica powders and thin silica layers	5
2.2 Synthesis routes for silica powders and thin layers	6
2.3 Various type of precursors	7
2.3.1 Inorganic silicon compounds	8
2.3.2 Organic silicon compounds	9
3 Theoretical background of combustion and chemical kinetics	11
3.1 Modeling of laboratory experiment configurations	11
3.1.1 Constant-pressure homogeneous reactor	12
3.1.2 One-dimensional laminar flames	12
3.2 Transport properties	14
3.3 Modeling of chemical kinetics	18
3.3.1 Reaction stoichiometry	19
3.3.2 Mass-action kinetics	19
3.4 Mechanism development	24
3.4.1 Finite rate chemistry	26
3.4.2 Sources of data	27
3.5 Reaction rate theories	28

3.5.1	Collision theory and reaction rate limit	28
3.5.2	Transition state theory	30
3.5.3	QRRK and RRKM theories	32
4	Chemical informatics	35
4.1	Computational chemistry	36
4.2	Thermochemistry	37
4.2.1	Atomization energy method	37
4.2.2	Isodesmic reaction method	38
4.3	Group-additivity method	39
4.4	Combinatorics	41
4.5	Response surface and linear regression methodologies	42
4.6	Mechanism optimization and reduction	43
4.6.1	Genetic algorithm-based optimization	43
4.7	Graph-based representation of chemical systems	47
4.8	Cantera	48
5	Thermochemistry of stable Si–C–H-containing compounds	50
5.1	Abstract	50
5.2	Introduction	51
5.3	Methodology	52
5.3.1	Quantum chemical calculation	52
5.3.2	Group additivity method	55
5.3.3	First-Order Response-Surface Methodology	56
5.4	Representation of the thermodynamic properties	58
5.5	Results and discussions	59
5.6	Conclusion	63
5.7	Acknowledgements	63
6	Thermochemistry of organosilane compounds and organosilyl radicals	66
6.1	Abstract	66
6.2	Introduction	67
6.3	Methodology	68
6.3.1	Isodesmic reactions and uncertainty	68
6.3.2	Computational chemistry	70
6.3.3	Group additivity method	71
6.3.4	Regression analysis	72

6.4	Results and discussions	72
6.4.1	Sensitivity analysis of Si–C–H GAVs of stable species	72
6.4.2	GAVs of Si–C–H-centered radicals	75
6.4.3	GAVs of Si–C–H-adjacent radicals	76
6.4.4	GAVs of Si–C–H species with Si=C bonds	77
6.5	Conclusion	79
6.6	Acknowledgment	79
7	Thermochemistry of stable Si–C–H–O-containing compounds	80
7.1	Abstract	80
7.2	Introduction	81
7.3	Methodology	82
7.3.1	Computational chemistry	82
7.3.2	Atomization energy method	83
7.3.3	Isodesmic reactions and uncertainty	83
7.3.4	Group additivity method	88
7.3.5	Multivariable linear regression	88
7.4	Results and discussions	88
7.4.1	GAVs of Si–C–H–O species	88
7.4.2	GAVs of Si–C–H–O species with Si=O bonds	92
7.4.3	GAVs of cyclic siloxanes	95
7.5	Conclusion	97
7.6	Acknowledgment	99
8	A chemical reaction mechanism development for TMS combustion	100
8.1	Abstract	100
8.2	Introduction	101
8.3	Experiment	103
8.4	Modeling approach	104
8.5	Calculation of thermodynamic data	105
8.6	Reaction mechanism optimization	105
8.7	Results and discussions	106
8.7.1	Thermodynamics data	106
8.7.2	Kinetics model	108
8.7.3	Comparison with different loads of TMS	123
8.8	Conclusion	127
8.9	Acknowledgements	129

9 Conclusion and outlook	130
References	132
Appendix A The author's other publications	150
A.1 Thermochemistry of Oxygen-Containing Organosilane Radicals and Uncertainty Estimations of Organosilane Group-Additivity Values	150
A.2 Experimental and numerical study on the influence of equivalence ratio on key intermediates and silica nanoparticles in flame synthesis	151
A.3 Comparative study of flame-based SiO ₂ nanoparticle synthesis from TMS and HMDSO: SiO-LIF concentration measurement and detailed simulation	156
A.4 Investigation of a high Karlovitz, high Pressure premixed jet flame with heat losses by LES	157
A.5 Large-Eddy Simulation of a Lifted High-Pressure Jet-Flame with Direct Chemistry	158
A.6 Kinetics of the thermal decomposition of ethylsilane: shock-tube and modeling study	159

List of figures

1.1 Schematic of top-down and bottom-up synthesis approaches. Adapted figure from Nunes et al. [1] with permission from Elsevier.	2
3.1 Schematics of reaction mechanism development. The figure is based on that from Senkan (1992) [2] and is reproduced with permission from Elsevier.	25
3.2 Size of selected detailed and skeletal mechanisms for hydrocarbon fuels. The figure is based on that from Lu and Law [3] and is reprinted with permission from Elsevier.	27
3.3 Schematic of a reaction potential energy for an endothermic reaction.	30
4.1 Combinatorial arrangement for three possible Si, C, and H atoms for four possible ligands for Si- and C-atom-centered groups (left) and Benson groups contributing to TMS (right).	40

4.2	Schematics of the genetic algorithm-based optimization. The figure is based on that from Sikalo et al. (2014) [4] and is reproduced with permission from Wiley.	44
4.3	Bipartite graph with the nodes being represented by chemical species and reactions. The left set of elements in this graph refers to the developed TMS mechanism and the right set of elements refers to the C1 mechanism from Li et al. [5]. See text for further explanation.	48
5.1	Potentials of the CH ₃ (a) and SiH ₃ (b) rotors in 1,1-disilyl-ethane with maxima at 825 and 535 cm ⁻¹	53
5.2	Combinatorial arrangement for three possible Si, C, and H atoms for four possible ligands for Si- and C-atom-centered groups (left) and Benson groups contributing to TMS (right).	56
5.3	B3LYP/6-31G(2df,p) geometry-optimized structures of the 22 Si-C-H molecules considered for deriving group-additivity values.	64
5.4	(a) Comparison of calculated enthalpies of formation with available data shown in Table 5.1, (b) Comparison of the G4/atomization with the regressed GAVs.	65
5.5	(a) GAVs residuals versus fitted values, (b) GAVs residuals versus fitted values.	65
6.1	Combinatorial arrangements of SiH ₃ , CH ₃ , and H ligands at three possible locations in Si- and C-radical-adjacent species (categories A and B) and Si- and C-radical-centered species.	71
6.2	Residuals of the calculated ΔH_f° values from the G4/isodesmic reaction values.	75
7.1	(a) Energy potential of an internal SiH ₃ rotor in (SiH ₃) ₂ C(CH ₃)(OH) with a maximum at nearly 750 cm ⁻¹ ; (b): energy potential of an OH rotor in the same molecule, illustrating the asymmetric hindered rotor potential.	83
7.2	Structure of D5 (cyc-Si ₅ O ₅ (CH ₃) ₁₀) obtained from B3LYP/6 311G(2d,d,p) calculation. See text for the colored arrows with number labeling.	97
8.1	Potentials of CH ₃ (left) and OH rotors in trimethyl-silanol (Si(CH ₃) ₃ OH) with maxima at 400 and 175 cm ⁻¹	107
8.2	Mole-fraction profiles of the major species along the as a function of height above burner (HAB) in flame A. The points are experimental data and the curved lines are the simulation results. The colored area shows the uncertainty range of the measured data.	109

8.3	Sensitivity of major species' mole fractions on the measured temperature; simulations are performed with experimental temperature, shifted +100 K up, and shifted -100 K down. The colored areas represent the uncertainties of mole-fraction and temperature measurements. Symbols: experiment; lines: simulations.	110
8.4	Measured and calculated CH ₄ mole-fraction profiles as a function of height above burner (HAB). The colored area represents the uncertainty range of the measurement. Simulations were performed with the C1-C3 mechanism of Ranzi et al. [6] (blue dashed line) and the C1 mechanism from Li et al. [5] (black line)	112
8.5	Schematics of the reaction pathway for the oxidation of TMS based on the list of reactions in table 3. The red-colored reactions are introduced as global reactions.	113
8.6	Measured and calculated mole-fraction profiles for TMS in the flame B. The colored area shows the uncertainty range of the measurement. Symbols: experiment; line: simulation.	115
8.7	Measured and simulated mole-fraction profiles of (CH ₃) ₃ SiCH ₂ O ₂ and OSi(CH ₃) ₃ as a function of HAB for Flame B. The colored area shows the uncertainty range of a factor of two for the measured data.	115
8.8	a: RRKM calculations for reaction Si(CH ₃) ₂ O → (CH ₃)SiO + CH ₃ , for tautomerization Si(CH ₃) ₂ O → (CH ₃)(OH)SiCH ₂ , and for the reverse process (CH ₃)(OH)SiCH ₂ → Si(CH ₃) ₂ O. All calculations were carried out for 30 mbar and cover 600–1200 K; b: Relative stationary point energies (values in parentheses are relative to the energy of Si(CH ₃) ₂ O) for the unimolecular reactions of Si(CH ₃) ₂ O calculated at the G4 level of theory (present work).	116
8.9	Measured and simulated profiles of Si(CH ₃) ₃ OH and Si(OH) ₃ . The colored area shows the uncertainty range of a factor of two for the measured data.	119
8.10	Measured and simulated profiles of SiO ₂ and Si(OH) ₄ . The colored area shows the uncertainty range of a factor of two for the measured data.	120
8.11	Reaction pathways of element of Si for gas-phase species at 800 K and 30 mbar.	120
8.12	Measured and simulated profiles of Si ₄ O ₁₀ H ₄ . The colored area shows the uncertainty range of a factor of two for the measured data.	121

8.13	a: RRKM calculations for CH ₄ and H ₂ O elimination reactions of Si(CH ₃) ₃ OH; both calculations were carried out for 30 mbar and 600-1200 K. b: Relative stationary point energies (values in parentheses are relative to the energy of Si(CH ₃) ₃ OH) for the unimolecular reactions of Si(CH ₃) ₃ OH calculated at the G4 level of theory (present work).	123
8.14	Measured and simulated mole-fraction profiles of major species as a function of HAB for a series of TMS doping concentrations: 400 ppm (flame C), 600 ppm (flame B), and 800 ppm (flame D). Symbols: experiments, lines: simulations.	125
8.15	Measured and simulated mole-fraction profiles of Si-containing species along the HAB for a series of TMS doping concentrations: 400 ppm (Flame C), 600 ppm (Flame B), and 800 ppm (flame D). Symbols: experiments, lines: simulations.	127
8.16	Measured and simulated mole-fraction profiles of Si ₄ O ₁₀ H ₄ along the HAB for a series of TMS doping concentrations: 400 ppm (Flame C), 600 ppm (Flame B), and 800 ppm (Flame D). Symbols: experiments, lines: simulations.	128
A.1	Measured (symbols) and simulated (lines) mole fraction profiles of main species (e.g. H ₂ , H ₂ O, TMS, O ₂ , CO, CO ₂) and temperature profiles in neat (open symbols) and doped (closed symbols) H ₂ /O ₂ /Ar/TMS-flames. Error bars show the uncertainties of measured temperature and mole fractions. . .	153
A.2	Measured (symbols) and simulated (lines) mole fraction profiles of SiO ₂ , Si(OH) ₄ , and Si ₄ O ₁₀ H ₄ in TMS-doped H ₂ /O ₂ /Ar-flames.	155

List of tables

5.1	ΔH_f° (kJ/mol) of 22 reference species for the training set in this section, comparing the atomization and isodesmic methods.	61
5.2	GAVs of organosilane compounds calculated by atomization method (units: ΔH_f° : kJ/mol, S° and C_p : J/mol K).	62
6.1	Comparison between CCSD(T)/CBS and G4 based ΔH_r° (kJ/mol) values for selected isodesmic reactions.	70

6.2	GAVs of stable Si–C–H molecules (Set 3: A re-evaluation of results from atomization method) (units: ΔH_f° : kJ/mol, S° and C_p : J/mol K).	73
6.3	ΔH_f° (in kJ/mol) of 19 added reference compounds, comparing the current G4/isodesmic reaction values with those evaluated using the GAVs of Si–C–H species obtained from set 1 based on atomization energy [7], set 2 using the training set from [7] with ΔH_f° from the G4/isodesmic reaction method, and set 3 with 19 new compounds added into the training set (see text).	74
6.4	Group contributions to ΔH_f° , S° , and C_p for Si–C–H radicals (units: ΔH_f° : kJ/mol, S° and C_p : J/mol K).	76
6.5	GAV for ΔH_f° , S° , and C_p of radical-adjacent groups (categories A and B) (units: ΔH_f° : kJ/mol, S° and C_p : J/mol K).	77
6.6	GAV for ΔH_f° , S° , and C_p of double-bonded groups (units: ΔH_f° : kJ/mol, S° and C_p : J/mol K).	78
7.1	Isodesmic reactions and their standard reaction enthalpies (ΔH_r° , kJ/mol) computed using G4, G4MP2, and CBSQB3 composite methods for the Si–C–H–O system.	86
7.2	Comparison of ΔH_f° (kJ/mol) and uncertainties calculated for the training set.	89
7.3	GAVs of ΔH_f° (298 K), S° (298 K) and $C_p(T)$ for stable and single-bonded Si–C–H–O species. The GAVs of ΔH_f° are based on the G4/isodesmic reaction values listed in Table 7.2; the C_p and S° are calculated at the RRHO (rigid-rotor and harmonic-oscillator) level with molecular parameters obtained using the B3LYP/6-31G(2df,p) method. (unit: ΔH_f° : kJ/mol. S° and C_p : J/mol K)	91
7.4	Comparison of ΔH_f° (kJ/mol) reported in ref [8] and those predicted by the present GAVs.	93
7.5	Isodesmic reactions used for the species with Si=O double bonds and their standard enthalpies of reactions (kJ/mol) calculated at several levels of theory.	94
7.6	Enthalpies of formation ΔH_f° (kJ/mol) values and uncertainties of double-bonded Si=O species determined from the respective isodesmic reactions of Table 7.5	94
7.7	GAVs of ΔH_f° (298 K), S° (298 K) and $C_p(T)$ for Si=O containing species. The GAVs of ΔH_f° are based on the G4/isodesmic reaction values listed in Table 7.5; the C_p and S° are calculated at the RRHO level with molecular parameters obtained using the B3LYP/6-31G(2df,p) method. (units: ΔH_f° : kJ/mol, S° and C_p : J/mol K).	94

7.8	Isodesmic reactions used for the cyclosiloxane species their standard enthalpies of reactions (kJ/mol) calculated at the CBSQB3 level of theory. . .	96
7.9	The training set species and their standard ΔH_f° (kJ/mol) values and estimated uncertainties of cyclo-siloxanes from CBSQB3/isodesmic reaction.	98
7.10	GAVs of ΔH_f° (298 K), S° (298 K) and $C_p(T)$ for D3, D4, and D5 derivatives (units: ΔH_f° : kJ/mol, S° and C_p : J/mol K).	99
8.1	Summary of flame conditions in the present work. Flow rates are in standard liter per minute (273.15 K, 1013.25 mbar).	103
8.2	Standard enthalpies of formation predicted by the G4-method.	108
8.3	List of reactions for describing TMS oxidation. Units of $k = AT^b \exp(-E_a/RT)$ are cm, s, mol, and K. As described in the text: Simulations were carried out using global reactions 14, 18, and 19. Reactions 14a-e, 18a-f, and 19a-e are suggested to explain the underlying chemistry behind these global processes and are discussed in the text. Also reactions 21 and 25-28 are global reactions. $\text{Si}_2(\text{OH})_8$ is envisioned as a hydrogen-bonded adduct of two $\text{Si}(\text{OH})_4$ molecules.	111
8.4	Source of reaction rates used in the TMS mechanism.	124

Nomenclature

Symbols

$[X_k]$	Concentration of species X_k
$\alpha_{k,i}$	Collisional efficiency
β	Collision efficiency
β_j	Group additivity value of group j
δ_k	Dipole moment
$\dot{\omega}_k$	Volumetric molar production
\dot{m}''	Mass flux
ε_k	Lennard-Jones potential well-depth
η_k	Viscosity of species k
\hat{h}	Heat transfer coefficient
λ	Thermal conductivity
λ_k	Individual species conductivity
$\Omega_{kk}^{(2,2)*}$	Collision integral
ρ	Fluid density
σ_{ij}	Reduced collision diameter
σ_k	Collision diameter for the " $k - k$ " interaction potential
\mathbf{V}_k	Diffusion velocity vector of species k

A	Surface area
C^\ddagger	Activated complex
c_p	Heat capacity
D_{ij}	Binary diffusion coefficients
D_{kk}	Self-diffusion coefficient
E_a	Activation energy
f_ξ	Fitness function
h	Planck's constant
$H_{f,298}^\circ$	Standard enthalpy of formation
h_k	Enthalpy of species k
$j_{k,z}$	Diffusive mass-flux of species k
k	Rate constant
k_e	Excitation rate constant
k_B	Boltzmann constant
$K_{c,i}$	Equilibrium constant of reaction i
$k_{f,i}$	Forward rate constants
$k_{r,i}$	Reverse rate constants of reaction i
m_{ij}	Reduced molecular mass
M_k	Molecular weight of species k
m_k	Molecular mass of species k
N_a	Avogadro number
N_r	Number of reactions
N_s	Number of species
P	Steric factor

P_r	Reduced pressure
q^\ddagger	Partition function for the activated complex
q_i	Rate of progress of reaction i
R	Universal gas constant
S_L	Laminar burning velocity
T_∞	Environment temperature
T_k^*	Reduced temperature
$U(x_i)$	Uncertainty of reference species i
$v'_{k,i}$	Stoichiometric coefficient of forward reaction i
$v''_{k,i}$	Stoichiometric coefficient of reverse reaction i
V_k	Diffusion velocities
X_k	Mole-fraction of species k
Y_k	Mass fractions
Y_k	Mass-fraction of species k
T_b	Boiling temperature

Abbreviations

CC	Coupled-Cluster
CFD	Computational Fluid Dynamics
CVC	Chemical Vapor Condensation
CVD	Chemical Vapor Deposition
DFT	Density Functional Theory
FSP	Flame Spray Pyrolysis
GA	Genetic Algorithm
GAVs	Group Additivity Values

- HAB Height Above the Burner
- HF Hartree–Fock
- LIF Laser-Induced Fluorescence
- NIST National Institute of Standards and Technology
- NNI Non-next-nearest Neighbor Interactions
- PECVD Plasma-Enhanced Chemical Vapor Deposition
- QM Quantum Mechanics
- QRRK Quantum Rice Ramsperger Kassel)
- QSPR Quantitative Structure-Property Relationship
- RES Resonance Corrections
- RF Radio-Frequency
- RRK Rice Ramsperger Kassel
- RSC Ring Strain Corrections
- RSM Response Surface Methodology

Chapter 1

Introduction

1.1 Motivation

Nanoparticles are commonly used in industrial applications such as semiconductor devices, dirt-repellent surfaces, cancer treatment, and fuel cells. Particles of nanosize structure with diameters below 100 nm are at the core of this technology. The size, shape, and size distribution of particles determine their physical and chemical properties. By using nanoparticles, new materials can be produced stronger, lighter, more durable, and more reactive among other qualities. The synthesis methods are designed in a way to yield the desired particle properties. Carbon black, titanium dioxide (TiO_2), and silicon dioxide (SiO_2) dominate the aerosol-made material market by volume and value followed by zinc oxide (ZnO), nickel (Ni), tungsten carbide (WC), and others.

There are two major industrial approaches for nanoparticle synthesis. The first approach is the bottom-up method that allows the manipulation of particles at a molecular level. This method is favorable due to the lower cost of production and is achieved by liquid-phase and gas-phase synthesis. The sol-gel method is an example of a bottom-up method achieved by liquid-phase synthesis using metal-organic precursors in a solvent to form inorganic materials. The liquid-phase processes are generally time-consuming and need many steps to achieve pure dry powders as the final nanoparticle product. The advantages and an updated review of the liquid-phase synthesis of nanoparticles are discussed in [9–12]. The second approach is the top-down method that begins with larger initial structures to nanoscale structures. Mechanical milling is an example of a top-down method for the synthesis of metal oxide nanoparticles such as zinc oxide, titanium oxide, and vanadium oxide [13, 14]. A schematic of both methods is shown in Fig. 1.1.

Gas-phase synthesis of particles is performed in flow reactors such as hot-wall reactors and plasma reactors, where the synthesis process differs on how energy is supplied to the

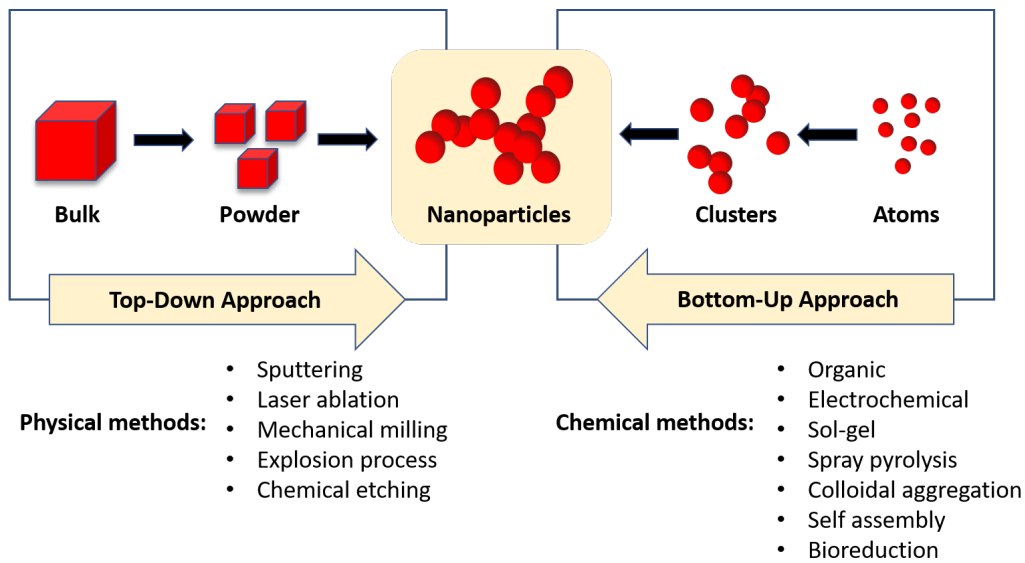


Fig. 1.1 Schematic of top-down and bottom-up synthesis approaches. Adapted figure from Nunes et al. [1] with permission from Elsevier.

system. Heat energy is necessary to activate the required gas-phase reactions. Hot-wall reactors are used to exploit the wall heat transfer method that operates under a wide range of conditions. They are designed to have maximum control over the temperature history of the particles. The process design is challenging due to the axial and radial temperature gradients. Another alternative to provide the energy source is by a plasma (microwave, radio-frequency, or electric arc). Plasma reactors are very common for the investigation of nanoparticle synthesis in laboratory scales [15, 16]. The plasma is achieved by high energy, which leads to the ionization of atoms and molecules in the reactor. An exhaustive review of the gas-phase synthesis of nanoparticles can be found in [17]. While gas-phase synthesis is widely used in industrial processes, a deep understanding of it remains very challenging. Schulz et al. [18] have reviewed the state of the art in the gas-phase synthesis of functional nanomaterials, focusing on the scientific challenges concerning the precursor chemistry and particle formation.

Flame synthesis is by far the most widely used gas-phase method by almost 90% (by value and volume) production of aerosol-made commodities including carbon-black (Cabot, Columbia), fumed silica (Cabot, EVONIK), pigmentary titania (DuPont, Kerr-McGee), and optical fibers (Heraeus, Sumitomo) [19]. Several million metric tons of nanoparticles are annually produced with flame reactors in industry [19]. Many parameters influence the characteristics of the final nanoparticle product within a few milliseconds in the flame synthesis. The flame temperature and particle residence time are the most important parameters [20]. The flame temperature field is influenced by the initial reactants and burner geom-

etry. The scale-up and design of flame aerosol reactors are also investigated by Wegner and Pratsinis [21] for the gas-phase synthesis of silica nanoparticles. The final nanoparticle product size depends on the reactant mixing configuration [22]. The turbulence and buoyancy effects can dramatically change the flame structures and affect the chemical reaction kinetics investigations [23]. Therefore, most of the experimental investigation of flame synthesized nanoparticles are done with laminar premixed flat flame [24], stabilized either at the cooled burner matrix (burner stabilized) [25, 26] or a cooled plate placed downstream (stagnation-point stabilized) [27].

Choice of precursors has also a significant influence on the characteristics of the final nanoparticle product. Kammler et al. [19] review the choice of precursors in flame synthesis of nanoparticles. Zachariah and Semerjian [28] and Ehrman et al. [29] specifically studied different silica precursors. The most studied silicon-organic precursor in the literature is tetraethoxysilane (TEOS) since it is cheap and safe [30–34]. In order to be able to predict the heat release rate in the combustion processes and also calculating the equilibrium state, the thermodynamics properties of species involved in the combustion process are required. Thermodynamics data of silicon-organic compounds are usually calculated in the literature for a specific precursor [8]. In this work, the focus is to provide a comprehensive database for the thermodynamic properties of silicon-organic compounds independent from the choice of a precursor. The developed tetramethylsilane (TMS) mechanism and the thermodynamic properties of silicon-organic compounds are going to help understand the kinetics behind the flame synthesized silica nanoparticles.

1.2 Novelty of the work

This thesis presents the following novel contributions:

- The calculation of thermodynamic properties of silicon-organic molecules representing the Si–C–H and Si–C–H–O system. The quantum chemical calculation, group additivity method, and multivariate regression analysis are used to regress the group additivity values (GAVs). The GAVs for a wide range of silicon-organic compounds are reported that can be used for the calculation of thermodynamics properties of many larger silicon-organic compounds without running quantum mechanical simulations.
- The development of a chemical kinetics model for the combustion of tetramethylsilane (TMS) as a precursor for the synthesis of silica nanoparticles. The mechanism development is based on the experimental data in a low-pressure laminar flame. The developed mechanism is validated against the new experiments.

- The extension of the genetic algorithm-based optimization technique to consider all three parameters of Arrhenius expression of the rate coefficients for the optimization against the experimental data.

1.3 Structure of this thesis

The subsequent chapters of this thesis are structured as follows:

Chapter 2 covers various techniques for the synthesis of silica, as well as the commercial significance of silica powders and thin-films in industry. A literature review of important contributions to different choice of precursors for the silica nanoparticles synthesis is presented at the end of this chapter.

Chapter 3 describes a detailed theoretical background of one-dimensional laminar flames and homogeneous reactor, as well as the kinetics modeling and mass-action kinetic. At the end of this chapter, the reaction mechanism development and its requirements are discussed. Theoretical discussions in Chapter 3 can be applied generally to any materials synthesis such as titania (TiO_2), iron oxide (Fe_2O_3) and is not limited to silica (SiO_2).

Chapter 4 describes the mathematical methods and computer assisted algorithms that are used to optimize reaction mechanisms and calculate thermochemistry of Silicon-organic species, such as group additivity method, regression analysis, and genetic algorithm-based optimization technique.

Chapter 5, 6, and 7 provide the thermodynamics properties of Si-containing compounds as well as providing the group additivity values (GAVs) for complete Si-C-H and Si-C-H-O systems. These chapters provide the complete database needed for thermochemistry of Si-containing compounds.

Chapter 8 presents the development and validation of a reaction mechanism for TMS-doped flames. The kinetic model for combustion of TMS is developed based on the experimental data and the resulting mechanism is validated for different load of TMS.

Chapter 9 provides a summary of the conclusions of this thesis and suggests areas for future investigations.

Chapter 2

Gas-phase synthesis of Silica nanoparticles

Gas-phase synthesis of silica nanoparticles with specific control of the size, morphology, and particle size distribution and agglomeration index requires a deep understanding of the underlying synthesis process and kinetics knowledge. Providing a certain amount of energy to initiate the reactions is essential. Among the many material systems synthesized via the gas-phase route, silica is of particular interest because of its technical and commercial significance. The versatility of silica-based products and precursor materials drives interest in process modeling.

This chapter focuses on an overview of the application and importance of silica/precursor reaction kinetics. The subsequent chapter is then dedicated to the theoretical background of combustion and chemical modeling.

2.1 Commercial significance of silica powders and thin silica layers

Silica is one of the most versatile gas-phase synthesized materials. The commodities cover: nano-powders with a wide range of application, thin layers as an electrical or chemical barrier, and glass of well-defined composition. There are several advantages of the gas-phase synthesis of materials:

1. Well adjustable composition of the material. In the case of electronic or optical materials, dopants can be added and mixed into the material at a level of homogeneity not achievable by mixing in the liquid phase. [35].

2. High-purity of nanoparticles is determined by the purity of the gaseous or liquid precursors. [21].
3. Adjustable size properties, from nano-particles or layers of few molecules thickness up to bulk materials
4. Continuous processes in contrast to the discontinuous batch reactors.

Silica (SiO_2) is composed of the two most abundant elements in the earth's crust. It is used widely in industrial applications and it can be found in products which we use every day. It exists mostly in the form of quartz as the second most common mineral in the earth's crust. Gas-phase synthesis of silica is achieved in a variety of techniques for different applications. Silica nanoparticles are widely used as fillers in plastics, rubbers, and coatings as well as ingredients in food, pesticides, and personal care products. Silica applications have also been explored in the field of biotechnology for biosensing and drug delivery.

Fumed silica is formed in flame pyrolysis of silicon tetrachloride through the growth and aggregation of SiO_2 seed. It has a very low bulk density and a large surface area. It is used in industrial applications as an adsorbent due to its high specific surface area that can create a powder containing up to 95% water. Fumed silica is also used as a reinforcement filler to enhance the mechanical properties of silicone rubbers. Fumed silica is used to control the rheological properties of adhesives and sealants.

Hydrophilic and hydrophobic fumed silica powders are used as anti-settling agents to enable dispersion and to stabilize pigments, filler materials during production and storage. The hydrophilic fumed silica powders are also widely used in the food industries as food additives. They are odorless and can be added to foods without affecting the taste and color. Other applications of fumed silica are as an agent for anticaking, transparency, and heat stabilization.

Silica thin-layers have gained considerable attention in the last decade because of their various industrial applications including superhydrophilic self-cleaning surface glass, UV protection films, anti-reflection coatings, ion barriers in flat panel displays such as liquid crystal displays, and insulating materials [36, 37]. The biggest application of insulating silica thin-layers is in the semiconductor industries [38–40].

2.2 Synthesis routes for silica powders and thin layers

Silica nanomaterials are produced in a variety of methods. The methods have advantages and disadvantages in the control of shape and size as well as production scale and manufacturing

costs. Two major process routes are used in the synthesis of silica from the gas-phase. Least common, but established process, is the pyrolysis of oxygen-containing silicon compounds in plasmas for the formation of thin layers. [41]. The vast majority of all silica synthesis follows by combustion. [35].

Chemical vapor deposition (CVD) is a gas-phase process widely used materials-processing technology. CVD is a versatile deposition technique since a wide range of reactants and precursors can be used to deposit a given film. CVD reactors are categorized into hot-wall and cold-wall. In hot-wall reactors, the surrounding walls are heated. In cold-wall reactors, only the substrate holder is heated. The most common variation of CVD is a plasma-enhanced chemical vapor deposition (PECVD) that has the advantage of operation at lower temperature [42, 43, 41].

Silica nanoparticles are also produced through the high-temperature flame decomposition of metal-organic precursors. This process is also referred to as chemical vapor condensation (CVC) [44]. In a typical CVC process, silica nanoparticles are produced by reacting silicon tetrachloride, (SiCl_4) with hydrogen and oxygen [45].

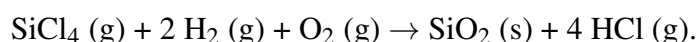
The flame environment provides the source of energy to initiate the reaction and particle nucleation. Combustion synthesis is widely used because of its efficiency, continuous process, and scaled-up production [19]. There are many flame reactor configurations for feeding the flame with precursors in vapor or mixed with liquid fuel [46, 47]. Flame reactors have a variety of regimes like premixed, non-premixed, laminar, and turbulent. Mueller et al. [48] investigated the scaling-up of nanoparticle synthesis by the versatile flame spray pyrolysis (FSP) process. Wegner and Pratsinis [49] investigated the scaling-up of diffusion flame aerosol reactors. A lot of effort has been made for the investigation of FSP reactors using CFD simulations [50–52]. Stark and Pratsinis [53] investigated aerosol flame technology. They gave a deeper understanding of the process of making more sophisticated products with high functionality rather than pure silica and titania.

2.3 Various type of precursors

The properties of the product may depend on the properties of the precursor. Oxygen-containing compounds form silica already at low temperatures, other compounds have favorable combustion properties. Chlorine-free precursors are safer in their handling and do not require closed process loops. Moreover, the kinetics of the precursor decomposition and combustion determine such important design parameters as process energy consumption, residence time, and the mass flow rate of necessary support gases, either inert or combustible.

2.3.1 Inorganic silicon compounds

The dominant route of silica nanoparticle synthesis is in continuous flame hydrolysis of silicon tetrachloride (SiCl_4). In the flame environment, the hydrogen and oxygen react with SiCl_4 . The formation of SiO_2 can be described by hydrolysis of SiCl_4 . The overall reaction is as follow:



This synthesis route is very successful in the industry for the production of fumed silica due to cheap H_2 along with the ability to sell hydrochloric acid (HCl). The fumed silica manufactured by Evonik is produced by this technique. A hydrogen flame that contains SiCl_4 burns continuously in the reaction chamber producing the desired SiO_2 and HCl. The exhaust hot gas needs to be cooled down before collecting the solid silica. The solid silica still contains HCl on the surface that needs to be removed by the deacidification step. The manufacture of optical fibers can also be performed by the modified chemical vapor deposition process involving SiCl_4 oxidation in pipe flow [54]. A lot of efforts have been made to investigate the silica synthesis with SiCl_4 as a precursor for kinetics study, diagnostics, and numerical modeling [55–59].

Silicon nanoparticles are used in a wide range of industrial applications such as biomedical, thermoelectric, and microelectronic applications. So et al. [60] synthesized the nanopowder from a gas-phase precursor of monosilane (SiH_4) by a radio-frequency (RF) thermal plasma. The RF thermal plasma provides a high-temperature and contamination-free environment to produce pure silicon materials. Ultrafine powders with a mean particle diameter (20–30) nm can be also synthesized from high purity SiH_4 by laser-induced gas-phase reactions. Tamir and Berger [61] observed the formation of circular Si grains during the decomposition of SiH_4 molecules from SiH_4/Ar gas mixture under excimer laser irradiation. Khokhlov et al. [62] used the technology of CVD synthesis of ultradispersed silicon powders (nc-Si) in laser-induced SiH_4 gas reactions. Kim et al. [63] synthesized silicon (Si) nanoparticles by using pyrolysis at atmospheric and low pressure and investigated the characteristics of the Si nanoparticles that are used in applications such as flash memory and energy device fabrication. Plasma-enhanced chemical vapor deposition (PECVD) in silane-hydrogen (SiH_4/H_2) mixtures are widely also used to synthesize silicon thin films [64].

2.3.2 Organic silicon compounds

In the last decade, the gas-phase production of silica by hexamethyldisiloxane (HMDSO), tetraethoxysilane (TEOS), and tetramethylsilane (TMS) as halide-free and inexpensive precursors has increased. Many experimental and numerical studies have been performed to investigate the characterization of silica nanoparticles by using HMDSO, TEOS, and TMS as precursors. In the following, some of the state-of-the-art contributions are shortly discussed.

Herzler et al. [30] carried out a single-pulse shock tube experiment to investigate the decomposition of TEOS. They observed ethylene and ethanol as the major final products and developed a kinetic model that quantitatively accounts for the observed products. The experimental study to measure ignition delay times of TEOS and HMDSO mixtures diluted with dry and humid synthetic air was performed by Abdali et al. [65, 66]. The ignition delay times were also measured as a function of water vapor concentration in the initial gas mixture. A kinetic model and an inception pathway for the flame synthesis of silica nanoparticles from TEOS was created by Shekar et al. [31]. They developed the kinetic model by generating reactions for species that were observed in high concentrations at equilibrium. In their model Si(OH)_4 was hypothesized to be the final product of TEOS decomposition.

Nurkowski et al. [33, 34] developed a detailed kinetic model for the thermal pyrolysis of TEOS. The chemical mechanism was developed based on an analogy to an existing mechanism for the decomposition and combustion of ethanol [67]. They also provided a skeletal mechanism for a hydrogen–oxygen environment. Thermodynamic properties for Si-containing species are calculated via the balanced reactions method and the developed mechanism is validated against the experimental data.

HMDSO is one of the most commonly used materials in the plasma treating process, primarily used for coating in industry. The thermochemistry and the kinetics of HMDSO are still not well understood, despite the huge interest in HMDSO as a cheap and safe precursor in the industry. HMDSO is liquid, with reasonable vapor pressure, not poisonous, and not explosive. The experimental and numerical studies of HMDSO have been also challenging. Chagger et al. [68] investigated the combustion of HMDSO in an opposed diffusion flame. They proposed a preliminary reaction mechanism for the formation of SiO_2 . Feroughi et al. [69] investigated the flame synthesis of silica in a HMDSO-doped premixed H_2/O_2 flat flame. The comprehensive in situ and inline diagnostics techniques are used as well as the CFD simulations based on a simple model for gas-phase reactions and particle formation and growth. The only intermediate species that could be detected was the gas-phase silicon oxide (SiO) via laser-induced fluorescence (LIF). In their experiments, a double peak behavior of SiO mole-fraction was observed, similar to other silica precursors [70, 71]. Chrystie et al. [72] studied the influence of the precursor on the gas-phase reactions before the formation of

silica nanoparticles with a focus on SiO-based chemistry. They measured temperature fields in the flame and quantitative SiO mole-fraction profiles [73, 72] along with the height above the burner (HAB) via LIF-imaging using NO and SiO as target species. They also observed an intermediate minimum in SiO concentration that occurs in the reaction zone (the double peak behavior).

TMS is used as a precursor in the production of SiC films and particles by CVD reactors. It has the advantage to be a safe, non-explosive, and non-corrosive precursor [74]. Sela et al. [75] investigated the decomposition of tetramethylsilane ($\text{Si}(\text{CH}_3)_4$; TMS) and tetramethoxysilane (TMOS) behind reflected shock waves and derived elementary kinetics mechanisms [76]. The first attempt to analyze the high-temperature combustion chemistry of TMS was undertaken by Reed [77]. TMS pyrolysis was previously studied, e.g. by Baldwin et al. [78], Clifford et al. [79], and Taylor and Milazzo [80]. In all these studies, a combination of a flow reactor with gas chromatography is applied to detect major stable reaction products. Recently, Karakaya et al. [81] proposed a possible decomposition pathway of TMS in a $\text{H}_2/\text{O}_2/\text{Ar}$ flame and discussed the formation of stable monomers and the first smaller silicon oxide clusters based on their experimental observations.

Chapter 3

Theoretical background of combustion and chemical kinetics

Gas-phase synthesis of (nano-) materials involves chemical transformation and material transport as inseparable physical processes. Modeling of the gas-phase synthesis requires therefore a description of the flow and of the chemical reaction kinetics. The theoretical framework involves continuum mechanics for description of the transport at the device or reactor scale, kinetic gas theory at the scale of molecular collisions and quantum mechanics in the description of intra-molecular processes. While the gas-phase synthesis process is described at the reactor volume scale, the processes at next smaller scales are represented via closure models. It is a big advantage of gas-phase processes, in particular at moderate pressure, that the closure relations can be deduced from higher-level theories. The integral effects of molecular collisions are described by the kinetic gas-theory, the mechanics and thermodynamics of molecules are described by quantum-mechanics.

The focus of this chapter is to provide an overview of the theoretical framework used for description of chemically reacting flows and the model simplifications necessary to conduct the research reported in this thesis.

3.1 Modeling of laboratory experiment configurations

In the real world, production scale facilities are inappropriate as a source for detailed understanding of the underlying physics and chemistry. Usually, the production process exhibits a complex flow field with a wide residence time spectrum and is inaccessible to detailed measurements of the local thermochemical state. In the reaction kinetics research, a set of standard experiments exists, which were designed to provide a good accessibility

and additionally provide either a steady, laminar, nearly one-dimensional flow field, or to provide a perfectly mixed state where all transport phenomena could be neglected. Such simplified setups are described by sets of ordinary differential equations derived from the general conservation laws [82]. The measured data from such experiments, act then as support points for development and validation of models. The modeling of one-dimensional laminar flames and zero-dimensional reactors are described in the following sections.

3.1.1 Constant-pressure homogeneous reactor

The batch reactor, the plug-flow reactor, and the perfectly stirred reactor are popular laboratory reactors for the investigation of chemical kinetics. Shock tube experiments are widely used to measure ignition delay time and species compositions over time. In the homogeneous reactor model the convective changes are neglected and only local changes are considered. This simplification enables the investigation of complex chemical kinetics models and reduces the computational time. The thermal energy equation for a constant-pressure homogeneous reactor simplifies as:

$$\rho c_p \frac{dT}{dt} = - \sum_{k=1}^{N_s} h_k \dot{\omega}_k M_k + \frac{\hat{h}A}{V} (T_\infty - T) \quad (3.1)$$

In the above equation, \hat{h} is the heat transfer coefficient, $\dot{\omega}_k$ denotes the volumetric molar production (destruction) rate of species k determined by chemical kinetics, h_k is the enthalpy of species k , M_k is molecular weight of species k , A is the surface area, T_∞ is the known environmental temperature.

3.1.2 One-dimensional laminar flames

Burner-stabilized laminar premixed flames are primarily used to study the chemical kinetics of combustion specially for the nanoparticle synthesis in flames. Modeling of premixed laminar flames facilitates the interpretation of experimental data and the influence of flow-field properties on the product nanoparticles. The properties of the combustion flow-field such as equivalence ratio can affect the properties of the product particles in the synthesis flames [20, 19]. The formation of stable and fully oxidized nanoparticles is normally obtained in flames burning under fuel-lean condition [20].

The properties of nanoparticles depend strongly on the temperature of the flame, the decomposition of the precursor, and the particle formation [83]. The pressure of a laminar flame is also playing an important role in the characteristics of the synthesized nanoparticles.

The synthesis of nanoparticles in flames is normally done with low-pressure flames which have several advantages over the atmospheric flames. For example, precursors decompose at lower temperatures, and particle residence times are shorter, which leads to significant reduction in collision of “hot” particles, and hence inhibiting agglomeration [84]. The differences between low pressure and atmospheric pressure synthesis of nanoparticles in flat flames are discussed by Glumac et al. [85]. The flat flames are also an excellent configuration for applying diagnostic techniques. Flat flames give an opportunity to adjust the equivalence ratio of the flames and the pressure to narrow or widen the flame zone [86].

A flame is called stoichiometric when the fuel and oxidizer consume each other completely to form the final products in a global reaction. If there is an excess of oxidizer, it is called lean flame. The mathematical description for gas-phase chemically reacting flow consists of a set of partial differential equations, namely the conservation equations that describe the temporal and spatial variation of all the properties that describe the state of the system (e.g., species mass fractions, specific enthalpy, pressure and velocity field). Modeling of flames has to consider that the governing processes (i.e., flow, molecular transport, and chemical reaction) occur at time scales that differ by orders of magnitude. Therefore, many simplifications are applied on the general conservation equations to facilitate the interpretation and validation of kinetics for combustion of precursors in the gas-phase synthesis of nanoparticles. The governing equations are simplified for one-dimensional steady flow as follow:

Mass conservation equation:

$$\frac{\partial \rho}{\partial t} + \frac{\partial \rho u}{\partial z} = 0 \quad (3.2)$$

Momentum conservation equation:

$$\rho \frac{\partial u}{\partial t} + \rho u \frac{\partial u}{\partial z} = -\frac{\partial p}{\partial z} + \frac{\partial}{\partial z} \left(\mu \frac{\partial u}{\partial z} \right) \quad (3.3)$$

Species conservation equation:

$$\rho \frac{\partial Y_k}{\partial t} + \rho u \frac{\partial Y_k}{\partial z} = -\frac{\partial j_{k,z}}{\partial z} + \dot{\omega}_k M_k \quad (3.4)$$

Thermal energy equation:

$$\rho C_p \frac{\partial T}{\partial t} + \rho u C_p \frac{\partial T}{\partial z} = \frac{\partial}{\partial z} \left(\lambda \frac{\partial T}{\partial z} \right) - \sum_{k=1}^{N_s} C_{pk} j_{k,z} \frac{\partial T}{\partial z} - \sum_{k=1}^{N_s} h_k \dot{\omega}_k M_k \quad (3.5)$$

In the above equations, ρ is the fluid density, p is the pressure, λ is the thermal conductivity, h_k is the enthalpy of species k , $j_{k,z}$ is the diffusive mass-flux of species k , Y_k is the mass-fraction of species k , $\dot{\omega}_k$ denotes the volumetric molar production (destruction) rate of species k determined by chemical kinetics, M_k is the molecular weight of species k , N_s is the number of species in the mixture, μ is the dynamic viscosity of the fluid.

Boundary conditions

In a burner-stabilized flame, the mass flux \dot{m}'' [$\text{kg m}^{-2}\text{s}^{-1}$] and inlet temperature are known. In a freely propagating flame, the flame speed is calculated at a specified pressure and inlet temperature. The governing equations for both the burner-stabilized and freely propagating flames are the same, but the boundary conditions are different. The species mass fractions are not suitable to be specified as boundary conditions, due to the diffusion of species on the flame side of the burner to the burner surface. Therefore, the balance of the species fluxes at the burner surface can be written as:

$$\dot{m}'' \varepsilon_k = \dot{m}'' Y_k + \rho Y_k V_k, \quad (3.6)$$

where the mass fractions Y_k , diffusion velocities V_k , and mass density ρ are computed as part of the solution. Alternatively, the boundary condition can be stated as:

$$\varepsilon_k = Y_k + \frac{j_{k,z}}{\dot{m}''}, \quad (3.7)$$

where the values of ε_k are specified. For the adiabatic freely-propagating flame, \dot{m}'' is an eigenvalue that is determined as part of the solution. Therefore, an additional constraint is needed. The temperature is specified at some specific mesh point and at these points the energy equation (3.5) must be satisfied and the temperature must be equal to the specified temperature. At the burner surface and at the hot boundary, all gradient must be zero to prevent diffusive losses of species or energy from the system. Once the mass-flux \dot{m}'' is determined, the laminar burning velocity is calculated from $S_L = \dot{m}''/\rho$.

3.2 Transport properties

Transport data are needed to account for heat and mass transfer during the simulation of one-dimensional flames. These quantities are diffusivity, viscosity, and thermal conductivity of the species. There are mainly two approaches to describing the transport properties of the mixture, depending on the application, namely the mixture-averaged and the multicomponent

approach. The multicomponent formulation is more accurate in comparison to the mixture-averaged approach, but it is computationally very expensive. A detailed description of the transport properties is given by Bird [87] and Hirschfelder et al. [88].

Viscosity

Reacting flows are always dealing with mixtures of fluids. Thus, the mixture viscosity is evaluated from the individual species properties. Pure species viscosities are given by the standard kinetic theory expression:

$$\mu_k = \frac{5}{16} \frac{\sqrt{\pi m_k k_B T}}{\pi \sigma_k^2 \Omega_{kk}^{(2,2)*}}, \quad (3.8)$$

where σ_k is the collision diameter for the " $k-k$ " interaction potential, m_k is the molecular mass of species k , k_B is the Boltzmann constant, T is the temperature, and $\Omega_{kk}^{(2,2)*}$ is the collision integral which depends on the reduced temperature T_k^* and the reduced dipole moment, expressed as:

$$T_k^* = \frac{k_B T}{\epsilon_k}, \quad \delta_k^* = \frac{1}{2} \frac{\mu_k^2}{\epsilon_k \sigma_k^3}, \quad (3.9)$$

where ϵ_k is the Lennard-Jones potential well-depth and δ_k is the dipole moment.

The mixture viscosity is formulated by Wilke [89] as follow:

$$\mu_{mix} = \sum_{k=1}^{N_s} \frac{X_k \mu_k}{\sum_{j=1}^{N_s} X_j \phi_{kj}}, \quad (3.10)$$

where

$$\phi_{kj} = \frac{1}{\sqrt{8}} \left(1 + \frac{M_k}{M_j}\right)^{-\frac{1}{2}} \left[1 + \left(\frac{\mu_k}{\mu_j}\right)^{\frac{1}{2}} \left(\frac{M_j}{M_k}\right)^{\frac{1}{4}}\right]^2. \quad (3.11)$$

In the above equations, X_k is mole fraction and M_k is the molecular weight of the species k .

Thermal conductivity

The thermal conductivity of a mixture must be derived in terms of the individual species conductivity. It can be calculated by the expression proposed by Marthur and Saxena [90]:

$$\lambda_{mix} = \frac{1}{2} \left(\sum_{k=1}^{N_s} X_k \lambda_k + \frac{1}{\sum_{k=1}^{N_s} X_k / \lambda_k} \right), \quad (3.12)$$

where λ_k is individual species conductivity. The λ_k are computed based on the translational, rotational, and vibrational contributions as given by Warnatz [91].

$$\lambda_k = \frac{\eta_k}{M_k} (f_{trans.} C_{v,trans.} + f_{rot.} C_{v,rot.} + f_{vib.} C_{v,vib.}), \quad (3.13)$$

where η_k is the pure species viscosity of the k th species. In the Eq. 3.13, the f are the following functions:

$$f_{trans.} = \frac{5}{2} \left(1 - \frac{2 C_{v,rot.} A}{\pi C_{v,trans.} B} \right), \quad f_{rot.} = \frac{\rho D_{kk}}{\eta_k} \left(1 + \frac{2 A}{\pi B} \right), \quad f_{vib.} = \frac{\rho D_{kk}}{\eta_k}. \quad (3.14)$$

In the Eq. 3.14, D_{kk} is the "self-diffusion" coefficient defined by kinetic gas theory [88]. The A and B are defined as:

$$A = \frac{5}{2} - \frac{\rho D_{kk}}{\eta_k}, \quad B = Z_{rot.} + \frac{2}{\pi} \left(\frac{5 C_{v,rot.}}{3 R} + \frac{\rho D_{kk}}{\eta_k} \right). \quad (3.15)$$

The molar heat capacity C_v relationships are different depending on the structure of the molecule. If the molecule is linear:

$$C_{v,trans.} = \frac{3}{2}R, \quad C_{v,rot.} = R, \quad C_{v,vib.} = C_v - \frac{5}{2}R. \quad (3.16)$$

If the molecule is not linear:

$$C_{v,trans.} = \frac{3}{2}R, \quad C_{v,rot.} = \frac{3}{2}R, \quad C_{v,vib.} = C_v - 3R. \quad (3.17)$$

Mass diffusion

The species diffusive mass-flux vector is defined as

$$\mathbf{j}_\alpha = \rho Y_\alpha \mathbf{V}_\alpha. \quad (3.18)$$

The diffusive mass-flux term can be estimated using equal diffusivities for all species, multi-component or mixture-averaged approaches. The \mathbf{V}_k denotes the diffusion velocity vector of species k , which in the multi-component method includes Stefan-Maxwell diffusion, diffusion due to a pressure gradient, diffusion due to a body force, and the Soret effect. The exact evaluation of V_k requires the solution of a linear system of size N_s^2 at every computational point which is very complicated. The simplifying assumption is to consider equal diffusivities for each species that shows unity Lewis number properties. This assumption fails to include the differential diffusion fluxes that are particularly important for light species. A common method to include the differential fluxes in an affordable manner is the mixture-average diffusivity assumption, which employs individual mass diffusivity for each species that depends on the temperature and the thermal differential diffusion. Thus, the diffusion velocity vector of species k can be evaluated by Fick's formulation:

$$\mathbf{V}_k = -\frac{1}{X_k} D'_{km} \nabla X_k. \quad (3.19)$$

The "mixture-averaged" diffusion coefficient D'_{km} is calculated from the binary diffusion coefficients D_{ij} as:

$$D'_{km} = \frac{1 - Y_k}{\sum_{j \neq k} X_j / D_{kj}}. \quad (3.20)$$

The mass diffusion coefficient is derived from the kinetic theory of gases. The binary diffusion coefficient mentioned in Eq. (3.20) is described by the Chapman-Enskog theory:

$$D_{ij} = \frac{3}{16} \frac{\sqrt{2\pi k_B^3 T^3 / m_{ij}}}{p \pi \sigma_{ij}^2 \Omega_{ij}^{(1,1)*}}, \quad (3.21)$$

where k_B is the Boltzmann constant, m_{ij} is the reduced molecular mass, σ_{ij} is the reduced collision diameter, and $\Omega_{ij}^{(1,1)*}$ is the collision integral. The m_{ij} and σ_{ij} can be evaluated as:

$$m_{ij} = \frac{m_i m_j}{m_i + m_j}, \quad \sigma_{i,j} = \frac{\sigma_i \sigma_j}{2}. \quad (3.22)$$

Lennard-Jones potential

The Lennard-Jones potential is often used as the intermolecular potential function to estimate transport properties between molecules i and j as a function of distance [82]:

$$u_{ij}(r_{ij}) = 4\varepsilon_{ij} \left[\left(\frac{\sigma_{ij}}{r_{ij}} \right)^{12} - \left(\frac{\sigma_{ij}}{r_{ij}} \right)^6 \right], \quad (3.23)$$

where ε_{ij} governs the strength of the interaction, σ_{ij} defines a net collision diameter. The r_{ij} is the distance between the centers of mass of molecules i and j . The term proportional to r_{ij}^{-12} dominating at short distances, models the repulsion. The attractive term proportional to r_{ij}^{-6} dominates at large distances.

The most reliable method for obtaining the Lennard-Jones parameters is to experimentally measure the viscosities as a function of temperature for the pure species and fit the experimental data using Eq. (3.8) using ε and σ as adjustable parameters. If experimental transport property data are not available, empirical relationships among physical properties can be used.

The well-depth ε is the maximum energy of attraction between a pair of molecules and the collision diameter σ is the distance at which the intermolecular potential between the two molecules is zero. The Lennard-Jones parameters for many silicon-organic compounds are not available. The volume-increments V_i for Si, H, CH₃, OH, CH₂, and O are 29.7, 2.8, 19.6, 9.7, 16.5, and 6.0 Å³, respectively [92, 93]. The Lennard-Jones potential parameters are estimated for the Si-containing species using the following equations:

$$\varepsilon[K] = 1.2T_b \quad (3.24)$$

$$\sigma[\text{Å}] = 1.45 \left(\sum_{i=1}^n V_i \right)^{1/3} \quad (3.25)$$

In Eq. (3.24), T_b is the boiling point of the corresponding species.

3.3 Modeling of chemical kinetics

Chemical processes can be modeled by detailed kinetic reaction mechanisms which consist of several hundreds or even thousands of reaction steps. Detailed reaction mechanisms are developed for deeper understanding of chemical processes in many fields of science such as combustion, atmospheric chemistry, and process engineering [94]. They describe the

chemical kinetics and the thermodynamics of a chemical process. Chemical kinetics is about how fast chemical reactions proceed and thermodynamics on the other hand is about how stable is one state versus another. In the following section, a brief introduction to the basics of chemical kinetics is given.

3.3.1 Reaction stoichiometry

The stoichiometry of a reaction equation defines the molar ratio between reactants and products. Often, reaction equations describe global chemical processes. Equation (3.26) shows, for example, the global reaction equation for the complete combustion of methane:



Such a global reaction is often based on a complex reaction mechanism consisting of a multitude of elementary reactions. An elementary reaction in turn is a single step reaction.

The global reaction equation for methane combustion can be written similarly to a mathematical expression as follow:

$$1 \text{ CO}_2 + 2 \text{ H}_2\text{O} - 1 \text{ CH}_4 - 2 \text{ O}_2 = 0 . \quad (3.27)$$

In equation (3.27), the chemical species can be denoted by the vector X indexed by k . And the multiplication factors, i.e., the stoichiometric coefficients, by vector v . In this case, $X_1 = \text{"CO}_2\text{"}$, $X_2 = \text{"H}_2\text{O"}$, $X_3 = \text{"CH}_4\text{"}$, $X_4 = \text{"O}_2\text{"}$, and $v_1 = 1$, $v_2 = 2$, $v_3 = -1$, and $v_4 = -2$. The eq. (3.27) as any other reaction equation can be written as follow:

$$\sum_{k=1}^{N_s} v_k X_k = 0, \quad (3.28)$$

where N_s is the total number of species involved in the reaction.

3.3.2 Mass-action kinetics

The rate of reaction can be observed by watching the consumption of a reactant or the formation of a product over time. The rate expression for a general reaction presented in Eq. (3.28) is

$$-\frac{d[X_k]}{dt} = k \prod_{k=1}^{N_s} [X_k]^{v_k}, \quad (3.29)$$

where the factor k is the rate constant and $[X_k]$ represents the concentration of species X_k . In a detailed kinetic reaction mechanism, the set of elementary reactions containing N_r reactions with N_s species can be described as:

$$\sum_{k=1}^{N_s} v'_{k,i} X_k = \sum_{k=1}^{N_s} v''_{k,i} X_k \quad (i = 1, \dots, N_r), \quad (3.30)$$

where $v'_{k,i}$ and $v''_{k,i}$ refer to stoichiometric coefficient of species k in the forward and reverse direction of reaction i , respectively. The rate of progress q_i of reaction i is calculated from forward and reverse reaction rate:

$$q_i = k_{f,i} \prod_{k=1}^{N_s} [X_k]^{v'_{k,i}} - k_{r,i} \prod_{k=1}^{N_s} [X_k]^{v''_{k,i}}, \quad (3.31)$$

where the $k_{f,i}$ and $k_{r,i}$ are the forward and the reverse rate constants for the reaction i , respectively. The q_i in Eq. (3.31) can be positive or negative, depending on which direction of the reaction is proceeding faster. The net production or consumption of species k is

$$\dot{\omega} = \sum_{i=1}^{N_r} v_{k,i} q_i, \quad (3.32)$$

where $v_{k,i}$ is the net stoichiometric coefficient for species k in the reaction i ($v_{k,i} = v''_{k,i} - v'_{k,i}$).

Third-body reactions

Often, radical recombinations require a collision partner, M. When radicals recombine, a highly energized complex is formed. During a recombination involving a collision partner M, energy is transferred from the energized complex to M such that the recombination can lead to the formation of a product. The product of such a reaction is a highly energized intermediate that has to lose the excess energy in another collision with any other molecules present in the system. It should be noted that certain species have enhanced collisional efficiencies which affect the rate of reaction more than other collisional partners. Therefore, the collisional efficiency $\alpha_{k,i}$ is introduced. When calculating the rate-of-progress for reaction i in which a third body is needed, the concentration of the effective third body must be considered:

$$q_i = \left(\sum_{k=1}^{N_s} \alpha_{k,i} [X_k] \right) \left(k_{f,i} \prod_{k=1}^{N_s} [X_k]^{v'_{k,i}} - k_{r,i} \prod_{k=1}^{N_s} [X_k]^{v''_{k,i}} \right). \quad (3.33)$$

If all the molecules present in the system contribute equally as third bodies, then $\alpha_{k,i} = 1$ for all k , and the total concentration of the mixture is

$$[M] = \sum_{k=1}^{N_s} [X_k]. \quad (3.34)$$

Temperature dependence of rate constants

The reaction rate often has a strong temperature dependence. The reaction rate coefficients can be described by a three parameter Arrhenius equation [95]:

$$k_{f,i}(T) = AT^\beta e^{-E_a/RT}, \quad (3.35)$$

where the A , β , E_a , and R are pre-exponential factor, temperature exponent, activation energy, and universal gas constant of the reaction i , respectively.

Pressure dependence of rate constants

Under certain conditions, the rate constants of some reactions are also pressure dependent at a given temperature. If a single species undergoes chemical transformation turning to the final products, the corresponding reaction is called unimolecular reaction. For example, the decomposition of H_2O_2 plays a very important role in the combustion of hydrogen, syngas, and small hydrocarbons. For this reaction, as well as for many other unimolecular reactions, it was observed that at a given temperature the reaction order depends on the pressure. At lower pressures, such a reaction can behave like a second-order reaction, whereas at high pressures, the reaction rate behaves like a first-order reaction. The first attempt to describe this behavior was developed by Lindemann in 1922 [96]. The intermediate pressures in which the decomposition kinetics shifts from first-order to second-order is called "fall-off region". The Arrhenius rate parameters are required for both the high- and low-pressure limiting case, and the Lindemann formulation [97, 98] relate them to produce a pressure-dependent rate expression. The low-pressure rate constants is given as:

$$k_0 = A_0 T_0^\beta e^{-E_0/RT}, \quad (3.36)$$

and the high-pressure rate constants are expressed as:

$$k_\infty = A_\infty T_\infty^\beta e^{-E_\infty/RT}. \quad (3.37)$$

The first-order rate coefficient at any pressure can be calculated by the expression:

$$k = k_{\infty} \left(\frac{P_r}{1 + P_r} \right) F. \quad (3.38)$$

In the Eq. (3.38), F is equal to 1 for the Lindemann theory and the P_r is called reduced pressure and expressed by:

$$P_r = \frac{k_0 [M]}{k_{\infty}}, \quad (3.39)$$

where $[M]$ is the concentration of the mixture and can be calculated by Eq. (3.34) if all the molecules present in the system contribute equally as third bodies. The Lindemann approach can be improved by introducing more complex expression for F proposed by Gilbert et al [99]. The Troe formulation of F is expressed as:

$$\log F = \left[1 + \left(\frac{\log P_r + c}{n - d (\log P_r + c)} \right)^2 \right]^{-1} \log F_{\text{cent}}, \quad (3.40)$$

where the c , n , and d are constants [100, 101] and expressed as:

$$c = -0.4 - 0.67 \log F_{\text{cent}}, \quad n = 0.75 - 1.27 \log F_{\text{cent}}, \quad d = 0.14, \quad (3.41)$$

and

$$F_{\text{cent}} = (1 - A) \exp\left(\frac{-T}{T_3}\right) + A \exp\left(\frac{-T}{T_1}\right) + \exp\left(\frac{-T_2}{T}\right). \quad (3.42)$$

The four extra parameters in Eq. (3.42), A , T_3 , T_1 , and T_2 must be defined in order to represent the fall-off curve with Troe parameterisation.

The Lindemann theory is the simplest theory of unimolecular reaction rates [102]. The Lindemann theory proposes a second-order bimolecular reaction of C with M, which is the collisional partner and represents any chemical species in the gas:



Applying the steady-state approximation to the concentration of C^* gives:

$$[C^*] = \frac{k_e [C] [M]}{k_s [M] + k_d}, \quad (3.45)$$

and the rate of products A and B is

$$\frac{d[A]}{dt} = \frac{d[B]}{dt} = \frac{k_d k_e [A][M]}{k_s [M] + k_d}. \quad (3.46)$$

Therefore, the Lindemann expression for the unimolecular rate constant is:

$$k_{uni} = \frac{k_d k_e [M]}{k_s [M] + k_d}. \quad (3.47)$$

Reversible reaction steps

Theoretically, all elementary reactions are reversible, which means the final products can react with each other and form the reactants. In detailed kinetics reaction mechanisms, a reaction step is considered as reversible reaction if the reaction step is denoted by the two-way arrow or equal symbols within the reaction step expression or the reversible reaction is represented in a pair of irreversible reaction steps. Writing a reversible reaction as a pair of irreversible reaction in detailed kinetic reaction mechanisms is a way to decouple the calculation of reverse rate from the thermodynamics properties to reduce the impact of uncertainty of thermodynamic data. The reverse rate constant $k_{r,i}$ is also strongly dependent on temperature and can be written in Arrhenius equation form. By having reliable thermodynamics properties, the reverse rate constants can be determined from forward reaction coefficient and equilibrium constant.

Chemical equilibrium is a state in which the rate of the forward reaction equals the rate of the backward reaction. In other words, there is no net change in concentrations of reactants and products. When the reaction i is in chemical equilibrium, Eq. 3.31 can be written as:

$$k_{f,i} \prod_{k=1}^{N_s} [X_k]^{v'_k} = k_{r,i} \prod_{k=1}^{N_s} [X_k]^{v''_k}, \quad (3.48)$$

$$\frac{k_{f,i}}{k_{r,i}} = \frac{\prod_{k=1}^{N_s} [X_k]^{v''_k}}{\prod_{k=1}^{N_s} [X_k]^{v'_k}}, \quad \frac{k_{f,i}}{k_{r,i}} = \prod_{k=1}^{N_s} [X_k]_e^{v''_k}, \quad (3.49)$$

$$\frac{k_{f,i}}{k_{r,i}} = K_{c,i}, \quad k_{r,i} = \frac{k_{f,i}}{K_{c,i}} \quad (3.50)$$

where subscript e denotes the concentrations values at equilibrium and $K_{c,i}$ is the equilibrium constant for reaction i in concentration units. The $K_{c,i}$ can be calculated from $K_{p,i}$, which is

the equilibrium constant in pressure units:

$$K_{c,i} = K_{p,i} \left(\frac{P^\circ}{RT} \right)^{v_i}, \quad (3.51)$$

where v_i is the net change in the number of gas-phase species in the reaction:

$$v_i = \sum_{k=1}^{N_s} (v''_{k,i} - v'_{k,i}). \quad (3.52)$$

The $K_{p,i}$ is not pressure dependent and it only depends on properties at the standard pressure $p = p^\circ$. The $K_{p,i}$ can be expressed from the reaction thermochemistry:

$$K_{p,i} = \exp \left(\frac{\Delta S_{r,i}^\circ}{R} - \frac{\Delta H_{r,i}^\circ}{RT} \right), \quad (3.53)$$

where $\Delta S_{r,i}^\circ$ and $\Delta H_{r,i}^\circ$ are the net change in entropy and enthalpy of the reaction i , respectively.

3.4 Mechanism development

The creation of a chemical kinetic model involves the definition of stoichiometries for each reaction and provision of thermodynamic data for the species in the mechanism. The thermodynamic data are needed for estimation of heat release of the reactions and the reverse rate constants by knowing the forward rate constant. Kinetic and transport data are also needed. It is also worth to mention that reaction mechanisms often undergo updates and revisions over time when new experimental data for the validation of mechanisms are available or more accurate thermodynamic data are required or simply new reaction steps and intermediate species are identified. Developing a reaction mechanism for a practical process is complicated, since the chemistry may involve hundreds of species and thousands of reactions. Therefore, it is preferred to start with an existing model to extend or optimize the model. Unfortunately, in the case of TMS combustion, there is no reaction mechanism available and only few reaction pathways based on experimental observations are suggested and few thermodynamic data are calculated. This makes the development of the reaction mechanism for the TMS combustion a tedious task. There are two approaches for reaction mechanism development: manual generation of mechanisms and automatic mechanism generation. The manual generation of mechanisms, which is the case for TMS combustion discussed in chapter 5 of this work, begins with the selection of important species based on experimental observations. The intermediate species which are necessary in order to predict the production rates of the key products also need to be considered. The types of reactions that can occur between these species need to be specified.

Figure 3.1 shows the schematics of the mechanism development procedure, which shows the importance of both experimental and theoretical methods. It also emphasizes that the mechanisms continuously need to be updated by new measurements and theoretical calculations.

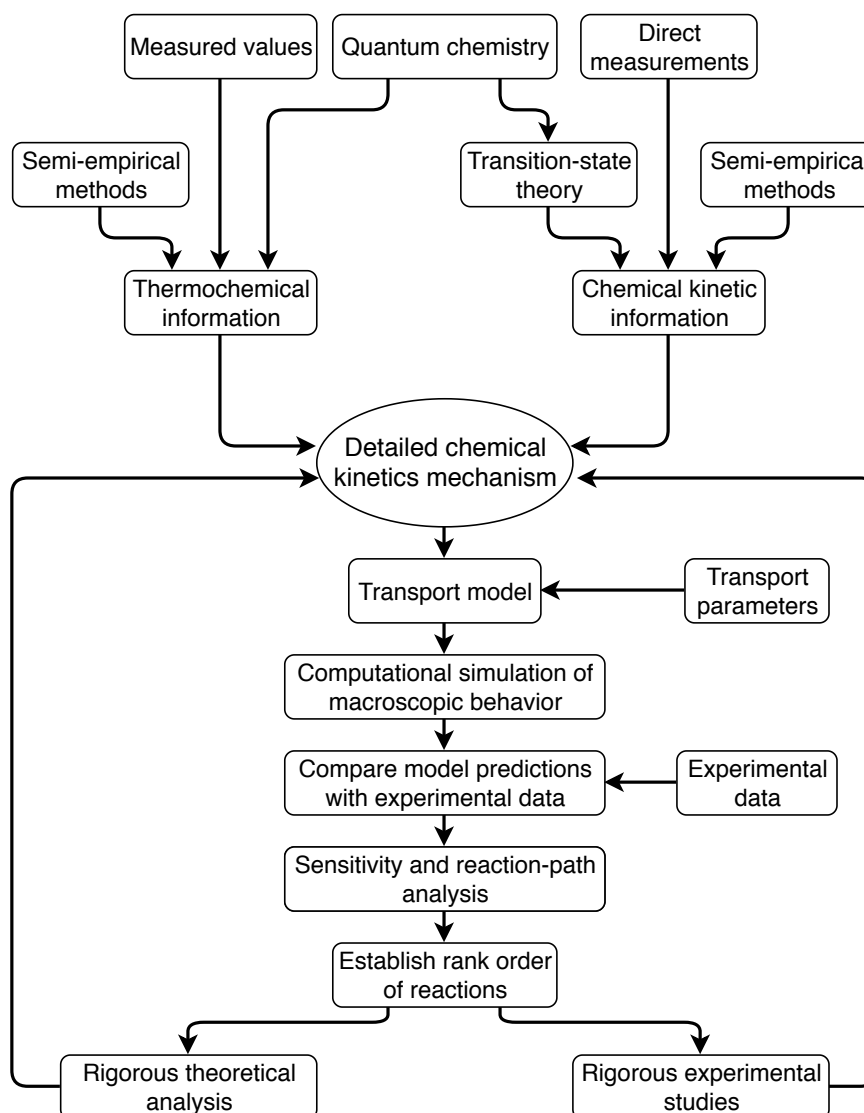


Fig. 3.1 Schematics of reaction mechanism development. The figure is based on that from Senkan (1992) [2] and is reproduced with permission from Elsevier.

3.4.1 Finite rate chemistry

In chemically reacting flows, the mixing of reactants is a very important phenomenon which can affect the overall reaction rate. If the mixing is slow in comparison to chemical reaction, the system is diffusion or mixing controlled, and if the mixing is faster than the reactions, the system is kinetically controlled. Finite rate chemistry implies a kinetically controlled process, which can be described at different levels of complexity. The description of the chemistry in reacting flows can be simplified to a one-step global reaction only, or it can be described by a detailed reaction mechanism involving hundreds of species. In the following, a short description of finite rate chemistry models is given.

Global reactions

The use of one or several global reactions is the simplest way to describe finite rate chemistry. The global reactions are widely used in industrial CFD simulations. On the other hand, there are some disadvantages that the global reaction mechanisms are constrained within a narrow region of operating conditions and the investigation of intermediates during the combustion process is not possible.

Detailed reaction mechanisms

In contrast to the global reaction mechanisms, the detailed reaction mechanisms are the most complex chemical models. The detailed reaction mechanisms normally contain hundreds or even thousands of species. Theoretically, there is no limitation for the detailed mechanisms in terms of number of species and reactions. The comprehensiveness of a detailed mechanism is recognized by prediction of all possible combustion phenomena over all observed ranges of conditions [103]. Although the experimental data are considered for the development of detailed mechanisms, the main purpose of a detailed mechanism is to provide insight into chemical processes in which experiments are not available or difficult or expensive to be performed. One of the major advantages of detailed mechanisms is their application as a reference to interpret experimental results and their help to provide ideas for further experiments.

Skeletal reaction mechanisms

Increases in both chemical kinetics knowledge and the computational resources led to very large detailed reaction mechanisms. Fig. 3.2 shows the size of some detailed mechanisms for hydrocarbon fuels over the last two decades [3]. It shows how the size of mechanisms

tends to grow with time. The 2D or 3D CFD simulations with a detailed mechanism is computationally expensive. Therefore, it is necessary to reduce the size of a detailed reaction mechanism in a way to predict the key target accurately. There are a variety of methods [104–107] to reduce the size of the detailed mechanism by removing unimportant species and reactions which lead to a so-called "skeletal reaction mechanism". During the reduction of species or reactions, the accuracy of a skeletal mechanism may decrease. In another word, the skeletal mechanism is the result of a trade-off between complexity and accuracy.

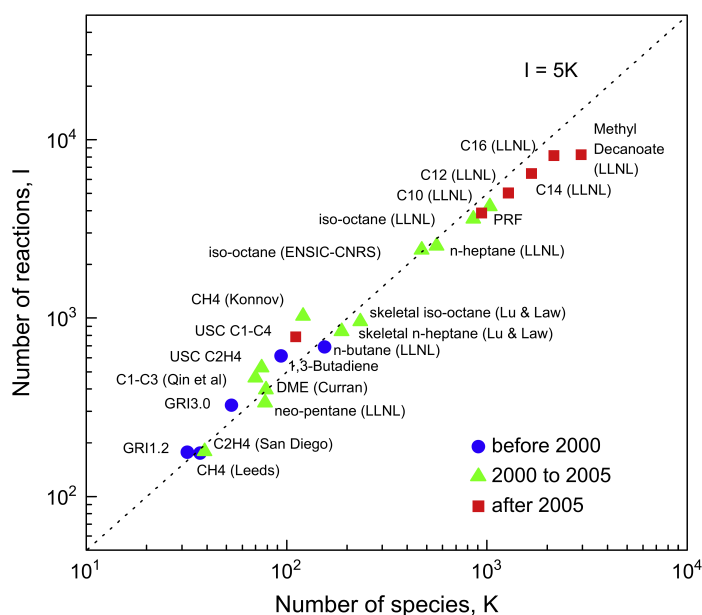


Fig. 3.2 Size of selected detailed and skeletal mechanisms for hydrocarbon fuels. The figure is based on that from Lu and Law [3] and is reprinted with permission from Elsevier.

3.4.2 Sources of data

In order to develop a chemical reaction mechanism, it is necessary to provide thermodynamic and transport data as well as the reaction kinetics parameters for species and reactions, respectively. The thermochemistry of a large number of species is available as 7- or 9-coefficients NASA polynomials or as tabulated values. There are well-known databases [108–111] available in the literature, which makes access to the thermodynamic data easy. There are also a number of software packages which calculate thermodynamic properties automatically [112–114]. In addition, there are online chemical kinetic databases such as by NIST [109] which provide the elementary reaction steps and corresponding reaction rate parameters. Compilations of skeletal and detailed reaction mechanisms are also useful, which are available online by many research groups such as Respecth [115], Creck modeling group

[116], and Combustion Chemistry Center [117]. It should be noted that the thermochemistry of Si-containing species is very limited in the above-mentioned databases.

3.5 Reaction rate theories

Chemical kinetics is about how fast a chemical species is formed or consumed during a chemical reaction. The law of mass action describes the chemical kinetics of reactions in the gas phase. The rates are dependent on the concentrations of the chemical species involved in the reaction. The reaction rate constant can be determined by experiments such as shock tube experiments [75, 118]. So far, rate constants, which appear in the rate laws of chemical reactions, are regarded as empirical quantities, which have to be determined experimentally. On the other hand, rate constants can be predicted using theoretical models, which consider the relation between microscopic (individual molecules) properties and macroscopic rate quantities (rate constants, product branching ratios). The collisional theory is the most basic model that attempts to understand individual elementary reactions at the molecular level.

3.5.1 Collision theory and reaction rate limit

Collision theory is the simplest model to describe the reaction rate of an elementary bimolecular reaction $A + B \rightarrow P$ [119, 120]. For a reaction to take place, two molecules A and B need to collide. However, not every collision leads to a reaction. The collision must have enough energy to overcome the activation barrier and the molecules must have the correct orientation. Every reaction rate theory must take the energy requirement into account. Therefore, there are three factors which influence the successful reactive collision [121, 82]. First of all, the collision rate between two potential reactants, which means the number of collisions per second. The collision rate (frequency) itself depends on three factors which are: the number of reactant molecules per unit volume, the size of the two collision partners, and the relative velocity of the collision partners. The collision frequency between molecules A and B can be described as:

$$Z_{AB} = \frac{N_A}{V} \frac{N_B}{V} \pi \sigma_{AB}^2 v_{rel}, \quad (3.54)$$

where N_A and N_B are the numbers of molecules A and B. The number density of A and B are N_A/V and N_B/V , respectively. The σ_{AB} is the collision diameter. The collision cross-section can be thought of as the target area that one collision partner presents to the second. The simplest collision cross-section can be determined by assuming molecules A and B as hard spheres. In Eq. (3.54), the relative velocity distributions is obtained from the

Maxwell-Boltzmann distribution:

$$v_{rel} = \sqrt{\frac{8k_B T}{\pi m_{AB}}}, \quad (3.55)$$

where m_{AB} is the reduced mass and is given by:

$$m_{AB} = \frac{m_A m_B}{m_A + m_B}. \quad (3.56)$$

For a successful collision, the reactants must collide with enough kinetic energy to break the original bonds and form new bonds to form the product. The energy barrier is also called activation energy (see Fig. 3.3). The fraction of collisions with enough energy to overcome the activation energy, E_a is given by:

$$f = \exp\left(\frac{-E_a}{RT}\right). \quad (3.57)$$

The third factor is the steric factor, P which is introduced to account for the disagreement between measured rate constants and those calculated by collision theory. The steric factor represents the efficiency of the collision and ranges from 0 to 1.

Considering all the factors mentioned above, the temperature dependent rate constant of the gas-phase reaction is expressed as:

$$k(T) = P \underbrace{\frac{N_A}{V} \frac{N_B}{V} \pi \sigma_{AB}^2}_{A} \sqrt{\frac{8k_B T}{\pi m_{AB}}} \exp\left(\frac{-E_a}{RT}\right). \quad (3.58)$$

In a successful collision, the upper limit of collision rate of bimolecular reaction, may be given by:

$$k_{coll} = P \frac{N_A}{V} \frac{N_B}{V} \pi \sigma_{AB}^2 \sqrt{\frac{8k_B T}{\pi m_{AB}}} N_a, \quad (3.59)$$

where N_a is the Avogadro number. The Eq. (3.58) has the Arrhenius form and the terms before the exponential term are the pre-exponential factor A , of the Arrhenius equation. The pre-exponential factor can be therefore interpreted as the frequency of collisions, in which the reactants have a suitable orientation for a reactive collision. A more advanced kinetic theory was developed by Eyring and Polanyi [122] and is designated as transition state theory, which will be explained in the following section.

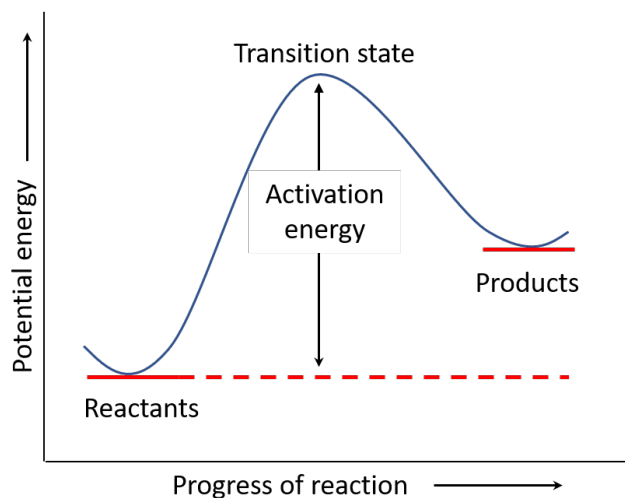


Fig. 3.3 Schematic of a reaction potential energy for an endothermic reaction.

3.5.2 Transition state theory

Transition-state theory is one of the earliest attempts to formulate the chemical reaction rates from first principles [123–125]. Transition-state theory assumes that the reactants are in equilibrium with an activated complex C^\ddagger , which is an intermediate during the bimolecular reaction $A + B \rightleftharpoons C^\ddagger \rightarrow D + E$. There is an energy barrier called activation energy, which is a certain amount of energy required for the reaction to occur. The transition state, C^\ddagger , is formed at maximum energy (See Fig. 3.3). For the sake of simplicity, there is no reverse reaction $D + E \rightarrow C^\ddagger$. The activated complex C^\ddagger is also assumed as a distinct chemical species, which decomposes rapidly. The equilibrium constant in concentration units is expressed as:

$$K_c^\ddagger = \frac{[C^\ddagger]}{[A][B]}. \quad (3.60)$$

The rate of reaction is equal to the number of activated complex decomposing to form the product:

$$rate = \nu[C^\ddagger] = \nu[A][B]K_c^\ddagger. \quad (3.61)$$

The Eq. 3.61 can be written as:

$$rate = k[A][B] = \nu[A][B]K_c^\ddagger, \quad k = \nu K_c^\ddagger, \quad (3.62)$$

where k is the rate constant, K_c^\ddagger is the equilibrium constant, and the $\nu = \frac{k_B T}{h}$ is the frequency of vibration. The k_B is the Boltzmann's constant and h is the Planck's constant. The Eq.

(3.62) can be written as:

$$k = \frac{k_B T}{h} K_c^\ddagger (M^{1-m}), \quad (3.63)$$

where M^{1-m} makes the units equal; with M the molarity and m the molecularity of the reaction. The equilibrium constant K_c^\ddagger can be calculated by absolute, fundamental properties such as bond length, atomic mass, and vibration frequency.

Similar to Eq. (3.51), the equilibrium constant in pressure unit can be written as:

$$K_p^\ddagger = K_c^\ddagger \left(\frac{p^\circ}{RT} \right)^{-v^\ddagger}, \quad (3.64)$$

where v^\ddagger is the net change in the number of gas-phase species ($v^\ddagger = 0$ and $v^\ddagger = -1$ for unimolecular and bimolecular reactions, respectively). The Eq. (3.64) can be reformulated in terms of the partition functions of each species,

$$K_p^\ddagger = \frac{(q^\ddagger/\mathcal{A})}{(q_A/\mathcal{A})(q_B/\mathcal{A})} e^{-E_0/RT}, \quad (3.65)$$

where q^\ddagger is the partition function for the activated complex and the q_A and q_B are the partition functions of reactants and the \mathcal{A} is Avogadro's number. The partition function is dimensionless and is used to evaluate how the populations of various energy states are partitioned among all possible values. The partition function is equal to the sum of the number of quantum states in the specific energy level multiplied by the Boltzmann population factor of that level [126]. The E_0 is the internal energy which for an ideal gas is equal to H_0 . By replacing K_p^\ddagger in Eq. (3.64) with Eq. (3.65), and solving for C^\ddagger based on Eq. (3.60), one can obtain:

$$[C^\ddagger] = \frac{(q^\ddagger/\mathcal{A})}{(q_A/\mathcal{A})(q_B/\mathcal{A})} e^{-E_0/RT} \left(\frac{p^\circ}{RT} \right)^{v^\ddagger} [A][B]. \quad (3.66)$$

The production rate of products is assumed to equal the decomposition rate of C^\ddagger times a concentration of C^\ddagger . The rate constant of an activated complex is:

$$k_{rxn} = v_{RC} \frac{(q^\ddagger/\mathcal{A})}{(q_A/\mathcal{A})(q_B/\mathcal{A})} e^{-E_0/RT} \left(\frac{p^\circ}{RT} \right)^{v^\ddagger}, \quad (3.67)$$

where v_{RC} is the decomposition rate of C^\ddagger . By replacing q^\ddagger with $q_\ddagger \frac{k_B T}{h v_{RC}}$, where q_\ddagger is the partition function for all degrees of freedom of a activated complex except the reaction

coordinate, k_{rxn} can be written as:

$$k_{rxn} = \frac{k_B T}{h} \frac{(q_{\ddagger}/\mathcal{A})}{(q_A/\mathcal{A})(q_B/\mathcal{A})} e^{-E_0/RT} \left(\frac{p^\circ}{RT}\right)^{\nu_{\ddagger}} \quad (3.68)$$

Further simplification leads to the well known transition state theory rate constant:

$$k_{rxn} = \frac{k_B T}{h} \frac{q_{\ddagger}}{\bar{q}_A \bar{q}_B} e^{-E_0/RT} \mathcal{A}, \quad (3.69)$$

where the \bar{q} 's are the partition functions per unit volume. The Avogadro number gives the rate constant in molar units. The h is the Planck constant. This equation relates reaction rate constants with molecular properties, which are included in the partition functions (translational, rotational and vibrational partition functions). If the molecular properties from spectroscopic data or quantum chemical calculations are available, the rate constants can be predicted by transition state theory.

3.5.3 QRRK and RRKM theories

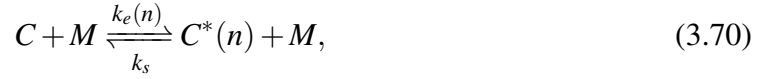
The Lindemann theory, discussed earlier in this chapter, has two shortcomings [127, 82], which are as follows:

- The bimolecular step takes no account of the energy dependence of activation, and the Lindemann theory underestimates the excitation rate constant k_e .
- The unimolecular step fails to take into account that an unimolecular reaction specifically involves one particular form of molecular motion.

To compensate the first shortcoming, Hinshelwood [128] showed that the k_e can be much larger than predicted using simple collision theory when the energy transfer into the internal degrees of freedom is taken into account.

The second shortcoming of the Lindemann theory can be corrected by RRK theories, which were developed by Rice, Ramsperger, and Kassel [129–131] for further improvement of unimolecular reaction theory. Kassel [132] extended the RRK theory to account for quantum effects which is known as QRRK theory and later Marcus [133] further generalized the unimolecular reactions theory by taking the transition state theory [123] into account, which is known as RRKM theory. The QRRK theory assumes that a sufficient amount of a molecule internal vibrational energy must be localized in a given vibrational mode for an unimolecular reaction to occur. A new step is added to the Lindemann mechanism in which the excited molecule C^* forms an activated complex C^\ddagger before a reaction happens. The model assumes that the reaction rate coefficient for the excitation step is not constant. The

rate constants for formation of C^* and C^\ddagger depends on n and m , the total number of vibrational quanta transferred to the excited intermediate C^* and activated complex C^\ddagger , respectively. The reaction scheme in the QRRK theory for unimolecular decomposition is stated as:



where the $k_{act}(n,m)$ is the rate constant for the formation of the activated complex, in which at least m quanta of vibrational energy have accumulated in a critical bond out of the total of n . The QRRK model assumes that vibrational energy can freely flow from one vibrational mode in the molecule to another. Reaction (3.71) is called activation step, which forms the activated complex C^\ddagger .

The activated complex reacts very quickly when it is formed. The reaction happens within the first vibrational period after formation of C^\ddagger . Applying the steady state assumption, the $k_{act}(n,m)$ is expressed as:

$$k_{act}(n,m) = k_\ddagger \frac{[C^\ddagger(n,m)]}{[C^*(n)]}. \quad (3.73)$$

Similar to Hinshelwood's theory, the probability of locating n vibrational quanta among the s vibrational modes can be calculated also in QRRK theory with further simplification and reformulation. The final QRRK expression for unimolecular rate constant is :

$$k_{uni} = \sum_{n=m}^{\infty} \frac{k_d(n,m)k_e(n)[M]}{k_s[M] + k_d(n,m)}, \quad (3.74)$$

where the excitation rate constant $k_e(n)$ is :

$$k_e(n) = k_s \frac{(n+s-1)!}{n!(s-1)!} \alpha^n (1-\alpha)^s, \quad (3.75)$$

with $\alpha = e^{-x}$ and $x = hv/k_B T$. The h is Planck's constant and ν is the frequency of vibrational mode s .

The de-excitation rate constant k_s is :

$$k_s = \beta k_{HS}, \quad (3.76)$$

where β is collision efficiency and k_{HS} is the hard-sphere rate constant. And the rate constant for the decomposition of the C^\ddagger is :

$$k_d(n, m) = A_\infty \frac{(n - m + s - 1)!n!}{(n - m)!(n + s - 1)!} \quad (3.77)$$

Even though the QRRK theory has been used to estimate rate constant data of elementary reactions, the RRKM theory, named after Rice, Ramsperger, Kassel and Marcus, has become the widely accepted and used theory today. In the limit of infinite pressure, RRKM theory turns into the transition state theory. RRKM theory is a microcanonical theory which determines the rate constant as a function of energy E and not temperature T . The theory considers the actual vibrational frequencies of the molecule. In RRKM theory, the k_{act} of Eq. (3.73) in QRRK theory is replaced by :

$$k_{act}(\varepsilon) = \frac{W(\varepsilon')}{N(\varepsilon)h}, \quad (3.78)$$

where $W(\varepsilon')$ is the total number of states of the activated complex, $N(\varepsilon)$ is the density of states in the reactant molecule at energy ε , and h is the Planck's constant. The energy ε' is the energy of the activated complex in excess of the critical energy, $\varepsilon' = \varepsilon - \varepsilon^0$. The RRKM theory is the state of the art for unimolecular reaction theories. The RRKM theory calculations in the Chapter 5 of this work are done by the KiSTheIP code developed by Canneaux et al. [134]. In the KiSTheIP code, the Laplace-transform based on the inversion of the partition functions is used for the calculation of the sum of states $W(\varepsilon')$ and density of states $N(\varepsilon)$. The temperature-dependent rate constant is calculated by using the following expression [134]:

$$k(T) = \frac{\sigma Q_1^\ddagger}{Q_2 Q_1 h} e^{-\frac{E_0}{k_b T}} \int_0^\infty \frac{W(\varepsilon') e^{-\frac{E}{k_b T}}}{1 + \frac{k(E_0 + E + \langle \delta E_j \rangle)}{\omega}} dE, \quad (3.79)$$

where σ is the reaction path degeneracy, h is the Planck's constant, Q_2 is the partition function of the active degrees of freedom (vibrations + critical moment of inertia) of the reactant, Q_1^\ddagger and Q_1 are the partition functions for adiabatic rotations of the transition state and of the reactant, respectively. The E_0 is the zero-point-corrected threshold energy. The strong collision approximation is used assuming that every collision deactivates with $\omega = \beta_c Z_{LJ} [M]$ being the effective collision frequency where β_c is the collisional efficiency, Z_{LJ} is the Lennard-Jones collision frequency and $[M]$ is the total gas concentration. Z_{LJ} are calculated using the Lennard-Jones parameters: ε/k_b (K) and σ (cm).

Chapter 4

Chemical informatics

The focus of this chapter is to provide an overview of the mathematical methods and computational techniques which are used for the calculation of thermodynamics properties, estimation of group-additivity values (GAVs), and reaction mechanism reduction and optimization. These techniques and methods are used in this work for the development of an extensive database for the thermochemistry of organosilane and for the development and validation of the tetramethylsilane (TMS) mechanism.

In general, chemical informatics is defined as the field of solving chemical problems with the aid of computers. Chemical informatics methods use mathematical and statistical methods to extract and analyze information from the chemical system. They are widely used in chemical industries, pharmaceutical, and biotechnology research. One of the most well-known techniques in chemical informatics is the quantitative structure-property relationship modeling (QSPR) that relates the chemical structures to chemical and physical properties. Another popular method in the field of chemical informatics is the group-additivity method. It is a robust technique for the estimation of thermochemical properties of chemical compounds for which experimental data are not available. Due to the easy implementation of the group-additivity method in automated computer programs, it is widely implemented in automatic reaction mechanism generators. The group-additivity method breaks down the molecules into smaller groups and relates the thermochemical properties of smaller groups to bigger molecules. Group-additivity method and QSPR modeling similar to any other statistical method depend on the number of data sets for accurate out-of-sample prediction.

The ultimate goal of this thesis is to provide a comprehensive database for the thermochemical properties of Si–C–H- and Si–C–H–O-containing species. By applying computer-aided modeling, the chemical data is transferred into the information and from information to knowledge. Thermochemical properties and GAVs of species are stored in metadata for further investigation on the thermochemistry of organosilanes with other techniques such

as machine learning as an outlook of this thesis. The genetic-algorithm based optimization technique as another example of computer-aided modeling is discussed in this chapter.

4.1 Computational chemistry

Computational chemistry is a branch of chemistry using computer simulations to make chemical predictions such as predictions of molecular structures, thermodynamic data, or chemical reactivities. Depending on the chemical problem addressed, these simulations can be based primarily on principles of quantum physics or on a combination of quantum and classical physics. The 1998 nobel prize in chemistry, awarded to Walter Kohn and John Pople for the development of density functional theory, a widely applied quantum chemical method, is regarded as an event which established computational chemistry as its own field within chemical sciences. When the mathematical description of chemistry is well-developed, it can be automated for implementation on a computer. The goal in this section is to briefly explain the calculation of macroscopic thermochemical properties in terms of molecular properties, including rotational constants and molecular vibrations by means of quantum mechanics (QM). The basic premise of QM were devised by Heisenberg, Schrödinger, Born, and Pauli which are the basis for nearly all computational chemistry methods. The Schrödinger equation is [135]:

$$\hat{H}\Psi(\mathbf{r}) = \Psi(\mathbf{r})E. \quad (4.1)$$

In this equation, electrons are considered as particles having a wave-like character. This wave-character is expressed by the wave function $\Psi(\mathbf{r})$, in which \mathbf{r} represents the coordinates necessary to describe a system of particles (here: electrons). \hat{H} is the Hamiltonian operator which in classical mechanics expresses the total energy or a sum of the kinetic energy and potential energy, and E is the eigenvalue of the eigenfunction Ψ or the total energy of the system. Except in case of an one-eletron system, such as the H atom, the Schrödinger equation can only be solved numerically. There are different functions which can be used to approximate the wave functions such as Gaussian-type wave functions. The numerical solutions yield the eigenvalues, which allow to derive molecular properties. Different electronic-structure methods can be applied to solve the Schrödinger equation numerically such as: Hartree–Fock (HF) theory, density functional theory (DFT), and coupled-cluster (CC) methods. In most of these methods, the wave function $\Psi(\mathbf{r})$ of the electronic Schrödinger equation is varied to try to minimize the potential energy of a system. All quantum-chemical calculations in this disseration have been conducted with the Gaussian09 software package [136].

4.2 Thermochemistry

As mentioned earlier in Chapter 2, the thermochemical properties, specific heat, enthalpy of formation, and entropy are important for combustion analysis. Thermochemical properties help us to compute the equilibrium constants that allow to relate the reverse rate constants of a reaction to forward rate constants. In addition, thermochemical properties are important to calculate the heat release and the adiabatic flame temperature during a combustion process. In case of a lack of experimentally measured thermochemical data, it is necessary to calculate the thermochemical properties of the species by means of quantum chemistry. Quantum chemistry allows us to achieve optimized molecular geometries and also to calculate the molecular properties such as rotational constants and molecular vibrations. The molecular properties are related to macroscopic thermochemical properties by means of statistical mechanics.

By calculating the partition functions which are divided in electronic, rotational, translational and vibrational functions, the thermodynamic quantities like the internal energy, enthalpies, and entropies can be predicted. If standard enthalpy of formation and heat capacities are known, enthalpy of formation at a particular temperature can be calculated as [137]:

$$H_{f,T}^{\circ} = H_{f,298}^{\circ} + \int_{298}^T C_{p,T} dT. \quad (4.2)$$

In the case of entropy, the entropy at a particular temperature is calculated as [137]:

$$S_T^{\circ} = S_{298}^{\circ} + \int_{298}^T \frac{C_{p,T}}{T} dT. \quad (4.3)$$

The enthalpies of formation are important in combustion processes as the heat release in an arbitrary reaction can be calculated from the difference of enthalpies of products and reactants, the so called enthalpy of reaction. If the reaction enthalpy is positive, the reaction absorbs heat and it is called endothermic. If the reaction enthalpy is negative, it releases heat and it is called exothermic.

4.2.1 Atomization energy method

The enthalpy of atomization is defined as the enthalpy change when a molecule decomposes to its constituent atoms. The enthalpy of atomization has always a positive value and is defined as the enthalpy change of a hypothetical reaction, in which a total separation of all atoms in a molecule takes place. In such a reaction, a molecule is separated into its constituent elements. The standard enthalpies of formation can be calculated using the atomization

energy method. In this method, the enthalpy of formation at 0 K, $\Delta H_f^\circ(0 \text{ K})$, is obtained as the difference between the *ab initio* calculated (ai) atomization enthalpy of a compound and the experimentally determined enthalpies of formation of the gaseous atoms [137]:

$$\begin{aligned} \Delta H_f^\circ(0 \text{ K}, \text{Si}_a \text{C}_b \text{H}_c \text{O}_d) = & a\Delta H_{f, \text{gas,exp}}^\circ(0 \text{ K}, \text{Si}) + b\Delta H_{f, \text{gas,exp}}^\circ(0 \text{ K}, \text{C}) \\ & + c\Delta H_{f, \text{gas,exp}}^\circ(0 \text{ K}, \text{H}) + d\Delta H_{f, \text{gas,exp}}^\circ(0 \text{ K}, \text{O}) - [aH_{\text{ai}}^\circ(0 \text{ K}, \text{Si}) + bH_{\text{ai}}^\circ(0 \text{ K}, \text{C}) \\ & + cH_{\text{ai}}^\circ(0 \text{ K}, \text{H}) + dH_{\text{ai}}^\circ(0 \text{ K}, \text{O}) - H_{\text{ai}}^\circ(0 \text{ K}, \text{Si}_a \text{C}_b \text{H}_c \text{O}_d)] \quad (4.4) \end{aligned}$$

By applying enthalpy corrections for the atomic elements, $H^\circ(298 \text{ K}) - H^\circ(0 \text{ K})$, and the reactant molecule to $\Delta H_f^\circ(0 \text{ K})$, standard enthalpies of formation, $\Delta H_f^\circ(298 \text{ K}, \text{Si}_a \text{C}_b \text{H}_c \text{O}_d)$, are calculated [137]. The enthalpy corrections for the molecules are extracted from the results of quantum chemical calculations.

4.2.2 Isodesmic reaction method

The *ab initio* calculations perform better for the calculation of relative energies than the absolute energies. By writing the compound as being part of an isodesmic reaction, it will be possible to calculate the energy of the compound relative to those of the other species in such a reaction. This has an advantage which leads to a cancellation of the systematic errors in the *ab initio* calculations. Isodesmic reactions are hypothetical bond re-arrangement reactions, in which the number of bond types remains the same between the reactants and products [138]. The error in atomization energy scales with the molecular size. In contrast, isodesmic reactions conserve the bond types such that systematic errors tend to cancel out. The following reaction is an example for an isodesmic reaction for the calculation of ΔH_f° of $(\text{CH}_3)_4\text{Si}$:



The number of C-H and Si-C bonds are equal on both sides of the reaction. Due to the equal number of bonds of a given type for both sides, the systematic error in *ab initio* calculations will be canceled out. Of course, we still have the constraint that the experimental values for other species in the reaction must be known. The standard enthalpy of formation of $(\text{CH}_3)_4\text{Si}$ can be estimated now by the calculation of the reaction enthalpy H_{RXN} based on a quantum-chemical calculation:

$$\Delta H_f^\circ((\text{CH}_3)_4\text{Si}) = 4 \Delta H_f^\circ(\text{CH}_3\text{SiH}_3) - 3 \Delta H_f^\circ(\text{SiH}_4) - H_{\text{RXN}}.$$

The success of the isodesmic reaction method strongly depends on the availability of heats of formation for other species. It should be noted that different isodesmic reactions can be set up in order to estimate the ΔH_f° of the species. Different isodesmic reaction may lead to different ΔH_f° values. In some cases the average ΔH_f° values may be a proper approach.

Uncertainties of the ΔH_f° values derived from the G4/isodesmic reaction method were estimated by the “root sum squares” of the uncertainties in the reference species:

$$U_c = \sqrt{\sum_{i=1}^n [C_i U(x_i)]^2}, \quad (4.5)$$

where U_c is the combined uncertainty, c_i are the stoichiometric coefficients in the isodesmic reaction, and $U(x_i)$ is the uncertainty of reference species i . The isodesmic reaction method may not be feasible for large molecules when no useful isodesmic reactions can be defined because of a lack of reference compounds with known thermochemistry. In such cases, atomization energy is sometimes the only viable option.

4.3 Group-additivity method

Group-additivity method is a powerful empirical method for estimation of thermochemical properties and yet a very simple method for implementation in computer programs. The development and extension of the group-additivity method were mostly done by Benson [139] and Ritter [112], respectively. The group-additivity method states that the thermochemical properties of a species are linearly dependent on the functional constituent groups that contribute in the molecule.

Benson [139] defines a functional group as a part of a molecule, consisting of a central polyvalent atom (ligancy ≥ 2) and all its neighbors. A group is written as $X-(A)_i(B)_j(C)_k(D)_l$ where X is the central atom attached to i A-atoms, j B-atoms, etc. As an example, the groups involved in TMS are shown in Fig. 4.1. Two distinct groups $(C-(H)_3(Si))$ and $(Si-(C)_4)$ are contributing to TMS properties. To name the groups, the central atom comes first and is then followed by neighbor atoms in brackets in alphabetical order. The standard enthalpy of formation $H_{f,298}^\circ$ and heat capacity $c_{p,298}$ of TMS can be calculated as:

$$H_{f,298}^\circ[\text{TMS}] = 4 \times H_{f,298}^\circ[\text{C}-(\text{H})_3(\text{Si})] + 1 \times H_{f,298}^\circ[\text{Si}-(\text{C})_4] + \epsilon_{H_f} \quad (4.6)$$

$$C_{p,298}[\text{TMS}] = 4 \times C_{p,298}[\text{C}-(\text{H})_3(\text{Si})] + 1 \times C_{p,298}[\text{Si}-(\text{C})_4] + \epsilon_{C_p} \quad (4.7)$$

where ϵ is the corrections for non-bonding interactions which is negligible for linear additivity. The standard entropy s_{298}° can also be calculated by group-additivity method,

but the entropy needs to be corrected to account for the molecular symmetry. A symmetric molecule is associated with smaller entropy in comparison with an asymmetric molecule since the symmetry increases the predictivity of the spatial orientation. The symmetry number σ is defined as the number of identical spatial configurations obtained by the rotation of a molecule around itself. After introducing the correction term to account for the influence of molecular structure on entropy, the standard entropy can be calculated as:

$$S_{298}^{\circ}[\text{TMS}] = 4 \times S_{298}^{\circ}[\text{C}-(\text{H})_3(\text{Si})] + 1 \times S_{298}^{\circ}[\text{Si}-(\text{C})_4] - R \ln(\sigma) + \varepsilon_{H_f^{\circ}} \quad (4.8)$$

where R is the universal gas constant. To account for interactions in the molecule reaching further than the nearest neighbors of each atom, non-next-nearest neighbor interactions (NNI; e.g., gauche or cis interactions), resonance corrections (RES) and ring strain corrections (RSC) have been introduced [140–142]. While with the group-additivity method it is quite simple to estimate thermodynamics properties of large molecules, the above-mentioned corrections for each molecule makes it a tedious task. In this work, we did not include the corrections for non-bonding interactions as well as the entropy correction with molecular symmetry.

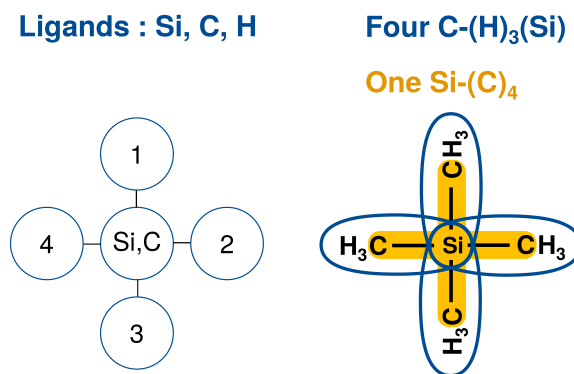


Fig. 4.1 Combinatorial arrangement for three possible Si, C, and H atoms for four possible ligands for Si- and C-atom-centered groups (left) and Benson groups contributing to TMS (right).

In order to derive GAVs, the group values need to be trained against experimental data if available or theoretically calculated data. Many efforts have been made to calculate thermodynamics properties of a huge list of molecules to be able to train groups. Cohen and Benson [143] tabulated thermochemical values for 37 hydrocarbon groups, 61 oxygen-containing groups, 59 nitrogen-containing groups, 58 organometallic groups and 65 organophosphorous and organoboron groups. Later, corrections for non-bonding interactions were updated by Benson [139].

Many publications reported GAVs for a variety of stable molecules and radicals [144, 145, 142, 141]. The derivation of GAVs for a certain class of chemical compounds requires the availability of a minimum set of thermochemical data. Bjorkman et al. [146] calculated ΔH_f° for 57 carbenium ions and from this theory-based dataset, they determined 16 GAVs by applying multiple regression. From these 57 values, they constructed 48 groups. From these 48 groups, 32 GAVs were available in the literature. They fixed these 32 GAVs, and the remaining 16 GAVs were derived through the method of multiple linear regression. For obtaining GAVs for silicon-containing species, a similar approach like Bjorkman et al. [146] is applied in this work and when any of GAVs are available, the GAVs are fixed during regression.

The drawbacks of group-additivity methods are that they are not useful when corrections for non-bonding interactions are required. As they do not consider the molecular structure, they may not deliver accurate estimations for isomers and conformers. Meanwhile, due to the conceptual simplicity and reasonable accuracy, GA has been widely used in automated mechanism generation, where it requires more programming effort to implement and more computational resources to conduct *ab initio* calculations for predicting thermochemical data [114, 147, 148]. Currently, available programs for the automatic generation of reaction mechanisms are limited to hydrocarbon chemistry. Hence, extending GAV to the Si–C–H and Si–C–O–H systems is beneficial to a wide array of material synthesis problems and reaction mechanism generation.

4.4 Combinatorics

Preparing a proper training set to have a complete list of molecules needed for the regression of GAVs is a very important prework. The accuracy of regressed GAVs is going to be dependent on the accuracy of calculated values in the training set. A proper test set is needed to be able to evaluate the performance of the regressed GAVs for estimation of new molecules which have not been in the training set. During the course of this work, we try to evaluate the group-additivity estimated values with the experimental values if available.

To set up the training set and account for the whole set of possible molecules in each chemical systems, a combinatorial approach is used to build specific structural types of molecules which contain unique functional groups. For this purpose, the ligands can be located around the central Si or C atoms as shown in Fig. 4.1. In these structures, the ligands can be located in any location around a central atom. Hence, the combinatorics relation for

“combinations with repetition” can be used to find the number of all possible groups:

$$\left(\binom{n}{k} \right) = \binom{n+k-1}{k} = \frac{(n+k-1)!}{k!(n-1)!} \quad (4.9)$$

where n is the number of ligands such as $-\text{Si}$, $-\text{C}$, $-\text{H}$, and $-\text{O}$ and k is the number of possibilities to distribute the ligands around the locations of central atoms.

4.5 Response surface and linear regression methodologies

The Response-Surface Methodology (RSM) is a collection of mathematical and statistical techniques for modeling the relationships between several independent variables and one or more response variables. The method was introduced by Box and Wilson [149]. The objective is to optimize the response y_i (output variable), which is a function f of the independent variables β_j (input variables). In most RSM problems, the response function is unknown, but with the help of the group-additivity method, a proper approximation for f is developed. This approximation can be defined by a linear function of the independent variables, resulting in a first-order model, where ε_i is an error term.

$$y_i = f(\beta_1, \beta_1, \beta_1, \dots, \beta_p) + \varepsilon \quad (4.10)$$

The goal is to fit the response surface to find the region where the optimal response occurs. Based on group-additivity method, for a given property of the i th molecule in the training set ($y_i = \Delta H_f^\circ$, $S^\circ(298 \text{ K})$, or $C_p(T)$), we have:

$$y_i = \sum_{j=1}^p x_{ij} \beta_j + \varepsilon_i \quad (4.11)$$

where x_{ij} is the number of j th group in the molecule, β_j is its corresponding GAV, p is the total number of groups and ε_i is the residue. Rewriting Eq. 4.11 in matrix form, we have:

$$\mathbf{Y} = \mathbf{X}\boldsymbol{\beta} + \boldsymbol{\varepsilon} \quad (4.12)$$

where \mathbf{Y} contains the thermochemical data of the n training compounds, \mathbf{X} is a $(n \times p)$ matrix, and $\boldsymbol{\beta}$ contains the GAVs of p groups. Eq. 4.12 is solved simultaneously for the standard enthalpy of formation ΔH_f° , the entropy S , and the heat capacities C_p for eight temperatures between 200 and 4000 K considering all species in the training set. For example, in case of stable Si–C–H–O species, we have $n = 62$ and $p = 34$. In the multivariable regression, the $\boldsymbol{\beta}$

are estimated by minimizing the sum of the least squares, yielding:

$$\boldsymbol{\beta} = (\mathbf{X}^T \mathbf{X})^{-1} \mathbf{X}^T \mathbf{Y} = \mathbf{X}^* \mathbf{Y}, \quad (4.13)$$

where the matrix \mathbf{X}^T is called the pseudo-inverse of matrix \mathbf{X} . The analysis is carried out to check whether the fitted values are suitable approximations of the actual values. An analysis of variance and regression was performed; and the coefficients of determination R^2 are also calculated.

4.6 Mechanism optimization and reduction

Optimization of reaction mechanisms is mostly done to compensate the lower accuracy of reduced reaction mechanisms in comparison to the detailed reaction mechanisms. Reduced mechanisms are computationally efficient but due to the elimination of many reaction steps, they need to be optimized to deliver the same prediction quality as the detailed reaction mechanisms. Optimization of a reaction mechanism means to tune its reaction rate constants to match the correct overall behavior of the detailed mechanism or the available experimental data.

In the frame of gas-phase synthesis of nanoparticles, the kinetic models for the combustion of precursors can also be optimized against the available experimental data. The rate constants of reactions can be tuned until the quantitatively measured mole fraction profiles of the target species are captured. The genetic algorithm-based reduction and optimization approach used in this work, was developed and explained in detail by Sikalo et al. [4, 150]. In this work, the genetic algorithm-based optimizer is extended in order to be able to define experimental data as a reference for optimization. In addition, altering the three parameters of the Arrhenius expression for a reaction rate constant is now possible. Figure 4.2 illustrates the activity flowchart of a genetic algorithm-based optimization procedure. In the following, a brief summary of the existing optimization approach is presented.

4.6.1 Genetic algorithm-based optimization

Initialization

A genetic algorithm (GA) is a method for solving both constrained and unconstrained optimization problems based on natural selection. The algorithm modifies a population of individual solutions. In every generation, the GA selects the fittest chromosomes and uses them as as parents to produce the children for the next generation. Therefore, the first

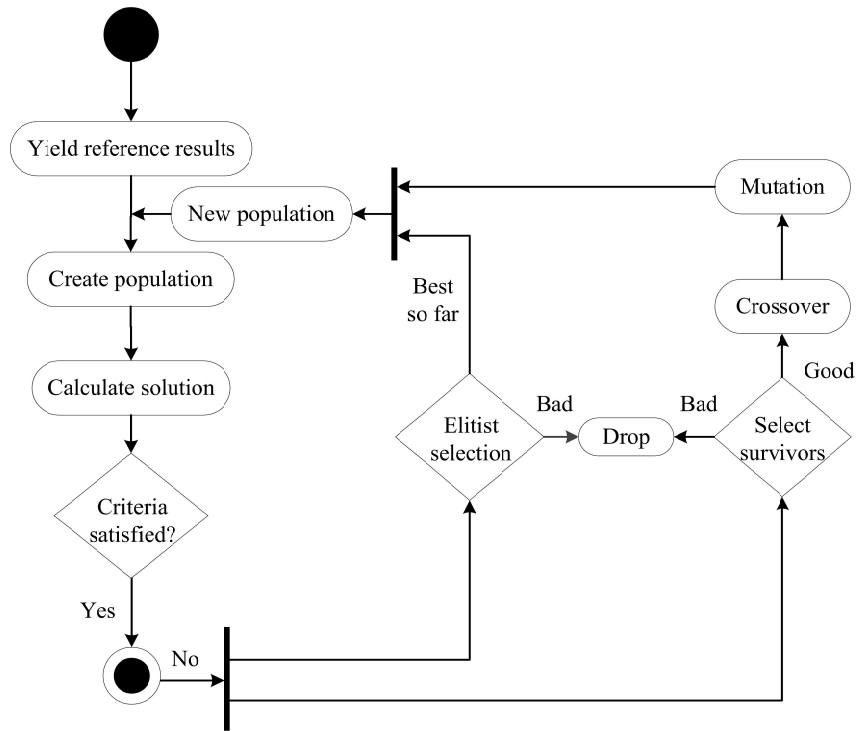


Fig. 4.2 Schematics of the genetic algorithm-based optimization. The figure is based on that from Sikalo et al. (2014) [4] and is reproduced with permission from Wiley.

step is to translate the chemical reaction mechanisms into a chromosome and the Arrhenius parameters (pre-exponential factor (A), temperature exponent (b), and activation energy (E_a)) are the genes. The length of each chromosome is constant and is equal to the number of reactions (N_r) considered for optimization times three. The chromosome can be formulated as:

$$\alpha = [\alpha_{1,A}, \alpha_{1,b}, \alpha_{1,E_a}, \dots, \alpha_{N_r,A}, \alpha_{N_r,b}, \alpha_{N_r,E_a}] \in [0, U_r] \quad (4.14)$$

where U_r defines the maximum uncertainty limit which α values can reach. The α values in Eq. 4.14 are the genes (real-values) which are the multiplier of the initial Arrhenius parameters. It means the initial solution is the current non-optimized reaction mechanism with $\alpha = 1$. In case of the TMS combustion mechanism developed in this work, some of the rate constants were not known and the initialization is only possible by assuming reasonable values for the pre-exponential factors, temperature exponents, and activation energies of those reactions. The initial values for unknown rate constants can be assumed by analogies to similar reactions. The initial population is evaluated for a one-dimensional burner stabilized flame to compare how well the mole fraction of desired species performs compared to the experimental mole fractions as a reference.

Selection

The selection process is applied to choose the most adopted individuals of the population, so that they become the parents to the new population for the next generation. A scheme widely used in GA is the selection per tournament [151, 152]. By this scheme, a certain number of individuals is chosen from the population and the individuals with the best quality are selected for making a new population. This scheme guarantees a minimum of diversity and gives all the individuals a chance to be selected, therefore the best individuals of the population will not be always selected to have offspring. In comparison to other selection schemes, the tournament selection is computationally more efficient.

To be sure that the best solutions are not going to be lost during the selection, a so-called elitism introduced by De Jong [153] is used. The elitism preserves the best solution and copies it unchanged to the next generation. The best solutions preserved by elitism are available to have offspring for the next generation. Once a better solution is found, it is going to be replaced as "the best solution so far" by elitism.

Crossover

At this stage, all the chromosomes are paired and the genes of the two parents are exchanged with a predefined rate. There are several methods for crossing [154]. The most used methods are as follow:

- Crossing based on a single-point: the two individuals selected to play the role of parents, are recombined by means of randomly chosen single point, from which the genes of the two chromosomes are swapped, yielding the children.
- Multiple-point crossing: in this type of crossing, multiple points are randomly selected. In this way, and in a manner analogous to the single-point crossing, the genes will be exchanged to form the two new children.
- Uniform crossing: in this type of crossing, each gene of the parents has a 50% chance to be swapped. Uniform crossing is extremely useful when the search space is very big [155].
- Arithmetic crossing: This type of crossing is suitable for non-binary chromosomes. The offspring gene takes the mean value of the parents. It has the disadvantage that only one offspring is generated at the crossing of two parents.

Mutation

A mutation operator aims to bring new characteristics or gene values which do not exist in the population. It is done by altering only a small number of randomly chosen genes in the chromosomes with a predefined rate. The mutation rate tune the magnitude of changes to be made in an individual to produce the mutated individual. Mutation is a very important stage in the genetic algorithm method because it introduces diversity and helps to find the global minimum during optimization.

Fitness function

A fitness function to rank the fitness (quality) of chromosomes based on the predefined criteria is required during the evolution of the population of chromosomes. A fitness function should measure how close a chromosome is to the desired solution. Finding an efficient fitness function is the most important step in the development of a genetic algorithm-based optimizer. A proper fitness function reduces the size of the search space and leads to a faster convergence. Developing efficient fitness functions in genetic algorithm techniques is investigated in [156]. In this work, the evaluation of a candidate solution is based on the mole fraction profile of target species along the height above the burner (HAB) during the simulation of a one-dimensional burner-stabilized flame. The genetic algorithm-based optimization technique developed by Sikalo et al. [4, 150] has a variety of options for evaluation of candidate solutions such as ignition delay time in a homogeneous reactor, laminar flame speed, adiabatic flame temperature, etc. The advantage of this method is that the general fitness function can be defined as a combination of fitness functions at different operating conditions. The fitness function is expressed as:

$$f_{fit} = \frac{1}{N_c} \sum_{c=1}^{N_c} f_{fit,c} \quad (4.15)$$

where $f_{fit,c}$ is a fitness function for a single operation condition and N_c is the number of operating conditions. The single $f_{fit,c}$ function is expressed as:

$$f_{fit,c} = \frac{\sum_{i=1}^{N_\xi} w_i f_\xi}{\sum_{i=1}^{N_\xi} w_i}, \quad (4.16)$$

where N_ξ is the number of the optimization targets and f_ξ is the fitness function for every single target with the corresponding weighting factor w_i . To give an example to show the capability of genetic algorithm-based optimizer, a skeletal mechanism for methane can be optimized against the detailed methane reaction mechanism for two different conditions (lean

and rich mixtures) and for the lean mixture the flame speed and CH₄ mole fraction profile can be defined as optimization target and for the rich mixture the adiabatic flame temperature and maximum concentration of CO are defined as optimization target. The general fitness function can be defined by merging Eqs. 4.15 and 4.16. The mathematical expressions for all different types of fitness functions are discussed in detail in the work of Sikalo et al. [4, 150].

Encoding

The genetic algorithm-based optimizer makes it possible to consider only a subset of reactions in the reaction mechanism and leave the rest of the reactions untouched. It allows decreasing the search space that leads to faster convergence and more efficient optimization. The protection of some reactions from the optimizer also has an advantage to not violate the well-known sub-mechanisms from the literature. In case of the combustion of nanoparticle precursors in H₂/O₂ flames [157], the syngas mechanism [5] that describes the base flame chemistry can be protected from the optimizer. The optimizer tries to alter the Arrhenius rate expression parameters until the prediction of the target species molar fraction is achieved.

4.7 Graph-based representation of chemical systems

A graph-based description of chemical systems has been introduced for more than two centuries. From the description of molecules to reaction mechanisms, graphs are widely used to not only visualize but to investigate the various interactions in the chemical systems using graphs. The most important advantage of defining chemical systems as graphs is applying graph theory. The interest to study the chemical bonds led to the evolution of a variety of graph-theoretical concepts and theorems. Balaban is one of the pioneers in chemical graph theory [158]. The chemical graph theory is widely used for formalizing the chemical systems, exploring reaction mechanisms [159], reduction of reaction mechanisms [160], and analysis of chemical processes [161]. In this work, we used a bipartite graph definition to visualize the TMS reaction mechanism that we developed and to understand the interaction of Si-containing species with the base flame radicals and combustion intermediates.

Figure 4.3 shows a bipartite graph generated by the Gephi software [162]. The nodes shown in this graph represent (i) chemical species and (ii) reactions, for the developed TMS mechanism merged with the C1 mechanism from Li et al. [5]. The edges between these nodes show how chemical species are involved in specific reaction. An arrow toward a reaction node specifies the source node as reactants involved in this reaction and an edge away from a reaction node specifies the target node as products involved in this reaction. The left

set of elements in this graph refers to the TMS sub-mechanism. Dark red circles represent Si-containing species within the TMS sub-mechanism, and bright red circles represent reactions accordingly. The right set of the elements refers to the C1 mechanism of Li et al. [5]. Dark blue circles represent chemical species within the C1 mechanism and bright blue circles represent reactions. The bipartite graph may not be the best approach for visualization of a chemical reaction mechanism, but it gives the opportunity to have a graphical representation for interaction of different sub-mechanisms in a chemical reaction mechanism.

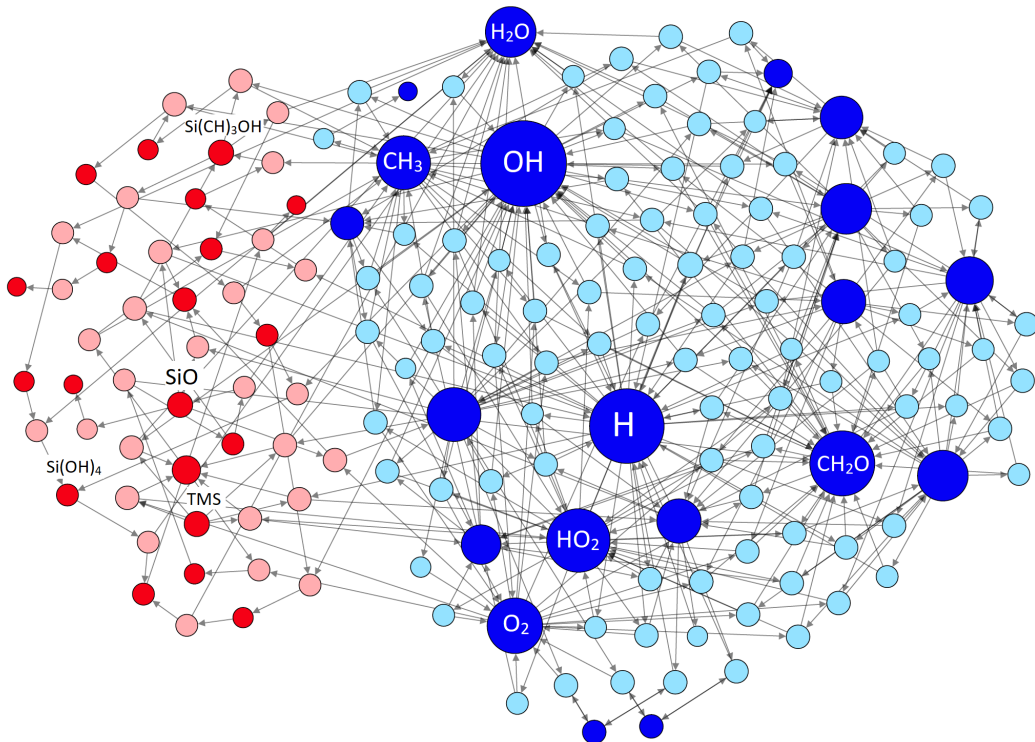


Fig. 4.3 Bipartite graph with the nodes being represented by chemical species and reactions. The left set of elements in this graph refers to the developed TMS mechanism and the right set of elements refers to the C1 mechanism from Li et al. [5]. See text for further explanation.

4.8 Cantera

Cantera [163] is an open-source library consisting of tools for simulation of problems related to thermodynamics, chemical reaction kinetics, and transport processes. It supports four programming languages that give access to many environments: Python, MATLAB, FORTRAN, and C++. Cantera provides various models for the simulations of reacting flows such as one-dimensional laminar free propagating flames, time-dependent perfectly stirred

reactors, stagnation flames, and burner-stabilized flames. Being open-source gives Cantera an advantage in that the numerical algorithms and models can be customized for specific applications. Another advantage of Cantera in chemical kinetics studies is that one can only focus on the reaction mechanism development without the complexity of the numerical solution of reacting flows. To run a simulation the desired model such as a burner-stabilized flame can be called from the desired interface such as Python. And the boundary conditions and the reaction mechanism are required to be specified as inputs. The reaction mechanism provides the list of species, list of reactions, thermodynamics properties, and transport data. Cantera supports the reaction mechanisms in CHEMKIN [164] format as input. For the simulations in this work, Cantera is used as a chemical kinetic library in the Python environment.

Chapter 5

Response surface and group additivity methodology for estimation of thermodynamic properties of organosilanes

Authors: H. Janbazi, O. Hasemann, C. Schulz, A. Kempf, I. Wlokas, S. Peukert

This chapter including all text, figures and tables was previously published in 'International Journal of Chemical Kinetics, 50, H. Janbazi, O. Hasemann, C. Schulz, A. Kempf, I. Wlokas, S. Peukert, Response surface and group additivity methodology for estimation of thermodynamic properties of organosilanes, 681-690, 2018' and is reprinted with permission from Wiley. The author of this thesis contributed the development of regression analysis code and thermochemistry metadata, the validation of results, and writing the paper. The author S. Peukert contributed quantum chemical calculations, discussion, and supervision. The authors O. Hasemann, C. Schulz, A. kempf, and I. Wlokas contributed proof-reading and guidance.

5.1 Abstract

Group-additivity methods simplify the determination of thermodynamic properties of a wide range of chemically-related species involved in detailed reaction schemes. In this paper, we expand Benson's group additivity method to organosilanes. Based on quantum-chemical calculations, the thermodynamic data of 22 stable silicon-organic species are calculated, presented in the form of NASA polynomials, and compared to the available experimental

data. Based on this theoretical database, a complete set of 24 Si- and C-atom-centered, single-bonded and non-radical group-additivity values (GAV) for enthalpy of formation, standard entropy, and heat capacity at temperatures from 200 to 4000 K is derived through unweighted multivariate linear regression.

5.2 Introduction

Organic silicon-containing compounds such as hexamethyldisiloxane (HMDSO, $(\text{CH}_3)_3\text{SiO-Si}(\text{CH}_3)_3$), tetraethoxy-silane (TEOS, $\text{Si}(\text{OC}_2\text{H}_5)_4$), and tetramethylsilane (TMS, $\text{Si}(\text{CH}_3)_4$), as well as monosilane (SiH_4) are popular precursors for the synthesis of silicon-based nanoparticles and coatings (primarily silica, SiO_2) via combustion processes [48, 165, 166, 31, 167]. The development of detailed reaction schemes so far suffers from the lack of knowledge of the thermodynamic properties of the reaction intermediates. While in combustion science, complex reaction mechanisms and comprehensive thermodynamics databases have been developed for hydrocarbon species used as fuels, in materials synthesis, chemical kinetics modeling and therefore the development of reaction mechanisms and thermodynamics databases are far less developed but of similar importance. So far, the Si–H–O-system was investigated mostly in the context of SiH_4 combustion. Reaction schemes for SiH_4 combustion have been developed in the last decade [167, 168]. Recently, Feroughi et al. [69] proposed a simple global HMDSO combustion reaction scheme. However, due to the unknown thermodynamic properties of some intermediate species, it was not possible to develop detailed reaction models. This is one example that emphasizes the need to obtain thermodynamic data for silicon-organic molecules.

The present study determines thermodynamic parameters, including standard enthalpy of formation ΔH_f° , entropy S , and heat capacities $C_p(T)$ for a temperature range from 200 to 4000 K, which covers the relevant conditions for particle synthesis from flames. To achieve this, we used Benson's group additivity [139, 143] method in a systematic and automated approach. Unfortunately, so far, almost no group additivity values (GAVs) are known for silicon-organic molecules representing the Si–C–H system. Due to the lack of experimental thermochemicals data for silicon-organic molecules, it is not possible to develop GAVs based on experimental results. Recent developments in computational chemistry have made it possible to determine accurate enthalpies of formation from *ab initio* calculations. This development makes it possible to determine some of the missing GAVs from theory. The aim of this study is to derive a consistent and accurate set of GAVs for silicon organic molecules based on accurate standard enthalpies of formation obtained from high-level G4 *ab initio* calculations.

5.3 Methodology

5.3.1 Quantum chemical calculation

All quantum chemical calculations were performed at the G4 level of theory using the GAUSSIAN 09 software [169, 136]. Standard enthalpies of formation were calculated using the atomization energy method. In this method, the enthalpy of formation at 0 K, $\Delta H_f^\circ(0 \text{ K})$, is obtained as the difference between the ab initio calculated (ai) atomization enthalpy of a compound and the experimentally determined enthalpies of formation of the gaseous atoms:

$$\begin{aligned} \Delta H_f^\circ(0 \text{ K}, \text{Si}_a \text{C}_b \text{H}_c) = & a\Delta H_{f, \text{gas,exp}}^\circ(0 \text{ K}, \text{Si}) + b\Delta H_{f, \text{gas,exp}}^\circ(0 \text{ K}, \text{C}) \\ & + c\Delta H_{f, \text{gas,exp}}^\circ(0 \text{ K}, \text{H}) - [aH_{\text{ai}}^\circ(0 \text{ K}, \text{Si}) + bH_{\text{ai}}^\circ(0 \text{ K}, \text{C}) \\ & + cH_{\text{ai}}^\circ(0 \text{ K}, \text{H}) - H_{\text{ai}}^\circ(0 \text{ K}, \text{Si}_a \text{C}_b \text{H}_c)] \quad (5.1) \end{aligned}$$

This equation includes the enthalpies of formation of the atomic constituents: $\Delta H_f^\circ(0 \text{ K}, \text{Si}) = 446.2 \text{ kJ/mol}$, $\Delta H_f^\circ(0 \text{ K}, \text{C}) = 711.5 \text{ kJ/mol}$, and $\Delta H_f^\circ(0 \text{ K}, \text{H}) = 216.1 \text{ kJ/mol}$. By applying enthalpy corrections for the molecules and atomic elements, $H^\circ(298 \text{ K}) - H^\circ(0 \text{ K})$, to $\Delta H_f^\circ(0 \text{ K})$, standard enthalpies of formation at 298 K, ΔH_f° , are calculated [137]:

$$\begin{aligned} \Delta H_f^\circ = & \Delta H_f^\circ(0 \text{ K}, \text{Si}_a \text{C}_b \text{H}_c) + [H^\circ(298 \text{ K}) - H^\circ(0 \text{ K}, \text{Si}_a \text{C}_b \text{H}_c) \\ & - a[H^\circ(298 \text{ K}) - H^\circ(0 \text{ K}, \text{Si})] - b[H^\circ(298 \text{ K}) - H^\circ(0 \text{ K}, \text{C})] \\ & - c[H^\circ(298 \text{ K}) - H^\circ(0 \text{ K}, \text{H})] \quad (5.2) \end{aligned}$$

The enthalpy corrections for the gas atoms are 3.18 kJ/mol for Si, 1.05 kJ/mol for C, 4.23 kJ/mol for H, and the enthalpy corrections for the molecules are extracted from the results of quantum chemical calculations. Based on molecular properties (molecular structures, vibrational frequencies, and moments of inertia) obtained from quantum chemical calculations, thermodynamics data for heat capacity $C_p(T)$, enthalpy of formation $H_f(T)$, and entropy $S(T)$ have been derived by using the GPOP (Gaussian Post Processor) program [170]. The vibrational frequencies, calculated by the B3LYP/6-31G(2df,p) method during the G4 procedure, were scaled by 0.99 for the zero-point energy calculation and by 0.97 for the vibrational partition function calculations. Internal rotations around the bonds of CH₃ and SiH₃ groups attached to carbon and/or silicon atoms were treated as hindered rotations by using the Pitzer-Gwin approximation¹⁵ as implemented in the GPOP program. Rotational barrier heights for CH₃ and SiH₃ rotors (typically ranging from 280 to 1220 cm⁻¹) have been obtained from relaxed potential energy surface (PES) scans with dihedral angles used

as coordinates for the scans. Figure 5.1 shows CH₃ and SiH₃ PES scan for CH₃ and SiH₃ rotors of 1,1-disilyl-ethane.

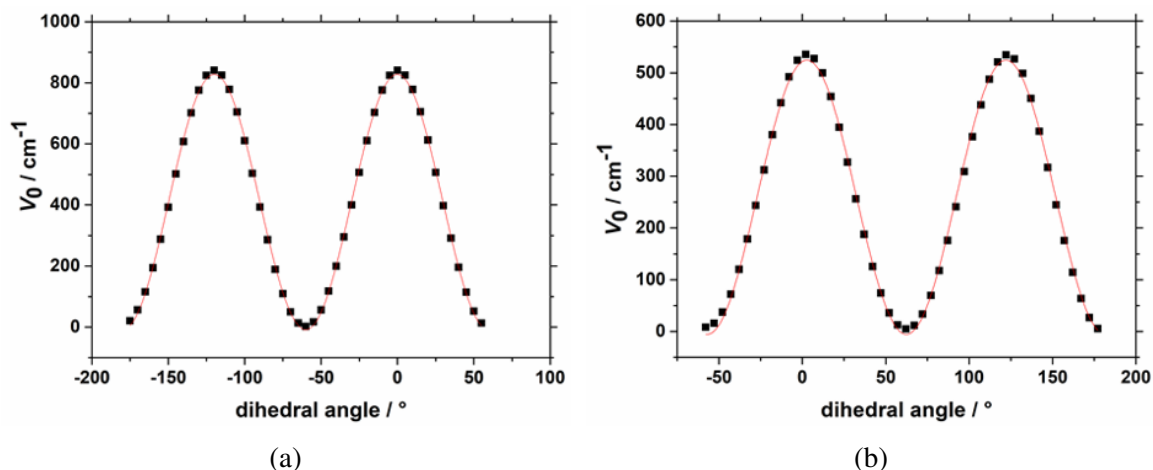


Fig. 5.1 Potentials of the CH₃ (a) and SiH₃ (b) rotors in 1,1-disilyl-ethane with maxima at 825 and 535 cm⁻¹.

Enthalpies of formation obtained by experiments are only available for few silanes and silicon organic compounds. Experimental values for ΔH_f° can be found for disilane (Si₂H₆) [171], trisilane (Si₃H₈) [172], tetramethylsilane (TMS) and its derivatives, SiH_x(CH₃)_y [173, 174]. For silanes, Si_xH_y, ambiguities regarding standard enthalpies of formation were previously discussed. For Si₂H₆ and Si₃H₈, Gunn and Green [171, 172] measured $\Delta H_f^\circ = 71.6 \pm 1.3$ kJ/mol and 108.4 kJ/mol. For Si₃H₈, no uncertainty was stated by Gunn and Green [172]. Based on a revision of $\Delta H_f^\circ(0 \text{ K, Si})$, the experimental value for $\Delta H_f^\circ(\text{Si}_2\text{H}_6)$ was increased by 8.4 kJ/mol [175]. Feller and Dixon [176] performed detailed *ab initio* calculations for silicon-containing compounds Si_xH_y and SiF_y and made a comparison with experimental data sets. They concluded that there is no clear evidence supporting a revision of $\Delta H_f^\circ(0 \text{ K, Si})$. Therefore, they recommended to use the original experimental value $\Delta H_f^\circ(\text{Si}_2\text{H}_6) = 71.6$ kJ/mol and in this context, we also decided to use the original value $\Delta H_f^\circ(\text{Si}_3\text{H}_8) = 108.4$ kJ/mol measured by Gunn and Green [171, 172] for comparison between experiment and theory.

Based on the comparison between G4 calculations and limited experimental data for Si₂H₆, Si₃H₈, TMS and its derivatives Si(CH₃)_xH_y, we find a ‘good’ agreement between experimental and calculated enthalpies of formation, i.e. the calculations are ± 8.0 kJ/mol within the experimentally obtained values. Except for trimethylsilane, SiH(CH₃)₃, the calculated values for ΔH_f° are within the stated experimental uncertainties. Calculated and available experimental data are presented in Table 5.1.

To further support the application of the G4 method, we have also calculated ΔH_f° for those six compounds in table 5.1, for which experimental data are available, by using two other composite methods: CBS-QB3 [177] and W1BD [178]. Among these three composite methods, CBS-QB3 is the most cost-effective one, whereas W1BD requires higher computational resources than G4. The CBS-QB3 and W1BD based data are also presented in table 5.1. The mean absolute deviations (MAD) between the *ab initio* calculated and experimental values are 9.2 kJ/mol for CBS-QB3, 3.4 kJ/mol for G4, and 8.9 kJ/mol for W1BD. For those few compounds, the G4 method shows the best performance. CBS-QB3 and W1BD show similar MAD values, which is not expected. In case of the W1BD composite method, one can observe a systematic deviation to experimental data with increasing number of Si–H bonds. W1BD based enthalpies agree very well with experimental enthalpies of tetramethyl- and trimethylsilane. With an increasing number of Si–H bonds, i.e. for dimethyl- and methylsilane, the deviation to experimental values substantially increases. This becomes also evident when comparing results of W1BD calculations with experimental data of disilane and trisilane (see Table 5.1): The deviations are 12.3 kJ/mol for disilane and 17.5 kJ/mol for trisilane. In case of W1BD, it would be necessary to employ a bond-additive correction (BAC) for Si–Si and Si–H bonds to obtain very good agreement between theoretical and experimental thermochemical data. In case of the CBS-QB3 method, deviations for compounds with a larger number of Si–H bonds are not that pronounced as it is the case for W1BD. However, comparing CBS-QB3-based enthalpies with the data for tetramethyl- and trimethylsilane suggests that also empirical corrections for Si–C bonds may be necessary.

BAC are well established for hydrocarbons and oxygenated hydrocarbons. Regarding silicon organic species, Allendorf and Melius [179] as well as Ho and Melius [180] used empirical BAC to improve theory-based thermodynamics parameters for compounds in the Si–O–C–H system. Recently, Phadungsukanan et al. [8] expanded these studies. They performed *ab initio* calculations using B3LYP and B97-1 functionals. ΔH_f° values were obtained using isodesmic reactions. The reported error range of the ΔH_f° values calculated using isodesmic reactions is between 5 and 40 kJ/mol. Phadungsukanan et al. [8] discussed the possibility of an error in the BAC from Ho and Melius. If only few experimental data are available or if experimental data exhibit substantial uncertainties of even 30 to 40 kJ/mol, which applies for compounds like $(\text{CH}_3)_2\text{Si}=\text{CH}_2$ or $\text{Si}(\text{OCH}_3)_4$ (see Allendorf and Melius [179] as well as Ho and Melius [180]), then applying BAC with a bias on particular data can give reason for additional errors.

In this work, we did not include BAC or any other empirical corrections. Taking a look at the G4-based ΔH_f° values and comparing them with the limited available experimental ΔH_f° data, we cannot see a clear systematic difference, at least for tetramethylsilane and

its derivatives, i.e. tri-, di-, and methylsilane. Also, the deviations between G4 theory and measured standard enthalpies of formation of disilane and trisilane are within the experimental uncertainties. With increasing size of the molecules, also the G4 method will probably result in larger errors. However, one should note that this method already contains empirical corrections, which are called “higher level corrections” [169]. These are empirical terms that were included in order to correct energy calculations for molecular species, radicals and different atoms, and these correction terms may be the reason why the G4 method seems to work quite well for Si–C–H-containing molecular species. It is interesting to note that Simmie and Somers demonstrated that even for the thermochemistry of the molecular hydrocarbon compounds $C_xH_yO_z$, the G4 is outperforming the W1BD method [181, 182]. Therefore, these results suggest applying the G4 method without any further additional empirical corrections in order to derive thermochemical data of smaller silanes and Si–C-containing molecules.

5.3.2 Group additivity method

Benson [139] defines a group as a part of a molecule, consisting of a central polyvalent atom (ligancy ≥ 2) and all its neighbors. A group is written as $X-(A)_i(B)_j(C)_k(D)_l$ where X is the central atom attached to i A-atoms, j B-atoms, etc. Cohen and Benson [143] tabulated thermochemical values for 37 hydrocarbon groups, 61 oxygen-containing groups, 59 nitrogen-containing groups, 58 organometallic groups and 65 organophosphorous and organoboron groups. Later, corrections for non-bonding interactions were updated by Benson [139]. As an example, the groups involved in TMS are shown in Fig. 5.2. Two distinct groups are contributing to TMS properties. To name the groups, the central atom comes first and is then followed by neighbor atoms in brackets in alphabetical order.

Many publications reported GAVs for a variety of stable molecules and radicals [144, 142, 145, 141]. The derivation of GAVs for a certain class of chemical compounds requires the availability of a minimum set of thermochemical data. Bjorkman et al. [146] calculated ΔH_f° for 57 carbenium ions and from this theory-based dataset, they determined 16 GAVs by applying multiple regression. From these 57 values, they constructed 48 groups. From these 48 groups, 32 GAVs were available in the literature. They fixed these 32 GAVs, and the remaining 16 GAVs were derived through the method of multiple linear regression. For obtaining GAVs for silicon-containing species, we applied a similar method like Bjorkman et al. [146], but since almost no GAVs are available, we did not fix any GAVs in our procedure, i.e. all groups are involved in the regression, which is explained in section 5.3.3.

Doncaster and Walsh [173] derived six GAVs contributing to ΔH_f° of organosilanes. However, no high-temperature data of $C_p(T)$ and H_f were provided. Therefore, these six GAVs cannot be used for combustion modeling. For the C–(H)₃(Si) group, they assigned the

same value as for the C–(C)(H)₃ group as suggested by Benson [139], but our calculation for the C–(H)₃(Si) group indicates that this is not an appropriate analogy.

Thus, we focus on the Si–C–H chemistry to estimate GAVs for Si and C containing molecules to extend the applicability of Benson’s group additivity method for estimating thermodynamic properties of larger organosilane compounds. All groups are Si- and C-atom-centered groups with four neighbors attached by single bonds.

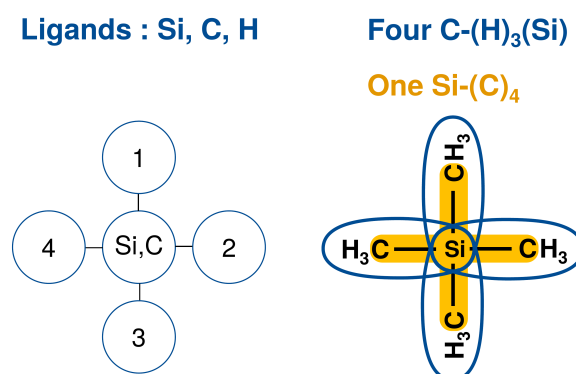


Fig. 5.2 Combinatorial arrangement for three possible Si, C, and H atoms for four possible ligands for Si- and C-atom-centered groups (left) and Benson groups contributing to TMS (right).

The combinatorial approach (Fig. 5.2) to build all possible groups that contain Si, C, and H atoms leads to 30 Si- and C-atom-centered groups. We are interested in 24 groups among these groups that contain Si. The other six groups contain only C and H atoms and the GAVs of these groups are known. Among the Si–C–H-containing species, 22 species are chosen that contain our 24 groups of interest. In other words, these 24 groups contribute to the thermodynamics data of 22 species. These groups and their contributions to ΔH_f° , S , and C_p are shown in Table 2. The molecular structures of the Si–C–H compounds considered (see Table 1) are shown in Fig. 5.3.

5.3.3 First-Order Response-Surface Methodology

The Response-Surface Methodology (RSM) is a collection of mathematical and statistical techniques for modeling the relationships between several independent variables and one or more response variables. The method was introduced by Box and Wilson [149]. The objective is to optimize the response y_i (output variable), which is a function f of the independent variables β_j (input variables).

In most RSM problems, the response function is unknown, but with the help of the group-additivity method, a proper approximation for f is developed. This approximation can

be defined by a linear function of the independent variables, resulting in a first-order model, where ε_i is an error term.

$$y_i = f(\beta_1, \beta_1, \beta_1, \dots, \beta_p) + \varepsilon \quad (5.3)$$

To get the best approximation for the response function, a wide collection of data is needed. Due to the lack of experimental values, the required dataset was obtained by quantum chemical calculations. The goal is to fit the response surface to find the region where the optimal response occurs. From the theory-based dataset, a first-order model, which is a multivariate linear regression (MLR) model, is formed for all n species simultaneously which can be written in matrix form as in Eq. (5.4). This equation is solved for standard enthalpy of formation ΔH_f° , entropy S , and heat capacities C_p for eight temperatures between 200 and 4000 K. The matrix X and vector β are independent of the choice of thermodynamic data and only the vectors Y and ε change by changing the choice of thermodynamic data.

$$y_i = X_{ij}\beta_j + \varepsilon_i \quad (5.4)$$

In Eq. 5.4, the vector Y_i is the thermodynamics data of species i . The element x_{ij} specifies the number of times group j is present in species i . The vector β_j contains the GAVs for group j , the vector ε_i the error terms. In this study, i runs from 1 to 22 and j from 1 to 24. If X is a quadratic matrix and $\det(X) \neq 0$, then the linear system $Y = X\beta + \varepsilon$ has a unique least-squares solution. However, in the present work, X is not a quadratic matrix. Therefore, the least-squares method is used to find the coefficients of vector β by minimizing the summed square of residuals (Eq. 5.5).

$$\varepsilon_i = \sum |Y - X\beta|^2 \quad (5.5)$$

Theoretically, a global minimum results from the following equation if $X^T X$ is invertible:

$$\beta = (X^T X)^{-1} X^T Y = X^* Y, \quad (5.6)$$

The matrix X^* is called the pseudo-inverse of matrix X .

To illustrate the construction of the matrix X , an example of groups contributing to the thermodynamics of five Si–C–containing molecules is shown in Fig. S1 in the Supporting Information. The complete matrix, which is created in our study, contains 22 species and 24 groups.

5.4 Representation of the thermodynamic properties

The thermodynamic properties of molecules, such as enthalpy of formation or specific heat capacity as a function of temperature, were first represented by polynomials by Lewis and Randall [183]. In 1961, Zeleznik and Gordon [184] proposed a method for simultaneous regression of thermodynamic properties to represent more than one property by a single polynomial. Thermodynamic properties are often represented by the well-known NASA seven-coefficient polynomials. For many species, for which thermodynamic data are not available, it is necessary to reproduce NASA polynomials from data points measured in experiments or derived from theoretical calculations. The seven-coefficient polynomials that describe the enthalpy of formation, the entropy, and the heat capacity as a function of temperature are shown in Eqs. 5.7 to 5.9.

$$\frac{C_p(T)}{R} = a_0 + a_1T + a_2T^2 + a_3T^3 + a_4T^4 \quad (5.7)$$

$$\frac{H(T)}{RT} = a_0 + \frac{a_1T}{2} + \frac{a_2T^2}{3} + \frac{a_3T^3}{4} + \frac{a_4T^4}{5} + \frac{a_5}{T} \quad (5.8)$$

$$\frac{S(T)}{R} = a_0 \ln T + a_1T + \frac{a_2T^2}{2} + \frac{a_3T^3}{3} + \frac{a_4T^4}{4} + a_6 \quad (5.9)$$

In this study, we used Wilhoit's method [185] to extrapolate heat capacities of species for a larger range of temperature. The method uses the following fitting function for the heat capacity:

$$C_p = C_p(0) + [C_p(\infty) - C_p(0)] y^2 \left[1 + (y-1) \sum_{i=0}^n a_i y^i \right] \quad (5.10)$$

The normalized temperature $y = T/(T+B)$ varies from 0 to 1, where B is a scaling factor that determines how rapidly C_p approaches $C_p(\infty)$. The low-temperature-limit heat capacity $C_p(0)$ is $(7/2)R$ for linear molecules and $4R$ for nonlinear molecules, where R is the ideal gas constant. The classical high-temperature value $C_p(\infty)$ is $(3N - 3/2)R$ for linear molecules and $(3N - 2)R$ for nonlinear ones, where N is the number of atoms in the molecules. In this work, the heat capacity is extrapolated with a fourth order polynomial when it's needed, which means n in Eq. 5.10 is considered as three.

5.5 Results and discussions

In this study, quantum-chemical calculations at the G4 level of theory were conducted using the atomization energy method for estimating the thermochemistry of stable molecules of which the thermodynamic data are not available in the literature.

Enthalpies of formation obtained by experiments are only available for few silanes and silicon organic compounds. Based on the comparison between G4 calculations and limited experimental data for Si_2H_6 , Si_3H_8 , TMS and its derivatives $\text{Si}(\text{CH}_3)_x\text{H}_y$, we find a ‘good’ agreement between experimental and calculated enthalpies of formation, i.e. the calculations are ± 8.0 kJ/mol within the experimentally obtained values. Except for trimethylsilane, $\text{SiH}(\text{CH}_3)_3$, the calculated values for ΔH_f° are within the stated experimental uncertainties. Calculated and available experimental data are presented in Table 5.1.

To further support the application of the G4 method, we have also calculated ΔH_f° for those six compounds in table 5.1, for which experimental data are available, by using two other composite methods: CBS-QB3 [177] and W1BD [178]. Among these three composite methods, CBS-QB3 is the most cost-effective one, whereas W1BD requires higher computational resources than G4. The CBS-QB3 and W1BD based data are also presented in table 5.1. The mean absolute deviations (MAD) between the *ab initio* calculated and experimental values are 9.2 kJ/mol for CBS-QB3, 3.4 kJ/mol for G4, and 8.9 kJ/mol for W1BD. For those few compounds, the G4 method shows the best performance. CBS-QB3 and W1BD show similar MAD values, which is not expected. In case of the W1BD composite method, one can observe a systematic deviation to experimental data with increasing number of Si–H bonds. W1BD based enthalpies agree very well with experimental enthalpies of tetramethyl- and trimethylsilane. With an increasing number of Si–H bonds, i.e. for dimethyl- and methylsilane, the deviation to experimental values substantially increases. This becomes also evident when comparing results of W1BD calculations with experimental data of disilane and trisilane (see Table 5.1): The deviations are 12.3 kJ/mol for disilane and 17.5 kJ/mol for trisilane. In case of W1BD, it would be necessary to employ a bond-additive correction (BAC) for Si–Si and Si–H bonds to obtain very good agreement between theoretical and experimental thermochemical data. In case of the CBS-QB3 method, deviations for compounds with a larger number of Si–H bonds are not that pronounced as it is the case for W1BD. However, comparing CBS-QB3-based enthalpies with the data for tetramethyl- and trimethylsilane suggests that also empirical corrections for Si–C bonds may be necessary.

BAC are well established for hydrocarbons and oxygenated hydrocarbons. Regarding silicon organic species, Allendorf and Melius [179] as well as Ho and Melius [180] used empirical BAC to improve theory-based thermodynamics parameters for compounds in the Si–O–C–H system. Recently, Phadungsukanan et al. [8] expanded these studies. They

performed *ab initio* calculations using B3LYP and B97-1 functionals. ΔH_f° values were obtained using isodesmic reactions. The reported error range of the ΔH_f° values calculated using isodesmic reactions is between 5 and 40 kJ/mol. Phadungsukanan et al. [8] discussed the possibility of an error in the BAC from Ho and Melius. If only few experimental data are available or if experimental data exhibit substantial uncertainties of even 30 to 40 kJ/mol, which applies for compounds like $(\text{CH}_3)_2\text{Si}=\text{CH}_2$ or $\text{Si}(\text{OCH}_3)_4$ (see Allendorf and Melius [179] as well as Ho and Melius [180]), then applying BAC with a bias on particular data can give reason for additional errors.

In this work, we did not include BAC or any other empirical corrections. Taking a look at the G4-based ΔH_f° values and comparing them with the limited available experimental ΔH_f° data, we cannot see a clear systematic difference, at least for tetramethylsilane and its derivatives, i.e. tri-, di-, and methylsilane. Also, the deviations between G4 theory and measured standard enthalpies of formation of disilane and trisilane are within the experimental uncertainties. With increasing size of the molecules, also the G4 method will probably result in larger errors. However, one should note that this method already contains empirical corrections, which are called “higher level corrections” [169]. These are empirical terms that were included in order to correct energy calculations for molecular species, radicals and different atoms, and these correction terms may be the reason why the G4 method seems to work quite well for Si–C–H-containing molecular species. It is interesting to note that Simmie and Somers demonstrated that even for the thermochemistry of the molecular hydrocarbon compounds $\text{C}_x\text{H}_y\text{O}_z$, the G4 is outperforming the W1BD method [181, 182]. Therefore, these results suggest applying the G4 method without any further additional empirical corrections in order to derive thermochemical data of smaller silanes and Si–C-containing molecules.

Enthalpies of formation, standard entropies and heat capacities in the range from 200 to 2000 K are calculated for a set of 22 stable molecules. The calculated values are compared to the few experimental values reported in the literature. Figure 5.4a shows the *ab initio* data that was considered as reliable thermodynamic data since they closely match the data available in open literature [171–174]. The maximum deviation and the mean absolute deviation between *ab initio* data and the data available in the literature is 8 and 3.4 kJ/mol, respectively.

By using the abovementioned multivariate linear regression (MLR) model, 24 GAVs were determined for Si–C–H chemistry. These groups are listed in Table 5.2 along with their enthalpy of formation, standard entropy, and heat capacity at various temperatures. As previously mentioned, Doncaster and Walsh [173] assumed a thermochemical analogy between C–Si- and C–C-containing groups to get reasonable estimations for thermodynamic parameters of Si–C–H compounds. They assigned the value of the C–(C)(H)₃ group [139]

Table 5.1 ΔH_f° (kJ/mol) of 22 reference species for the training set in this section, comparing the atomization and isodesmic methods.

Species	Atomization method			G4/isodesmic	Exp.
	CBS-QB3	G4	W1BD		
disilane	61.0	70.6	59.3		71.6±1.3 ^a
trisilane	95.0	106.1	90.9		108.4 ^b
2-silyl-trisilane		134.1		149.7 ± 6.6	
1,1,1-trimethyl-disilane		-112.7		-118.1 ± 13.2	
2,2-dimethyl-trisilane		-11.9		-9.2 ± 10.2	
2-methyl-trisilane		49.2		56.8 ± 7.0	
2-methyl-2-silyl-trisilane		77.6		88.3 ± 8.2	
disilyl-methane		5.8		5.8 ± 9.0	
trisilyl-methane		30.7		29.5 ± 12.7	
tetrasilyl-methane		41.1		38.5 ± 16.5	
1,1,1-trisilyl-ethane		20.8		18.8 ± 12.7	
2-silyl-2-methyl-propane		-89.3		-90.0 ± 5.8	
2-silyl-propane		-59.1		-59.2 ± 5.8	
2,2-disilyl-propane		-23.6		-20.6 ± 6.1	
methyl-silane	-36.2	-30.4	-39.0		-29.0±4.0 ^c
dimethyl-silane	-94.3	-91.6	-102.5	-95.1 ± 9.1	-95.0±4.0 ^c
trimethyl-silane	-155.1	-155.3	-167.9	-163.8 ± 13.0	-163.0±4.0 ^c
tetramethyl-silane	-218.1	-237.9	-234.7	-234.4 ± 16.9	-233.2±3.2 ^{c,d}
neo-pentasilane		154.3		173.0 ± 8.2	
1,1-dimethyl-disilane		-48.2		-48.6 ± 9.5	
1-methyl-disilane		12.9		17.4 ± 6.1	
1,1-disilyl-ethane		-2.8		-3.5 ± 9.0	

^aRef. [171]. ^bRef.[172]. ^cRef.[173]. ^dRef.[174].

Table 5.2 GAVs of organosilane compounds calculated by atomization method (units: ΔH_f° : kJ/mol, S° and C_p : J/mol K).

Groups	ΔH_f°	S°	$C_p(T)$							
			298 K	400 K	500 K	600 K	800 K	1000 K	1500 K	2000 K
C-(C)(Si) ₃	12.3	-121.5	30.7	33.0	33.4	33.4	34.1	34.1	33.8	33.0
C-(C) ₂ (Si) ₂	27.0	-143.3	31.2	35.4	36.0	35.6	35.9	35.2	33.9	31.3
Si-(C) ₂ (H) ₂	-0.14	47.3	30.3	37.7	43.6	48.3	55.2	59.7	65.2	67.7
Si-(C) ₄	-48.7	-138.1	22.1	26.1	27.5	28.1	29.6	30.4	31.4	31.2
C-(C)(H)(Si) ₂	5.6	-32.6	28.1	32.4	35.1	37.1	40.9	43.3	46.8	47.9
Si-(C)(H) ₂ (Si)	25.0	63.6	33.4	39.8	44.7	48.6	54.5	58.5	64.1	66.7
Si-(C) ₃ (H)	-21.6	-47.4	27.3	33.1	36.7	39.1	42.9	45.4	48.6	50.4
C-(C) ₃ (Si)	20.4	-167.6	27.5	33.5	35.2	35.4	36.3	35.5	33.5	29.4
Si-(C)(H) ₃	16.9	131.3	35.9	44.0	50.8	56.5	65.1	71.2	79.5	83.5
C-(Si) ₄	-26.4	-110.8	27.5	30.3	31.9	32.9	33.9	34.4	34.5	35.1
Si-(H) ₃ (Si)	35.3	141.1	39.6	47.2	53.4	58.6	66.6	72.3	80.2	84.1
Si-(H)(Si) ₃	28.3	-10.2	32.0	36.4	39.2	41.2	44.3	46.3	49.0	50.3
C-(H) ₃ (Si)	-47.3	126.6	30.9	37.3	43.0	48.2	56.5	63.1	73.8	80.0
Si-(Si) ₄	13.1	-99.6	28.1	30.3	31.4	32.0	32.6	32.9	33.1	33.2
Si-(H) ₂ (Si) ₂	35.5	68.9	35.9	42.1	46.6	50.1	55.6	59.4	64.7	67.3
C-(C) ₂ (H)(Si)	8.4	-53.9	26.5	31.9	34.9	36.9	40.9	43.1	46.1	45.8
Si-(C) ₃ (Si)	-6.15	-122.3	26.3	28.5	29.6	30.2	31.1	31.5	32.1	31.8
Si-(C) ₂ (H)(Si)	11.2	-23.9	29.1	33.6	36.8	39.2	42.7	44.9	48.1	49.2
Si-(C) ₂ (Si) ₂	12.1	-112.1	28.9	30.9	31.7	31.9	32.4	32.5	32.7	32.4
Si-(C)(H)(Si) ₂	25.9	-15.3	30.9	35.2	38.2	40.3	43.6	45.7	48.5	49.8
C-(C)(H) ₂ (Si)	-7.42	32.8	24.6	31.2	37.1	42.5	50.8	56.5	65.6	69.2
Si-(C)(Si) ₃	19.1	-101.8	28.5	30.3	31.3	31.7	32.3	32.6	32.8	32.8
C-(H)(Si) ₃	-19.8	-18.7	23.3	28.9	33.4	36.8	40.9	43.8	47.6	50.1
C-(H) ₂ (Si) ₂	-28.0	58.2	27.2	33.4	38.6	42.9	49.0	53.8	60.9	65.2

(-42.8 kJ/mol) for the C-(H)₃(Si) group for standard enthalpy of formation. However, we have determined a group additivity value of -47.3 kJ/mol for the standard enthalpy of formation for the C-(H)₃(Si) group. Using the new determined value of the C-(H)₃(Si) group to reproduce the standard enthalpy of formation of TMS showed better agreement with measured data [173, 174] for TMS. This indicates that the assumption of such group-increment analogies between hydrocarbons and Si-C-H molecules can result in correspondingly larger errors for larger Si_xC_yH_z species.

Figure 5.4(b) compares the enthalpies of formation used in the regression to the values that are fitted by our regressed GAVs. The plot shows a nearly perfect agreement of group-additivity re-calculated thermodynamics data and the calculated values from G4 theory, which proves the group additivity method as a convenient tool to obtain thermodynamics data of organosilanes. The maximum deviation and the mean absolute deviation between group-additivity re-calculated thermodynamics data and the *ab initio* calculation is 0.01 and 0.003 kJ/mol, respectively.

A model adequacy test is done to check if the fitted model is a suitable approximation for the true response surface. The analyses of variance and regression were performed assuming that the ϵ_i have a normal distribution. Figure 5.5a shows the residuals on the vertical axis over the fitted values on the horizontal axis. The residuals scatter around the mean line, confirming

the linear relationship between GAVs and the thermodynamics data of species, which is suggested by Benson [139]. In addition, the residuals form a horizontal band around the mean line, showing that the variances of the error terms are comparable, there are no outliers. It should be noted that the mean line slightly deviates from zero. For this magnitude of (normalized) residuals, the deviations of the order of 1×10^{-13} are negligible. The accuracy of regressed GAVs can be increased by having the thermodynamic data of more species as the input data for regression, but in this study with only 22 input values, the regressed GAVs reproduces the G4 values very well as shown in Fig. 5.4b. The normal probability plot in Fig. 5.5b gives the theoretical percentiles of the normal distribution versus the observed data. This plot shows the residuals on the y axis and the theoretical percentiles of the normal distribution on the x axis. The best-fit line shows the linear relationship between the residuals and the theoretical percentiles. Therefore, the results support the assumption that the error terms follow a normal distribution. The coefficient of determination R^2 was 98%, indicating that the data are close to the fitted regression line and that the model explains all the variability of the dependent data around its mean.

5.6 Conclusion

In this study, thermodynamic properties of Si-containing species have been obtained from G4 quantum chemical calculations. A comparison based on a set of few available experimental data suggests that among three composite methods, CBS-QB3, G4, and W1BD, the G4 method is the most reliable method to estimate thermodynamics data of Si–C–H-containing compounds. Group-additivity values for 24 Si-containing groups were determined by applying a multivariate linear regression (MLR) model. The regression analysis proved the quality of fit of our group additivity method combined with the response-surface methodology for generating thermodynamics data of species for which no experimental data are available.

5.7 Acknowledgements

We gratefully acknowledge financial support by the German Research Foundation (DFG, FOR 2284, WL63/1 and SCHU1369/25).

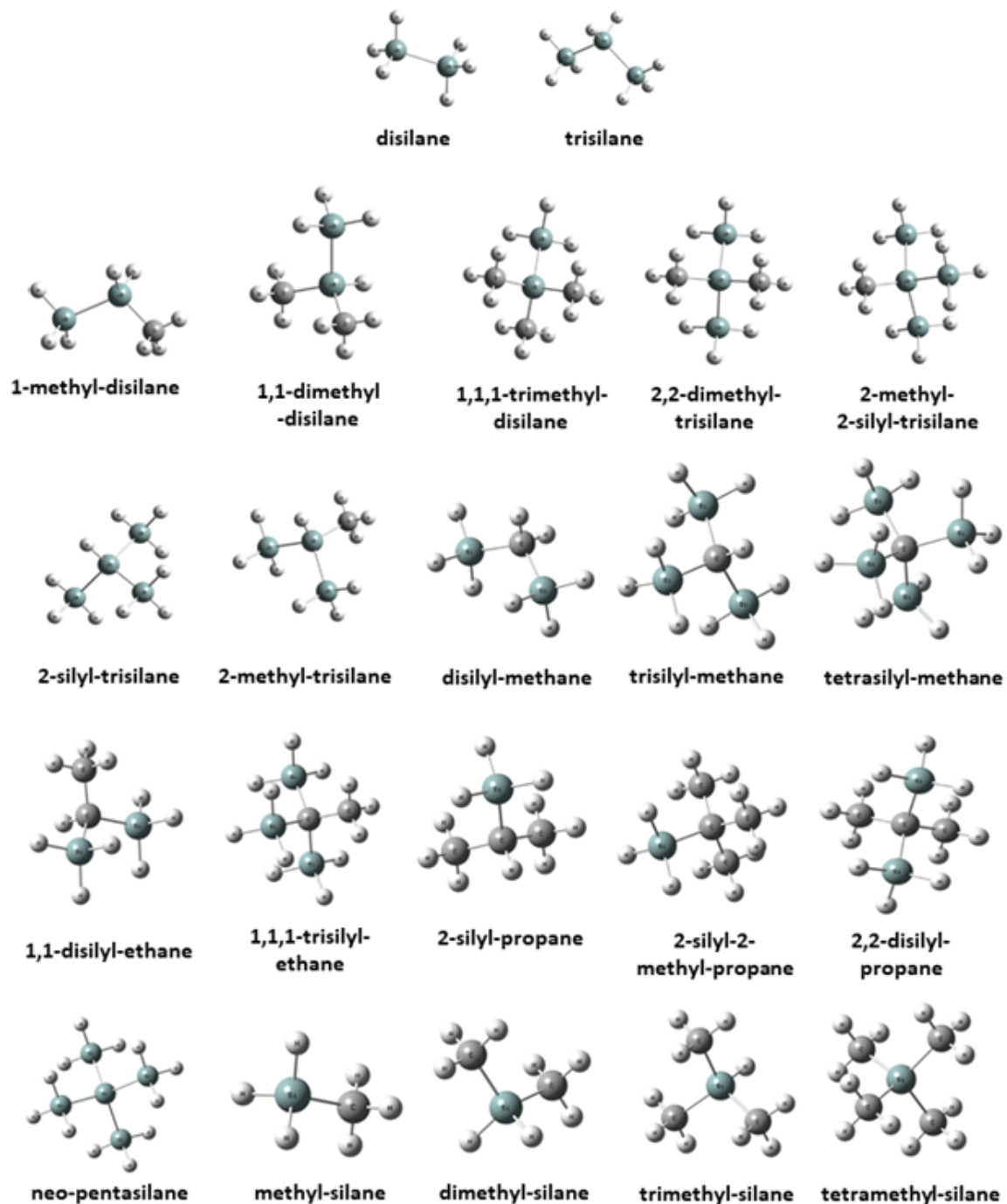


Fig. 5.3 B3LYP/6-31G(2df,p) geometry-optimized structures of the 22 Si-C-H molecules considered for deriving group-additivity values.

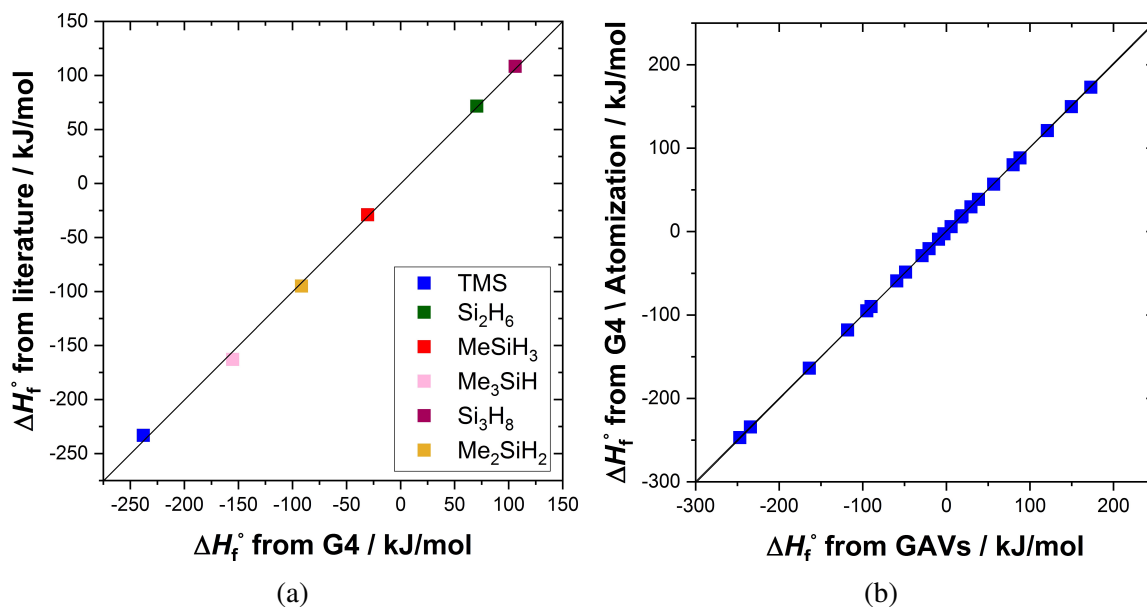


Fig. 5.4 (a) Comparison of calculated enthalpies of formation with available data shown in Table 5.1, (b) Comparison of the G4/atomization with the regressed GAVs.

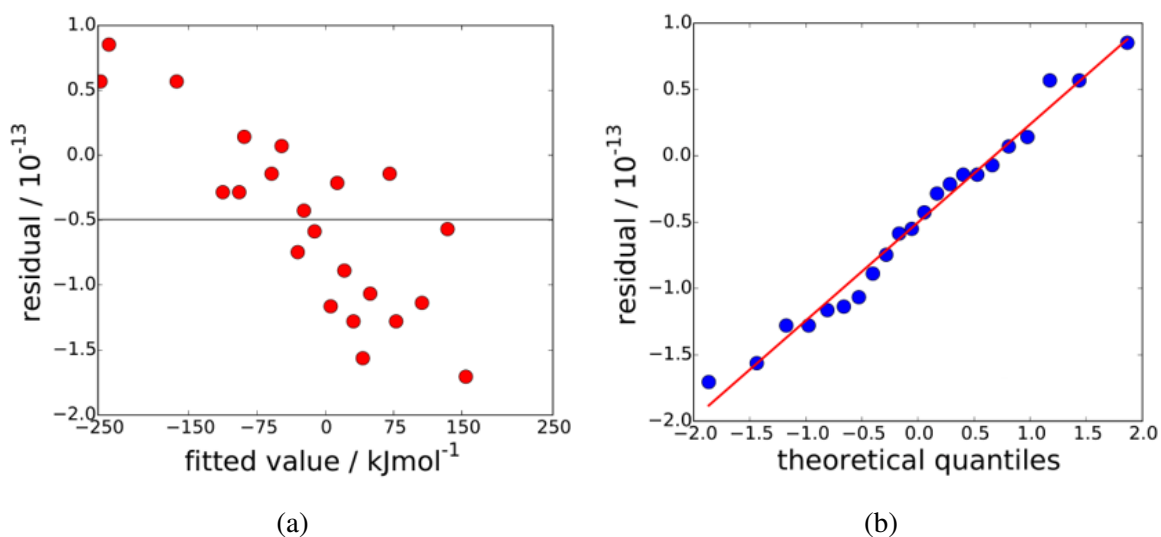


Fig. 5.5 (a) GAVs residuals versus fitted values, (b) GAVs residuals versus fitted values.

Chapter 6

Thermochemistry of organosilane compounds and organosilyl radicals

Authors: H. Janbazi, C. Schulz, I. Wlokas, H. Wang, S. Peukert

This chapter including all text, figures and tables was previously published in 'Proceedings of the Combustion Institute, 38, H. Janbazi, C. Schulz, I. Wlokas, H. Wang, S. Peukert, Thermochemistry of organosilane compounds and organosilyl radicals, 1259-1267, 2021' and is reprinted with permission from Elsevier. The author of this thesis contributed the development of regression analysis code and thermochemistry metadata, the validation of results, and writing the paper. The author S. Peukert contributed quantum chemical calculations, discussion, and supervision. The authors C. Schulz, I. Wlokas, and H. Wang contributed proof-reading and guidance.

6.1 Abstract

Si–C–H-containing radicals and stable species are present in the oxidation of silicon-organic compounds such as methyl and ethyl silanes, which are frequently-used precursors for the synthesis of silicon-based nanoparticles and coatings via combustion processes. Silicon-containing intermediates interact with flame radicals and thus play a major role in flame chemistry and influence flame propagation. Mechanistic understanding of these effects is hampered by very limited thermochemical properties available for relevant organosilane species. This paper presents quantum-chemical calculations and isodesmic reaction schemes for the determination of temperature-dependent heat of formation, entropy, and heat capacity of Si–C–H radicals and molecules, from which group additivity values (GAVs) were obtained from combinatorial considerations. The data for 22 stable Si–C–H species are revised using

isodesmic reactions and the related 24 GAVs were refined by considering 19 additional stable Si–C–H species. In addition, quantum chemical calculations are made to calculate the thermochemistry of 61 radicals and used to derive 56 GAVs for Si–C–H containing radicals for the first time.

6.2 Introduction

Gas-phase synthesis in flame reactors enables a continuous production of high-purity nanoparticles on industrial scales [18]. Efforts have been made in the last decades to develop chemical kinetics reaction mechanisms for describing pyrolysis and oxidation of nanoparticle precursors in flames [31, 167]. Mechanisms comprise thermochemical properties of chemical species, transport data, and rate coefficients of reactions. Thermochemical data play an important role as they are involved in kinetics by means of reversible reactions and calculation of heat release in conservation equations. In addition, thermochemical data can be used for estimating rate coefficients through correlating energy barriers with activation energies [122].

Experimental thermochemical data of Si-organic compounds are scarce. Most of the available data have relied on quantum-chemistry calculations. Quite extensive attempts have been made by Allendorf and Melius [179] and Ho and Melius [180] for a range of Si–C–H and Si–C–H–O species. In those studies, correlations between molecular structure and standard enthalpies of formation and bond dissociation energies have been derived. Other studies were devoted to specific materials systems like tetramethylsilane ($\text{Si}(\text{CH}_3)_4$; TMS) [186, 73] or tetraethoxysilane ($\text{Si}(\text{OC}_2\text{H}_5)_4$; TEOS) [33, 34, 8]. In addition, we have used group additivity (GA) to estimate the thermochemical properties for a wide range of organosilane species [7].

Benson's group-additivity method [139] has been widely used for estimating thermochemical properties [142], especially for hydrocarbon species [143, 187]. Due to its conceptual simplicity and reasonable accuracy, GA has been widely used in automated mechanism generation (e.g., [147]). Deriving group-additivity values (GAVs) requires an extensive and reliable database of thermochemical properties. Unlike hydrocarbons, data for Si-organic species are scarce, and for this reason, our previous GA study was focused on stable Si–C–H species. The focus of the current work is on free radicals and small molecules containing Si=C double bonds for which reliable thermochemical property values are unavailable. These compounds are intermediates of organosilane combustion, and their thermochemical data are critical to the development of reaction mechanisms for the precursor chemistry in silica nanoparticle-producing flames.

The aim of this study is (i) to calculate the thermochemical properties of a pool of organosilyl radicals by quantum-chemical calculations using isodesmic reactions, (ii) to perform regression analysis to calculate GAVs for the radical groups in Si–C–H system, and (iii) to report GAVs for standard enthalpy of formation (ΔH_f°), standard entropy (S), and heat capacities (C_p) from 298 to 2000 K. The chemical species considered in the pool of Si–C–H compounds were chosen based on combinatorial considerations to derive GAVs that can be generically applied to predict thermochemical data of any Si–C–H-containing stable species and radicals.

6.3 Methodology

6.3.1 Isodesmic reactions and uncertainty

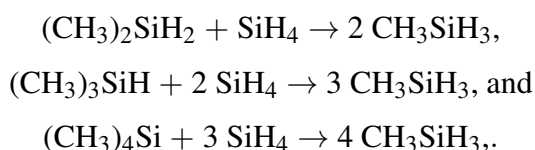
Isodesmic reactions are hypothetical bond re-arrangement reactions, in which the number of bond types remains the same between the reactants and products. In our first paper in these series of publications [7], the thermochemical properties of Si–C–H-containing organosilanes were calculated based on the atomization energy. A comparison of the bond-energy derived and experimental ΔH_f° values of disilane (Si_2H_6), trisilane (Si_3H_8), methyl- (CH_3SiH_3), dimethyl- ($(\text{CH}_3)_2\text{SiH}_2$), trimethylsilane ($(\text{CH}_3)_3\text{SiH}$), and tetramethylsilane ($(\text{CH}_3)_4\text{Si}$) showed good agreement with the maximum deviation smaller than 8 kJ/mol. In the last two papers, we extended our early approach to include the use of isodesmic reactions to reassess the standard-state heat of formation of stable Si–C–H species and hence the GAVs for the molecular groups, and to derive GAVs for Si–C–H radicals, Si=C species, stable Si–C–H–O, and Si=O species for two separate reasons:

1) For reducing the error in GAVs, it is necessary to expand the database of the reference compounds, especially larger molecular species.

2) The error in atomization energy scales with the molecular size. In contrast, isodesmic reactions conserve the bond types such that systematic errors tend to cancel out.

For $(\text{CH}_3)_2\text{SiH}_2$, $(\text{CH}_3)_3\text{SiH}$, and $(\text{CH}_3)_4\text{Si}$, the standard reaction enthalpies (ΔH_f°) were obtained using the G4 composite method [188] implemented in Gaussian09 [136] for the isodesmic reactions

Examples of isodesmic reactions are:



In the above reactions, SiH₄ and CH₃SiH₃ are regarded as reference species. The aforementioned method is hereafter referred to as the G4/isodesmic reaction method.

The accuracy of the ΔH_f° value of the reference species is critical to deriving accurate ΔH_f° values for the target compounds. Hence, our initial study included an evaluation of the literature ΔH_f° values for the reference species. Using ΔH_f° of SiH₄ of Gunn and Green [171], we obtained the $\Delta H_f^\circ = -91.3, -156.2,$ and -223.0 kJ/mol for (CH₃)₂SiH₂, (CH₃)₃SiH, and (CH₃)₄Si, respectively, compared to the experimental values of $-95 \pm 4,$ $-163 \pm 4,$ and -233 ± 4 kJ/mol. Clearly, the deviations are rather large, and with an increase in the size of methylsilanes, the deviations increase. To this end, we note that the revised ΔH_f° value of Becerra and Walsh [175] yielded more satisfactory results: $\Delta H_f^\circ = -95.1, -163.8,$ and -234.4 kJ/mol for (CH₃)₂SiH₂, (CH₃)₃SiH, and (CH₃)₃SiH, respectively. The same observations were made when Si₂H₆ and Si₃H₈ are used as reference species in alternative isodesmic reactions.

The revised ΔH_f° values for SiH₄ (34.3 ± 1.2 kJ/mol), Si₂H₆ (80.0 ± 1.5 kJ/mol), and Si₃H₈ (121 ± 4.4 kJ/mol) enable better predictions for the ΔH_f° value of methylsilanes. The ΔH_f° values of other reference species were adopted from the active thermochemical tables [110] for CH₄ (-74.5 ± 0.1 kJ/mol), C₂H₆ (-84.0 ± 0.1 kJ/mol), and •CH₃ (146.7 ± 0.1 kJ/mol), the NIST database [109] for •SiH₃ (200.5 ± 2.5 kJ/mol), Doncaster and Walsh [173] for CH₃SiH₃ (-29.0 ± 4.0 kJ/mol) and Shin et al. [189] for H₂Si=CH₂ (179.9 ± 12.6 kJ/mol).

Uncertainties of the ΔH_f° values derived from the G4/isodesmic reaction method were estimated by the “root sum squares” of the uncertainties in the reference species:

$$U_c = \sqrt{\sum_{i=1}^n [c_i U(x_i)]^2}, \quad (6.1)$$

where U_c is the combined uncertainty, c_i are the stoichiometric coefficients in the isodesmic reaction, and $U(x_i)$ is the uncertainty of reference species i . In addition, the uncertainty of the G4-level ΔH_f° value was assumed to be ± 4.2 kJ/mol because this is the typical threshold of “chemical accuracy” that composite methods try to achieve. To check whether this assumed uncertainty $U(\Delta H_f^\circ)$ is justified, the ΔH_f° values of selected isodesmic reactions were calculated at CCSD(T)/aug-cc-pVTZ and CCSD(T)/aug-cc-pVQZ levels of theory. The resulting energies were extrapolated to the complete basis set (CBS) limit using the formula.

$$E_{\text{CCSD(T)/CBS}} = E_{\text{CCSD(T)/QZ}} + \frac{(E_{\text{CCSD(T)/QZ}} - E_{\text{CCSD(T)/TZ}}) 4^4}{(5^4 - 4^4)}. \quad (6.2)$$

To determine ΔH_f° values, enthalpy corrections at the 6-31(2df,p) theory level were added to the CCSD(T)/CBS energies for each species involved in the respective isodesmic

Table 6.1 Comparison between CCSD(T)/CBS and G4 based ΔH_f° (kJ/mol) values for selected isodesmic reactions.

No.	Isodesmic reaction	CCSD(T)/CBS	G4
1	$(\text{CH}_3)_2\text{SiH}_2 + \text{SiH}_4 \rightarrow 2 \text{CH}_3\text{SiH}_3$	2.7	2.8
2	$\text{H}_2\text{Si}=\text{CH}(\text{CH}_3) + \text{CH}_4 \rightarrow \text{H}_2\text{Si}=\text{CH}_2 + \text{C}_2\text{H}_6$	7.0	9.4
3	$(\text{CH}_3)_2\text{SiH}_2 + \text{CH}_3\text{SiH}_3 \rightarrow 2 (\text{CH}_3)_2\text{SiH}_2 + \bullet\text{SiH}_3$	-6.6	-5.3
4	$(\text{SiH}_3)_2\text{SiH}_2 + \text{CH}_4 \rightarrow \text{CH}_3\text{SiH}_3 + \bullet\text{CH}_3$	13.3	14.6
5	$(\text{SiH}_3)_2\text{SiH}_2 + \text{SiH}_4 \rightarrow \text{Si}_2\text{H}_6 + \bullet\text{SiH}_3$	12.0	13.2

reactions. The 6-31(2df,p) method is included in the G4 scheme for geometry optimization and frequency analysis. Table 6.1 shows a comparison between CCSD(T) and G4 based ΔH_f° data of five isodesmic reactions. These reactions were chosen, because the species involved can still be handled well by applying the CCSD(T)/aug-cc-pVQZ method.

According to the comparison presented in Table 6.1, $U(\Delta H_f^\circ) = \pm 4.2$ kJ/mol seems reasonable. It clearly suggest that the computed enthalpy of reaction is not very sensitive to the choice of the method. Previously, we used 22 reference compounds to develop GAVs for stable Si–C–H species [7]. To improve the accuracy, we recalculated ΔH_f° using the G4/isodesmic reaction method for an additional set of 19 reference compounds, all of which are larger in molecular sizes than previously considered. The resulting 41 reference compounds form the training set for deriving GAVs for the non-radical Si–C–H compounds. Many of the reference compounds themselves serve also as the reference species in the isodesmic reactions of the Si–C–H radicals. Results are then applied to derive GAVs of Si–C–H radical-centered and adjacent groups as well as groups for species with Si=C bonds.

6.3.2 Computational chemistry

All quantum-chemical calculations were performed at the G4 level of theory using the GAUSSIAN 09 package [169, 136]. The $C_p(T)$, $H_f^\circ(T)$, and $S^\circ(T)$ values were derived by using the GPOP (Gaussian Post Processor) program [170] from the calculated molecular properties. Lowest energy conformers were identified from relaxed potential energy surface (PES) scans at the B3LYP/6-31G(2df,p) level of theory for the $-\text{CH}_3$, $-\text{SiH}_3$, $-\text{CH}_2\bullet$, and $-\text{SiH}_2\bullet$ moieties with dihedral angles used as relevant coordinates. Internal rotations around the bonds of ligands attached to carbon and/or silicon atoms were treated as hindered rotations using the Pitzer-Gwinn approximation [190]. Rotational barrier heights were obtained from relaxed PES scans (B3LYP/6-31G(2df,p) theory level) for $-\text{CH}_3$, $-\text{SiH}_3$, $-\text{CH}_2\bullet$, and $-\text{SiH}_2\bullet$ rotors.

6.3.3 Group additivity method

Benson defined a group as a polyvalent atom (ligancy ≥ 2) in a chemical compound surrounded by its ligands [139]. The radical groups are classified into radical-centered groups, which have a central radical atom, and radical-adjacent groups, which have a radical ligand atom. We considered all possible Si–C–H-containing radical-centered and radical-adjacent groups using a combinatorial approach.

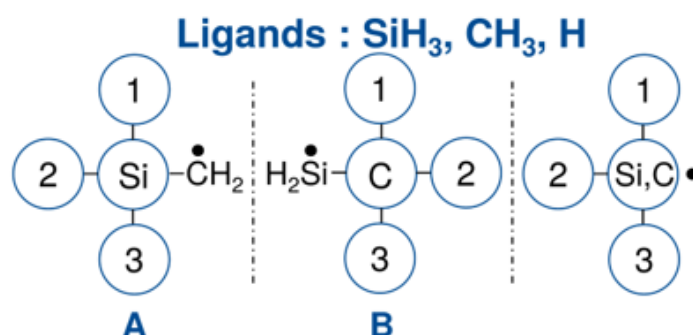


Fig. 6.1 Combinatorial arrangements of SiH_3 , CH_3 , and H ligands at three possible locations in Si- and C-radical-adjacent species (categories A and B) and Si- and C-radical-centered species.

The $-\text{SiH}_3$, $-\text{CH}_3$, and $-\text{H}$ ligands can be located around the Si or C radical centers, as shown in Fig. 6.1. In these structures, the location of the ligands are not essential on chemical equivalence. Hence, the combinatorics relation for “combinations with repetition” can be used to find the number of all possible groups:

$$\left(\binom{n}{k} \right) = \binom{n+k-1}{k} = \frac{(n+k-1)!}{k!(n-1)!} \quad (6.3)$$

For both radical-centered and radical-adjacent species, the number of elements n ($n = 3$ for $-\text{SiH}_3$, $-\text{CH}_3$, and $-\text{H}$) and k is the number of possibilities to distribute the ligands around the locations of the central atoms ($k = 3$). Therefore, ten Si- and ten C-radical-centered groups and altogether also ten Si- and ten C-radical-adjacent groups may be obtained from the combinatorial rule. Among the radical-centered groups, we are interested in 15 of them containing Si. The other five radical-centered groups contain C and H atoms only and are already well known. Regarding radical-adjacent groups, we are interested in those groups that contain Si as the central atom bonded with adjacent radical carbon (the $-\text{CH}_2\bullet$ moiety) and C as central atom bonded with adjacent radical silicon (the $-\text{SiH}_2\bullet$ moiety). For these two types of groups, the combinatorial approach gives ten possible GAVs for each type. Hereafter, we label these two types as category A (central Si atom bonded to a $-\text{CH}_2\bullet$

moiety) and category B (central C atom bonded to a $-\text{SiH}_2\bullet$ moiety). These two categories of radical-adjacent groups are expected to appear quite often in the flame chemistry of organosilanes. Radical-adjacent groups that only contain C–C bonds are again well known from hydrocarbon chemistry and those that contain Si–Si bonds are not considered because they are not important to the combustion chemistry of Si–C–H compounds. In derived GAVs, “R” is used to indicate the atom with an unpaired electron.

6.3.4 Regression analysis

GAVs are derived by a regression analysis [191]. The training set consists of the thermochemical data of reference compounds obtained from quantum chemistry calculations on isodesmic reactions. The regression analysis was performed for ΔH_f° , entropy S° , and heat capacity C_p for eight temperature values from 298 to 2000 K. The methodology is described in detail in ref. [7].

6.4 Results and discussions

6.4.1 Sensitivity analysis and reevaluation of Si–C–H GAVs of stable species

The accuracy of the regression analysis depends on the accuracy of the species in the training set. It also relies on how often a specific group appears in the training set. Those groups that appear seldomly in the training set are expected to have large errors than those that appear often. In this case, the coefficient of determination is close to unity and the residuals between recalculation of training set species with regressed GAVs and *ab initio* calculated values have very small values [7].

To reevaluate the GAVs developed earlier [7], the thermochemical properties of 19 new Si–C–H-containing species were evaluated using isodesmic reactions. These species were chosen so that every GA group contributes to the training set at least twice. To test the sensitivity of the regressed GAVs to the choice of the training species, we compared the predictions of three sets of GAVs with the G4/isodesmic reaction results. Set 1 is taken from our earlier study [7] in which the ΔH_f° values were derived from atomization energy. Set 2 uses the same training species from the earlier study but their ΔH_f° values were re-evaluated the G4/isodesmic reaction method. Lastly, set 3 includes the same species as in set 1 and 2, with ΔH_f° values from set 2, and it also includes the new 19 Si–C–H compounds derived from the G4/isodesmic reaction method. In total, set 3 contains 41 species. Table 6.3 lists the

Table 6.2 GAVs of stable Si–C–H molecules (Set 3: A re-evaluation of results from atomization method) (units: ΔH_f° : kJ/mol, S° and C_p : J/mol K).

Groups	ΔH_f°	S°	$C_p(T)$							
			298 K	400 K	500 K	600 K	800 K	1000 K	1500 K	2000 K
C–(C)(Si) ₃	5.0	–110.3	31.0	36.3	39.4	41.5	43.9	45.0	45.7	44.8
C–(C) ₂ (Si) ₂	25.5	–134.3	31.5	36.6	39.1	40.3	41.2	41.3	40.3	36.2
Si–(C) ₂ (H) ₂	–3.5	52.5	30.7	38.8	45.1	50.1	57.0	61.7	67.9	70.4
Si–(C) ₄	–51.6	–129.2	25.4	31.7	35.8	38.4	41.1	42.6	44.2	43.7
C–(C)(H)(Si) ₂	2.5	–27.8	28.3	33.7	37.8	40.9	45.4	48.4	52.3	52.9
Si–(C)(H) ₂ (Si)	23.3	64.4	35.8	44.2	50.4	55.1	61.7	66.2	72.2	74.8
Si–(C) ₃ (H)	–26.2	–32.9	27.2	33.6	38.2	41.5	45.8	48.7	52.3	53.2
C–(C) ₃ (Si)	19.8	–164.1	28.9	35.3	38.9	40.7	41.4	41.2	39.2	32.2
Si–(C)(H) ₃	18.9	128.1	36.0	43.5	49.7	55.0	63.1	68.9	76.9	80.7
C–(Si) ₄	–38.3	–102.3	34.6	41.1	44.3	45.8	47.7	48.4	49.0	50.3
Si–(H) ₃ (Si)	40.4	138.4	38.4	45.7	51.7	56.7	64.6	70.2	78.0	81.9
Si–(H)(Si) ₃	27.8	0.3	35.1	40.1	43.2	45.3	48.5	50.6	53.4	54.8
C–(H) ₃ (Si)	–46.0	124.9	30.6	36.3	41.7	46.6	54.7	61.2	71.9	78.1
Si–(Si) ₄	10.2	–82.2	36.9	40.9	42.7	43.6	44.9	45.4	45.9	46.1
Si–(H) ₂ (Si) ₂	38.7	75.3	37.8	44.2	48.8	52.3	57.8	61.7	66.9	69.5
C–(C) ₂ (H)(Si)	8.7	–52.6	27.0	32.7	37.0	40.2	44.2	46.9	50.0	47.9
Si–(C) ₃ (Si)	–19.4	–116.6	28.5	34.6	38.4	40.7	43.1	44.4	45.8	45.5
Si–(C) ₂ (H)(Si)	3.9	–21.4	30.7	37.4	42.1	45.4	49.7	52.4	55.9	57.0
Si–(C) ₂ (Si) ₂	2.2	–98.9	31.1	34.5	36.1	36.9	37.9	38.3	38.7	38.4
Si–(C)(H)(Si) ₂	22.2	–7.9	33.2	38.3	41.7	44.1	47.5	49.8	52.7	53.9
C–(C)(H) ₂ (Si)	–12.9	45.4	27.0	33.1	38.5	43.1	49.9	55.0	62.5	64.8
Si–(C)(Si) ₃	12.8	–87.1	34.7	38.4	40.2	41.1	42.3	42.8	43.3	43.2
C–(H)(Si) ₃	–27.8	–8.0	24.2	31.5	37.2	41.5	46.7	50.2	54.8	58.0
C–(H) ₂ (Si) ₂	–32.4	65.6	28.2	36.0	42.3	47.4	54.5	59.8	67.5	72.2

ΔH_f° values predicted by the three GAV sets and their maximum absolute deviations (MAXs) and mean absolute deviations (MADs) from the G4/isodesmic reaction results. It is apparent that the MAX from set 2 is decreased from 10.5 to 6.2 kJ/mol and that the use of set 3 further decreases the MAX to less than 2 kJ/mol.

Figure 6.2 visualizes the absolute residue of the three GAV sets. It also shows the sensitivity of GAV to the choice of the training species and their accuracy in the training set. By including the 19 species, the maximum and mean absolute deviations are drastically decreased with significantly improved GAVs. The GAVs of set 3 are reported in table 6.2.

To conclude this section, an example for the application of GAVs for predicting ΔH_f° of single-bonded Si–C–H species is given, which can be compared with data from literature. For hexamethyldisilane ((CH₃)₃SiSi(CH₃)₃), the present GAVs yield $\Delta H_f^\circ = -314.8$ kJ/mol. Pilcher et al. [192] deduced $\Delta H_f^\circ((\text{CH}_3)_3\text{SiSi}(\text{CH}_3)_3) = -303.7 \pm 5.5$ kJ/mol from calorimetric measurements. Boatz and Gordon reported $\Delta H_f^\circ((\text{CH}_3)_3\text{SiSi}(\text{CH}_3)_3) = -313.8$ kJ/mol [193]. Their value was derived from the isodesmic reaction $(\text{CH}_3)_3\text{SiSi}(\text{CH}_3)_3 + 2\text{CH}_3\text{SiH}_3 \rightarrow (\text{CH}_3)_4\text{Si} + \text{Si}_2\text{H}_6$, whose ΔH_f° was obtained from quantum-chemical calculations at the MP2/6-31G(d)//RHF/3-21G level of theory. The present GAV prediction agrees very well with the ab initio based value from Boatz and Gordon [193] and, considering experimental

Table 6.3 ΔH_f° (in kJ/mol) of 19 added reference compounds, comparing the current G4/isodesmic reaction values with those evaluated using the GAVs of Si–C–H species obtained from set 1 based on atomization energy [7], set 2 using the training set from [7] with ΔH_f° from the G4/isodesmic reaction method, and set 3 with 19 new compounds added into the training set (see text).

Compounds	G4/isodesmic reaction	Group Additivity		
		Set 1	Set 2	Set 3
(SiH ₃)SiH ₂ –SiH ₂ (CH ₃)	55.0 ± 7.0	48.5	58.4	56.4
(SiH ₃)CH ₂ –SiH ₂ (CH ₃)	–61.8 ± 12.8	–58.5	–60.3	–63.0
(SiH ₃) ₂ SiH–SiH ₂ (CH ₃)	85.1 ± 8.2	76.6	87.1	85.9
(SiH ₃) ₂ CH–SiH ₂ (CH ₃)	–40.1 ± 16.6	–33.5	–36.6	–39.5
(CH ₃) ₃ Si–SiH ₂ (CH ₃)	–178.9 ± 17.3	–170.3	–180.7	–180.0
(CH ₃)SiH ₂ –CH(CH ₃) ₂	–125.6 ± 9.1	–124.9	–125.3	–126.6
(CH ₃) ₂ (SiH ₃)Si–SiH ₂ (CH ₃)	–71.9 ± 13.9	–69.5	–71.9	–72.1
(CH ₃) ₂ SiH–CH ₂ (SiH ₃)	–132.1 ± 6.7	–127.2	–129.0	–131.7
(SiH ₃) ₂ (CH ₃)Si–SiH ₂ (CH ₃)	24.5 ± 11.2	20.1	25.7	24.9
(CH ₃)SiH ₂ –CH ₂ (CH ₃)	–104.2 ± 9.1	–97.7	–104.2	–105.3
(CH ₃)SiH ₂ –C(CH ₃) ₂ (SiH ₃)	–92.9 ± 12.8	–89.4	–86.7	–90.9
(CH ₃)SiH ₂ –C(SiH ₃) ₂ (CH ₃)	–49.7 ± 16.6	–44.2	–47.3	–49.6
(CH ₃)SiH ₂ –SiH(CH ₃)(SiH ₃)	–5.8 ± 10.2	–8.4	–5.9	–6.1
(CH ₃) ₂ SiH–SiH ₂ (CH ₃)	–109.9 ± 13.3	–105.7	–111.2	–110.7
(CH ₃)SiH ₂ –CH(CH ₃)(SiH ₃)	–70.9 ± 12.8	–67.8	–68.9	–71.0
(CH ₃)SiH ₂ –SiH ₂ (CH ₃)	–44.3 ± 9.5	–44.6	–45.2	–45.3
(SiH ₃) ₃ C–SiH ₂ (CH ₃)	–32.3 ± 20.5	–23.0	–27.6	–31.1
(CH ₃)SiH ₂ –Si(SiH ₃) ₃	107.2 ± 9.6	96.7	110.4	108.6
(CH ₃) ₃ Si–CH ₂ (SiH ₃)	–204.1 ± 20.8	–201.6	–199.6	–203.0
MAX		10.5	6.2	2.0
MAD		5.0	2.2	0.8

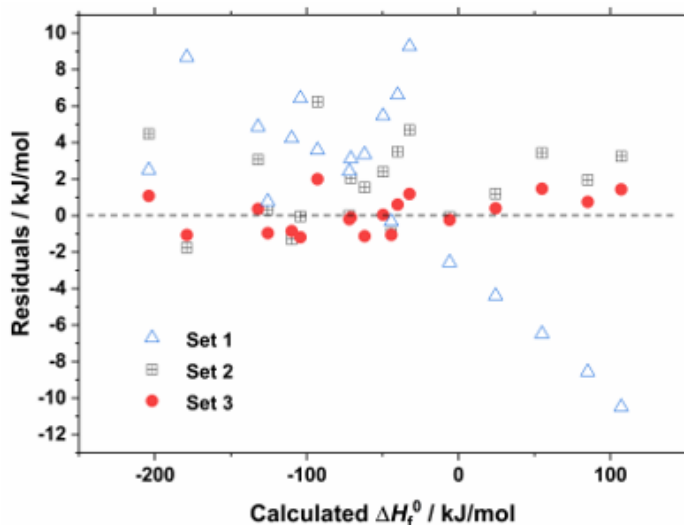
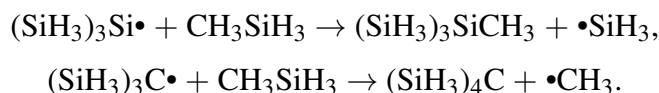


Fig. 6.2 Residuals of the calculated ΔH_f° values from the G4/isodesmic reaction values.

errors and uncertainties related with the GAVs, is in good agreement with the calorimetric measurements from Pilcher et al. [192].

6.4.2 GAVs of Si–C–H-centered radicals

The GAVs derived for radical-centered groups are regressed from 31 radical species in the training set. Examples of the isodesmic reactions are:



Almost no experimental ΔH_f° data are available for comparison. Dávalos and Baer [194] derived ΔH_f° data of $(\text{CH}_3)_3\text{Si}^+$ molecule ions and $(\text{CH}_3)_3\text{Si}\cdot$ radicals from dissociative photoionization experiments. According to ref. [194], $\Delta H_f^\circ((\text{CH}_3)_3\text{Si}\cdot) = 14.8 \pm 2.0$ kJ/mol. The G4/isodesmic reaction method yields $\Delta H_f^\circ((\text{CH}_3)_3\text{Si}\cdot) = 11.2 \pm 7.0$ kJ/mol.

We discussed the distinction between radical-centered and radical-adjacent groups from a combinatorial consideration. In practice, however, a strict distinction is not possible and for this reason, radical-adjacent groups also contribute to the thermochemical data of the training set. Therefore, Table 6.4 lists the regressed GAVs for seven radical-adjacent and for 15 radical-centered groups in the training set for ΔH_f° , $S^\circ(T)$, and $C_p(T)$. During the regression analysis, GAVs of C–(H)₃(Si), Si–(C)(H)₃, and C–(RC)(H)₃ were held fixed. For C–(H)₃(Si) and Si–(C)(H)₃, the GA values are taken from the results discussed in Section 3.1; the values for C–(RC)(H)₃ are assumed to be equal to those of C–(C)(H)₃ as suggested

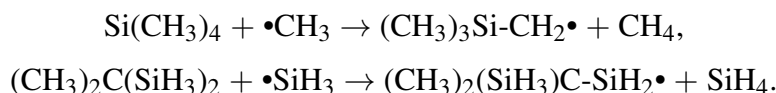
Table 6.4 Group contributions to ΔH_f° , S° , and C_p for Si–C–H radicals (units: ΔH_f° : kJ/mol, S° and C_p : J/mol K).

Group	ΔH_f°	S°	$C_p(T)$							
			298 K	400 K	500 K	600 K	800 K	1000 K	1500 K	2000 K
C–(RC)(H) ₂ (Si)	–29.3	52.4	26.4	34.3	40.0	44.4	51.2	56.1	64.2	70.9
RSi–(C)(H)(Si)	54.8	66.6	12.0	13.9	15.5	17.0	19.4	21.2	23.8	25.1
Si–(H) ₃ (RSi)	100.2	149.5	48.7	57.1	63.5	68.7	76.9	82.6	90.6	94.6
RSi–(C) ₂ (Si)	–26.0	–21.9	2.2	2.8	3.2	3.6	4.0	4.3	4.9	5.3
Si–(C)(H) ₂ (RSi)	81.3	70.2	42.4	50.0	55.4	59.6	65.8	70.0	75.7	78.2
RSi–(C) ₃	–45.6	–27.4	1.9	2.7	3.3	3.7	4.3	4.7	5.7	6.3
RC–(C) ₂ (Si)	108.0	–41.4	13.2	15.6	18.1	20.3	22.9	24.4	25.1	21.6
RSi–(H) ₂ (Si)	132.6	146.1	27.5	31.8	35.1	37.9	42.6	46.0	50.8	53.2
RSi–(Si) ₃	–20.5	–20.3	5.5	6.7	7.4	7.8	8.3	8.5	8.6	8.6
RC–(H)(Si) ₂	12.8	65.1	9.9	12.6	14.5	15.9	18.0	19.7	22.5	25.0
RSi–(C) ₂ (H)	40.0	62.7	12.1	14.7	16.8	18.6	21.4	23.5	26.6	28.2
Si–(RC)(H) ₃	94.3	136.6	44.4	53.9	61.7	68.0	77.2	83.6	92.2	96.1
RC–(C)(Si) ₂	27.9	–22.9	3.4	4.7	5.8	6.8	7.9	8.5	8.6	7.3
RC–(H) ₂ (Si)	84.2	140.4	21.8	25.7	28.6	31.1	35.1	38.5	44.5	48.4
RSi–(H)(Si) ₂	58.9	63.4	15.6	18.5	20.5	22.0	24.6	26.3	28.8	29.9
RSi–(C)(H) ₂	120.9	139.7	26.0	31.3	35.5	38.9	44.2	48.1	53.4	56.2
RC–(Si) ₃	–69.2	–15.6	2.9	3.3	3.3	3.1	3.0	2.8	2.4	3.4
C–(H) ₂ (Si)(RSi)	30.1	63.4	35.2	43.3	49.6	54.7	61.7	66.8	74.2	78.5
Si–(RC)(C)(H) ₂	70.9	56.0	38.8	47.6	54.2	59.2	66.3	71.1	77.4	79.8
RC–(C)(H)(Si)	99.3	55.9	13.0	15.8	18.7	21.2	24.6	27.2	30.6	30.9
C–(H) ₃ (RSi)	18.5	124.0	37.9	45.6	52.3	58.0	66.8	73.7	84.5	90.5
RSi–(C)(Si) ₂	–18.2	–18.4	0.9	0.8	1.0	1.2	1.3	1.5	1.7	1.8
MAX	1.5	5.0	2.5	2.5	2.5	2.5	2.4	2.4	2.4	2.4
MAD	0.5	1.9	1.1	1.3	1.3	1.4	1.4	1.4	1.4	1.5
RMS	0.7	2.6	1.4	1.5	1.6	1.6	1.6	1.7	1.7	1.7

by Sabbe et al. [142]. The regression statistics at eight different temperatures are shown in Table 6.4. The statistical parameters show a perfect regression to calculate GAVs. Overall, MAX is < 2.0 kJ/mol for ΔH_f° , < 5.1 J/mol K for S° , and < 2.6 J/mol K for C_p .

6.4.3 GAVs of Si–C–H-adjacent radicals

Table 6.4 lists the GAVs for regressed radical-adjacent groups. For calculating ΔH_f° value of the reference radicals, isodesmic reactions similar to those of the centered radicals have been employed, e.g.,



For regression analysis, 20 radical species were included in the training set. They were chosen to for the 20 groups of interest. The number of reference compounds is equal to the number of groups, which leads to a unique solution for the regression analysis. As mentioned before, a strict separation between radical-centered and radical-adjacent species is not always

Table 6.5 GAV for ΔH_f° , S° , and C_p of radical-adjacent groups (categories A and B) (units: ΔH_f° : kJ/mol, S° and C_p : J/mol K).

Category A	ΔH_f°	S°	$C_p(T)$							
			298 K	400 K	500 K	600 K	800 K	1000 K	1500 K	2000 K
Si-(RC)(H) ₃	93.4	141.5	46.3	55.8	63.5	69.8	78.9	85.4	94.0	97.8
Si-(RC)(C) ₂ (Si)	48.4	-106.6	39.1	45.2	48.9	51.1	53.7	55.0	56.4	56.0
Si-(RC)(H)(Si) ₂	89.9	-14.3	48.1	54.9	58.9	61.6	65.7	68.2	71.5	72.6
Si-(RC)(C)(H)(Si)	73.4	-20.6	41.4	48.2	52.7	55.9	60.3	63.0	66.6	67.6
Si-(RC)(H) ₂ (Si)	94.7	60.5	44.8	51.8	56.9	60.8	66.9	71.1	76.7	79.1
Si-(H) ₃ (Si)	40.4	138.4	38.4	45.7	51.7	56.7	64.6	70.2	78.0	81.9
Si-(RC)(C)(H) ₂	71.4	51.1	36.9	45.7	52.3	57.4	64.5	69.3	75.6	78.0
Si-(RC)(C) ₃	20.1	-121.8	31.5	39.6	44.7	47.9	51.4	53.3	55.3	55.0
Si-(RC)(C) ₂ (H)	46.3	-36.6	34.2	44.0	50.8	55.5	61.4	65.0	69.5	70.6
Si-(RC)(Si) ₃	79.4	-83.5	42.9	48.8	51.8	53.5	55.6	56.6	57.7	57.8
Si-(RC)(C)(Si) ₂	67.7	-100.3	45.0	50.0	52.5	53.8	55.6	56.4	57.3	57.0
C-(H) ₃ (Si)	-46.0	124.9	30.6	36.3	41.7	46.6	54.7	61.2	71.9	78.1
RC-(H) ₂ (Si)	84.2	140.4	21.8	25.7	28.6	31.1	35.1	38.5	44.5	48.4
Category B										
C-(C) ₂ (RSi)(Si)	85.7	-140.7	33.6	40.4	45.3	48.8	53.1	55.3	56.8	53.5
C-(C)(H)(RSi)(Si)	61.6	-31.1	34.8	41.7	46.8	50.6	55.6	58.8	62.9	63.1
C-(C) ₂ (H)(RSi)	70.6	-56.6	29.5	35.0	40.1	44.4	50.5	54.5	59.1	57.4
C-(H) ₂ (Si)(RSi)	29.8	58.4	35.7	44.4	51.0	56.3	63.5	68.6	76.2	80.5
C-(C)(H) ₃	-42.9	127.1	25.3	32.1	38.4	44.1	53.4	60.6	72.5	81.0
C-(H)(RSi)(Si) ₂	32.8	-7.4	36.4	45.3	51.6	56.1	61.6	65.2	69.7	72.5
C-(C)(RSi)(Si) ₂	62.7	-109.5	38.0	44.7	48.8	51.3	54.2	55.6	56.4	55.1
C-(H) ₃ (RSi)	18.8	129.0	37.3	44.5	50.8	56.4	65.0	71.8	82.5	88.4
C-(C) ₃ (RSi)	81.7	-158.8	29.6	34.7	38.8	42.0	46.2	48.4	49.7	44.0
C-(C)(H) ₂ (RSi)	50.7	47.7	32.4	37.8	42.7	47.0	53.4	58.2	65.3	67.0
C-(RSi)(Si) ₃	21.9	-88.9	37.1	44.6	49.3	52.4	55.8	57.5	58.9	60.2
Si-(C)(H) ₃	18.9	128.1	36.0	43.5	49.7	55.0	63.1	68.9	76.9	80.7
RSi-(C)(H) ₂	120.9	139.7	26.0	31.3	35.5	38.9	44.2	48.1	53.4	56.2

feasible. In deriving the GAVs of radical-adjacent Si-C-H species, the training set required to consider also the contribution of radical-centered species. Two radical-centered GAVs (RC-(H)₂(Si) and RSi-(C)(H)₂) were considered and fixed at their values as listed in Table 6.4 for deriving the GAVs of radical-adjacent compounds.

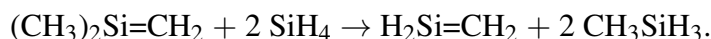
6.4.4 GAVs of Si-C-H species with Si=C bonds

Table 6.6 summarizes the GAVs derived for Si-C-H species with Si=C double bonds. Sila-ethylenes can be important intermediates as a result of Si-C-H-radical decomposition, e.g., (CH₃)₃Si-CH₂• → •CH₃ + (CH₃)₂Si=CH₂. By considering only those species with H or CH₃ ligands bonded to the C and Si atoms of a Si=C core, we have a total of nine species as a part of the training set for regression analysis. We excluded the SiH₃ ligands bonded to C or Si atoms of the Si=C core, because these species (e.g., H₂Si=C(SiH₃)₂) are unlikely to play a role in the combustion of Si-organic precursors. Isodesmic reactions were formulated for the nine reference compounds with H₂Si=CH₂ used as a reference compound. For H₂Si=CH₂,

Table 6.6 GAV for ΔH_f° , S° , and C_p of double-bonded groups (units: ΔH_f° : kJ/mol, S° and C_p : J/mol K).

Groups	ΔH_f°	S°	$C_p(T)$							
			298 K	400 K	500 K	600 K	800 K	1000 K	1500 K	2000 K
$C_{d,si}-(C)_2$	-9.2	8.4	8.3	10.4	12.3	13.8	16.3	18.1	20.7	22.2
$C_{d,si}-(H)_2$	79.3	125.7	30.1	35.9	40.0	43.1	47.8	51.4	57.1	60.2
$Si_{d,c}-(C)_2$	-21.8	12.9	7.4	8.9	10.6	12.2	14.7	16.6	19.8	21.5
$Si_{d,c}-(H)_2$	95.2	124.1	29.8	35.4	39.5	42.7	47.8	51.7	57.5	60.6
$C_{d,si}-(C)(H)$	41.5	73.9	17.1	20.3	23.2	25.7	29.8	32.9	37.6	40.1
$C-(H)_3(Si_{d,c})$	-5.4	96.8	33.1	40.1	46.6	52.2	60.6	67.2	77.6	83.4
$Si_{d,c}-(C)(H)$	38.3	71.1	18.4	22.3	25.3	27.7	31.2	33.9	38.1	40.4
$C-(C_{d,si})(H)_3$	23.0	90.7	33.6	41.1	47.7	53.4	62.3	68.9	79.0	84.5

only isogyric reactions like $H_2Si=CH_2 + CH_4 = C_2H_4 + SiH_4$ can be formulated, which yields $\Delta H_f^\circ = 191.7$ kJ/mol (with $\Delta H_f^\circ(C_2H_4) = 52.4$ kJ/mol [20]). In isogyric reactions, the number of electron pairs remains fixed between the reactants and products, but the number of bond types can change. Isogyric reaction was applied by Boatz and Gordon [28] to calculate $\Delta H_f^\circ(H_2Si=CH_2)$: $2H_2 + C + Si \rightarrow H_2Si=CH_2$. They obtained $\Delta H_f^\circ(H_2Si=CH_2) = 194.6$ kJ/mol and used this value as a reference species in subsequent analyses using isodesmic reactions for other Si=C species. Here, we used the same approach, but instead, we relied on the experimental ΔH_f° value for $H_2Si=CH_2$ from the ion cyclotron resonance experiment from Shin et al. [23], which yielded $\Delta H_f^\circ = 179.9 \pm 12.6$ kJ/mol for $H_2Si=CH_2$. An example of the isodesmic reactions is:



For sila-isobutene ($(CH_3)_2Si=CH_2$), the only experimental ΔH_f° value available was that of Brix et al. [195] from photolysis of 1,1-dimethyl-sila-cyclobutane. They reported $\Delta H_f^\circ((CH_3)_2Si=CH_2) = 36 \pm 7$ kJ/mol. Using $\Delta H_f^\circ(H_2Si=CH_2) = 179.9$ kJ/mol [189], the G4/isodesmic reaction method gives $\Delta H_f^\circ((CH_3)_2Si=CH_2) = 45.6 \pm 15.7$ kJ/mol, which is inline with the experimental value after considering the uncertainties in both values. On the other hand, if we use the isogyric reaction result at 191.7 kJ/mol, we found $\Delta H_f^\circ((CH_3)_2Si=CH_2) = 57.5$ kJ/mol, which is outside the uncertainty limits of Brix et al. [195].

The nomenclature for double-bonded groups follows that of Benson but with slight modification. We write a double-bonded centered and adjacent atom in a group as $X_{d,i}$ for which X is involved in a double bond with atom i. As an example, $(CH_3)_2Si=CH_2$ contains two $C-(H)_3(Si_{d,c})$, one $Si_{d,c}-(C)_2$, and one $C_{d,si}-(H)_2$ groups.

6.5 Conclusion

Group-additivity values of non-radical Si–C–H species were evaluated using the G4/isodesmic reaction method and an extended training set for regression analysis. The thermochemical data (ΔH_f° , S° , and C_p) of 19 newly added species were calculated and a sensitivity analysis was performed to investigate the sensitivity of the resulting GAVs to the choice of training species. Also, a network of self-consistent isodesmic reactions has been developed for Si–C–H radical species. By taking a combinatorial approach and applying regression analysis, the GAVs for 56 radical-centered and radical-adjacent groups were evaluated. Since the decomposition of Si–C–H radicals can produce species with Si=C bonds, GAVs were also derived for species containing the Si=C bonds. Issues in establishing a network of isodesmic reactions for Si=C species are discussed.

6.6 Acknowledgment

We gratefully acknowledge financial support by the German Research Foundation (DFG, FOR 2284, WL 63/1-2 and SCHU 1369/25, project 262219004). HW acknowledges the support of the Humboldt Research Award that enabled the collaborative work.

Chapter 7

A Group Additivity Methodology for Predicting the Thermochemistry of Oxygen-containing Organosilanes

Authors: H. Janbazi, C. Schulz, I. Wlokas, H. Wang, S. Peukert

This chapter including all text, figures and tables was previously published in 'International Journal of Chemical Kinetics, 52, H. Janbazi, C. Schulz, I. Wlokas, H. Wang, S. Peukert, A Group Additivity Methodology for Predicting the Thermochemistry of Oxygen-containing Organosilanes, 918-932, 2020' and is reprinted with permission from Wiley. The author of this thesis contributed the development of regression analysis code and thermochemistry metadata, the validation of results, and writing the paper. The author S. Peukert contributed quantum chemical calculations, discussion, and supervision. The authors C. Schulz, I. Wlokas, and H. Wang contributed proof-reading and guidance.

7.1 Abstract

A combinatorial approach was applied to devise a set of reference Si–C–H–O species that is used to derive group-additivity values (GAVs) for this class of molecules. The reference species include 62 stable single-bonded, 19 cyclic, and nine double-bonded Si–C–H–O species. The thermochemistry of these reference species, i.e., the standard enthalpy of formation, entropy, and heat capacities covering the temperature range from 298 to 2000 K was obtained from quantum chemical calculations using several composite methods, including G4, G4MP2 and CBSQB3, and the isodesmic reaction approach. To calculate the GAVs from the *ab initio* based thermochemistry of the compounds in the training set,

a multivariable linear regression analysis is performed. The sensitivity of GAVs to the different composite methods is discussed and thermodynamics properties calculated via group additivity are compared with available *ab initio* calculated values from the literature.

7.2 Introduction

Organic silicon-containing compounds like siloxanes are frequently used precursors for the synthesis of silica (SiO_2) nanoparticles, coatings, and SiO_2 -containing nanocomposites. The combustion chemistry of specific precursor compounds such as silane (SiH_4) [167, 196], tetramethylsilane ($\text{Si}(\text{CH}_3)_4$; TMS) [81, 73, 186], and tetraethoxysilane ($\text{Si}(\text{OC}_2\text{H}_5)_4$; TEOS) [33, 34, 8] was studied in detail. In these studies, the related thermochemical data were developed and usually estimated for the specific reaction systems, and a generalized, self-consistent thermochemical database for the precursor compounds and reaction intermediates are unavailable.

The work of Ho and Melius [180] was the first attempt to calculate a larger number of chemical species generally related to the Si–C–H–O system. They conducted MP4 calculations and applied bond-additivity corrections to compute standard enthalpies of formation and trends in the bond dissociation energies. Still, thermodynamics data for a wide range of Si–C–H–O containing compounds independent of the choice of a specific precursor species are scarce. This situation presents a major impediment in developing detailed mechanisms of reaction processes required for a more detailed understanding of material nucleation problems and the design of practical materials synthesis processes.

An approach for systematic estimation of thermochemical data is the group-additivity method [139], which has been routinely applied to estimating thermochemical data of hydrocarbons [142, 145] and oxygenated hydrocarbons [144, 143]. In this method, group-additivity values (GAV) may be derived from experimental thermochemical data. Because experimental data can be scarce especially for certain reactive systems, the derivation of GAV often must rely on quantum chemical calculations (see, e.g., Yamada et al. [197], Dellon et al. [198], and Janbazi et al. [7]). The benefit of the group-additivity (GA) method is that they are much easier to implement in codes for automatic mechanism generation, whereas it requires more programming effort to implement and more computational resources to conduct *ab initio* calculations for predicting thermochemical data [114, 147]. Currently, available programs for automatic generation of reaction mechanisms are limited to hydrocarbon chemistry. Hence, extending GAVs to the Si–C–H–O system is beneficial to a wide array of material synthesis problems and reaction mechanism generation.

The current paper aims (i) to carry out *ab initio* calculations for a selected pool of reference species, (ii) to perform a linear regression analysis to provide GAVs from the reference species, and (iii) to compare the results of the GAV approach with results from the atomization-energy method and with an isodesmic reaction network approach.

7.3 Methodology

7.3.1 Computational chemistry

Quantum chemical calculations were carried with three composite methods: G4 [188], G4MP2 [169], and CBS-QB3 [199]. All of them are implemented in the GAUSSIAN 09 [136] package. Standard enthalpies of formation were calculated by (i) using the atomization-energy method and (ii) by employing isodesmic reaction schemes. Heat capacities ($C_p(T)$) and entropies ($S(T)$) were derived from molecular properties (vibration frequencies and moments of inertia) also from quantum chemical calculations, using the GPOP (Gaussian post processor) program [170]. For deriving GAVs, only the results from the G4 computations were considered. For the purpose of method comparison, all three composite methods were used to calculate standard enthalpies of formation. Within the G4 and G4MP2 protocols, geometry optimizations and vibrational frequency analyses were carried out at the B3LYP/6-31G(2df,p) level of theory and the computed frequency values are scaled by 0.99 for the zero point energy and by 0.97 for the vibrational partition-function to account for the anharmonic effect. In case of the CBS-QB3 method, the geometry optimization and frequency calculations were conducted at the B3LYP/6-311G(2d,d,p) theory level.

For hindered internal rotations the energy barriers were obtained from relaxed potential energy surface (PES) scans at the B3LYP/6-31G(2df,p) level of theory with dihedral angles used as coordinates for the scans. Many internal rotors show symmetric potentials (Figure 7.1; left). However, OH moieties typically exhibit asymmetric potentials with respect to the dihedral angle (Figure 7.1; right).

Internal rotations of the $-\text{CH}_3$, $-\text{SiH}_3$, and $-\text{OH}$ groups about the bonds with carbon or silicon atoms having symmetric potentials were treated using the Pitzer-Gwinn approximation. For asymmetric potentials (e.g., of the OH moieties), the potential was fitted to a function given by $V(\alpha) = a_0 + [a_1 \cos(c_1 \alpha) + \dots + a_6 \cos(c_6 \alpha)] + [a_7 \sin(c_1 \alpha) + \dots + a_{12} \sin(c_6 \alpha)]$, where α is the dihedral angle, a_1 through a_{12} are the fitting parameters, and c_1 through c_6 are constants. An eigen-problem solver (BEx1D) was used to obtain the partition function of hindered internal rotation from $V(\alpha)$.

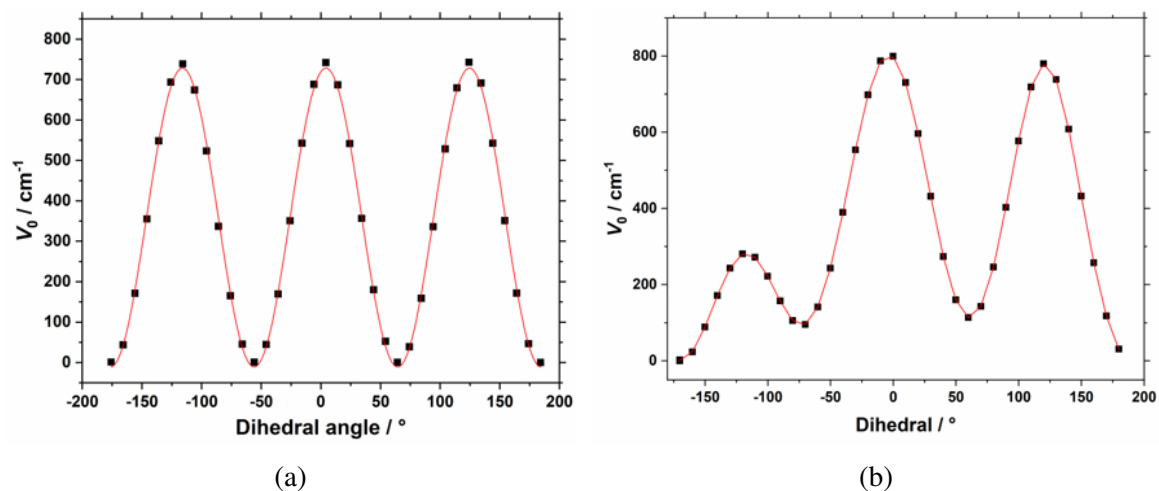


Fig. 7.1 (a) Energy potential of an internal SiH_3 rotor in $(\text{SiH}_3)_2\text{C}(\text{CH}_3)(\text{OH})$ with a maximum at nearly 750 cm^{-1} ; (b): energy potential of an OH rotor in the same molecule, illustrating the asymmetric hindered rotor potential.

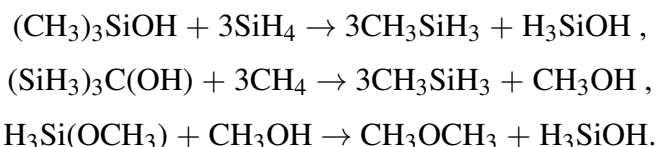
7.3.2 Atomization energy method

In an earlier work [7], we examined the enthalpy of formation of Si–C–H organosilane species using the atomization energy method. In it, the enthalpy of formation at 0 K is calculated as the difference between the theoretical atomization energy of a target species and the experimentally determined enthalpies of formation of the constituent atoms. Enthalpies of formation of the atoms were taken from version 1.122d of the Active Thermochemical Tables (ATcT) [200, 201, 110] and from Chase [108]. The enthalpies of formation of the atoms adopted are: 446.0 kJ/mol for Si [108], 246.8 kJ/mol for O [202], 711.4 kJ/mol for C [110], and 216.0 kJ/mol for H [110], all at 0 K. According to the ATcT, the uncertainties regarding the enthalpies of C, H, and O are less than 0.05 kJ/mol. According to ref. [108], the enthalpy of formation of Si(g) at 0 K is assigned with an uncertainty of ± 8 kJ/mol. By applying sensible enthalpy corrections, standard enthalpies of formation at 298 K may be calculated [137]. The aforementioned approach will be referred to hereafter as the G4/atomization energy method. In the course of this work, two other composite methods (G4MP2 and CBS-QB3) were used, but in applying the atomization method only the results based on the G4 computations were considered.

7.3.3 Isodesmic reactions and uncertainty

A key disadvantage of the atomization-energy method is that its error scales with the molecular size; and for some of the large molecules considered here, it becomes a problem as far

as the accuracy is concerned. In contrast, isodesmic reactions conserve the bond types in such a way that systematic errors tend to cancel out [203]. For improving the accuracy, it is beneficial to invoke the use of isodesmic reactions. Examples of isodesmic reactions are:

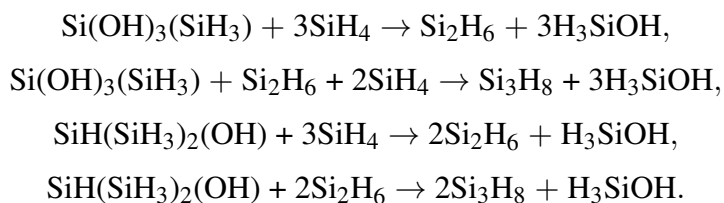


For which the standard reaction enthalpies may be computed by quantum chemistry methods. In the above reactions, $(\text{CH}_3)_2\text{SiH}_2$, $(\text{CH}_3)_3\text{SiH}$, $(\text{CH}_3)_4\text{Si}$, $(\text{CH}_3)_3\text{SiOH}$, $(\text{SiH}_3)_3\text{C}(\text{OH})$, and $\text{H}_3\text{Si}(\text{OCH}_3)$ are the species whose standard enthalpies of formation are to be determined. The other species are employed as reference compounds, i.e., their ΔH_f° values are known. In the current work, the following species (their standard enthalpy of formation) were regarded as reference compounds (reference values): SiH_4 ($\Delta H_f^\circ = 34.3 \pm 1.2$ kJ/mol [175]), CH_4 ($\Delta H_f^\circ = -74.5 \pm 0.1$ kJ/mol [110]), Si_2H_6 ($\Delta H_f^\circ = 80.0 \pm 1.5$ kJ/mol [175]), C_2H_6 ($\Delta H_f^\circ = -84.0 \pm 0.1$ kJ/mol [110]), CH_3SiH_3 ($\Delta H_f^\circ = -29 \pm 4$ kJ/mol [173]), CH_3OH ($\Delta H_f^\circ = -200.8 \pm 0.2$ kJ/mol [110]), $\text{C}_2\text{H}_5\text{OH}$ ($\Delta H_f^\circ = -234.6 \pm 0.2$ kJ/mol), CH_3OCH_3 ($\Delta H_f^\circ = -184.0 \pm 0.5$ kJ/mol [110]), and $\text{C}_2\text{H}_5\text{OC}_2\text{H}_5$ ($\Delta H_f^\circ = 250.8 \pm 2$ kJ/mol [25]). Also, H_3SiOH , and $\text{H}_2\text{Si}=\text{O}$ are regarded also as the reference compounds, even though no experimental ΔH_f° data are available. The ΔH_f° values of these two species are obtained from the G4/atomization energy method, which yields $\Delta H_f^\circ = -285.2$ kJ/mol for H_3SiOH and $\Delta H_f^\circ = -102.5$ kJ/mol.

The G4 method is assumed to provide thermochemical data with an accuracy of ± 4.2 kJ/mol. Accuracies of quantum chemical methods are reported in terms of mean absolute deviations (MAD), which correspond to a confidence interval of 50%. According to Ruscic, the 95% confidence interval is regarded as the universally accepted standard expression of uncertainty in thermochemistry [201] and since the MAD is approximately three times smaller than the 95% confidence interval, the uncertainties of the G4/atomization enthalpies of H_3SiOH and $\text{H}_2\text{Si}=\text{O}$ are estimated to be ± 12.6 kJ/mol.

For some Si–C–H–O species, alternative isodesmic reactions are possible, but since a relatively small number of reference compounds was used in this work, the possibility to identify multiple isodesmic reactions per Si–C–H–O species is limited. Below are two

examples for which alternative isodesmic reactions are possible.



The first two reactions are possibilities to estimate ΔH_f° of $\text{Si(OH)}_3(\text{SiH}_3)$, and the last two reactions are possibilities to estimate ΔH_f° of $\text{SiH(SiH}_3)_2(\text{OH})$. For $\text{Si(OH)}_3(\text{SiH}_3)$, $\Delta H_f^\circ = -947.6$ kJ/mol and $\Delta H_f^\circ = -945.2$ kJ/mol. For $\text{SiH(SiH}_3)_2(\text{OH})$, $\Delta H_f^\circ = -189.2$ kJ/mol and $\Delta H_f^\circ = -184.4$ kJ/mol. For other target compounds, the deviations between two possible isodesmic reactions range from 1 – 6 kJ/mol.

When establishing the network of isodesmic reactions, we attempted to consider only those compounds with the lowest possible uncertainties as reference species. Alternative isodesmic reactions were only formulated to check that there are no conspicuous differences between two possible alternative reactions with regard to the calculated ΔH_f° values. Due to the small differences in calculated ΔH_f° values obtained from alternative isodesmic reactions, we assume that we have established a consistent network of isodesmic reactions.

For all isodesmic reactions considered herein, the standard reaction enthalpies (ΔH_f°) were obtained using composite methods, including G4, G4MP2, and CBSQB3, all of which have been widely used for thermochemical analysis. In combination with isodesmic reactions, these composite methods are assumed to achieve reaction enthalpies within an accuracy of ca. ± 4.2 kJ/mol.

The methods just discussed are referred to as the G4/, G4MP2/, or CBSQB3/isodesmic reaction method hereafter. Most of the GAVs shown in this manuscript are derived from the G4/isodesmic reaction approach. An exception was made for large cyclosiloxanes, for which only CBSQB3 calculations are possible given our computational resources. Table 7.1 shows the isodesmic reactions used for single-bonded Si–C–H–O compounds and their standard reaction enthalpies from G4, G4MP2 and CBSQB3 calculations. In this and other related tables hereafter, the target species is always given by first reactant species, while the second reactant species and reaction products are the reference species for which the ΔH_f° values are known.

Table 7.1 Isodesmic reactions and their standard reaction enthalpies (ΔH_r° , kJ/mol) computed using G4, G4MP2, and CBSQB3 composite methods for the Si–C–H–O system.

Reaction	G4	G4MP2	CBSQB3
$\text{Si(OH)(SiH}_3)_3 + 3\text{SiH}_4 \rightarrow 3\text{Si}_2\text{H}_6 + \text{H}_3\text{SiOH}$	2.9	0.5	5.0
$\text{Si(OH)(SiH}_3)_2(\text{SiH}_2\text{CH}_3) + 4\text{SiH}_4 \rightarrow \text{H}_3\text{SiOH} + \text{CH}_3\text{SiH}_3 + 3\text{Si}_2\text{H}_6$	4.6	2.0	7.1
$\text{Si(OH)}_3(\text{SiH}_3) + 3\text{SiH}_4 \rightarrow \text{Si}_2\text{H}_6 + 3\text{H}_3\text{SiOH}$	69.1	66.2	66.8
$\text{Si(OH)}_3(\text{SiH}_2\text{CH}_3) + 4\text{SiH}_4 \rightarrow 3\text{H}_3\text{SiOH} + \text{Si}_2\text{H}_6 + \text{CH}_3\text{SiH}_3$	67.9	64.9	66.1
$\text{Si(OH)}_2(\text{SiH}_3)_2 + 3\text{SiH}_4 \rightarrow \text{Si}_2\text{H}_6 + 3\text{H}_3\text{SiOH}$	20.8	18.1	20.8
$\text{Si(OH)}_2(\text{SiH}_3)(\text{SiH}_2\text{CH}_3) + 4\text{SiH}_4 \rightarrow 2\text{Si}_2\text{H}_6 + \text{CH}_3\text{SiH}_3 + 2\text{H}_3\text{SiOH}$	19.5	16.7	20.1
$\text{Si(SiH}_3)_2(\text{OH})(\text{CH}_3) + 3\text{SiH}_4 \rightarrow 2\text{Si}_2\text{H}_6 + \text{CH}_3\text{SiH}_3 + \text{H}_3\text{SiOH}$	4.6	4.2	6.5
$\text{Si(SiH}_3)_2(\text{OH})(\text{CH}_2\text{SiH}_3) + 4\text{SiH}_4 \rightarrow 3\text{Si}_2\text{H}_6 + \text{CH}_3\text{SiH}_3 + \text{H}_3\text{SiOH}$	17.2	15.8	23.7
$\text{SiH(SiH}_3)_2(\text{OH}) + 3\text{SiH}_4 \rightarrow 2\text{Si}_2\text{H}_6 + \text{H}_3\text{SiOH}$	-4.6	-6.0	-4.0
$\text{SiH(OH)(SiH}_3)(\text{SiH}_2\text{CH}_3) + 3\text{SiH}_4 \rightarrow 2\text{Si}_2\text{H}_6 + \text{CH}_3\text{SiH}_3 + \text{H}_3\text{SiOH}$	-4.0	-5.6	-3.0
$\text{Si(CH}_3)_2(\text{OH})(\text{SiH}_3) + 3\text{SiH}_4 \rightarrow \text{Si}_2\text{H}_6 + 2\text{CH}_3\text{SiH}_3 + \text{H}_3\text{SiOH}$	15.4	16.4	17.3
$\text{Si(OH)(CH}_3)(\text{SiH}_3)(\text{CH}_2\text{SiH}_3) + 3\text{SiH}_4 + \text{CH}_4 \rightarrow \text{Si}_2\text{H}_6 + 3\text{CH}_3\text{SiH}_3 + \text{H}_3\text{SiOH}$	31.9	29.8	32.3
$\text{SiH(CH}_3)_2(\text{OH}) + 2\text{SiH}_4 \rightarrow 2\text{CH}_3\text{SiH}_3 + \text{H}_3\text{SiOH}$	22.1	22.1	21.6
$\text{SiH(OH)(CH}_3)(\text{CH}_2\text{SiH}_3) + 2\text{SiH}_4 + \text{CH}_4 \rightarrow 3\text{CH}_3\text{SiH}_3 + \text{H}_3\text{SiOH}$	36.5	35.2	36.6
$\text{SiH}_2(\text{SiH}_3)(\text{OH}) + \text{SiH}_4 \rightarrow \text{Si}_2\text{H}_6 + \text{H}_3\text{SiOH}$	-4.9	-5.5	-5.0
$\text{SiH}_2(\text{OH})(\text{SiH}_2\text{CH}_3) + 2\text{SiH}_4 \rightarrow \text{Si}_2\text{H}_6 + \text{CH}_3\text{SiH}_3 + \text{H}_3\text{SiOH}$	-8.1	-8.7	-7.8
$\text{SiH}_2(\text{CH}_3)(\text{OH}) + \text{SiH}_4 \rightarrow \text{CH}_3\text{SiH}_3 + \text{H}_3\text{SiOH}$	11.7	11.5	11.0
$\text{SiH}_2(\text{OH})(\text{CH}_2\text{SiH}_3) + \text{CH}_4 + \text{SiH}_4 \rightarrow 2\text{CH}_3\text{SiH}_3 + \text{H}_3\text{SiOH}$	23.5	22.1	23.1
$\text{Si(CH}_3)_2(\text{OH})(\text{SiH}_3) + 3\text{SiH}_4 \rightarrow \text{CH}_3\text{SiH}_3 + \text{Si}_2\text{H}_6 + 2\text{H}_3\text{SiOH}$	40.9	39.0	40.3
$\text{Si(OH)}_2(\text{SiH}_3)(\text{CH}_2\text{SiH}_3) + \text{CH}_4 + 3\text{SiH}_4 \rightarrow \text{Si}_2\text{H}_6 + 2\text{CH}_3\text{SiH}_3 + 2\text{H}_3\text{SiOH}$	57.5	54.1	57.9
$\text{SiH(SiH}_3)(\text{OH})_2 + 2\text{SiH}_4 \rightarrow \text{Si}_2\text{H}_6 + 2\text{H}_3\text{SiOH}$	21.9	22.8	23.6
$\text{SiH(OH)}_2(\text{SiH}_2\text{CH}_3) + 3\text{SiH}_4 \rightarrow \text{CH}_3\text{SiH}_3 + \text{Si}_2\text{H}_6 + 2\text{H}_3\text{SiOH}$	22.4	21.0	22.4
$\text{SiH(CH}_3)_2(\text{OH}) + 2\text{SiH}_4 \rightarrow \text{CH}_3\text{SiH}_3 + 2\text{H}_3\text{SiOH}$	48.4	47.7	47.3
$\text{SiH(OH)}_2(\text{CH}_2\text{SiH}_3) + 2\text{SiH}_4 + \text{CH}_4 \rightarrow 2\text{CH}_3\text{SiH}_3 + 2\text{H}_3\text{SiOH}$	63.2	61.1	63.0
$\text{SiH(SiH}_3)(\text{CH}_3)(\text{OH}) + 2\text{SiH}_4 \rightarrow \text{CH}_3\text{SiH}_3 + \text{Si}_2\text{H}_6 + \text{H}_3\text{SiOH}$	5.5	4.8	5.3
$\text{SiH(OH)(SiH}_3)(\text{CH}_2\text{SiH}_3) + 2\text{SiH}_4 + \text{CH}_4 \rightarrow \text{Si}_2\text{H}_6 + 2\text{CH}_3\text{SiH}_3 + \text{H}_3\text{SiOH}$	19.1	17.0	19.1
$\text{C(SiH}_3)_3(\text{OH}) + 3\text{CH}_4 \rightarrow 3\text{CH}_3\text{SiH}_3 + \text{CH}_3\text{OH}$	6.3	-0.1	7.1
$\text{C(OH)(SiH}_3)_2(\text{SiH}_2\text{CH}_3) + 3\text{CH}_4 + \text{SiH}_4 \rightarrow 4\text{CH}_3\text{SiH}_3 + \text{CH}_3\text{OH}$	13.8	7.5	14.7
$\text{C(SiH}_3)_3(\text{OH}) + 3\text{CH}_4 \rightarrow \text{CH}_3\text{SiH}_3 + 3\text{CH}_3\text{OH}$	131.7	127.3	133.7
$\text{C(OH)}_3(\text{SiH}_2\text{CH}_3) + 3\text{CH}_4 + \text{SiH}_4 \rightarrow 2\text{CH}_3\text{SiH}_3 + 3\text{CH}_3\text{OH}$	139.9	135.6	142.4
$\text{C(SiH}_3)_2(\text{OH})_2 + 3\text{CH}_4 \rightarrow 2\text{CH}_3\text{SiH}_3 + 2\text{CH}_3\text{OH}$	24.4	19.3	25.9
$\text{C(OH)}_2(\text{SiH}_3)(\text{SiH}_2\text{CH}_3) + 3\text{CH}_4 + \text{SiH}_4 \rightarrow 3\text{CH}_3\text{SiH}_3 + 2\text{CH}_3\text{OH}$	46.6	41.5	48.5
$\text{C(SiH}_3)_2(\text{OH})(\text{CH}_3) + 3\text{CH}_4 \rightarrow 2\text{CH}_3\text{SiH}_3 + \text{C}_2\text{H}_6 + \text{CH}_3\text{OH}$	15.8	11.3	15.7
$\text{C(OH)(SiH}_3)_2(\text{CH}_2\text{SiH}_3) + 4\text{CH}_4 \rightarrow 3\text{CH}_3\text{SiH}_3 + \text{C}_2\text{H}_6 + \text{CH}_3\text{OH}$	14.9	9.1	15.1
$\text{CH(SiH}_3)_2(\text{OH}) + 2\text{CH}_4 \rightarrow 2\text{CH}_3\text{SiH}_3 + \text{CH}_3\text{OH}$	-10.1	-12.9	-9.2
$\text{CH(OH)(SiH}_3)(\text{SiH}_2\text{CH}_3) + 2\text{CH}_4 + \text{SiH}_4 \rightarrow 3\text{CH}_3\text{SiH}_3 + \text{CH}_3\text{OH}$	-3.7	-6.4	-2.6
$\text{C(CH}_3)_2(\text{OH})(\text{SiH}_3) + 3\text{CH}_4 \rightarrow 2\text{C}_2\text{H}_6 + \text{CH}_3\text{SiH}_3 + \text{CH}_3\text{OH}$	68.6	42.3	44.9
$\text{C(OH)(SiH}_3)(\text{CH}_3)(\text{CH}_2\text{SiH}_3) + 4\text{CH}_4 \rightarrow 2\text{C}_2\text{H}_6 + 2\text{CH}_3\text{SiH}_3 + \text{CH}_3\text{OH}$	44.2	40.0	44.7
$\text{CH}_2(\text{SiH}_3)(\text{OH}) + \text{CH}_4 \rightarrow \text{CH}_3\text{SiH}_3 + \text{CH}_3\text{OH}$	-7.6	-8.5	-7.3
$\text{CH}_2(\text{OH})(\text{SiH}_2\text{CH}_3) + \text{CH}_4 + \text{SiH}_4 \rightarrow 2\text{CH}_3\text{SiH}_3 + \text{CH}_3\text{OH}$	-7.6	-8.3	-6.9
$\text{C(SiH}_3)_3(\text{OH}) + 3\text{CH}_4 \rightarrow \text{CH}_3\text{SiH}_3 + \text{C}_2\text{H}_6 + 2\text{CH}_3\text{OH}$	72.4	68.7	73.6
$\text{C(OH)}_2(\text{CH}_3)(\text{SiH}_2\text{CH}_3) + 3\text{CH}_4 + \text{SiH}_4 \rightarrow \text{C}_2\text{H}_6 + 2\text{CH}_3\text{SiH}_3 + 2\text{CH}_3\text{OH}$	91.7	88.1	93.4
$\text{CH(SiH}_3)_2(\text{OH}) + 2\text{CH}_4 \rightarrow \text{CH}_3\text{SiH}_3 + 2\text{CH}_3\text{OH}$	47.7	45.2	48.8
$\text{CH(OH)}_2(\text{SiH}_2\text{CH}_3) + 2\text{CH}_4 + \text{SiH}_4 \rightarrow 2\text{CH}_3\text{SiH}_3 + 2\text{CH}_3\text{OH}$	54.2	51.8	55.7
$\text{CH(CH}_3)(\text{SiH}_3)(\text{OH}) + 2\text{CH}_4 \rightarrow \text{CH}_3\text{SiH}_3 + \text{C}_2\text{H}_6 + \text{CH}_3\text{OH}$	15.3	13.5	15.5
$\text{CH(OH)(SiH}_3)(\text{CH}_2\text{SiH}_3) + 3\text{CH}_4 \rightarrow 2\text{CH}_3\text{SiH}_3 + \text{C}_2\text{H}_6 + \text{CH}_3\text{OH}$	15.9	13.1	16.4
$\text{Si(OH)}_4 + 3\text{SiH}_4 \rightarrow 4\text{H}_3\text{SiOH}$	121.0	118.5	115.9
$\text{SiH}_3(\text{OCH}_3) + \text{CH}_3\text{OH} \rightarrow \text{H}_3\text{SiOH} + \text{CH}_3\text{OCH}_3$	-16.4	-17.3	-17.7

Continued on next page

Table 7.1 – Continued from previous page

Reaction	G4	G4MP2	CBSQB3
$\text{SiH}_2(\text{OH})_2 + \text{SiH}_4 \rightarrow 2\text{H}_3\text{SiOH}$	33.5	33.2	32.6
$\text{SiH}(\text{OH})_3 + 2\text{SiH}_4 \rightarrow 3\text{H}_3\text{SiOH}$	77.4	76.1	74.2
$\text{SiH}_3(\text{OC}_2\text{H}_5) + \text{C}_2\text{H}_5\text{OH} \rightarrow \text{C}_2\text{H}_5\text{OC}_2\text{H}_5 + \text{H}_3\text{SiOH}$	-10.3	-11.5	-11.2
$(\text{SiH}_3)\text{O}(\text{SiH}_3) + 2\text{C}_2\text{H}_5\text{OH} \rightarrow \text{C}_2\text{H}_5\text{OC}_2\text{H}_5 + 2\text{H}_3\text{SiOH}$	0.7	-0.9	0.3
$(\text{SiH}_3)\text{O}(\text{SiH}_2\text{CH}_3) + \text{SiH}_4 + 2\text{CH}_3\text{OH} \rightarrow \text{CH}_3\text{SiH}_3 + \text{CH}_3\text{OCH}_3 + 2\text{H}_3\text{SiOH}$	12.7	11.0	11.9
$\text{Si}(\text{OH})_3(\text{OCH}_3) + \text{CH}_3\text{OH} + 3\text{SiH}_4 \rightarrow 4\text{H}_3\text{SiOH} + \text{CH}_3\text{OCH}_3$	103.0	99.4	97.4
$\text{SiH}(\text{OH})_2(\text{OCH}_3) + \text{CH}_3\text{OH} + 2\text{SiH}_4 \rightarrow 3\text{H}_3\text{SiOH} + \text{CH}_3\text{OCH}_3$	59.1	56.9	55.4
$\text{SiH}_2(\text{OH})(\text{OCH}_3) + \text{CH}_3\text{OH} + \text{SiH}_4 \rightarrow 2\text{H}_3\text{SiOH} + \text{CH}_3\text{OCH}_3$	16.2	14.8	14.1
$\text{Si}(\text{CH}_3)_3(\text{OH}) + 3\text{SiH}_4 \rightarrow 3\text{CH}_3\text{SiH}_3 + \text{H}_3\text{SiOH}$	32.9	33.1	32.8
$\text{Si}(\text{OH})(\text{CH}_3)_2(\text{CH}_2\text{SiH}_3) + 3\text{SiH}_4 + \text{CH}_4 \rightarrow 4\text{CH}_3\text{SiH}_3 + \text{H}_3\text{SiOH}$	47.9	46.9	48.1
$\text{Si}(\text{CH}_3)_3(\text{OH})_3 + 3\text{SiH}_4 \rightarrow \text{CH}_3\text{SiH}_3 + 3\text{H}_3\text{SiOH}$	92.6	90.7	89.7
$\text{Si}(\text{OH})_3(\text{CH}_2\text{SiH}_3) + \text{CH}_4 + 3\text{SiH}_4 \rightarrow 2\text{CH}_3\text{SiH}_3 + 3\text{H}_3\text{SiOH}$	107.1	103.6	105.4
$\text{Si}(\text{CH}_3)_2(\text{OH})_2 + 3\text{SiH}_4 \rightarrow 2\text{CH}_3\text{SiH}_3 + 2\text{H}_3\text{SiOH}$	62.8	62.0	61.8
$\text{Si}(\text{OH})_2(\text{CH}_3)(\text{CH}_2\text{SiH}_3) + \text{CH}_4 + 3\text{SiH}_4 \rightarrow 3\text{CH}_3\text{SiH}_3 + 2\text{H}_3\text{SiOH}$	77.0	74.8	76.5

Uncertainties of the ΔH_f° values derived from the G4/isodesmic reaction method were estimated by the “root sum squares” of the uncertainties in the reference species:

$$U_c = \sqrt{\sum_{i=1}^n [C_i U(x_i)]^2}, \quad (7.1)$$

where U_c is the combined uncertainty, c_i are the stoichiometric coefficients in the isodesmic reaction, and $U(x_i)$ is the uncertainty of reference species i . By inspecting the differences between the three composite methods shown in Table 7.1 and by considering that also uncertainties of reaction enthalpies should be stated at the 95% confidence interval, an overall uncertainty of ± 8.4 kJ/mol is assumed to be a more realistic uncertainty estimate of the computed reaction enthalpies of isodesmic reactions.

In the majority of cases, i.e., in 49 out of 62 isodesmic reactions, the G4, G4MP2, and CBSQB3 ΔH_f° are within 4.2 kJ/mol of each other. We also calculated ΔH_f° values with CCSD(T) with the aug-cc-pVTZ and aug-cc-pVQZ basis sets for few selected reactions to check how well the G4-based reaction enthalpies match the CCSD(T)/CBS (complete bases set) results. This comparison is shown in the supplemental material.

Sixty-two Si–O–C–H references species were studied using isodesmic reactions at the G4, G4MP2 and CBSQB3 levels of theory, and by the G4 atomization energy. In addition, isodesmic reactions were applied to nine species with Si=O double bonds (also at the G4, G4MP2, and CBSQB3 levels of theory), and 19 cyclosiloxanes (at the CBSQB3 theory level only).

7.3.4 Group additivity method

A group as defined by Benson [139] is a polyvalent atom (ligancy ≥ 2) in a chemical compound surrounded by its ligands. The basic assumption is that thermochemical properties of an entire chemical compound can be determined from the group contributions within a molecule. In the current work, our focus is on obtaining GAVs for Si–C–H–O species. To do so, we used a combinatorial approach in recognizing the relevant groups which by means of them a comprehensive Si–C–H–O thermochemistry can be estimated, along with the “combinations with repetition” relation.

7.3.5 Multivariable linear regression

GAVs are derived by a regression analysis [191]. The training set consists of the thermochemical data of reference species obtained from quantum chemistry calculations on isodesmic reactions. The regression analysis was performed for ΔH_f° , entropy S° , and heat capacity C_p for eight temperature values from 298 to 2000 K. The methodology is described in detail in the supplemental material.

7.4 Results and discussions

7.4.1 GAVs of Si–C–H–O species

Thermochemical datasets have been reported for Si–C–H–O species by Ho and Melius [180] and Phadungsukanan et al. [8]. Ho and Melius carried out MP4(SDTQ) calculations and applied bond-additivity corrections (BAC) for moieties of the Si–C–H–O species system. When applying BAC for Si–O bonds, Ho and Melius [180] referred to G2 thermochemical data as relevant experimental reference data are unavailable. Phadungsukanan et al. [8] constructed a network of isodesmic reactions and obtained reaction enthalpies with DFT calculations. They incorporated the MP4 values of Ho and Melius and those of Allendorf et al. [204]. Table 7.2 lists the computed ΔH_f° values obtained in the present work. Where appropriate, we also compare our ΔH_f° values with literature values. In general, the current ΔH_f° values are within ~ 20 kJ/mol of the earlier theoretical results. The largest discrepancy is observed for $\text{SiH}_3(\text{OCH}_3)$. Our ΔH_f° values are 30 to 34 kJ/mol lower than that of Phadungsukanan et al. [8].

The GAVs were obtained from the regression analysis. The resulting values are listed in Table 7.3. In the regression procedure, we adopted the GAVs for O–(C)(H), C–(C)(H)₂(O) from Cohen and Benson [143], C–(C)(H)₃ from Sabbe et al. [142], C–(H)₃(Si), Si–(C)(H)₃,

Table 7.2 Comparison of ΔH_f° (kJ/mol) and uncertainties calculated for the training set.

Species	Atom.-G4	Isodesmic reaction			Lit.	Exp.
		G4	G4-MP2	CBSQB3		
Si(OH)(SiH ₃) ₃	-160.3	-151.0 ± 16.2	-148.6	-153.1		
Si(OH)(SiH ₃) ₂ (SiH ₂ CH ₃)	-220.3	-216.0 ± 17.0	-213.4	-218.4		
Si(OH) ₃ (SiH ₃)	-938.0	-947.6 ± 38.9	-944.5	-945.1		
Si(OH) ₃ (SiH ₂ CH ₃)	-995.1	-1009.6 ± 39.3	-1006.7	-1007.9		
Si(OH) ₂ (SiH ₃) ₂	-533.9	-534.1 ± 27.0	-531.3	-534.1		
Si(OH) ₂ (SiH ₃)(SiH ₂ CH ₃)	-591.0	-596.1 ± 27.5	-593.3	-596.7		
Si(SiH ₃) ₂ (OH)(CH ₃)	-264.2	-261.7 ± 16.3	-261.3	-263.6		
Si(SiH ₃) ₂ (OH)(CH ₂ SiH ₃)	-232.9	-228.6 ± 17.0	-227.2	-235.0		
SiH(SiH ₃) ₂ (OH)	-195.3	-189.2 ± 16.3	-187.8	-189.8		
SiH(OH)(SiH ₃)(SiH ₂ CH ₃)	-254.3	-253.0 ± 16.3	-251.5	-254.0		
Si(CH ₃) ₂ (OH)(SiH ₃)	-376.3	-381.5 ± 17.6	-382.4	-383.3		
Si(OH)(CH ₃)(SiH ₃)(CH ₂ SiH ₃)	-344.3	-352.4 ± 19.7	-350.4	-352.9		
SiH(CH ₃) ₂ (OH)	-424.0	-433.9 ± 15.8	-433.9	-433.4		
SiH(OH)(CH ₃)(CH ₂ SiH ₃)	-391.6	-402.8 ± 19.5	-401.4	-402.9		
SiH ₂ (SiH ₃)(OH)	-237.6	-234.5 ± 15.3	-233.9	-234.5		
SiH ₂ (OH)(SiH ₂ CH ₃)	-292.8	-294.7 ± 15.9	-294.1	-294.9		
SiH ₂ (CH ₃)(OH)	-355.2	-360.2 ± 15.7	-360.0	-359.5		
SiH ₂ (OH)(CH ₂ SiH ₃)	-320.2	-326.5 ± 17.2	-325.0	-326.1		
Si(CH ₃)(OH) ₂ (SiH ₃)	-655.0	-663.1 ± 27.1	-661.2	-662.5		
Si(OH) ₂ (SiH ₃)(CH ₂ SiH ₃)	-624.7	-634.2 ± 28.0	-630.8	-634.6		
SiH(SiH ₃)(OH) ₂	-589.4	-580.8 ± 26.7	-581.8	-582.6		
SiH(OH) ₂ (SiH ₂ CH ₃)	-636.5	-644.7 ± 27.1	-643.2	-644.7		
SiH(CH ₃)(OH) ₂	-705.1	-716.3 ± 27.0	-715.7	-715.3		
SiH(OH) ₂ (CH ₂ SiH ₃)	-673.1	-685.7 ± 17.3	-683.6	-685.5		
SiH(SiH ₃)(CH ₃)(OH)	-306.4	-308.3 ± 15.9	-307.5	-308.1		
SiH(OH)(SiH ₃)(CH ₂ SiH ₃)	-273.2	-276.4 ± 17.4	-274.3	-276.4		
C(OH)(SiH ₃) ₂ (SiH ₂ CH ₃)	-135.3	-141.4 ± 18.1	-135.1	-142.3		
C(SiH ₃)(OH) ₃	-541.4	-539.6 ± 9.3	-535.2	-541.6		
C(OH) ₃ (SiH ₂ CH ₃)	-608.0	-611.1 ± 11.7	-606.8	-613.6		
C(SiH ₃) ₂ (OH) ₂	-260.8	-260.5 ± 11.6	-255.4	-262.0		
C(OH) ₂ (SiH ₃)(SiH ₂ CH ₃)	-341.4	-346.0 ± 14.7	-340.9	-347.9		
C(SiH ₃) ₂ (OH)(CH ₃)	-134.6	-135.1 ± 11.6	-130.6	-135.0		
C(OH)(SiH ₃) ₂ (CH ₂ SiH ₃)	-86.8	-88.7 ± 14.7	-82.9	-88.9		
CH(SiH ₃) ₂ (OH)	-99.9	-99.7 ± 11.6	-96.9	-100.6		
CH(OH)(SiH ₃)(SiH ₂ CH ₃)	-164.7	-169.4 ± 14.7	-166.7	-170.5		
C(CH ₃) ₂ (OH)(SiH ₃)	-219.5	-242.9 ± 9.3	-216.6	-219.2		
C(OH)(SiH ₃)(CH ₃)(CH ₂ SiH ₃)	-171.8	-173.0 ± 11.6	-168.8	-173.5		
CH ₂ (SiH ₃)(OH)	-149.2	-147.7 ± 9.3	-146.8	-148.0		
CH ₂ (OH)(SiH ₂ CH ₃)	-207.6	-211.0 ± 11.7	-210.3	-211.8		
C(SiH ₃)(OH) ₂ (CH ₃)	-364.5	-363.5 ± 9.3	-359.8	-364.7		
C(OH) ₂ (CH ₃)(SiH ₂ CH ₃)	-442.1	-446.1 ± 11.7	-442.5	-447.8		
CH(SiH ₃)(OH) ₂	-330.9	-329.3 ± 9.3	-326.8	-330.4		
CH(OH) ₂ (SiH ₂ CH ₃)	-395.8	-399.1 ± 11.7	-396.7	-400.6		
CH(CH ₃)(SiH ₃)(OH)	-180.9	-180.1 ± 9.3	-178.3	-180.3		
CH(OH)(SiH ₃)(CH ₂ SiH ₃)	-134.6	-135.2 ± 11.6	-132.4	-135.7		
Si(OH) ₄	-1345.7	-1364.6 ± 51.2	-1362.0	-1359.4	-1342.2 ± 13.9 ^a	
SiH ₃ (OCH ₃)	-252.7	-252.0 ± 15.2	-251.0	-250.7	-218.0 ± 17.6 ^a	
SiH ₂ (OH) ₂	-631.8	-638.2 ± 38.7	-637.8	-637.2	-615.0 ± 4.4 ^a	
SiH(OH) ₃	-988.8	-1001.5 ± 38.8	-1000.2	-998.3	-981.6 ± 6.9 ^a	
SiH ₃ (OC ₂ H ₅)	-287.5	-291.1 ± 15.3	-289.9	-290.2	-276.6 ± 4.2 ^a	
(SiH ₃)O(SiH ₃)	-351.4	-353.5 ± 26.6	-351.8	-353.1	-331.8 ± 8.2 ^a	
(SiH ₃)O(SiH ₂ CH ₃)	-421.7	-428.7 ± 26.9	-427.0	-428.0		
Si(OH) ₃ (OCH ₃)	-1311.6	-1329.8 ± 51.2	-1326.2	-1324.2		
SiH(OH) ₂ (OCH ₃)	-954.6	-966.5 ± 38.8	-964.2	-962.7		
SiH ₂ (OH)(OCH ₃)	-598.5	-604.1 ± 26.6	-602.7	-601.9		
Si(CH ₃) ₃ (OH)	-493.1	-507.9 ± 19.7	-508.2	-507.9	-500.4 ± 4.6 ^b	-499.6 ± 4.2 ^b
Si(OH)(CH ₃) ₂ (CH ₂ SiH ₃)	-461.4	-477.5 ± 22.3	-476.5	-477.7		
Si(CH ₃)(OH) ₃	-1062.5	-1080.1 ± 39.1	-1078.1	-1077.1		

^aRef. [8]. ^bRef. [180].

Si-(C)₂(H)₂, Si-(C)(H)₂(Si), Si-(H)₃(Si), C-(C)(H)₂(Si) and C-(H)₂(Si)₂ from Janbazi et al. [203], because the values of these groups are well established. We intend to devise GAVs of Si-organic species in a hierarchical way, i.e., only Si-O containing groups are subject to the regression analysis, whereas well-established GAVs from the subset of Si-C-H and C-H compound classes remain protected against the regression. This approach was also applied to ensure consistency across already published GAV data. The C-(H)₃(O) group is the only non-Si containing group considered in the regression analysis. A similar approach was adopted by Dellon et al. [198] who fixed the values of 55 groups to either known values or analog values oxygenated hydrocarbons and molecule ions, while obtained 71 additional GAVs from 195 species.

The residuals in ΔH_f° are <0.3 kJ/mol, which are substantially smaller than the uncertainties in the ΔH_f° values. No outlier was found from the regression procedure. In Table 7.3, the GAVs for the enthalpy of formation are based on the G4/isodesmic reaction values only, as other methods produce ΔH_f° values that are generally within the uncertainty limits of the G4/isodesmic reaction values, as seen in Table 7.2. The GAVs for entropy and specific heats from G4 and CBSQB3 calculations differ somewhat due to the small differences in the molecular parameters calculated at the B3LYP/6-31(2df,p) and B3LYP/6-311G(2d,d,p) levels of theory. Here, we adopted the B3LYP/6-31(2df,p) values for generating the GAVs of Table 7.3.

Note that some entropy and specific heat GAVs show negative values. It is clear that chemical species cannot have negative entropies or heat capacities, but these GAVs represent contributions of specific groups to the overall thermochemistry of molecules. The negative values are indications that the presence of the associated group in a molecule reduces the specific heat contributions of the neighboring groups, e.g., by increasing the vibrational frequencies of the normal mode associated with the molecular moieties. In the framework of hydrocarbon thermochemistry, negative contributions of specific groups to entropies have been also reported by Sabbe et al. [145] and Paraskevas et al. [144].

To compare the GAV predictions against literature *ab initio* data, we list in Table 7.4 the enthalpies of formation of single-bonded molecules reported by Phadungsukanan et al. [8] It can be seen that the enthalpies of formation derived from the GAVs are in reasonable agreement with the literature values. The mean absolute deviation is 40 kJ/mol and the maximum absolute deviation is 80 kJ/mol. All of the GAV-derived ΔH_f° values are smaller than the theoretical values of Phadungsukanan et al. [8] These differences are also readily observed from Table 7.2 in which Phadungsukanan et al.'s values are compared to ours. We want to briefly comment on these differences. One reason for these differences is attributed to the choice of methods used to predict thermochemical data. Phadungsukanan

Table 7.3 GAVs of ΔH_f° (298 K), S° (298 K) and $C_p(T)$ for stable and single-bonded Si–C–H–O species. The GAVs of ΔH_f° are based on the G4/isodesmic reaction values listed in Table 7.2; the C_p and S° are calculated at the RRHO (rigid-rotor and harmonic-oscillator) level with molecular parameters obtained using the B3LYP/6-31G(2df,p) method. (unit: ΔH_f° : kJ/mol. S° and C_p : J/mol K)

Groups	ΔH_f°	S°	$C_p(T)$								
			298 K	400 K	500 K	600 K	800 K	1000 K	1500 K	2000 K	
C–(C) ₂ (O)(Si)	–7.0	–149.0	29.4	37.6	41.4	43.0	43.1	42.7	43.2	42.0	
Si–(C) ₂ (O) ₂	–78.5	–79.2	1.8	3.0	4.2	4.7	5.1	5.1	5.0	4.4	
Si–(C) ₂ (H) ₂	–3.5	52.5	30.7	38.8	45.1	50.1	57.0	61.7	67.9	70.4	
Si–(O) ₄	–115.8	–1.7	–19.8	–22.3	–24.4	–25.9	–28.0	–29.7	–31.7	–32.7	
C–(H)(O)(Si) ₂	20.4	–36.5	31.9	40.1	45.2	48.1	51.6	54.0	59.2	63.0	
Si–(C)(H)(O) ₂	–47.1	17.4	4.4	6.8	8.6	9.8	11.2	12.3	13.7	14.2	
Si–(C)(O) ₂ (Si)	–35.2	–55.2	6.9	6.9	6.3	5.4	3.4	1.9	–0.4	–1.8	
O–(C)(H)	–158.5	121.6	18.1	18.6	20.1	21.9	25.2	27.7	30.0	31.0	
Si–(C)(H) ₂ (Si)	23.3	64.4	35.8	44.2	50.4	55.1	61.7	66.2	72.2	74.8	
C–(C)(H) ₂ (O)	–33.5	31.9	21.9	30.1	37.0	42.6	49.4	54.6	62.9	66.7	
Si–(O) ₃ (Si)	–45.0	–26.4	–1.3	–3.9	–6.8	–9.4	–13.1	–15.7	–19.0	–20.5	
Si–(C) ₃ (O)	–58.9	–95.7	11.8	14.4	17.1	18.4	19.5	20.2	20.6	20.0	
Si–(C)(H)(O)(Si)	9.1	5.3	19.8	22.5	24.9	26.8	29.5	31.3	33.7	34.6	
Si–(C) ₂ (O)(Si)	–19.5	–73.8	17.1	17.9	19.0	19.4	19.6	19.7	19.6	19.0	
C–(C)(H)(O)(Si)	0.4	–47.8	27.0	36.0	41.8	45.6	50.0	53.0	58.9	62.6	
C–(O)(Si) ₃	30.0	–109.9	35.3	42.0	45.3	46.3	47.1	47.2	48.9	50.9	
Si–(C)(O) ₃	–98.6	–41.8	–8.6	–10.0	–11.0	–11.7	–12.7	–13.5	–14.5	–15.2	
Si–(H) ₃ (Si)	40.4	138.4	38.4	45.7	51.7	56.7	64.6	70.2	78.0	81.9	
O–(C)(Si)	–236.1	4.2	25.3	27.4	29.5	31.2	33.7	35.4	36.9	34.9	
Si–(C)(H) ₃	18.9	128.1	36.0	43.5	49.7	55.0	63.1	68.9	76.9	80.7	
Si–(O)(Si) ₃	38.9	–56.4	23.3	23.5	23.3	23.0	22.7	22.5	21.9	21.7	
O–(Si) ₂	–403.7	–24.6	43.4	49.7	53.5	55.5	57.9	59.3	61.3	61.5	
C–(H) ₃ (Si)	–46.0	124.9	30.6	36.6	41.7	46.6	54.7	61.2	71.9	78.1	
C–(O) ₃ (Si)	–84.5	–157.1	31.9	44.6	50.4	52.1	51.2	49.7	52.6	55.8	
Si–(H) ₂ (O)(Si)	38.6	84.5	20.3	24.3	28.1	31.3	36.2	39.8	44.5	46.9	
C–(O) ₂ (Si) ₂	10.2	–134.8	35.9	46.9	51.6	52.8	51.8	50.3	51.3	53.2	
C–(C)(O)(Si) ₂	27.3	–122.4	32.3	39.9	43.3	44.6	45.3	45.5	47.1	48.7	
Si–(H) ₂ (O) ₂	–13.9	122.4	8.3	12.7	16.1	18.8	22.3	24.8	28.2	29.9	
C–(H) ₃ (O)	–42.2	127.2	25.9	32.8	39.3	45.1	54.5	61.8	73.6	82.9	
C–(C)(O) ₂ (Si)	–29.6	–158.4	30.4	40.2	44.6	46.1	45.6	44.8	46.6	46.9	
Si–(H)(O) ₂ (Si)	2.5	37.7	10.1	10.5	10.1	9.7	9.6	9.6	9.9	10.2	
O–(H)(Si)	–312.0	84.5	33.6	38.7	42.2	44.6	47.6	49.8	53.4	55.6	
Si–(H) ₃ (O)	24.5	174.1	21.8	28.1	34.3	39.8	48.1	54.1	61.8	66.2	
Si–(H)(O)(Si) ₂	41.7	18.6	21.1	22.8	24.4	25.7	27.8	29.4	31.3	32.3	
C–(H) ₂ (O)(Si)	–5.5	40.9	27.8	35.1	40.9	45.2	51.4	56.1	65.1	70.8	
Si–(O) ₂ (Si) ₂	9.8	–44.8	9.5	8.4	6.7	5.2	3.3	2.0	0.3	–0.5	
C–(H)(O) ₂ (Si)	–31.9	–48.2	27.3	38.9	45.9	49.8	53.1	54.5	59.1	62.6	
C–(C)(H) ₂ (Si)	–12.9	45.4	27.0	33.1	38.5	43.1	49.9	55.0	62.5	64.8	
Si–(C) ₂ (H)(O)	–30.5	–6.4	13.7	16.9	20.3	22.7	25.9	28.0	30.7	31.5	
Si–(C)(H) ₂ (O)	–2.2	74.1	18.1	22.8	27.3	31.1	36.5	40.4	45.5	47.8	
C–(C)(H) ₃	–42.9	127.1	25.3	32.1	38.4	44.1	53.4	60.6	72.5	81.0	
Si–(H)(O) ₃	–64.7	70.3	–5.8	–6.0	–6.0	–5.5	–4.5	–3.8	–2.4	–1.8	
C–(H) ₂ (Si) ₂	–32.4	65.6	28.2	36.0	42.3	47.4	54.5	59.8	67.5	72.2	
Si–(C)(O)(Si) ₂	15.9	–80.9	23.1	24.2	24.7	24.8	24.8	24.7	24.5	24.1	

et al. [8] applied B3LYP and B97-1 functionals. According to a benchmark study by Krieg and Grimme [205], the B3LYP functional for example yields MAD of $\tilde{5}0.0$ kJ/mol from CCSD(T)/CBS reference energies of a test set of isodesmic reactions for organic species. On the other hand side, Phadungsukanan et al. set up an isodesmic reaction network, in which more than one isodesmic reaction per species was applied.

Between our work and the study from Phadungsukanan et al. [8], there is almost no overlap in the pool of reference species used in the isodesmic reaction network. In Phadungsukanan et al.'s network, for example, compounds like $\text{Si}(\text{OH})_4$, $\text{SiH}(\text{OH})_3$, and $\text{Si}(\text{OH})_3(\text{OCH}_3)$ are reference species, whereas we used isodesmic reactions to derive ΔH_f° of these species. For $\text{Si}(\text{OH})_4$ and $\text{SiH}(\text{OH})_3$, Phadungsukanan et al. [8] adopted ΔH_f° data computed by Allendorf et al. [204]: $\Delta H_f^\circ(\text{Si}(\text{OH})_4) = -1342.2$ kJ/mol and $\Delta H_f^\circ(\text{SiH}(\text{OH})_3) = -981.6$ kJ/mol. For $\text{Si}(\text{OH})_3(\text{OCH}_3)$, they adopted ΔH_f° from Ho and Melius [180]: $\Delta H_f^\circ(\text{Si}(\text{OH})_3(\text{OCH}_3)_3) = -1305.4$ kJ/mol. The isodesmic reactions in our work yield $\Delta H_f^\circ(\text{Si}(\text{OH})_4) = -1364.6$ kJ/mol, $\Delta H_f^\circ(\text{SiH}(\text{OH})_3) = -1001.5$ kJ/mol, and $\Delta H_f^\circ(\text{Si}(\text{OH})_3(\text{OCH}_3)_3) = -1329.8$ kJ/mol. These three molecules can be used to formulate another isodesmic reaction to determine ΔH_f° of $\text{SiH}_3(\text{OCH}_3)$: $\text{SiH}_3(\text{OCH}_3) + 3\text{Si}(\text{OH})_4 \rightarrow \text{Si}(\text{OH})_3(\text{OCH}_3) + 3\text{SiH}(\text{OH})_3$ for which the G4 composite method yields $\Delta H_f^\circ = -14.2$ kJ/mol. Using the ΔH_f° values of $\text{Si}(\text{OH})_4$, $\text{SiH}(\text{OH})_3$, and $\text{Si}(\text{OH})_3(\text{OCH}_3)$ from Allendorf et al. [204] and Ho and Melius [180], we obtain $\Delta H_f^\circ \text{SiH}_3(\text{OCH}_3) = -209.2$ kJ/mol. If we use our ΔH_f° values for $\text{Si}(\text{OH})_4$, $\text{SiH}(\text{OH})_3$, and $\text{Si}(\text{OH})_3(\text{OCH}_3)$, we obtain $\Delta H_f^\circ \text{SiH}_3(\text{OCH}_3) = -252.0$ kJ/mol (see Table 7.2). Our isodesmic reaction/G4 approach yield systematically lower ΔH_f° data of species, which served as reference species in the isodesmic reaction network of Phadungsukanan et al. [8] and these differences are then propagated in the prediction of the thermochemistry of larger Si–O–C–H species like $\text{Si}(\text{OCH}_3)(\text{OC}_2\text{H}_5)_3$ and $\text{Si}(\text{OH})_3(\text{OC}_2\text{H}_5)$ (see Table 7.4). Ho and Melius [180] described that they applied BAC to account for systematic errors in the *ab initio* calculations, but because of the lack of experimental data for Si–O–C–H species, they had to rely on G2-based thermochemical data of $\text{SiH}_2(\text{OH})_2$ and $\text{H}_2\text{Si}=\text{O}$ for obtaining BAC in the Si–O–H and Si–O–C–H systems. In the present work, our pool of reference species is largely based on compounds for which experimental ΔH_f° data are well known, and hence, we have confidence in our thermochemical data.

7.4.2 GAVs of Si–C–H–O species with Si=O bonds

Species with Si=O double bonds are often produced as intermediates during the oxidation of TMS and TEOS. Ho and Melius [180] studied the thermochemistry of several species with Si=O bonds, including $\text{O}=\text{Si}(\text{OC}_2\text{H}_5)_2$, $\text{O}=\text{Si}(\text{OH})_2$, $\text{O}=\text{Si}(\text{OCH}_3)\text{OH}$, and

Table 7.4 Comparison of ΔH_f° (kJ/mol) reported in ref [8] and those predicted by the present GAVs.

Species	Lit. [8]	GAVs/G4	Species	Lit. [8]	GAVs/G4
TEOS	-1301.9	-1385.7	SiH ₂ (OCH ₃) ₂	-535.1	-569.6
Si(OH) ₃ (OCH ₃)	-1305.4	-1329.8	SiH ₂ (OC ₂ H ₅) ₂	-607.5	-649
SiH(OC ₂ H ₅) ₃	-956.9	-1017.2	SiH(OH) ₃	-981.6	-1001
Si(OH) ₄	-1342.2	-1364.1	SiH ₂ (OH) ₂	-615.0	-638.2
Si(OH) ₃ (OC ₂ H ₅)	-1341.0	-1369.5	Si(OH) ₂ (OCH ₃) ₂	-1259.4	-1295.5
SiH ₃ (OC ₂ H ₅)	-276.6	-291.1	Si(OH) ₂ (OC ₂ H ₅) ₂	-1324.6	-1374.9
Si(OCH ₃)(OC ₂ H ₅) ₃	-1266.9	-1346	Si(OCH ₃) ₃ (OC ₂ H ₅)	-1199.8	-1266.6
Si(OCH ₃) ₂ (OC ₂ H ₅) ₂	-1235.7	-1306.3	SiH(OCH ₃) ₂ (OC ₂ H ₅)	-892.4	-937.8
Si(OH)(OCH ₃)(OC ₂ H ₅) ₂	-1282.2	-1340.6	Si(OH) ₂ (OCH ₃)(OC ₂ H ₅)	-1299.3	-1335.2
SiH(OCH ₃)(OC ₂ H ₅) ₂	-930.3	-977.5	SiH(OH)(OCH ₃)(OC ₂ H ₅)	-941.1	-972.1
Si(OH)(OC ₂ H ₅) ₃	-1309.2	-1380.3	SiH ₂ (OCH ₃)(OC ₂ H ₅)	-578.8	-609.3
SiH ₃ (OCH ₃)	-218.0	-251.4	SiH ₂ (OH)(OC ₂ H ₅)	-625.6	-643.6
SiH ₂ (OH)(OCH ₃)	-580.0	-603.9	Si(OCH ₃) ₄	-1172.3	-1226.9
SiH(OH)(OCH ₃) ₂	-901.4	-932.4	Si(OH)(OCH ₃) ₃	-1212.9	-1261.2
SiH(OH)(OC ₂ H ₅) ₂	-972.1	-1011.8	SiH(OCH ₃) ₃	-850.0	-898.1
SiH(OH) ₂ (OC ₂ H ₅)	-983.1	-1006.4	SiH(OH) ₂ (OCH ₃)	-946.0	-966.7

O=Si(OCH₃)₂. Davidson et al. [206] estimated the rate constants for the oxidation of sila-isobutene ((CH₃)₂Si=CH₂), producing (CH₃)₂Si=O as a product. (CH₃)₂Si=O was hypothesized to be an important intermediate for SiO production in TMS oxidation [81, 186]. Species with Si=O double bonds, such as O=Si(OC₂H₅)₂, O=Si(OH)(OC₂H₅), and (OH)₂Si=O, were also considered in the TEOS oxidation mechanism of Nurkowski et al. [34]. We considered the possibilities of SiH₃, CH₃, H, and OH as ligands to the Si=O moiety and used the combinatorial approach to generate species relevant to the subsequent GAV estimation. In deriving the ΔH_f° values from isodesmic reactions, H₂Si=O is used as the reference species. Since no experimental ΔH_f° value is available for H₂Si=O, its ΔH_f° is determined by the G4/atomization energy method, which yields $\Delta H_f^\circ = -102.5 \pm 4.2$ kJ/mol. Tables 7.5 and 7.6 list isodesmic reactions and the resulting ΔH_f° values of the nine relevant species, respectively. Clearly, the resulting ΔH_f° values are insensitive to the level of theory used.

A similar regression analysis was carried out for species listed in Table 7.6, with the resulting GAVs shown in Table 7.7. Again, the ΔH_f° values are based on G4/isodesmic reaction calculations, and S° (298 K) and $C_p(T)$ are derived from B3LYP/6-31G(2df,p) molecular parameters. The group nomenclature differ somewhat from Benson's convention. We write a double-bonded center atom X in a group as X_{d,i} where the subscript "d" denotes the double bond, and *i* refers to atom *i* with which X forms the double bond. For example, (CH₃)₂Si=O contains two C-(H)₃(Si_{d,o}) and one Si_{d,o}-(C)₂.

Table 7.5 Isodesmic reactions used for the species with Si=O double bonds and their standard enthalpies of reactions (kJ/mol) calculated at several levels of theory.

Reaction	G4	G4MP2	CBSQB3
$(\text{CH}_3)_2\text{Si}=\text{O} + 2\text{SiH}_4 \rightarrow \text{H}_2\text{Si}=\text{O} + 2\text{CH}_3\text{SiH}_3$	35.6	34.7	35.2
$(\text{CH}_3)\text{HSi}=\text{O} + \text{SiH}_4 \rightarrow \text{H}_2\text{Si}=\text{O} + \text{CH}_3\text{SiH}_3$	19.8	19.0	19.1
$(\text{OH})_2\text{Si}=\text{O} + 2\text{SiH}_4 \rightarrow \text{H}_2\text{Si}=\text{O} + 2\text{H}_3\text{SiOH}$	87.4	86.1	83.9
$(\text{OH})\text{HSi}=\text{O} + \text{SiH}_4 \rightarrow \text{H}_2\text{Si}=\text{O} + \text{H}_3\text{SiOH}$	55.5	54.6	53.7
$(\text{CH}_3)(\text{OH})\text{Si}=\text{O} + 2\text{SiH}_4 \rightarrow \text{H}_3\text{SiOH} + \text{CH}_3\text{SiH}_3 + \text{H}_2\text{Si}=\text{O}$	73.7	72.2	71.9
$(\text{SiH}_3)_2\text{Si}=\text{O} + 2\text{SiH}_4 \rightarrow \text{H}_2\text{Si}=\text{O} + 2\text{Si}_2\text{H}_6$	9.0	6.4	9.5
$(\text{SiH}_3)\text{HSi}=\text{O} + \text{SiH}_4 \rightarrow \text{H}_2\text{Si}=\text{O} + \text{Si}_2\text{H}_6$	3.2	2.0	3.4
$(\text{SiH}_3)(\text{CH}_3)\text{Si}=\text{O} + 2\text{SiH}_4 \rightarrow \text{CH}_3\text{SiH}_3 + \text{Si}_2\text{H}_6 + \text{H}_2\text{Si}=\text{O}$	22.3	20.8	22.8
$(\text{SiH}_3)(\text{OH})\text{Si}=\text{O} + 2\text{SiH}_4 \rightarrow \text{Si}_2\text{H}_6 + \text{H}_2\text{Si}=\text{O} + \text{H}_3\text{SiOH}$	63.9	61.7	63.2

Table 7.6 Enthalpies of formation ΔH_f° (kJ/mol) values and uncertainties of double-bonded Si=O species determined from the respective isodesmic reactions of Table 7.5

Species	G4	G4MP2	CBSQB3
$(\text{CH}_3)_2\text{Si}=\text{O}$	-264.7 ± 17.3	-263.8	-264.3
$(\text{CH}_3)\text{HSi}=\text{O}$	-185.6 ± 15.7	-184.8	-184.9
$(\text{OH})_2\text{Si}=\text{O}$	-828.9 ± 29.5	-827.5	-825.3
$(\text{OH})\text{HSi}=\text{O}$	-477.5 ± 19.7	-476.6	-475.7
$(\text{CH}_3)(\text{OH})\text{Si}=\text{O}$	-559.0 ± 20.2	-557.5	-557.2
$(\text{SiH}_3)_2\text{Si}=\text{O}$	-20.1 ± 15.6	-17.5	-20.7
$(\text{SiH}_3)\text{HSi}=\text{O}$	-60.0 ± 15.3	-58.8	-60.2
$(\text{SiH}_3)(\text{CH}_3)\text{Si}=\text{O}$	-142.5 ± 15.9	-140.9	-142.9
$(\text{SiH}_3)(\text{OH})\text{Si}=\text{O}$	-440.2 ± 19.9	-438.0	-439.5

Table 7.7 GAVs of ΔH_f° (298 K), S° (298 K) and $C_p(T)$ for Si=O containing species. The GAVs of ΔH_f° are based on the G4/isodesmic reaction values listed in Table 7.5; the C_p and S° are calculated at the RRHO level with molecular parameters obtained using the B3LYP/6-31G(2df,p) method. (units: ΔH_f° : kJ/mol, S° and C_p : J/mol K).

Groups	ΔH_f°	S°	$C_p(T)$							
			298 K	400 K	500 K	600 K	800 K	1000 K	1500 K	2000 K
Si _{d,o} -(C) ₂	-9.5	5.5	4.9	6.0	7.1	7.9	9.4	10.6	12.8	14.1
Si _{d,o} -(H)(Si)	-37.2	123.5	23.0	27.1	30.3	32.9	36.9	39.6	43.3	45.1
Si _{d,o} -(C)(Si)	7.9	8.7	4.3	5.5	6.5	7.3	8.7	9.8	11.5	12.5
Si _{d,o} -(H)(O)	-104.5	127.9	22.5	26.3	29.3	31.7	35.0	37.0	39.0	39.8
Si _{d,o} -(O) ₂	-82.9	-2.8	3.1	3.0	2.7	2.4	2.1	2.1	3.0	3.7
Si _{d,o} -(C)(H)	-58.0	126.5	23.7	27.6	30.8	33.5	37.5	40.5	44.6	46.7
Si _{d,o} -(O)(Si)	-44.4	10.2	3.6	4.6	5.4	5.8	6.2	6.2	5.7	5.4
O-(H)(Si _{d,o})	-373.0	144.7	35.9	41.6	45.6	48.6	52.3	54.7	58.1	60.1
C-(H) ₃ (Si _{d,o})	-127.6	158.5	41.6	49.8	56.9	62.9	71.9	78.7	89.2	94.9
Si _{d,o} -(C)(O)	-58.4	12.2	3.7	4.7	5.5	6.1	6.9	7.3	7.5	7.4
Si _{d,o} -(Si) ₂	25.5	21.5	12.0	13.2	14.1	14.9	16.2	17.1	18.5	19.2
Si-(H) ₃ (Si _{d,o})	-22.8	185.5	55.0	63.7	70.5	75.9	84.1	89.8	97.5	101.3

7.4.3 GAVs of cyclic siloxanes

GAVs were also derived for cyclo-siloxanes such as hexamethyl-cyclo-tetrasiloxane (cyc-Si₄O₄H₂(CH₃)₆) or tetramethyl-cyclo-pentasiloxane (cyc-Si₅O₅H₆(CH₃)₄). Specifically, we considered derivatives of compounds with different ring sizes: D3 (hexamethyl-cyclo-trisiloxane; Si₃O₃(CH₃)₆), D4 (octamethyl-cyclo-tetrasiloxane; Si₄O₄(CH₃)₈), and D5 (decamethyl-cyclo-pentasiloxane; Si₅O₅(CH₃)₁₀), because cyclosiloxanes such as D3, D4, and D5 are used as precursor materials for silicon polymer synthesis [207] and for the production of optical-grade fused silica and SiO₂ nanoparticles [208]. Common to methyl-substitute cyclo-siloxanes is the Si-(C)₂(O)₂ group, but cyclo-siloxanes are subject to different ring strain energy depending on the ring size, making it necessary to consider D3, D4, and D5 derivatives separately. Due to the molecular size, we used CBSQB3 calculations only since G4 and G4-MP2 are both too expensive. The list of isodesmic reactions used is presented in Table 7.8. In these reactions, SiH₄, H₃SiOH, and CH₃SiH₃ are the reference species; and the gas-phase ΔH_f° values of D3, D4, and D5 were taken Voronkov et al. [209]: $\Delta H_f^\circ = -1568.0 \pm 11.0$ kJ/mol for D3, -2138.0 ± 11.0 kJ/mol for D4, and -2708.0 ± 13.0 kJ/mol for D5. These ΔH_f° values are in reasonable agreement with the measurement of Tanaka et al. [210–212]. From ΔH_f° values measured for liquid D4, and D5 and estimated enthalpy of vaporization (45.6 and 46.0 kJ/mol for D4 and D5, respectively), [210] they found gas-phase $\Delta H_f^\circ = -2121.0$ kJ/mol for D4 and -2698.7 kJ/mol for D5. For D3, they derived a gas-phase ΔH_f° value of -1601.7 kJ/mol from a ΔH_f° value of -1656.9 kJ/mol measured for the solid state and an enthalpy of sublimation of 55.2 kJ/mol. Clearly, the gas-phase ΔH_f° values of D4 and D5 of Tanaka et al. [210] are in very good agreement with those of Voronkov et al. [209] D3 has a larger difference, however, with Tanaka et al.’s value being about 34 kJ/mol lower than that of Voronkov et al. The difference is probably still within the measurement uncertainties.

The minimum-energy geometries of D3 and D4 are symmetric for which each Si atom may be regarded as being equivalent. The consequence is that these species have two equivalent additivity groups containing CH₃. In cyc-Si₃O₃H₄(CH₃)₂ and cyc-Si₄O₄H₆(CH₃)₂, for example, which Si atoms the CH₃ groups are bonded is inconsequential as far as the group additivity is concerned; and the same applies to the OH ligands. D5 behaves differently as it has three non-equivalent types of Si atoms. As shown in Fig. 7.2, the Si atoms marked by the blue arrows (1 and 5) are equivalent; and those marked by the green arrows (3 and 4) are also equivalent. However, the Si atom marked by the orange arrow (2) is unique. This results in a range of isomers for which the ΔH_f° values can differ by as much as 45 kJ/mol. We conducted CBSQB3 calculations on all five isomers of “cyc-Si₅O₅H₈(CH₃)₂”, i.e., cyc-Si₅O₅H₈(CH₃)₂-vi where i = 1,5. As one would expect, the “cyc-Si₅O₅H₈(CH₃)₂”

Table 7.8 Isodesmic reactions used for the cyclosiloxane species their standard enthalpies of reactions (kJ/mol) calculated at the CBSQB3 level of theory.

Reaction	CBSQB3
cyc-Si ₃ O ₃ H ₄ (CH ₃) ₂ + 4CH ₃ SiH ₃ → D3 + 4SiH ₄	-72.1
cyc-Si ₃ O ₃ H ₂ (CH ₃) ₄ + 2CH ₃ SiH ₃ → D3 + 2SiH ₄	-35.5
cyc-Si ₃ O ₃ H ₄ (OH) ₂ + 6CH ₃ SiH ₃ → D3 + 2H ₃ SiOH + 4SiH ₄	-26.2
cyc-Si ₃ O ₃ H ₂ (OH) ₄ + 6CH ₃ SiH ₃ → D3 + 4H ₃ SiOH + 2SiH ₄	57.4
cyc-Si ₄ O ₄ H ₆ (CH ₃) ₂ + 6CH ₃ SiH ₃ → D4 + 6SiH ₄	-102.6
cyc-Si ₃ O ₃ H ₄ (CH ₃) ₄ + 4CH ₃ SiH ₃ → D4 + 4SiH ₄	-67.4
cyc-Si ₄ O ₄ H ₆ (OH) ₂ + 8CH ₃ SiH ₃ → D4 + 2H ₃ SiOH + 6SiH ₄	-54.3
cyc-Si ₄ O ₄ H ₄ (OH) ₄ + 8CH ₃ SiH ₃ → D4 + 4H ₃ SiOH + 4SiH ₄	28.0
cyc-Si ₅ O ₅ H ₁₀ + 10CH ₃ SiH ₃ → D5 + 10SiH ₄	-142.4
cyc-Si ₅ O ₅ H ₈ (OH) ₂ -v1 + 10CH ₃ SiH ₃ → D5 + 8SiH ₄ + 2H ₃ SiOH	-56.0
cyc-Si ₅ O ₅ H ₈ (OH) ₂ -v2 + 10CH ₃ SiH ₃ → D5 + 8SiH ₄ + 2H ₃ SiOH	-51.8
cyc-Si ₅ O ₅ H ₆ (OH) ₄ + 10CH ₃ SiH ₃ → D5 + 6SiH ₄ + 4H ₃ SiOH	31.1
cyc-Si ₅ O ₅ H ₈ (CH ₃) ₂ -v1 + 8CH ₃ SiH ₃ → D5 + 8SiH ₄	-102.6
cyc-Si ₅ O ₅ H ₈ (CH ₃) ₂ -v2 + 8CH ₃ SiH ₃ → D5 + 8SiH ₄	-149.8
cyc-Si ₅ O ₅ H ₈ (CH ₃) ₂ -v3 + 8CH ₃ SiH ₃ → D5 + 8SiH ₄	-105.8
cyc-Si ₅ O ₅ H ₈ (CH ₃) ₂ -v4 + 8CH ₃ SiH ₃ → D5 + 8SiH ₄	-105.9
cyc-Si ₅ O ₅ H ₈ (CH ₃) ₂ -v5 + 8CH ₃ SiH ₃ → D5 + 8SiH ₄	-102.6

isomers with two CH₃ groups bonded to Si atoms 1 and 5 are equivalent, and the “cyc-Si₅O₅H₈(CH₃)₂” isomers bonded to two CH₃ groups at positions 3 and 4 are also equivalent, whereas the “cyc-Si₅O₅H₈(CH₃)₂” isomer with both CH₃ groups bond to Si atom #2 is a unique isomer. We have the same issue for the “cyc-Si₅O₅H₈(OH)₂” isomers, but generally their ΔH_f° values differ much less (around 8.0 kJ/mol). Also, the “cyc-Si₅O₅H₈(OH)₂” isomers with the OH groups bonded to Si atoms 3 and 4 are equivalent, and expectedly so, the CBSQB3 electronic energies of the two isomers are also identical to each other. The isomer “cyc-Si₅O₅H₈(OH)₂-v2” with both of the OH groups bonded with Si atom 2 is a unique isomer and its ΔH_f° differs notably from those of other “cyc-Si₅O₅H₈(OH)₂” isomers. It is for this reason we computed the relevant isomers separately, as listed in Table 7.8. To obtain a more accurate estimation for the O-(Si)₂ group, it was also necessary to consider an additional D5 derivative: cyc-Si₅O₅H₁₀, whose ΔH_f° is derived from the isodesmic reaction/CBSQB3 approach and $C_p(T)$ and $S^\circ(T)$ are obtained from molecular properties optimized as a part of the CBSQB3 composite scheme. The cyc-Si₅O₅H₁₀ has only H atoms bonded to the Si atoms in the cyclo-siloxane ring. To be consistent with the GAVs derived from the previous section, the GAVs of (C-(H)₃(Si) and O-(H)(Si)) are fixed at their known values. The GAV for C-(H)₃(Si) was taken from our previous work [203], and that of O-(H)(Si) taken from Table 7.3. With these treatments, we reproduced the experimental ΔH_f° value for cyc-Si₅O₅H₁₀ to within 2.7 kJ/mol. Table 7.9 lists the calculated ΔH_f° values and their uncertainties for cyclo-siloxane species; and the corresponding GAVs are presented

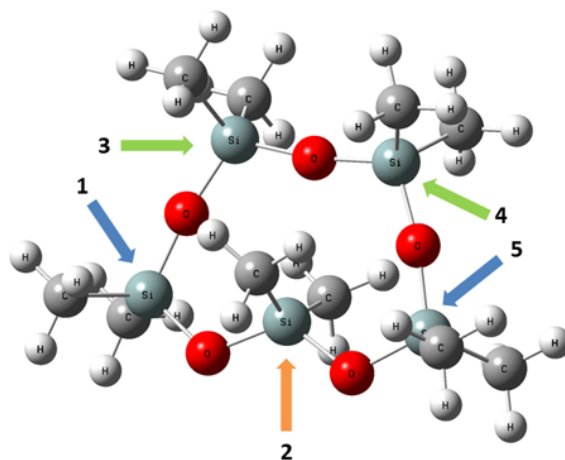


Fig. 7.2 Structure of D5 (cyc-Si₅O₅(CH₃)₁₀) obtained from B3LYP/6 311G(2d,d,p) calculation. See text for the colored arrows with number labeling.

in Table 7.10. Also for the CBS-QB3 based reaction enthalpies, we assumed an uncertainty of ± 8.4 kJ/mol.

The GAVs in Table 7.10 are separately listed for D3, D4, and D5. Such an isomer-related limitation is known for the group additivity method. With increasing molecular complexity, it usually becomes necessary to consider subsets of groups, which renders the method increasingly ineffective especially considering the ease with which quantum chemical calculations are becoming routine in recent time. Similar limitation may arise for large molecules when no useful isodesmic reactions can be defined because of a lack of reference compounds with known thermochemistry. In such cases, atomization energy is sometimes the only viable option. The D2 derivatives are examples of such cases: it represents the cyc-Si₂O₂(CH₃)₄ (tetramethyl-cyclodisiloxane) species for which the experimental thermochemistry is unavailable because of difficulties in isolating and characterizing it, despite the fact that mass spectrometric experiments do suggest its existence [213]. Yet the GAVs of D2 derivatives are useful for predicting the thermochemistry of larger silicon oxide clusters such as Si₄O₁₀H₄ or Si₅O₁₂H₄ [81, 186]. As the molecular analog of D2, these clusters comprise of Si atoms bridged by two O atoms [214].

7.5 Conclusion

Thermodynamic properties of 62 non-radical Si–C–H–O-containing species were calculated by means of G4/atomization energy and G4/isodesmic reaction methods. The standard enthalpies of formation calculated by these two methods were compared. As expected, the isodesmic-reaction approach gives a better accuracy than atomization-energy calculations.

Table 7.9 The training set species and their standard ΔH_f° (kJ/mol) values and estimated uncertainties of cyclo-siloxanes from CBSQB3/isodesmic reaction.

Category	Species	ΔH_f°
D3 derivatives	cyc-Si ₃ O ₃ H ₄ (CH ₃) ₂	-1242.6 ± 21.7
	cyc-Si ₃ O ₃ H ₂ (CH ₃) ₄	-1405.8 ± 16.2
	cyc-Si ₃ O ₃ H ₄ (OH) ₂	-1800.9 ± 37.8
	cyc-Si ₃ O ₃ SiH ₂ (OH) ₄	-2523.3 ± 57.6
D4 derivatives	cyc-Si ₄ O ₄ H ₆ (CH ₃) ₂	-1655.5 ± 28.6
	cyc-Si ₄ O ₄ H ₄ (CH ₃) ₄	-1817.3 ± 21.7
	cyc-Si ₄ O ₄ H ₆ (OH) ₂	-2216.2 ± 43.6
	cyc-Si ₄ O ₄ H ₄ (OH) ₄	-2937.3 ± 61.5
D5 derivatives	cyc-Si ₅ O ₅ H ₈ (OH) ₂ -v1	-2657.7 ± 50.7
	cyc-Si ₅ O ₅ H ₈ (OH) ₂ -v2	-2662.0 ± 50.7
	cyc-Si ₅ O ₅ H ₈ (OH) ₂ -v3	-2654.4 ± 50.7
	cyc-Si ₅ O ₅ H ₈ (OH) ₂ -v4	-2654.4 ± 50.7
	cyc-Si ₅ O ₅ H ₈ (OH) ₂ -v5	-2654.8 ± 50.7
	cyc-Si ₅ O ₅ H ₁₀	-1932.5 ± 44.5
	cyc-Si ₅ O ₅ H ₈ (CH ₃) ₂ -v1	-2098.9 ± 36.8
	cyc-Si ₅ O ₅ H ₈ (CH ₃) ₂ -v2	-2051.7 ± 36.8
	cyc-Si ₅ O ₅ H ₈ (CH ₃) ₂ -v3	-2095.7 ± 36.8
	cyc-Si ₅ O ₅ H ₈ (CH ₃) ₂ -v4	-2095.7 ± 36.8
	cyc-Si ₅ O ₅ H ₈ (CH ₃) ₂ -v5	-2098.9 ± 36.8

The thermochemistry of nine Si=O containing species and 19 cyclic siloxanes are also estimated by the G4/isodesmic and CBS-QB3/isodesmic reaction methods, respectively. A combinatorial approach was used to recognize the groups required to completely describe molecule categories of interest. Systematic regression analyses were performed to obtain the GAVs of 30 Si- and C-centered groups, three O-centered groups and groups which contribute to the thermochemistry of double-bonded and cyclic compounds. A statistical analysis demonstrates that the precision of the regressed GAVs strongly depends on the quantity of reference compounds considered in the training set, whereas the accuracy depends strongly on the quality of the thermochemical data of reference compounds. Lastly, we note that the GAVs must be updated regularly when new reliable data for reference compounds, experimental or theoretical, become available.

Combining the current work with a previous study, we now have a comprehensive suite of the GAVs for a range of Si containing species, including the single-bonded molecules of the Si-C-H species and their associated radicals, the species with Si=C bonds, and the stable Si-C-H-O species with single bonds and the species containing Si=O bonds. In addition, the GAVs are also available now for cyclo-siloxanes.

Table 7.10 GAVs of ΔH_f° (298 K), S° (298 K) and $C_p(T)$ for D3, D4, and D5 derivatives (units: ΔH_f° : kJ/mol, S° and C_p : J/mol K).

Groups	ΔH_f°	S°	$C_p(T)$							
			298 K	400 K	500 K	600 K	800 K	1000 K	1500 K	2000 K
D3 derivatives										
O-(Si) ₂	-312.4	15.0	23.9	29.5	33.4	36.3	40.0	42.4	45.3	46.5
Si-(C) ₂ (O) ₂	-118.8	-69.5	14.6	18.2	20.3	21.3	21.8	21.8	21.3	20.6
Si-(H) ₂ (O) ₂	-47.2	105.2	18.3	22.9	26.8	29.9	34.2	37.2	41.3	43.4
Si-(O) ₄	-146.4	-20.7	-8.9	-11.7	-13.6	-14.9	-16.0	-16.7	-17.4	-17.5
D4 derivatives										
O-(Si) ₂	-120.8	-66.7	15.1	18.6	20.6	21.7	22.2	22.2	21.7	20.9
Si-(C) ₂ (O) ₂	-322.2	12.0	25.1	30.5	34.4	37.2	41.0	43.4	46.3	47.5
Si-(H) ₂ (O) ₂	-51.4	109.7	18.8	23.3	27.1	30.2	34.5	37.6	41.6	43.7
Si-(O) ₄	-150.0	-30.9	-8.7	-11.4	-13.4	-14.6	-15.7	-16.4	-17.1	-17.1
D5 derivatives										
O-(Si) ₂	-331.1	-1.8	25.2	30.9	34.9	37.8	41.6	43.9	46.9	48.1
Si-(C) ₂ (O) ₂	-119.1	-71.2	15.2	18.9	20.9	21.9	22.4	22.4	21.9	21.1
Si-(H) ₂ (O) ₂	-55.4	102.8	19.1	23.5	27.3	30.4	34.7	37.7	41.8	43.9
Si-(O) ₄	-156.6	-33.4	-9.1	-11.5	-13.3	-14.5	-15.5	-16.2	-16.8	-16.9

Future efforts will aim at determining GAVs of Si-C-H-O-containing radicals and silylenes. Another possibility to further improve the thermochemistry of Si-C-H-O compounds could deal with considering multiple isodesmic reactions. Buerger et al. [215] described an algorithmic approach to setup reaction networks, which include several error-cancelling reactions per target compound such that one obtains distributions of ΔH_f° estimates. Nevertheless, the available GAVs enable us to estimate the thermochemistry of many Si-containing, organic species that are unavailable previously.

7.6 Acknowledgment

We gratefully acknowledge financial support by the German Research Foundation (DFG, FOR 2284, WL 63/1-2 and SCHU 1369/25, project 262219004). HW acknowledges the support of the Alexander von Humboldt Foundation for the Humboldt Research Award which enabled the collaborative work.

Chapter 8

Development and evaluation of a chemical kinetics reaction mechanism for tetramethylsilane-doped flames

Authors: H. Janbazi, Y. Karakaya, T. Kasper, C. Schulz, I. Wlokas, S. Peukert

This chapter including all text, figures and tables was previously published in 'Chemical Engineering Science 209, H. Janbazi, Y. Karakaya, T. Kasper, C. Schulz, I. Wlokas, S. Peukert, Development and evaluation of a chemical kinetics reaction mechanism for tetramethylsilane-doped flames 115209, 2020' and is reprinted with permission from Elsevier. The author of this thesis contributed the extension of genetic algorithm-based optimizer, running simulations, the validation of results, and writing the paper. The author Y. Karakaya contributed performing experiment and the post-processing of experimental data. The author S. Peukert contributed quantum chemical calculations, discussion, and supervision. The authors T. Kasper, C. Schulz, and I. Wlokas contributed proof-reading and guidance.

8.1 Abstract

Tetramethylsilane (TMS) is a precursor for flame synthesis of silica (SiO₂) nanoparticles. A chemical reaction mechanism was developed for the oxidation of TMS in a lean low-pressure ($p \approx 30$ mbar) H₂/O₂/Ar flame using species mole fractions, obtained from molecular-beam mass spectrometry (MBMS) measurements in a matrix-supported flat flame doped with 600 ppm TMS. The thermodynamic data of Si-containing species were determined from quantum-chemical calculations at the G4 level of theory. The formation and subsequent consumption of Si(OH)₄, one of the main products of TMS oxidation, and the formation of Si₄O₁₀H₄

clusters are hypothesized to be the primary pathway in the synthesis of silica nanoparticles. The reaction rate coefficients are either estimated via an algorithmic optimization procedure or are assumed based on analogies to similar reactions in the literature. The mechanism was further validated based on MBMS measurements with the same base flame doped with 400 and 800 ppm TMS.

8.2 Introduction

The importance of gas-phase nanoparticle synthesis by thermal decomposition of vapor-phase precursor compounds has motivated many experimental studies and numerical simulations with the goal to understand the underlying molecular and particle-forming processes [216, 21, 28]. Many studies on the Si/H/O system were conducted on SiH₄ combustion: Lindackers et al. [217] investigated low-pressure H₂/O₂/Ar flat flames doped with SiH₄. Britten et al. [168] developed a mechanism of 70 elementary reactions and 25 species for SiH₄ combustion. Besides SiH₄, other silicon-containing species were investigated in the context of materials synthesis. Shekar et al. [31] developed a kinetics mechanism that can be applied for numerical simulations of flames doped with tetraethylorthosilicate (TEOS). A detailed kinetics model of the thermal pyrolysis of TEOS was proposed by Nurkowski et al. [33]. In their model, possible pathways for TEOS decomposition were suggested based on analogies to ethanol combustion and, also in analogy to the ethanol high-temperature chemistry, a set of rate rules describing the decomposition of –OC₂H₅ moieties in TEOS has been derived. In addition, Nurkowski et al. [34] provided a skeletal mechanism for TEOS oxidation in H₂/O₂ flames. Recently, Chen et al. [218] described a detailed reaction mechanism for the oxidation of octamethylcyclotetrasiloxane (OMCTS).

Besides the radical-assisted oxidation in synthesis flames, precursor decomposition kinetics have also been investigated under pyrolytic conditions: Sela et al. [75] investigated the decomposition of tetramethylsilane (Si(CH₃)₄; TMS) and tetramethoxysilane (TMOS) behind reflected shock waves and derived elementary kinetics mechanisms [76]. In particular, TMS pyrolysis has been previously studied, e.g., by Baldwin et al. [78], Clifford et al. [79], and Taylor and Milazzo [80]. In all these studies, a combination of a flow reactor with gas chromatography was used to detect major stable reaction products. Under pyrolytic conditions, for example in chemical vapor deposition (CVD) reactors, TMS is also used as a precursor for the production of SiC films and particles and it has the advantage to be a safe, non-explosive and non-corrosive precursor [74].

TMS can be employed as precursor for the production of silica nanoparticles in flames. In a counter-flow diffusion flame, Zachariah and Semerjian [28] investigated the influence

of SiH₄, hexamethyldisiloxane (HMDSO), and TMS on the growth of silica particles and found that particle formation from TMS and HMDSO starts to occur later and at higher temperatures than from SiH₄. In another recent study on HMDSO- and TMS-doped flames, Chrystie et al. [72] studied the influence of the precursor on the gas-phase reactions before the formation of silica nanoparticles with focus on SiO-based chemistry. They measured temperature fields in the flame and quantitative SiO mole-fraction profiles [73, 72] along the height above the burner (HAB) via laser-induced fluorescence (LIF) imaging using NO and SiO as target species. They observed a double-peak behavior of SiO profiles, which was also reported by Zachariah and Burgess Jr [70], Glumac [71] and Feroughi et al. [69].

Despite the large interest in silica-nanoparticle synthesis from the oxidation of silanes, few studies have proposed detailed reaction mechanisms for the combustion of silanes. In many previous investigations, global reaction models or possible reaction pathways, without providing reaction rates and thermochemical species data, have been reported.

The first attempt to analyze the high-temperature combustion chemistry of TMS was undertaken by Reed [77], who used the TMS pyrolysis reaction scheme reported by Baldwin et al. [78] as a basis for developing a reaction model for TMS oxidation.

Recently, Karakaya et al. [81] proposed a possible decomposition pathway of TMS in a H₂/O₂/Ar flame and discussed the formation of stable monomers and the first smaller silicon oxide clusters based on their experimental observations. They conducted molecular-beam mass-spectrometry (MBMS) measurements on a premixed laminar low-pressure flame to detect Si-C-O-H- and Si-O-H-containing molecules as well as small hydrocarbons. Changes of mole fraction were observed along the HAB. Their quantitative measurements of temperature and species mole-fraction profiles are a stepping stone to the development of a kinetics mechanism. However, due to the unknown thermodynamic properties of many intermediate species and unknown reaction rates, it was not possible to test the performance of the postulated reaction pathways of TMS proposed by Karakaya et al. [81]. This is one example that emphasizes the need to obtain thermodynamic data for silanes and siloxanes as well as theoretical calculations of reaction rates to facilitate reaction mechanism development.

In this work, we propose a more detailed kinetics model for the oxidation of TMS, which is developed based on species mole-fraction profiles obtained during MBMS measurements in low-pressure flames. The possible reaction pathways between crucial intermediates are discussed. Rate coefficients of important reactions are estimated by means of optimizing our kinetics model against quantitative mole-fraction profiles, analogies to similar reactions in hydrocarbon chemistry, and theoretical calculations. In addition, the thermochemical data of many intermediate species during oxidation of TMS are also calculated for the first time. To better understand the structure of the mechanisms discussed in this work, reaction-path

Table 8.1 Summary of flame conditions in the present work. Flow rates are in standard liter per minute (273.15 K, 1013.25 mbar).

Flame	H ₂ /slm	O ₂ /slm	Ar/slm	ϕ	Pressure/mbar	TMS (ppm)	Ref.
A	0.545	0.455	1	0.6	30	0	Karakaya
B	0.545	0.455	1	0.6	30	600	Karakaya
C	0.545	0.455	1	0.6	30	400	This work
D	0.545	0.455	1	0.6	30	800	This work

analyses were carried out. Lastly, the developed mechanism is further validated through comparing predicted species profiles with experimental data from MBMS measurements in low-pressure H₂/O₂/Ar flames doped with 400 and 800 ppm TMS.

8.3 Experiment

The formation and depletion of selected reaction products of TMS combustion (e.g., SiO₂, CO₂, CO, CH₄) was investigated in laminar H₂/O₂/Ar low-pressure flat flames by MBMS. Details on the experiment, the data analysis, and uncertainties of the mole fractions can be found in Karakaya et al. [81] and only a brief description is given here: All flames were stabilized on a 36 mm diameter sintered bronze burner installed in a low-pressure reactor at 30±0.03 mbar. At various HAB, gas samples were taken from the flame along the center line of the burner through a quartz nozzle. The distance between burner matrix and nozzle was varied in a range of zero to 100 mm HAB. The chemical composition of the samples changes only in the axial direction.

The flame conditions of the present work are shown in Table 1. The change in the base flame's equivalence ratio due to doped amount of precursor is neglected. The errors for the reported mole fractions depend on the calibration procedure and range between 15% for major species, 30-60% for most hydrocarbon intermediates and TMS, and a factor of two for silicon-containing intermediates.

Flame temperature measurements close to the sampling probe were conducted with an aluminum oxide coated thermocouple (type S) with a thickness of $r = 200 \mu\text{m}$. A radiation correction for heat losses of the thermocouple is performed by the method described by Bahlawane et al. [219]. The uncertainty of the temperature measurement is evaluated to ± 100 K. Additionally, the temperature dependence of the argon signal (referred to as FKT function) is evaluated to get the relative perturbed temperature profile as described by Cool et al. [220] and Struckmeier et al. [221]. This temperature profile includes the influence of the nozzle on the flame temperature and will be used for the simulations of flame A–D.

8.4 Modeling approach

One-dimensional flames and their structures are popular targets for modeling studies to validate chemical kinetics reaction mechanisms. Considering detailed kinetics in 2D or 3D simulations of reactive flows significantly increases the computational cost and the complexity of the simulations. The experimental data, which were modeled in this study, were determined in a flat burner-stabilized flame, which provides a nearly one-dimensional flame structure for the region close to the burner surface.

In this work, temperature profiles of the low-pressure flames (flames C and D) are determined. Before their use in modeling, the temperature data were smoothed. During the optimization procedure, the laminar premixed flame was simulated with the prescribed temperature profile.

For developing a kinetics model for the oxidation of TMS, we first attempted to identify the major pathways that connect the precursor with the final products. Then we calculated thermochemical data, i.e., heat capacities, enthalpies of formation, and entropies, of Si-C-O-H-containing species. These thermochemical data were expressed in the format of NASA polynomials. Finally, we determined rate coefficients, either by analogy to hydrocarbon chemistry, by RRKM (Rice-Ramsperger-Kassel-Marcus) calculations or by optimization of the kinetics model against experimental data. The RRKM calculations were carried out with the KiSTheLP code [134]. The Lennard-Jones potential parameters were estimated for the Si-containing species using the rules in Eqs. (8.1) and (8.2). The well-depth ε is the maximum energy of attraction between a pair of molecules and the collision diameter σ is the distance at which the intermolecular potential between the two molecules is zero. The volume-increments V_i for Si, H, CH₃, OH, CH₂, and O are 29.7, 2.8, 19.6, 9.7, 16.5, and 6.0 Å³, respectively [92, 93].

$$\varepsilon[K] = 1.2T_b \quad (8.1)$$

$$\sigma[\text{\AA}] = 1.45 \left(\sum_{i=1}^n V_i \right)^{1/3} \quad (8.2)$$

In Eq. (8.1), T_b is the boiling point of the corresponding species.

8.5 Calculation of thermodynamic data

The required thermodynamic data of the species and intermediates involved in the reaction mechanism were determined from quantum-chemical calculations at the G4 level of theory using the GAUSSIAN 09 package [188, 136]. Standard enthalpies of formation were calculated using the atomization-energy method. In this method, the standard enthalpy of formation at 0 K is obtained as the difference between the *ab initio* calculated (ai) atomization enthalpy of a compound and the experimentally determined enthalpy of formation of the gaseous atom:

$$\begin{aligned} \Delta H_f^\circ(0 \text{ K}, \text{Si}_a \text{C}_b \text{H}_c \text{O}_d) = & a\Delta H_{f, \text{gas,exp}}^\circ(0 \text{ K}, \text{Si}) + b\Delta H_{f, \text{gas,exp}}^\circ(0 \text{ K}, \text{C}) \\ & + c\Delta H_{f, \text{gas,exp}}^\circ(0 \text{ K}, \text{H}) + d\Delta H_{f, \text{gas,exp}}^\circ(0 \text{ K}, \text{O}) - [aH_{\text{ai}}^\circ(0 \text{ K}, \text{Si}) + bH_{\text{ai}}^\circ(0 \text{ K}, \text{C}) \\ & + cH_{\text{ai}}^\circ(0 \text{ K}, \text{H}) + dH_{\text{ai}}^\circ(0 \text{ K}, \text{O}) - H_{\text{ai}}^\circ(0 \text{ K}, \text{Si}_a \text{C}_b \text{H}_c \text{O}_d)] \quad (8.3) \end{aligned}$$

In Eq. 8.3, $\Delta H_f^\circ(0 \text{ K}, \text{Si}) = 446.2 \text{ kJ/mol}$, $\Delta H_f^\circ(0 \text{ K}, \text{O}) = 246.8 \text{ kJ/mol}$, $\Delta H_f^\circ(0 \text{ K}, \text{C}) = 711.5 \text{ kJ/mol}$, and $\Delta H_f^\circ(0 \text{ K}, \text{H}) = 216.1 \text{ kJ/mol}$ [108]. By applying enthalpy corrections to $\Delta H_f^\circ(0 \text{ K})$, standard enthalpies of formation at 298 K, ΔH_f° , are calculated [137].

Simmie and Sheahan [222] reported that among the most common composite methods, CBS-QB3, CBS-APNO, G3 and G4, the G4 approach is the most accurate one for calculating enthalpies of formation via the atomization procedure. The results of our previous works, in which a numerical method for deriving group additivity values for Si–C–H-containing species was presented [7], suggests that this conclusion also applies for silicon-organic compounds. Consequently, the G4 method was used in this work for obtaining thermodynamic data for silicon organic molecules.

8.6 Reaction mechanism optimization

For all one-dimensional flame simulations in this paper, the devised TMS oxidation kinetics model is merged with the C1 mechanism from Li et al. [5]. The resulting mechanism was optimized against the experimental data with a genetic algorithm-based method; details of the optimization process can be found in the work by Sikalo et al. [4] and Sikalo et al. [150]. The optimization technique aims at finding improved reaction rate coefficients that minimize the error between the reaction mechanism and the reference data. In other words, the optimization alters the three Arrhenius parameters until the reaction mechanism predicts the reference data. In principle, predefined uncertainty ranges for each reaction in the mechanism can be considered for the optimization, but the elementary reactions of the

C1 hydrocarbon mechanism and the initial TMS oxidation steps, i.e. H-atom abstractions from TMS, were protected against the optimization algorithm.

For most of the reactions in the mechanism in Table 3, however, no uncertainty ranges are available, since none of these secondary reactions have been studied in detail by laboratory experiments or kinetics theories. The rate coefficients are estimated in such a way that the experimental data can be reproduced by the kinetics model. During the optimization procedure, the burner-stabilized flame model within the library of one-dimensional reacting flow models implemented in Cantera [163] is used for the evaluation of the deviation between experiment and simulation. Convergence can be achieved more easily if reasonable initial values of key rate coefficients are provided because the optimization technique allows only small changes during each iteration step. Therefore, initial estimates are used that are based on RRKM calculations, reaction analogies, experiments, or theory reported in literature. The activation energies (E_a/R) in the current mechanism were rounded to a precision of 1 K.

While reaction mechanisms for hydrocarbons are developed and iteratively improved based on a large body of experimental and theoretical data as well as experience with the reaction patterns of these molecules, such data and experience are simply not available to the same extent for TMS-based nanoparticle synthesis. The goal of this work is to develop an initial mechanism that represents the available data, even if the errors in the estimated rate coefficients could be high because the optimization procedure is not well constrained by a wide variation of validation experiments, experimental and theoretical rate coefficients, etc. The mechanisms and the simulations performed with this mechanism will help to identify promising targets for future experimental and theoretical investigations, which in turn will provide the necessary constraints and allow the gradual improvement of the reaction mechanism with respect to physical and chemical correctness.

8.7 Results and discussions

8.7.1 Thermodynamics data

Based on the molecular properties (molecular structures, frequencies and moments of inertia) obtained from the quantum chemical calculations, thermodynamic data $C_p(T)$, $H_f(T)$ and $S(T)$ were derived by using the GPOP program [170]. The vibrational frequencies calculated at the B3LYP/6-31G(2df,p) level of theory during the G4 procedure were scaled by 0.99 for the zero point energy calculation and by 0.97 for the vibrational partition function calculations [188]. Internal rotations around the bonds of CH₃ and OH groups attached to carbon and/or silicon atoms were treated as hindered rotations using the Pitzer-Gwinn approximation as

implemented in GPOP [190]. Rotational barrier heights for CH₃ and OH rotors were obtained from relaxed potential energy surface (PES) scans at the B3LYP/6-31G(2df,p) level of theory with dihedral angles used as coordinates for the scans. Fig. 8.1 shows an example for PES-scans of a CH₃ and OH moiety to obtain the barrier heights V_0 .

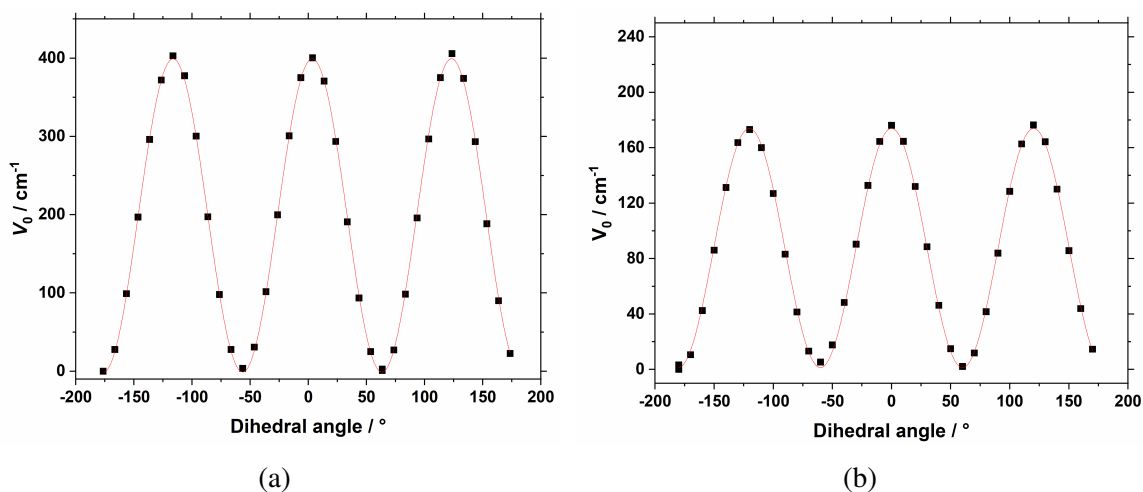


Fig. 8.1 Potentials of CH₃ (left) and OH rotors in trimethyl-silanol (Si(CH₃)₃OH) with maxima at 400 and 175 cm^{-1} .

It is difficult to assess the quality of the thermodynamic data due to the lack of experimental reference data. To develop group-additivity values for silicon-organic molecules containing Si, C, and H atoms, we have also calculated thermodynamic data for selected silanes. For these compounds, good agreement with available experimental thermodynamic data was obtained: The calculated values of ΔH_f° for SiH₄, Si₂H₆, Si₃H₈, and Si(CH₃)₄ are 28.0, 70.6, 106.1, and -237.9 kJ/mol, respectively. The corresponding experimental values are 34.1 [108], 71.5 [171], 108.4 [172], and -233.2 kJ/mol, respectively [173]. The deviations between calculated and experimental values are on average below 8.0 kJ/mol but it is more realistic to assume larger uncertainties regarding the thermochemical data of silicon-organic compounds than of hydrocarbon compounds. For sila-isobutene ((CH₃)₂SiCH₂), the G4-calculation gives $\Delta H_f^\circ = 60.7$ kJ/mol. Available experimental values are 20.9 [173], 36.0 [195], and 64.8 kJ/mol [223]. Allendorf et al. [204] calculated thermodynamic data for a series of different silicon-organic compounds and they obtained a value of 51.5 kJ/mol. For trimethylsilanol (Si(CH₃)₃OH), ΔH_f° calculated is -493.1 kJ/mol. The recommended reference value of ΔH_f° for this compound is reported to be -499.5 kJ/mol [173]. For the other silanols and corresponding radicals, it is not possible to clearly assess the error in calculated enthalpies of formation due to the lack of available experimental data. Table 8.2 lists the species, for which thermodynamic properties were calculated in the present work.

Table 8.2 Standard enthalpies of formation predicted by the G4-method.

Species	$\Delta H_f^\circ / (\text{kJ/mol})$	Species	$\Delta H_f^\circ / (\text{kJ/mol})$
$(\text{CH}_3)_2\text{SiCH}_2$	60.7	$\text{Si}(\text{CH}_3)_2\text{OH}$	-248.9
$(\text{CH}_3)_3\text{SiCH}_2$	-21.2	$\text{Si}(\text{CH}_3)\text{CH}_2\text{OH}$	-203.7
$\text{Si}(\text{CH}_3)_3$	24.1	TMS	-219.3
$\text{Si}(\text{CH}_3)_2$	136.9	$\text{Si}(\text{CH}_3)_2\text{O}$	-255.2
$\text{Si}(\text{CH}_3)$	301.1	$\text{Si}(\text{CH}_3)_2(\text{OH})_2$	-773.6
$\text{Si}(\text{CH}_3)_3\text{OH}$	-493.1	$\text{OSi}(\text{CH}_3)_3$	-219.2
$\text{Si}(\text{OH})_4$	-1345.6	$\text{OSi}(\text{OH})_2$	-811.2
$\text{Si}(\text{OH})_3$	-799.2	$\text{HSiO}(\text{OH})$	-471.1
$\text{Si}(\text{OH})_2$	-503.4	$(\text{CH}_3)_3\text{SiCH}_2\text{O}_2$	-143.5
$\text{Si}(\text{CH}_3)(\text{OH})_3$	-1062.5	$\text{Si}_4\text{O}_{10}\text{H}_4(\text{linear})$	-3599.5
$\text{Si}(\text{CH}_3)(\text{OH})_2$	-520.8	$(\text{CH}_3)_2\text{Si}(\text{CH}_2)(\text{OH})$	-293.9
$(\text{CH}_3)(\text{OH})\text{SiCH}_2$	-220.5	$(\text{CH}_3)\text{Si}(\text{CH}_2)(\text{OH})_2$	-574.4
$(\text{OH})_2\text{SiCH}_2$	-461.1	$(\text{CH}_3)\text{SiO}$	-100.4

Even though the uncertainties of calculated species cannot be reported because accurate experimental reference data are not available, the sensitivity of the simulations to the enthalpies of formation can be tested. A set of simulations is performed, in which the standard enthalpies of formation of TMS, $(\text{CH}_3)_3\text{SiCH}_2\text{O}_2$, $\text{OSi}(\text{CH}_3)_3$, and $(\text{CH}_3)_3\text{SiCH}_2$ were changed by ± 4.2 kJ/mol. The results are shown in the supplementary material. It can be seen that the modelling is not very sensitive to the ± 4.2 kJ/mol change of standard enthalpies of formation as one of the important thermodynamic properties.

8.7.2 Kinetics model

Figure 8.2 shows simulated and measured mole-fraction profiles of major species in an undoped $\text{H}_2/\text{O}_2/\text{Ar}$ flame (flame A). For sake of comparison, the predictions of three different reaction mechanisms are shown in comparison to the experimental profiles: The low-pressure lean $\text{H}_2/\text{O}_2/\text{Ar}$ flame was simulated with the hydrogen-combustion mechanism by Ó Conaire et al. [224], the C1 combustion mechanism by Li et al. [163], and the hydrogen and syngas combustion mechanism by Varga et al. [225]. The measured temperature profile of the undoped base flame is used as an input for the simulation. The slight deviations close to the burner surface can originate from the nozzle effect on the flame [221]. The simulated profiles using all three reaction mechanisms agree well with each other and thus the reaction mechanism of Li et al. [163] was chosen as base mechanism. The colored areas in Fig. 8.2 and the other figures containing measured mole-fraction data, represent experimental uncertainty ranges.

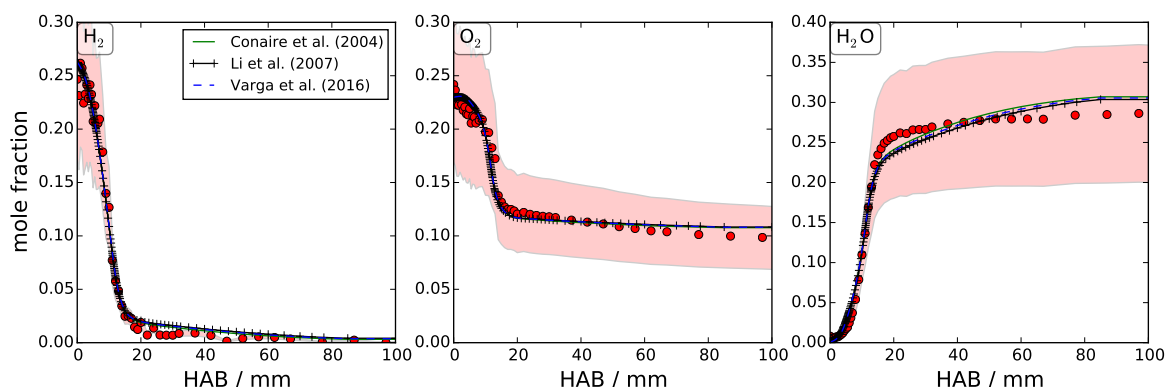


Fig. 8.2 Mole-fraction profiles of the major species along the as a function of height above burner (HAB) in flame A. The points are experimental data and the curved lines are the simulation results. The colored area shows the uncertainty range of the measured data.

Figure 8.3 shows the measured and calculated mole-fraction profiles of the major species O_2 , H_2 , H_2O , CO , and CO_2 in the flame doped with 600 ppm TMS (flame B) as well as the measured temperature profile of the doped flame, which is prescribed in the simulations.

For the simulations shown in Fig. 8.3 and the figures appearing thereafter (except Fig. 8.4), the reaction mechanism in Table 8.3 for TMS oxidation chemistry is merged with the C1 mechanism from Li et al. [163]. Table 8.3 includes the reactions related to TMS combustion and formation of silica clusters.

The simulations reproduce the experimental profiles quite well, but the deviation near the burner surface must be due to high diffusion rates in the flame that are not captured in the simulation. The error of the temperature measurement is ± 100 K. To consider the possible uncertainty of the temperature measurements, the experimental temperature profile is shifted 100 K up and down and the simulations are repeated. Figure 8.3 shows the effect of the assumed temperature on the predicted mole fractions of major species. It can be seen that temperature uncertainties within ± 100 K result in a shift of the calculated mole-fraction profiles along HAB, but altogether, the shape of the calculated profiles is not changed. Calculated mole fractions of Si-containing species are also sensitive to the prescribed temperature.

For the development of a TMS mechanism, the measured temperature is used. Considering the mole fraction data, the overall uncertainties are estimated to be ± 10 -30%. The uncertainty in measured temperatures also translates into an uncertainty in optimized rate coefficients. For most rate coefficients, a temperature error of ± 100 K leads to an increase/decrease by approximately a factor of two. For three rate coefficients, those of reactions R12, R20, and R26, the resulting uncertainties are substantially larger: In case of k_{12} and k_{26} , this temperature error results in an increase/decrease of around +300%

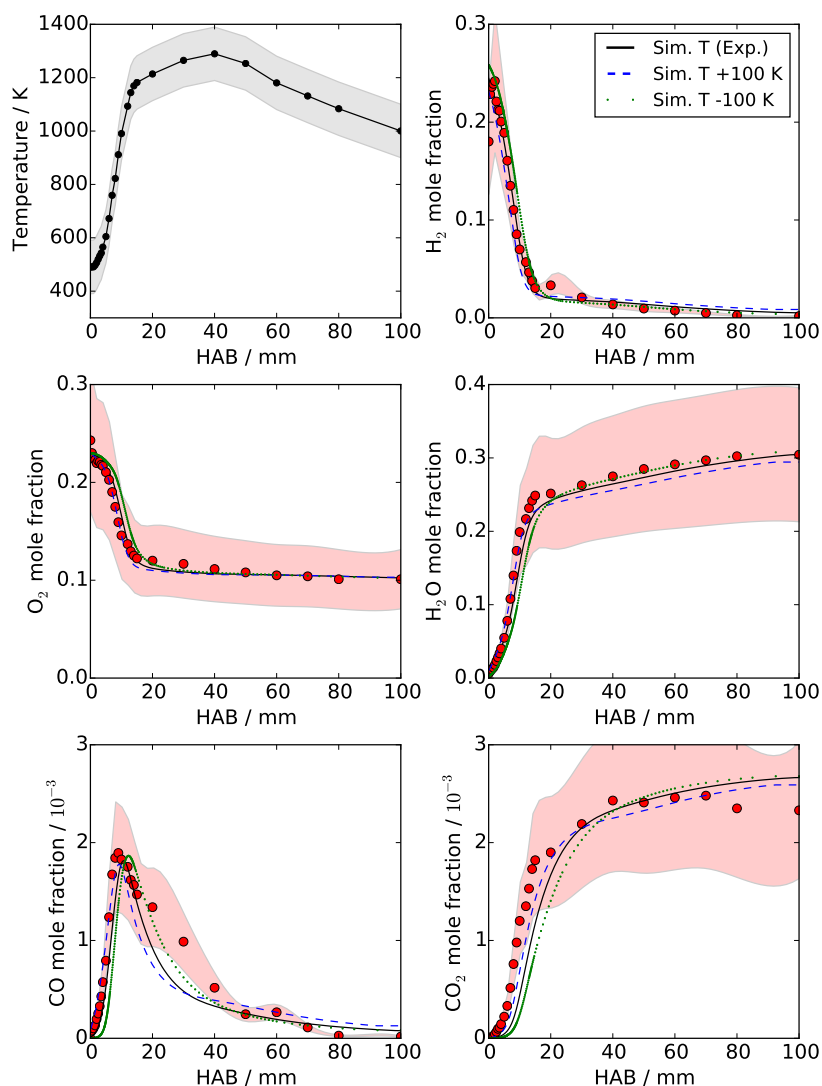


Fig. 8.3 Sensitivity of major species' mole fractions on the measured temperature; simulations are performed with experimental temperature, shifted +100 K up, and shifted -100 K down. The colored areas represent the uncertainties of mole-fraction and temperature measurements. Symbols: experiment; lines: simulations.

and -80%, respectively. The largest temperature sensitivity is observed for k_{20} , where we get an increase/decrease of around +550% and -90%, respectively. The reason for these pronounced temperature sensitivities are the higher activation energies of these three reactions in comparison to the other optimized reaction rate constants.

Figure 8.4 shows the measured and calculated mole-fraction profiles of CH_4 . One essential factor that influences the prediction of CH_4 is related to the mechanism, which is used for modeling the reactions of small hydrocarbons. When merging the TMS kinetics

Table 8.3 List of reactions for describing TMS oxidation. Units of $k = AT^b \exp(-E_a/RT)$ are cm, s, mol, and K. As described in the text: Simulations were carried out using global reactions 14, 18, and 19. Reactions 14a-e, 18a-f, and 19a-e are suggested to explain the underlying chemistry behind these global processes and are discussed in the text. Also reactions 21 and 25-28 are global reactions. $\text{Si}_2(\text{OH})_8$ is envisioned as a hydrogen-bonded adduct of two $\text{Si}(\text{OH})_4$ molecules.

No.	Reaction	A	b	E_a/R	Ref.
1	$\text{TMS} + \text{OH} = \text{H}_2\text{O} + (\text{CH}_3)_3\text{SiCH}_2$	1.48E + 05	2.56	162	This work
2	$\text{TMS} + \text{H} = \text{H}_2 + (\text{CH}_3)_3\text{SiCH}_2$	4.97E + 06	2.40	3101	[226]
3	$\text{TMS} + \text{O} = \text{OH} + (\text{CH}_3)_3\text{SiCH}_2$	2.50E + 06	2.50	2720	This work
4	$\text{TMS} + \text{O}_2 = \text{HO}_2 + (\text{CH}_3)_3\text{SiCH}_2$	3.98E + 11	0.00	25136	[77]
5	$\text{TMS} + \text{HO}_2 = \text{H}_2\text{O}_2 + (\text{CH}_3)_3\text{SiCH}_2$	1.00E + 13	0.00	9742	[77]
6	$(\text{CH}_3)_3\text{SiCH}_2 + \text{O}_2 = (\text{CH}_3)_3\text{SiCH}_2\text{O}_2$	5.00E + 12	0.00	4026	This work
7	$(\text{CH}_3)_3\text{SiCH}_2 = (\text{CH}_3)_2\text{SiCH}_2 + \text{CH}_3$	1.00E + 15	0.00	26580	This work
8	$(\text{CH}_3)_2\text{SiCH}_2 + \text{H} = \text{Si}(\text{CH}_3)_3$	1.06E + 12	0.51	620	This work
9	$\text{Si}(\text{CH}_3)_3 + \text{OH} = \text{Si}(\text{CH}_3)_3\text{OH}$	6.00E + 13	0.00	0	This work
10	$\text{Si}(\text{CH}_3)_3\text{OH} = (\text{CH}_3)_2\text{SiCH}_2 + \text{H}_2\text{O}$	1.84E + 12	0.37	36142	This work
11	$\text{Si}(\text{CH}_3)_3\text{OH} = \text{CH}_4 + \text{Si}(\text{CH}_3)_2\text{O}$	1.59E + 21	-2.3	32934	This work
12	$(\text{CH}_3)_3\text{SiCH}_2\text{O}_2 = \text{OSi}(\text{CH}_3)_3 + \text{CH}_2\text{O}$	1.40E + 12	0.00	10064	This work
13	$\text{OSi}(\text{CH}_3)_3 + \text{H}_2 = \text{Si}(\text{CH}_3)_3\text{OH} + \text{H}$	4.70E + 12	0.00	2617	This work
14	$\text{OSi}(\text{CH}_3)_3 + \text{M} \rightarrow 3 \text{CH}_3 + \text{SiO} + \text{M}$	1.20E + 13	0.00	4026	This work
14a	$\text{OSi}(\text{CH}_3)_3 = \text{Si}(\text{CH}_3)_2\text{O} + \text{CH}_3$	1.00E + 15	0.00	26580	This work
14b	$(\text{CH}_3)_2\text{SiCH}_2 + \text{O}_2 = \text{Si}(\text{CH}_3)_2\text{O} + \text{CH}_2\text{O}$	5.29E + 11	0.00	1804	[206]
14c	$\text{Si}(\text{CH}_3)_2\text{O} = (\text{CH}_3)\text{SiO} + \text{CH}_3$	1.93E + 76	-18.26	53265	This work
14d	$(\text{CH}_3)\text{SiO} = \text{CH}_3 + \text{SiO}$	3.00E + 12	0.00	33796	[218]
14e	$\text{Si}(\text{CH}_3)_2\text{O} = (\text{CH}_3)(\text{OH})\text{SiCH}_2$	5.33E + 27	-4.56	30450	This work
15	$\text{SiO} + \text{O}_2 = \text{SiO}_2 + \text{O}$	1.00E + 10	0.80	3249	[218]
16	$\text{SiO} + \text{OH} = \text{H} + \text{SiO}_2$	1.00E + 09	0.80	755	[218]
17	$\text{SiO} + \text{O} + \text{M} = \text{SiO}_2 + \text{M}$	2.5E + 12	0.00	2166	[218]
18	$\text{Si}(\text{CH}_3)_3\text{OH} + \text{OH} \rightarrow \text{Si}(\text{CH}_3)_2(\text{OH})_2 + \text{CH}_3$	1.60E + 08	2.65	2094	This work
18a	$\text{Si}(\text{CH}_3)_3\text{OH} + \text{H} = (\text{CH}_3)_2\text{Si}(\text{CH}_2)(\text{OH}) + \text{H}_2$	4.97E + 07	2.65	3101	This work
18b	$\text{Si}(\text{CH}_3)_3\text{OH} + \text{OH} = (\text{CH}_3)_2\text{Si}(\text{CH}_2)(\text{OH}) + \text{H}_2\text{O}$	1.48E + 05	2.56	162	This work
18c	$\text{Si}(\text{CH}_3)_3\text{OH} + \text{O} = (\text{CH}_3)_2\text{Si}(\text{CH}_2)(\text{OH}) + \text{OH}$	2.50E + 07	2.50	2720	This work
18d	$(\text{CH}_3)_2\text{Si}(\text{CH}_2)(\text{OH}) = (\text{CH}_3)(\text{OH})\text{SiCH}_2 + \text{CH}_3$	1.00E + 15	0.00	26580	This work
18e	$(\text{CH}_3)(\text{OH})\text{SiCH}_2 + \text{H}_2\text{O} = \text{Si}(\text{CH}_3)_2(\text{OH})_2$	3.60E + 09	0.43	3869	This work
18f	$\text{OSi}(\text{CH}_3)_3 = (\text{CH}_3)_2\text{Si}(\text{CH}_2)(\text{OH})$	1.00E + 13	0.00	10824	[77]
19	$\text{Si}(\text{CH}_3)_2(\text{OH})_2 + \text{OH} \rightarrow \text{Si}(\text{CH}_3)(\text{OH})_3 + \text{CH}_3$	1.70E + 08	2.65	4107	This work
19a	$\text{Si}(\text{CH}_3)_2(\text{OH})_2 + \text{H} = (\text{CH}_3)\text{Si}(\text{CH}_2)(\text{OH})_2 + \text{H}_2$	5.74E + 06	2.38	3583	This work
19b	$\text{Si}(\text{CH}_3)_2(\text{OH})_2 + \text{OH} = (\text{CH}_3)\text{Si}(\text{CH}_2)(\text{OH})_2 + \text{H}_2\text{O}$	1.48E + 05	2.56	162	This work
19c	$\text{Si}(\text{CH}_3)_2(\text{OH})_2 + \text{O} = (\text{CH}_3)\text{Si}(\text{CH}_2)(\text{OH})_2 + \text{OH}$	2.50E + 06	2.50	2720	This work
19d	$(\text{CH}_3)\text{Si}(\text{CH}_2)(\text{OH})_2 = (\text{OH})_2\text{SiCH}_2 + \text{CH}_3$	1.00E + 15	0.00	26580	This work
19e	$(\text{OH})_2\text{SiCH}_2 + \text{H}_2\text{O} = \text{Si}(\text{CH}_3)(\text{OH})_3$	3.60E + 09	0.43	3869	This work
20	$\text{Si}(\text{CH}_3)(\text{OH})_3 \rightarrow \text{CH}_3 + \text{Si}(\text{OH})_3$	1.00E + 15	0.00	13496	This work
21	$\text{Si}(\text{OH})_3 + \text{OH} = 0.5 \text{Si}_2(\text{OH})_8$	3.50E + 16	0.00	4277	This work
22	$\text{Si}(\text{OH})_3 + \text{OH} \rightarrow \text{Si}(\text{OH})_4$	2.60E + 14	0.00	3372	This work
23	$\text{SiO}_2 + \text{H}_2\text{O} \rightarrow \text{OSi}(\text{OH})_2$	1.31E + 10	0.00	4026	This work
24	$\text{OSi}(\text{OH})_2 + \text{H}_2\text{O} \rightarrow \text{Si}(\text{OH})_4$	1.17E + 13	0.00	0	This work
25	$\text{Si}_2(\text{OH})_8 \rightarrow 0.5 \text{Si}_4\text{O}_{10}\text{H}_4 + 3.0 \text{H}_2\text{O}$	4.89E + 05	0.00	12329	This work
26	$\text{Si}(\text{OH})_4 \rightarrow 0.25 \text{Si}_4\text{O}_{10}\text{H}_4 + 1.5 \text{H}_2\text{O}$	4.70E + 05	0.00	10165	This work
27	$\text{SiO} + (\text{SiO})_n \rightarrow (\text{SiO})_{n+1} \rightarrow \text{particles}$	8.70E + 14	1.93	4006	This work
28	$n \text{Si}_4\text{O}_{10}\text{H}_4 \rightarrow (\text{SiO}_2)_{4n}\text{O}_2\text{H}_4 + (2n-2) \text{H}_2\text{O} \rightarrow \text{particles}$	2.70E + 14	0.00	1258	This work

model with the C1-C3 mechanism by Ranzi et al. [6], the simulated mole fractions of CH_4 are within the experimental uncertainty range.

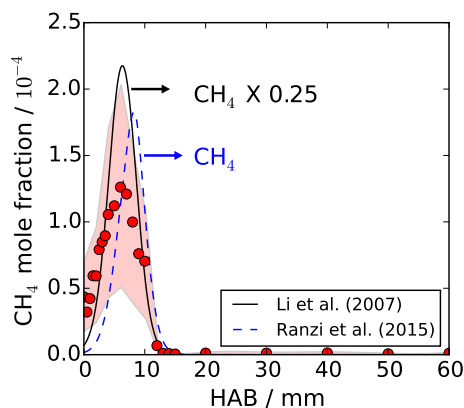


Fig. 8.4 Measured and calculated CH_4 mole-fraction profiles as a function of height above burner (HAB). The colored area represents the uncertainty range of the measurement. Simulations were performed with the C1-C3 mechanism of Ranzi et al. [6] (blue dashed line) and the C1 mechanism from Li et al. [5] (black line)

Another explanation for the over prediction of CH_4 is related to uncertainties in the underlying global reactions R14, R18, and R19, in which methyl radicals are assumed to be rapidly released by bond fissions. According to the present TMS mechanism, this fast release of CH_3 radicals leads to an over prediction of CH_4 . For clarification, all simulations were performed with global reactions R14, R18, and R19, instead of the elementary reactions R14a-e, R18a-f, and R19a-e (see Table 3) that are assumed to be behind the global reactions. For simulating mole fractions of Si-C-O-H-containing species, the present TMS oxidation model has been merged with the Li et al. [5] mechanism. Though the mechanism of Ranzi et al. [6] leads to a better prediction of the CH_4 mole fractions, we did not apply that mechanism for all simulations for the following reasons: First, the simulated mole fractions of Si-containing species are not affected by the hydrocarbon combustion model; second, the Ranzi et al. [6] mechanism is much larger than the Li et al. [5] mechanism. The Ranzi et al. [6] mechanism contains 107 species and more than 2600 reactions, whereas the Li et al. [5] mechanism includes only 19 species and less than 100 reactions which makes the simulations almost 12 times faster than those using the Ranzi et al. [6] mechanism. For the purpose of computational efficiency and since the simulations of Si-containing products and intermediates are not affected by the hydrocarbon combustion chemistry, the smaller mechanism was chosen. The mechanism of Ranzi et al. [6] predicts only the CH_4 mole-fraction profile better than Li et al. [5] mechanism and overall both mechanisms perform within the uncertainty ranges of the measurements. It can be concluded that the Si sub-

TMS is consumed completely at 8 mm HAB, at which the temperature rises up to 800 K, but according to the simulated mole-fraction profile, TMS is predicted to be completely consumed at 6 mm HAB. The simulated TMS profile shows a concave-up behavior in contrast to the concave-down behavior of the experiment. It is possible that the deviations are due to the probing effect which can affect the flame flow and temperature field. Hartlieb et al. [227] studied the effects of a sampling nozzle on the structure of a low-pressure flame. In addition, Deng et al. [83] investigated numerically perturbed laminar flames to enhance the interpretability of measurements obtained from mass spectrometry with molecular-beam sampling. It can be seen later in this work that the simulations predict the peak positions of Si-intermediates quite well which indicates that these profiles are less affected by sampling issues.

At the early stage, the depletion of TMS is initiated by H-atom abstractions through reactions with flame radicals OH, H, O, O₂, and HO₂, which are considered in our kinetics model in terms of reactions R1 to R5. The rate coefficients for R1 to R5 are taken either from literature or estimated based on analogies. The rate coefficients of the initial H-atom abstractions from TMS are not optimized in this work. At these temperatures, the primary step of the unimolecular TMS decomposition (a Si-C bond fission), is slow, i.e., $k < 10^{-3}\text{s}^{-1}$, and does not significantly contribute to its depletion. The consumption of TMS is caused in particular by the H-atom abstractions R1-R3. The rate coefficient for R1 is estimated by analogy to the reaction of OH + neopentane. The rate coefficients of this reaction were directly measured by Sivaramakrishnan et al. [228] by UV-absorption spectrometry behind reflected shock waves. For R2, the rate coefficient was taken from literature: Peukert et al. [226] conducted a shock-tube and modeling study on the reactions H + SiH₄ and H + TMS. They have shown that due to very similar C-H bond dissociation energies, TMS and the analog hydrocarbon, neo-pentane, have very similar reactivities towards H-atom abstractions. The rate coefficient of R3 is estimated in analogy to the reaction of O + neopentane calculated by Cohen and Westberg [229].

As a result of H-atom abstractions, (CH₃)₃SiCH₂ radicals are a primary Si-containing intermediate. They can either react with oxygen to form (CH₃)₃SiCH₂O₂ (R6) or they can dissociate to (CH₃)₂SiCH₂ by releasing CH₃ radicals (R7). The rate coefficient for R7 is estimated by analogy to Si(CH₃)₃ = Si(CH₃)₂ + CH₃ proposed by Sela et al. [75]. The (CH₃)₂SiCH₂ itself can further react with hydrogen to form Si(CH₃)₃ (R8). The rate coefficient for R8 is estimated by analogy to the reaction of H + iso-C₄H₈ calculated by Curran [230]. The peroxide species (CH₃)₃SiCH₂O₂ (or its isomers) has also been detected by Karakaya et al. [81] (Fig. 8.7). (CH₃)₃SiCH₂O₂ radicals in turn can decompose to OSi(CH₃)₃ and CH₂O (R12). The rate coefficients for R6 and R12 were initially taken from

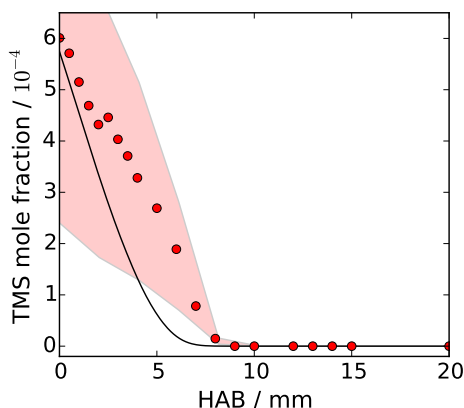


Fig. 8.6 Measured and calculated mole-fraction profiles for TMS in the flame B. The colored area shows the uncertainty range of the measurement. Symbols: experiment; line: simulation.

Davidson and Thompson [231] and optimized in such a way that the simulated profile of $(\text{CH}_3)_3\text{SiCH}_2\text{O}_2$ reproduces the measurement (Fig. 8.7).

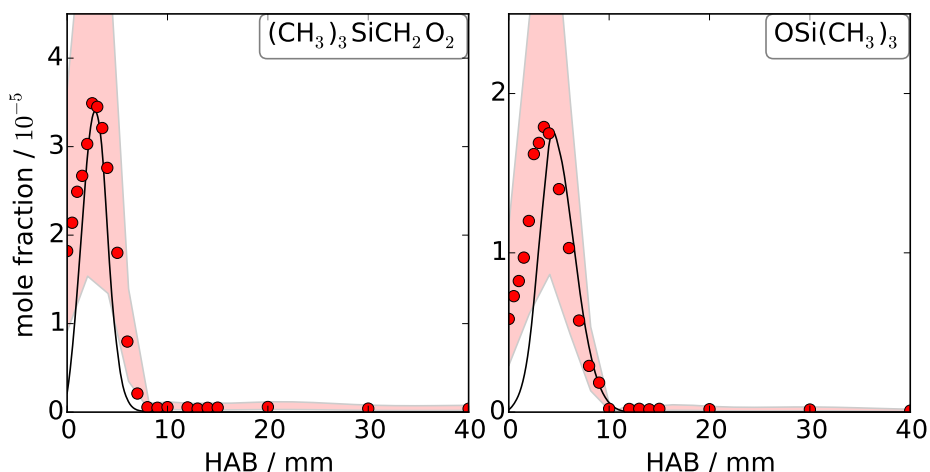


Fig. 8.7 Measured and simulated mole-fraction profiles of $(\text{CH}_3)_3\text{SiCH}_2\text{O}_2$ and $\text{OSi}(\text{CH}_3)_3$ as a function of HAB for Flame B. The colored area shows the uncertainty range of a factor of two for the measured data.

Figure 8.7 also shows measured and simulated $\text{OSi}(\text{CH}_3)_3$ profiles. The bimolecular reaction of $\text{OSi}(\text{CH}_3)_3$ and H_2 forms $\text{Si}(\text{CH}_3)_3\text{OH}$ (R13). Another possibility for $\text{OSi}(\text{CH}_3)_3$ consumption can be a stepwise release of CH_3 to form SiO . The rate coefficient for R14a is estimated by analogy to $\text{Si}(\text{CH}_3)_3 = \text{Si}(\text{CH}_3)_2 + \text{CH}_3$ proposed by Sela et al. [75]. The first Si–C bond fission from $\text{OSi}(\text{CH}_3)_3$ yields $\text{Si}(\text{CH}_3)_2\text{O}$, which is the Si-containing analog to acetone. In principle, this molecule is expected to be a stable species. $\text{Si}(\text{CH}_3)_2\text{O}$ itself can further decompose via Si–C bond fission or it can undergo tautomerization towards an enol.

With an energy barrier of 238.1 kJ/mol, the tautomerization $\text{Si}(\text{CH}_3)_2\text{O} = (\text{CH}_3)(\text{OH})\text{SiCH}_2$, with $(\text{CH}_3)(\text{OH})\text{SiCH}_2$ being the enol-form of the siloxane, is the energetically preferred process at low temperatures. The reverse reaction from the enol to the siloxane tautomer has a barrier height of 186.2 kJ/mol. These barrier heights were calculated using the G4 method and refer to $T = 0$ K and exclude zero-point energies. The equilibrium will be clearly on the side of the siloxane form $\text{Si}(\text{CH}_3)_2\text{O}$. Fig. 8.8 shows calculated rate coefficients of reactions R14c and R14e at $p = 30$ mbar over the 600–1200 K temperature range. Since argon is used as bath gas in the MBMS measurements, argon was also used as bath gas in these calculations. This procedure applies to all RRKM calculations reported in this work.

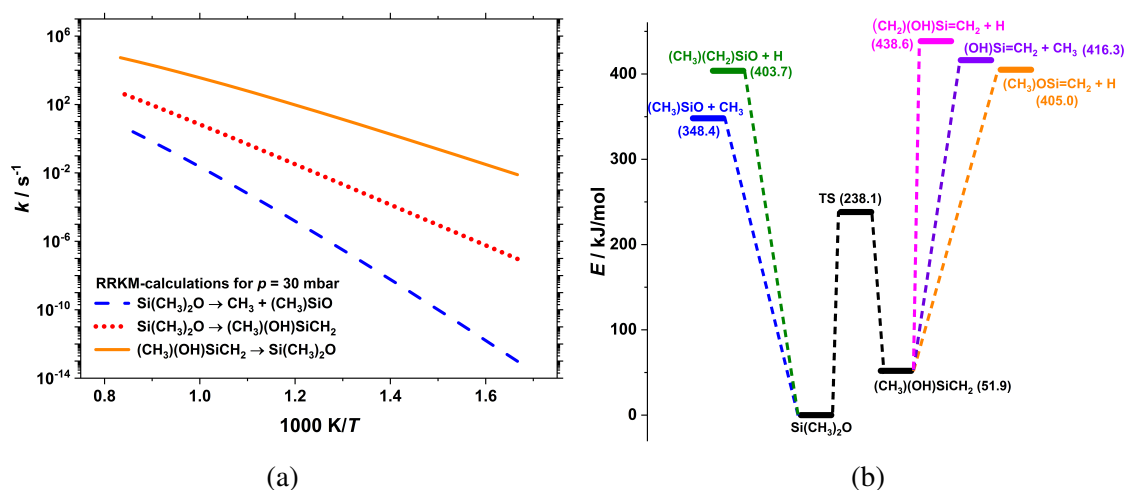


Fig. 8.8 a: RRKM calculations for reaction $\text{Si}(\text{CH}_3)_2\text{O} \rightarrow (\text{CH}_3)\text{SiO} + \text{CH}_3$, for tautomerization $\text{Si}(\text{CH}_3)_2\text{O} \rightarrow (\text{CH}_3)(\text{OH})\text{SiCH}_2$, and for the reverse process $(\text{CH}_3)(\text{OH})\text{SiCH}_2 \rightarrow \text{Si}(\text{CH}_3)_2\text{O}$. All calculations were carried out for 30 mbar and cover 600–1200 K; b: Relative stationary point energies (values in parentheses are relative to the energy of $\text{Si}(\text{CH}_3)_2\text{O}$) for the unimolecular reactions of $\text{Si}(\text{CH}_3)_2\text{O}$ calculated at the G4 level of theory (present work).

For calculating rate coefficients of the Si-C bond fission R14c, a RRKM Gorin model was applied [232, 233]. These reactions were also discussed by Karakaya et al. [81] and the theoretical rate coefficient data suggest that $\text{Si}(\text{CH}_3)_2\text{O}$ is primarily removed by Si-C bond fissions, since the equilibrium of the tautomerization process is on the side of $\text{Si}(\text{CH}_3)_2\text{O}$. Besides tautomerization, the enol form can also only decompose by bond fissions, which have bond dissociation energies above 335 kJ/mol (Fig. 8.8). In the low-pressure flame at temperatures below 1000 K, this unimolecular reaction should be negligible. The experimental evidence indicates that $\text{Si}(\text{CH}_3)_2\text{O}$, or an isomer with the same composition, is a reactive compound, even though it has not been observed in gas-phase studies before. To the best of our knowledge, it has only been detected by cryogenic infrared spectroscopy in an argon matrix

at temperatures around 12 K [234]. The reason for the high reactivity of $\text{Si}(\text{CH}_3)_2\text{O}$ remains unknown, but destruction by flame radicals may be a tentative explanation. The reactivity of this intermediate molecule may be regarded as an additional possible justification for assuming quite large rate coefficient values for the global reaction (R14). When we tried to use the sequence of reactions R14a-e, the genetic algorithm could not find optimized rate coefficients in such a way that it will be possible to simulate the experimental mole-fraction profiles of $\text{OSi}(\text{CH}_3)_3$ and of the subsequent products $\text{Si}(\text{OH})_x$ and SiO_2 . To circumvent the sequence of reactions R14a-e, the decomposition of the radical $\text{OSi}(\text{CH}_3)_3$ was written as a global reaction and led to successful optimization and simulation. These issues indicate that important pathways may be missing from the proposed mechanism but that the overall reaction sequence represented by reaction R14 is reasonable and in agreement with literature.

The global reaction $\text{OSi}(\text{CH}_3)_3 \rightarrow \text{SiO} + 3\text{CH}_3$ was considered in flame studies reported by Chagger et al. [68], Yeh et al. [235], and Ma et al. [236] on particle formation during HMDSO oxidation. The rate coefficient of the global reaction R14 is optimized to be able to reproduce the experimental $\text{OSi}(\text{CH}_3)_3$ mole-fraction profile. Similar to the intermediate $(\text{CH}_3)_3\text{SiCH}_2\text{O}_2$, the calculated peak and shape of $\text{OSi}(\text{CH}_3)_3$ are in a very good agreement with the measurement.

Experimental observations illustrate that $(\text{CH}_3)_2\text{SiOH}$, $(\text{CH}_3)\text{Si}(\text{OH})_2$, $\text{Si}(\text{OH})_3$, and $\text{Si}(\text{OH})_4$ are the most abundant species among the detected compounds. Karakaya et al. [81] proposed a series of reactions, which form $\text{Si}(\text{OH})_4$ starting from $\text{Si}(\text{CH}_3)_3\text{OH}$. One possibility consists in stepwise losses of methyl radicals and recombination of silyl with hydroxyl radicals. We also considered this as a possible pathway for $\text{Si}(\text{OH})_4$ formation, but with rate constants that are typical for C-C bond fissions of stable molecules as start values for an optimization procedure, the algorithm did not predict any significant formation of $\text{Si}(\text{OH})_4$.

Karakaya et al. provided another pathway to form $\text{Si}(\text{OH})_4$ by reaction of $\text{Si}(\text{CH}_3)_3\text{OH}$ with flame radicals H, O, and OH. They reported that due to high Si-C bond-dissociation energies of around 376 kJ/mol, these series of reactions R18a-f and R19a-e are more likely to happen. The rate coefficients for reaction of $\text{Si}(\text{CH}_3)_3\text{OH}$ with flame radicals H and OH and reaction of $\text{Si}(\text{CH}_3)_2(\text{OH})_2$ with H and OH are estimated again by analogy to reaction of TMS and neopentane with H and OH, respectively. Regarding $\text{Si}(\text{CH}_3)_3\text{OH}$, the calculated O-H bond-dissociation energy is 486.7 kJ/mol, and the calculated C-H bond-dissociation energy is 412.3 kJ/mol. Since bond-dissociation energies and reactivities towards H-atom abstraction correlate with each other, H-atom abstractions from the OH moieties of $\text{Si}(\text{CH}_3)_3\text{OH}$ and $\text{Si}(\text{CH}_3)_2(\text{OH})_2$ have not been considered. The rate coefficients of reactions of $\text{Si}(\text{CH}_3)_3\text{OH}$ and $\text{Si}(\text{CH}_3)_2(\text{OH})_2$ with O atoms are assumed to be analogue to the rate coefficients of

the O + neopentane abstraction, which were calculated by Cohen and Westberg [229] by transition-state theory. The rate coefficients of the unimolecular decomposition steps of $(\text{CH}_3)_2\text{Si}(\text{CH}_2)(\text{OH})$ and $(\text{CH}_3)\text{Si}(\text{CH}_2)(\text{OH})_2$ radicals to lose methyl groups are assumed based on analogy to $\text{Si}(\text{CH}_3)_3 = \text{Si}(\text{CH}_3)_2 + \text{CH}_3$ [75]. The rate coefficients of the hydration steps (18e and 19e) to form $\text{Si}(\text{CH}_3)_2(\text{OH})_2$ and $\text{Si}(\text{CH}_3)(\text{OH})_3$ are assumed based on analogy to $\text{H}_2\text{SiO} + \text{H}_2\text{O} = \text{HSiO}(\text{OH}) + \text{H}_2$ calculated by Zachariah and Tsang [237].

With the above mentioned rate-coefficient estimates for these reaction sets, the experimental $\text{Si}(\text{CH}_3)_3\text{OH}$, $\text{Si}(\text{OH})_3$, and $\text{Si}(\text{OH})_4$ mole fractions could not be matched and optimization required the introduction of two global reactions R18 and R19. The rate coefficients for reactions R18 and R19 are optimized so that our simulation is able to reproduce the measured $\text{Si}(\text{CH}_3)(\text{OH})_3$ mole-fraction profile. Fig. 8.9 shows that after optimizing R18 and R19, the shape and the maximum peak of the simulated $\text{Si}(\text{CH}_3)(\text{OH})_3$ mole-fraction profile are in a very good agreement with the measurements. Fig.8.9 also shows the simulated and measured profile of $\text{Si}(\text{OH})_3$. Now, the simulation can reproduce both, the profile shape and maximum. Unfortunately, the optimization procedure results in A and Tn factors that exceed the collision limit; for example, at $T = 900\text{K}$, $1.7 \times 10^8 T^{2.65} \approx 1.1 \times 10^{16} \text{ cm}^{-3} \text{ mol}^{-1} \text{ s}^{-1}$. The corresponding rate constant k_{R18} at 900 K is $1.05 \times 10^{15} \text{ cm}^3 \text{ mol}^{-1} \text{ s}^{-1}$. For the purpose of matching experimental mole fractions of $\text{Si}(\text{OH})_x$ and $\text{Si}(\text{CH}_3)_3\text{OH}$ species, it was not possible to avoid exceeding the collision limit. This observation indicates that other potentially important reaction pathways contributing to the formation and consumption of these species are missing. Furthermore, we suggest to treat the profile of $\text{Si}(\text{OH})_3$ as tentative, since we cannot exclude that the profile is overlapped by fragments of bigger silicon-containing species. The rate coefficients of reactions R19 and R20 were also optimized to fit the measured $\text{Si}(\text{OH})_3$ mole fractions.

There is a discussion in the literature about the contribution of SiO_2 and $\text{Si}(\text{OH})_4$ in the formation of silica nanoparticles. Many studies hypothesize that gas-phase SiO_2 is a major species that initiates the clustering and formation of silica nanoparticles. Other studies reported that $\text{Si}(\text{OH})_4$ is the major species that contributes the most to particle formation [33, 31]. In addition, some kinetics models available for silanes and siloxanes chose either SiO_2 or $\text{Si}(\text{OH})_4$ as the target species for their particle formation model. $\text{Si}(\text{OH})_4$ was found to be a major intermediate during the combustion of TEOS [31]. Shekar et al. [31] showed that the dimerization and dehydration of $\text{Si}(\text{OH})_4$ plays a key role in the formation of silica nanoparticles.

In this work, the dimerization of $\text{Si}(\text{OH})_4$ is introduced in terms of the global reaction R21 ($\text{Si}(\text{OH})_3 + \text{OH} \rightarrow 0.5\text{Si}_2(\text{OH})_8$). According to Shekar et al. [31], the species “ $\text{Si}_2(\text{OH})_8$ ” can be envisioned as a hydrogen-bonded complex of two $\text{Si}(\text{OH})_4$ molecules. This complex is

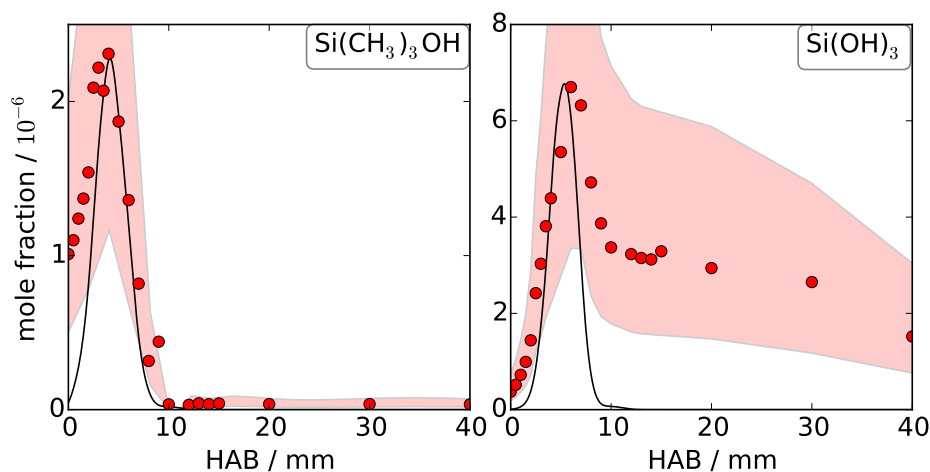


Fig. 8.9 Measured and simulated profiles of $\text{Si}(\text{CH}_3)_3\text{OH}$ and $\text{Si}(\text{OH})_3$. The colored area shows the uncertainty range of a factor of two for the measured data.

regarded as an intermediate towards the formation of large molecular clusters like $\text{Si}_4\text{O}_{10}\text{H}_4$ (Reaction R25). Without R21, $\text{Si}(\text{OH})_3$ would be quantitatively converted to $\text{Si}(\text{OH})_4$, which would be in contradiction with the measured MBMS data for $\text{Si}(\text{OH})_4$ mole fractions. In contrast, Feroughi et al. [238] suggested that nanoparticle formation takes place from the secondary chemistry of gaseous SiO_2 . According to the mass spectrometric data of Karakaya et al. [81], only low mole fractions of SiO_2 were detected in comparison to $\text{Si}(\text{OH})_4$.

Figure 8.10 depicts simulated mole-fraction profiles of SiO_2 and $\text{Si}(\text{OH})_4$ in comparison to the measured profiles. In this study, we considered a two-step hydration of SiO_2 (R23 and R24) described by Plane et al. [239] to form $\text{Si}(\text{OH})_4$. Plane et al. [239] estimated the rate coefficients for reactions of R23 and R24 using RRKM theory for mesospheric conditions, which could not be applied in our flame conditions. Consequently, we optimized the rate coefficients of R23 and R24, which led to very good agreement between experiment and simulation for SiO_2 and $\text{Si}(\text{OH})_4$ regarding the shape and peak. The shape of the profile suggests that $\text{Si}(\text{OH})_4$ is consumed faster than SiO_2 and reaches the equilibrium.

This observation is also reflected in our mechanism. Fig. 8.11 shows a reaction-path analysis for Si-containing gas-phase species involved in TMS oxidation at 800 K. The diagram in Fig. 8.11 indicates that $\text{Si}(\text{OH})_4$ is consumed faster than SiO_2 . The thickness and color intensity of each arrow in this diagram is relative to the maximum reaction rate at this temperature. The path analysis also illustrates that in the present model, the formation of large molecular silicon clusters like $\text{Si}_4\text{O}_{10}\text{H}_4$, which were detected by Karakaya et al. [81], primarily takes place via the path, which involves $\text{Si}(\text{CH}_3)_3\text{OH}$ and $\text{Si}(\text{OH})_3$.

$\text{Si}(\text{OH})_4$ is an important intermediate in our mechanism, since silicon clusters such as $\text{Si}_4\text{O}_{10}\text{H}_4$, $\text{Si}_5\text{O}_{12}\text{H}_4$, and $\text{Si}_6\text{O}_{14}\text{H}_4$ are suggested to be formed by stepwise addition of

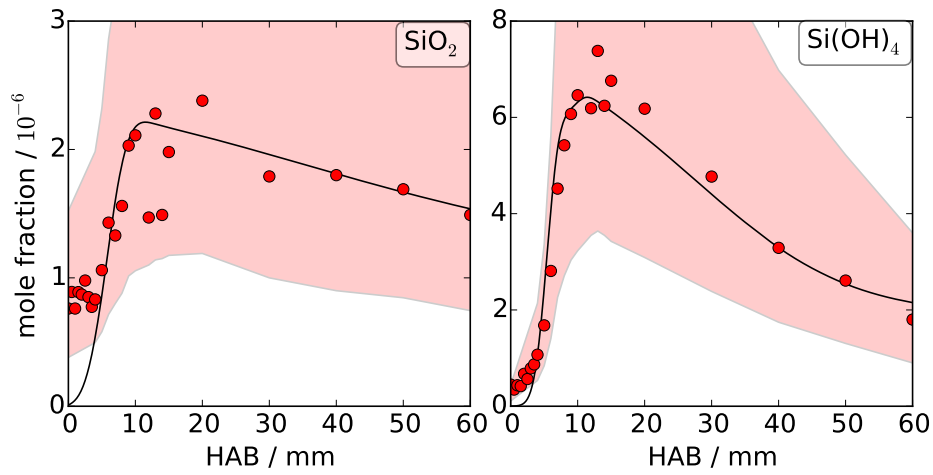


Fig. 8.10 Measured and simulated profiles of SiO_2 and Si(OH)_4 . The colored area shows the uncertainty range of a factor of two for the measured data.

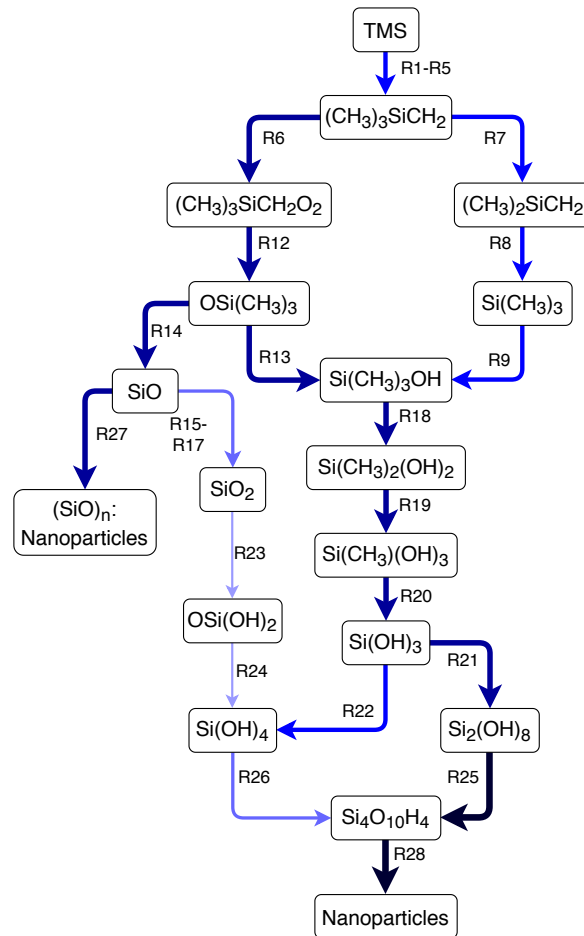


Fig. 8.11 Reaction pathways of element of Si for gas-phase species at 800 K and 30 mbar.

$\text{Si}(\text{OH})_4$ and elimination of H_2O . This assumption is in conflict with the mechanism published by Chen et al. [218] who assumed in their model that $\text{Si}(\text{OH})_4$, which is produced from hydrolysis of OMCTS, dehydrates to form SiO_2 as particle-forming species. Cluster structures like $\text{Si}_4\text{O}_{10}\text{H}_4$ are also reported in the experimental work of Xu et al. [240]. Timoshkin [241] shows that silicon oxide clusters can have different structures such as tetrahedral cages or linear chains. Fig. 8.12 shows the simulated and measured profiles of the $\text{Si}_4\text{O}_{10}\text{H}_4$ cluster. The rate coefficient of R28 is optimized to match the experimental $\text{Si}_4\text{O}_{10}\text{H}_4$ mole-fraction profile. The colored area shown in Fig. 8.12 shows the uncertainty range of the measured mole fractions. In the mechanism developed in this work, $\text{Si}_4\text{O}_{10}\text{H}_4$ is formed by self-clustering of $\text{Si}(\text{OH})_4$ (R26). The consumption of $\text{Si}_4\text{O}_{10}\text{H}_4$ and, correspondingly, the growth of larger Si-O-containing clusters are considered by introducing the global reaction (R28), which represents a self-clustering of $\text{Si}_4\text{O}_{10}\text{H}_4$:

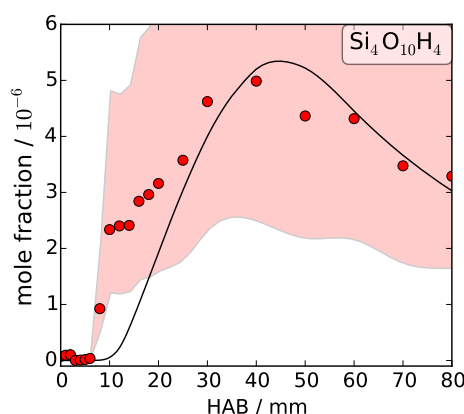
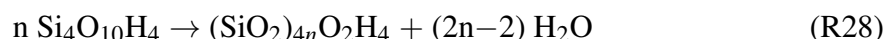
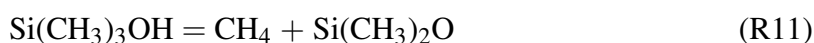


Fig. 8.12 Measured and simulated profiles of $\text{Si}_4\text{O}_{10}\text{H}_4$. The colored area shows the uncertainty range of a factor of two for the measured data.

With respect to silica particle formation, SiO and SiO_2 are generally regarded as the primary particle forming intermediate species. Karakaya et al. [81] did not detect SiO because of interference with the signal of carbon dioxide in mass spectrometry, but SiO was monitored selectively by laser-induced fluorescence in flames [72]. Zachariah and Burgess Jr [70] reported a double-peak structure in SiO mole-fraction profiles in SiH_4 doped counter-flow diffusion flames. Glumac [71] could also detect such behavior for SiO by performing LIF and emission spectroscopy in low-pressure H_2/O_2 /hexamethyldisilazane flames as well as Feroughi et al. [69], who observed it in low-pressure H_2/O_2 /HMDSO flames. A possible detailed cluster formation pathway has been described by Suh et al. [242], who suggested a clustering and self-clustering mechanism of SiO , SiO_2 , SiH_2O , and HSiOOH involving

the formation of metastable $(\text{SiO})_n$ clusters. In the present work, we have introduced one global reaction, R27, to also account for the possibility of nanoparticle formation by SiO. The measured SiO_2 mole fractions shown in Fig. 8.10 depend on the rate coefficients of reactions R15-R17, R23, and R27. For R15-R17, we have adopted rate coefficient data from the mechanism from Chen et al. [218] and the rate coefficient of R27 was optimized to match the experimental SiO_2 mole-fraction profile. Without R27, all intermediate SiO molecules would be transformed to SiO_2 according to R15–R17. Reaction R27 and R28 were both implemented in the mechanism to remove Si-containing species from the gas phase into the condensed phase. Originally, we suspected that the thermal decomposition of the intermediate compound $\text{Si}(\text{CH}_3)_3\text{OH}$ can have an impact on SiO and hence on SiO_2 production. Karakaya et al. [81] reported that there are two possible and energetically preferred unimolecular reaction channels: The elimination of CH_4 , and the elimination of H_2O .



Based on the present G4 calculations, the barrier heights for reaction R11 is calculated to be 270.3 kJ/mol and for reaction R10 to be 309.4 kJ/mol. Based on these values, R11 could have been a process contributing to the consumption of $\text{Si}(\text{CH}_3)_3\text{OH}$ at temperatures below 1000 K. Fig. 8.13 shows RRKM calculations of rate coefficients of reaction R11 and R10 at $p = 30$ mbar. Since reaction R11 yields $\text{Si}(\text{CH}_3)_2\text{O}$, which can decompose via Si–C bond fission to CH_3 radicals and SiO, we assumed that R11 might also influence the SiO_2 mole fractions and cluster formation. Using the calculated rate coefficients shown in Fig. 8.13 for 30 mbar, reaction R11 is too slow to have significant impact. Fig. 8.13 also includes a potential energy surface of the main $(\text{CH}_3)_3\text{SiOH}$ decomposition channels and it can be seen that at $T < 1000$ K, besides the elimination reactions, bond fissions will not contribute to the decomposition of this silanol. According to the present G4 calculation, the reverse reaction of H_2O elimination seems to be without a barrier, i.e., the energy of the products H_2O and sila-isobutene $(\text{CH}_3)_2\text{SiCH}_2$ is approximately 0.2 kJ/mol below the energy of the transition state structure. As mentioned in section 6.1 there is a substantial uncertainty regarding the calculated and experimentally determined thermochemistry of $(\text{CH}_3)_2\text{SiCH}_2$. It is very likely that also the reverse reaction between H_2O and $(\text{CH}_3)_2\text{SiCH}_2$ is a reaction with at least a small energy barrier.

When we tried to apply detailed reaction sequences (R14a–e, R18a–f, R19a–e) using the rate coefficients k_{11} obtained from the RRKM calculation, the algorithm did not determine

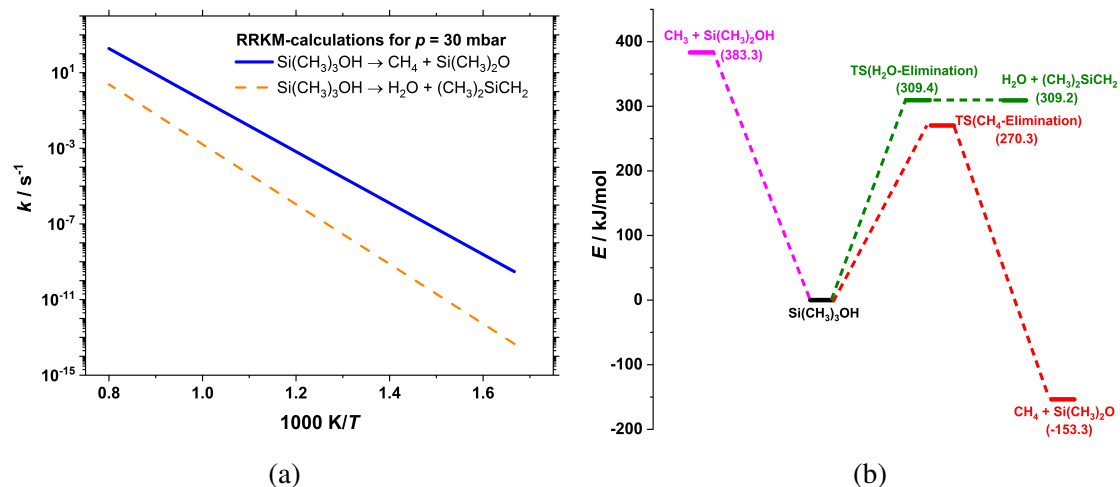


Fig. 8.13 a: RRKM calculations for CH_4 and H_2O elimination reactions of $\text{Si}(\text{CH}_3)_3\text{OH}$; both calculations were carried out for 30 mbar and 600-1200 K. b: Relative stationary point energies (values in parentheses are relative to the energy of $\text{Si}(\text{CH}_3)_3\text{OH}$) for the unimolecular reactions of $\text{Si}(\text{CH}_3)_3\text{OH}$ calculated at the G4 level of theory (present work).

an optimized rate coefficient that reasonably predicts SiO_2 and $\text{Si}(\text{OH})_x$ mole fractions. This is another reason why we had to employ the global reactions R14 and R18.

Altogether it was possible to devise a reaction mechanism that is able to reproduce measured mole fractions in a TMS-doped low-pressure $\text{H}_2/\text{O}_2/\text{Ar}$ flame. However, it turned out to be necessary to employ global reactions. When we tried to use more detailed reaction sequences with rate coefficients estimated by means of RRKM theory or analogies to similar reactions, the algorithm was not able to converge to a set of optimized rate coefficients that makes it possible to reproduce experimental data. This indicates that still important parts of TMS oxidation chemistry are missing and that - with respect to unimolecular reactions - one needs to be cautious to apply analogies between Si-containing species and analog hydrocarbons. Table 8.4 summarizes, which rate coefficient parameters were determined through analogy, calculation or optimization. In this study, we proposed rate coefficient parameters for a total number of 44 reactions (elementary and global reactions) and among them, 16 are based on analogies, nine are taken from literature, four were calculated by RRKM theory, and 16 were derived from optimization.

8.7.3 Comparison with different loads of TMS

The developed mechanism was further compared to new measurements performed in this study for other initial TMS mole fractions in flames C and D to substantiate the development of the present TMS mechanism. Figure 8.14 shows the measured and calculated mole-fraction

Table 8.4 Source of reaction rates used in the TMS mechanism.

Analogy	R1: Analogy to OH + neopentane [228] R3, R18(c), and R19(c): Analogy to O + neopentane [229] R7, R14(a), R(18)e, and R19(d): Analogy to $\text{Si}(\text{CH}_3)_3 = \text{Si}(\text{CH}_3)_2 + \text{CH}_3$ [75] R8: Analogy to H + iso- C_4H_8 [230] R18a and R19a: Analogy to TMS + H (R2) R18b and R19b: Analogy to TMS + OH (R1) R18e: Analogy to $\text{H}_2\text{SiO} + \text{H}_2\text{O}$ reported by [237]
Literature	R2: [226] R4, R5, and R18(f): [77] R14b: [206] R14d, R15, R16, and R17: [218]
Theoretical calculation	R10, R11, R14c, and R14e: RRKM theory
Optimization	R6 and R12: Optimized against experimental profile of $(\text{CH}_3)_3\text{SiCH}_2\text{O}_2$ R9, R18, and R19: Optimized against the experimental profile of $\text{Si}(\text{CH}_3)_3\text{OH}$ R13: Optimized against the experimental profile of $\text{Si}(\text{CH}_3)_3\text{OH}$ R14: Optimized against the experimental profile of $\text{OSi}(\text{CH}_3)_3$ R20, R21: Optimized against the experimental profile of $\text{Si}(\text{OH})_3$ R22 and R26: Optimized against the experimental profile of $\text{Si}(\text{OH})_4$ R23 and R27: Optimized against the experimental profile of SiO_2 R24: Optimized against the experimental profiles of SiO_2 and $\text{Si}(\text{OH})_4$ R25 and R28: Optimized against the experimental profile of $\text{Si}_4\text{O}_{10}\text{H}_4$

profiles of the major species O_2 , H_2 , H_2O , CO , and CO_2 as well as TMS. The experimental and simulated mole fractions of flame B (600 ppm TMS) are also given in this figure for the sake of comparison. The mole fractions in the legend indicate which molar percentage of precursor is doped into the flames. The uncertainties of mole fraction measurements for the 400-ppm and 800-ppm case are the same as for the 600-ppm case, which is discussed in the previous sections of this work. The colored areas that represent the uncertainty ranges of the experiments in the previous figures are not included in Fig. 8.14. Simulated mole fractions of major species and Si-containing intermediates are also sensitive to the uncertainties of the prescribed experimental temperatures.

The measured mole fractions of H_2 , O_2 , and H_2O as well as simulations are showing similar response to the change of initial TMS mole fractions. The slight shifts of species profiles toward the burner surface are due to the temperature differences caused by the presence of precursor in the flames. Simulations predict measured CO and CO_2 mole fractions within the uncertainty ranges. In Fig. 8.14, the simulations predict consumption of TMS at earlier HAB than the experimental observations. As discussed in the previous section,

the deviation can be due to sampling effects. The experimental observations demonstrate that TMS decomposes and oxidizes almost independent from the load of precursor for all three cases at almost 8 mm HAB. This behavior is well captured by simulations but only shifted 2 mm closer to the burner surface. It is worth to mention that the rate coefficients of H-atom abstractions of TMS (R1-R5) are either taken from literature or estimated by analogy to hydrocarbons chemistry and not optimized against the experimental profile of TMS. The reason for not optimizing the initial oxidation reactions of TMS is that the peak locations of Si-intermediates are perfectly captured by simulation results. Optimizing the rate constants of R1–R5 to catch the measured TMS slows the total consumption of TMS and all the simulated Si-intermediates shift farther from the burner surface.

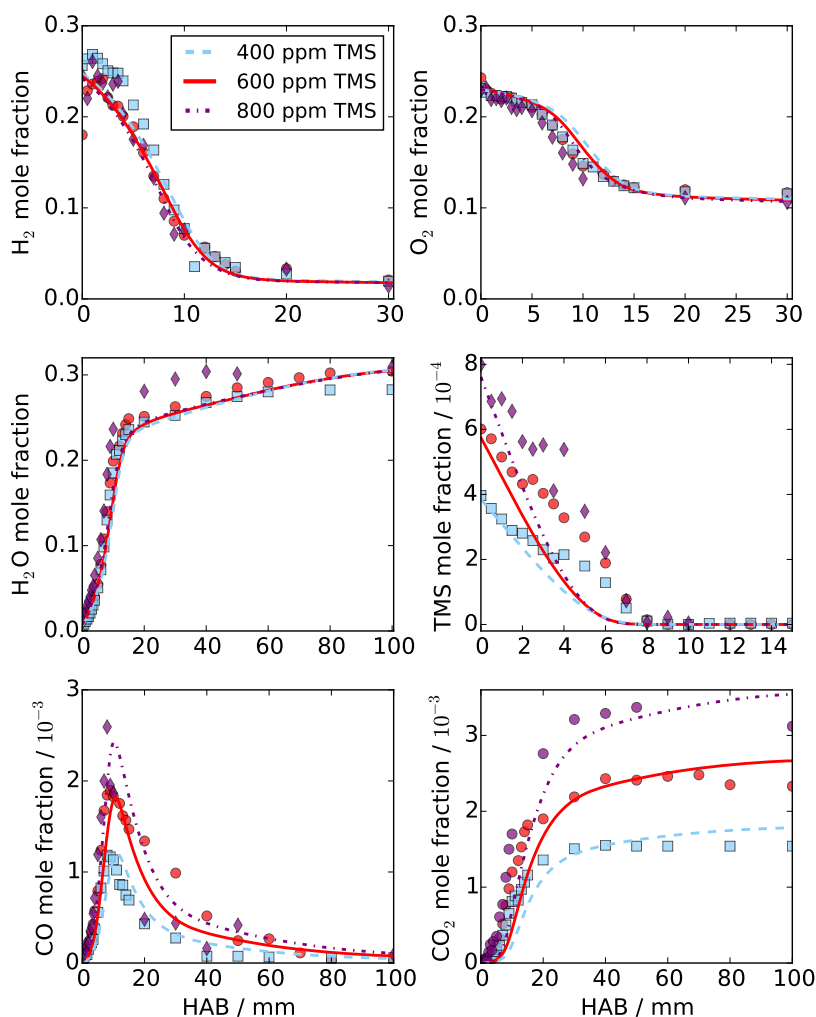


Fig. 8.14 Measured and simulated mole-fraction profiles of major species as a function of HAB for a series of TMS doping concentrations: 400 ppm (flame C), 600 ppm (flame B), and 800 ppm (flame D). Symbols: experiments, lines: simulations.

Figure 8.15 shows the comparison of simulated Si-containing intermediates with experimental values from measurements in flames with different TMS load. The TMS mechanism is developed based on experimental observation for the 600-ppm case and evaluated for the other two concentrations of precursor. For all species shown in Fig. 8.15, simulations predict the peak mole fractions for 600-ppm case very well. The simulation results are all within the uncertainty ranges of measurements. The uncertainty ranges are not shown in Fig. 15 due to an overlap of the ranges, which makes it difficult to interpret the results. The measured mole fractions demonstrate that $(\text{CH}_3)_3\text{SiCH}_2\text{O}_2$, $\text{OSi}(\text{CH}_3)_3$, and $\text{Si}(\text{CH}_3)_3\text{OH}$ as major Si-containing species are completely consumed at almost 8 mm HAB where the precursor is also completely consumed. The measured mole fractions of all Si-containing species indicate that the peak locations of intermediates do not shift toward the burner surface in contrast to the base flame major species. Simulated SiO_2 mole fraction overpredict the experiment for the 400-ppm case and underpredict for 800-ppm case, but the simulated SiO_2 profiles are in the uncertainty ranges of the corresponding measurements. The substantially reduced signal-to-noise ratio of the SiO_2 mole-fraction profile in the flame doped with 800 ppm is tentatively interpreted as an indication that condensation processes to solid SiO_2 occur. Figure 8.16 shows measured and simulated mole fractions of $\text{Si}_4\text{O}_{10}\text{H}_4$ along the HAB. Peak locations shift toward the burner surface and the formation of $\text{Si}_4\text{O}_{10}\text{H}_4$ increases rapidly by increasing the initial mole fraction of precursor.

As discussed earlier in this work, aggregation processes involving $\text{Si}_4\text{O}_{10}\text{H}_4$ are assumed to mainly contribute to the formation of larger silicon oxide clusters with the structure $(\text{SiO}_2)_{4n}\text{O}_2\text{H}_4$. Fig. 16 shows that the mole fraction of clusters decreases around $\text{HAB} = 50\text{--}60$ mm. It can only be hypothesized that the transformation from pure gas-phase clusters to nanoparticles takes places from 60 mm HAB and beyond. Unfortunately, there are no particle measurements for these TMS-doped low-pressure flames available yet, which are needed to further implement particle formations models in our mechanism.

It was not possible to detect nanoparticles in this work, because the mass spectrometric setup is designed and optimized for measuring small molecules up to mass-to-charge ratio $m/z = 400$, limiting detection to gaseous Si-containing clusters with up to six silicon atoms. The burner chamber was lightly coated by white particles from the synthesis flames. Measuring the solid state of the silicon dioxide particles by means of a quartz crystal microbalance is future work.

SiO could also not be detected in the experiments of this work because its signal could not be resolved from the signal of CO_2 . As discussed earlier in this work, SiO is assumed to be involved in the early cluster formation in the preheating zone and already consumed completely in the reacting zone. Consequently, SiO is assumed not to be responsible for the

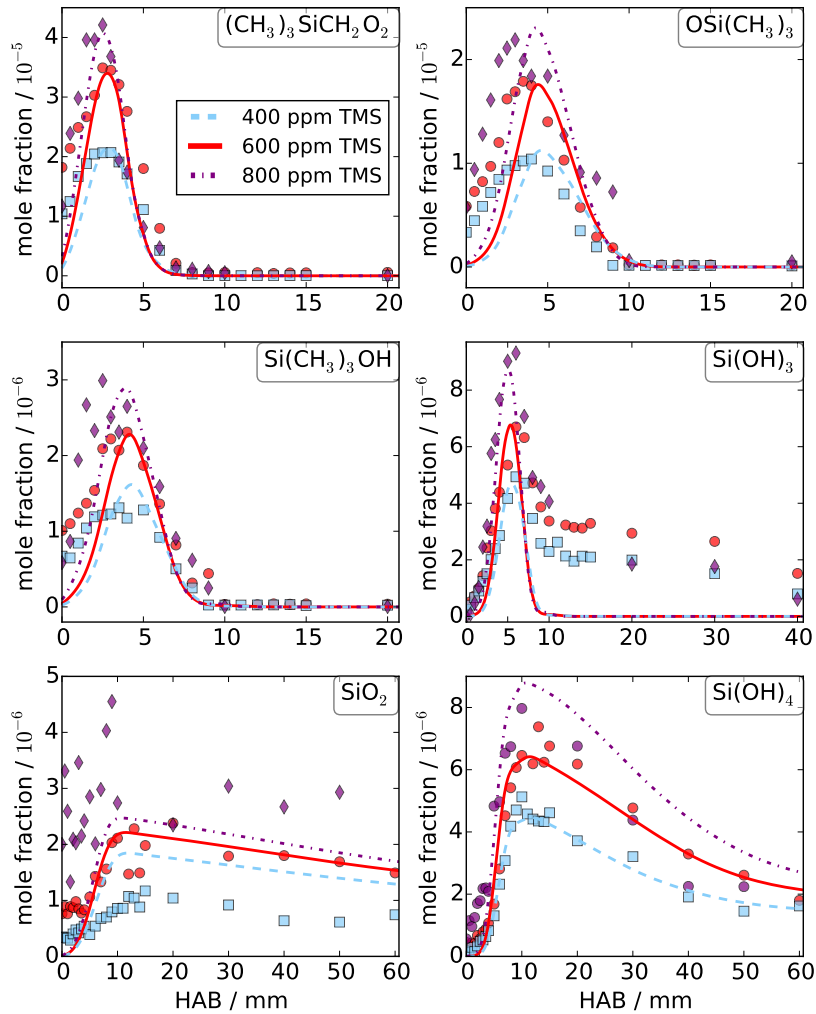


Fig. 8.15 Measured and simulated mole-fraction profiles of Si-containing species along the HAB for a series of TMS doping concentrations: 400 ppm (Flame C), 600 ppm (Flame B), and 800 ppm (flame D). Symbols: experiments, lines: simulations.

formation of silica-nanoparticles. Quantitative measurements for SiO would be appreciated for further work as another potentially important speciation target for mechanism validation. The evaluation of the developed mechanism for other equivalence ratios is subject of future work.

8.8 Conclusion

This work presents a reaction mechanism, which was developed to model the oxidation of TMS in a low pressure $\text{H}_2/\text{O}_2/\text{Ar}$ flame. To the best of our knowledge, this is the first attempt to develop a reaction mechanism that is validated against a dataset of quantitative

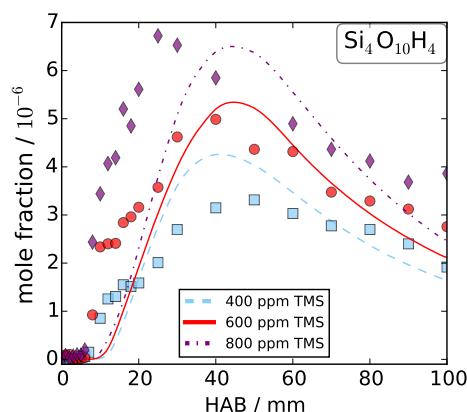


Fig. 8.16 Measured and simulated mole-fraction profiles of $\text{Si}_4\text{O}_{10}\text{H}_4$ along the HAB for a series of TMS doping concentrations: 400 ppm (Flame C), 600 ppm (Flame B), and 800 ppm (Flame D). Symbols: experiments, lines: simulations.

measurements made via molecular-beam mass spectrometry. Rate coefficients of the reactions included in this mechanism were derived by (1) using a genetic algorithm with experimentally determined mole-fraction profiles as target data for optimization, (2) by applying reactivity analogies, and (3) by using RRKM theory. As part of the mechanism development, also thermochemical and transport data have been calculated and estimated. The G4 composite method is used to calculate the thermodynamic data of Si-containing species. The present reaction mechanism contains 24 species and 28 reactions, and the small number of reactions in this mechanism will facilitate its application in chemical kinetics simulations for analyzing other TMS-doped synthesis flames.

The present results suggest that important issues of TMS oxidation chemistry are still not understood and that the development of a detailed reaction mechanism for TMS oxidation requires much more effort regarding future quantum chemical and/or experimental kinetics investigations. In particular, quantitative measurements of SiO and SiO_2 are needed. The need to employ global reactions in this reaction mechanism clearly indicates that reaction pathways are missing. Consequently, future work should target reactions connecting $\text{Si}(\text{OH})_3$ and $\text{Si}(\text{OH})_4$ as well as reaction sequences that can convert $\text{Si}(\text{OH})_4$ to SiO_2 or SiO and vice versa. Open questions also remain for example with respect to other detailed reaction pathways but also the major intermediates contributing to particle formation need to be better identified. It is important to extend the database to other fundamental experimental configurations, e.g., flow reactors that are less influenced by deviations from one-dimensionality. For future work, the combination of MBMS data and new optimization targets, the genetic algorithm has the potential to improve the mechanism.

8.9 Acknowledgements

The authors gratefully acknowledge the financial support by the German Research Foundation (DFG, FOR 2284, project number: 262219004, within WL 63/1, KA 3871/4, and SCHU 1369/25).

Chapter 9

Conclusion and outlook

The focus of the research conducted within the scope of this thesis was the development of a chemical kinetic reaction mechanism for the combustion of TMS in low pressure $H_2/O_2/Ar$ flames. During the development of the TMS mechanism, it is found that the thermochemistry of many Si-C-H and Si-C-H-O molecules was not available in the literature. The thermochemistry of species in the kinetic mechanisms is important since the heat release of the reactions and the reverse rate constants depend on the accurate thermodynamics data. Therefore, the thermochemistry of an exhaustive list of Si-containing species is calculated to provide a database for the Si-C-H and Si-C-H-O systems. The thermochemistry database gives a great opportunity to extend the developed TMS mechanism in the future by adding more intermediates. A complete list of GAVs of Si-C-H and Si-C-H-O systems was also calculated in this work. The GAVs have the advantage that they can be used to estimate thermodynamics data of a non-ending list of species much more faster than quantum chemical calculations. They can also be easily implemented in the automatic reaction mechanism generator programs. A combinatorial approach was used to choose compounds with unique groups of interest to GAV derivation. Quantum chemical calculations were used to calculate thermodynamic data of reference species in the training sets for derivation of GAVs. A systematic and automated regression analysis were performed to obtain the GAVs. At the end, the thermochemistry of species and the GAVs calculated in this work are stored in relational and non-relational databases. The bipartite graph representation discussed in chapter 4 is an example of non-relational databases.

As the science never stops and there is always room for improvement, there are some recommendations at this point.

- Chapter 5, 6, and 7 of this thesis covered a complete list of GAVs for stable and radical Si-C-H system as well as stable GAVs for Si-C-H-O system. It means the GAVs of radical Si-C-H-O system are missing. The radicals play an important role for

the prediction of major flame properties such as flame speed and ignition delay time. In order to be able to develop or extend the reaction mechanism for combustion to Si–C–H–O-containing precursors such as TEOS, the thermodynamics data of radicals are crucial. These sets of GAVs can be calculated with similar methods and procedures as discussed in this work.

- The uncertainties of GAVs are rarely reported in the literature. The uncertainties are assumed similar to the uncertainty of the quantum calculation method used for the calculation of the training set. It would be very interesting to calculate uncertainties of GAVs reported in this work. The uncertainties of new molecules estimated by group additivity method can be calculated by an error propagation law.
- The whole thermodynamics data of Si-containing species in our data base can be used as training data for a machine learning algorithm to find a pattern for estimation of radical species and compare the estimated species with the chemical quantum calculated species. This approach does not only extend the thermodynamics data of Si-containing species but also provides a great opportunity to apply machine learning algorithms to bring more insight into the thermochemistry of organosilanes.
- Chapter 8 of this thesis covered the development of a chemical kinetic reaction mechanism for the combustion of TMS. A similar approach based on the results of this work can be applied to develop a chemical kinetic reaction mechanism for the combustion of HMDSO or other precursors.
- A comprehensive database in relational and non-relational format for the thermochemistry of Si-containing species is provided in this work. These databases can be implemented in reaction mechanism generator programs or be published as stand-alone.

References

- [1] D. Nunes, A. Pimentel, L. Santos, P. Barquinha, L. Pereira, E. Fortunato, and R. Martins, “2—synthesis, design, and morphology of metal oxide nanostructures,” *Metal Oxide Nanostructures; Nunes, D., Pimentel, A., Santos, L., Barquinha, P., Pereira, L., Fortunato, E., Martins, R., Eds*, pp. 21–57, 2019.
- [2] S. M. Senkan, “Detailed chemical kinetic modeling: chemical reaction engineering of the future,” in *Advances in chemical engineering*, vol. 18, pp. 95–196, Elsevier, 1992.
- [3] T. Lu and C. K. Law, “Toward accommodating realistic fuel chemistry in large-scale computations,” *Prog. Energy Combust. Sci*, vol. 35, no. 2, pp. 192–215, 2009.
- [4] N. Sikalo, O. Hasemann, C. Schulz, A. Kempf, and I. Wlokas, “A genetic algorithm-based method for the automatic reduction of reaction mechanisms,” *Int. J. Chem. Kinet.*, vol. 46, no. 1, pp. 41–59, 2014.
- [5] J. Li, Z. Zhao, A. Kazakov, M. Chaos, F. L. Dryer, and J. J. Scire, “A comprehensive kinetic mechanism for CO, CH₂O, and CH₃OH combustion,” *Int. J. Chem. Kinet.*, vol. 39, no. 3, pp. 109–136, 2007.
- [6] E. Ranzi, C. Cavallotti, A. Cuoci, A. Frassoldati, M. Pelucchi, and T. Faravelli, “New reaction classes in the kinetic modeling of low temperature oxidation of n-alkanes,” *Combust. Flame*, vol. 162, no. 5, pp. 1679–1691, 2015.
- [7] H. Janbazi, O. Hasemann, C. Schulz, A. Kempf, I. Wlokas, and S. Peukert, “Response surface and group additivity methodology for estimation of thermodynamic properties of organosilanes,” *Int. J. Chem. Kinet.*, vol. 50, no. 9, pp. 681–690, 2018.
- [8] W. Phadungsukanan, S. Shekar, R. Shirley, M. Sander, R. H. West, and M. Kraft, “First-principles thermochemistry for silicon species in the decomposition of tetraethoxysilane,” *J. Phys. Chem. A*, vol. 113, no. 31, pp. 9041–9049, 2009.
- [9] G. Biskos, V. Vons, C. U. Yurteri, and A. Schmidt-Ott, “Generation and sizing of particles for aerosol-based nanotechnology,” *KONA Powder and Particle Journal*, vol. 26, pp. 13–35, 2008.
- [10] A. Karatutlu, A. Barhoum, and A. Sapelkin, “Liquid-phase synthesis of nanoparticles and nanostructured materials,” in *Emerging Applications of Nanoparticles and Architecture Nanostructures*, pp. 1–28, Elsevier, 2018.
- [11] G. Niraula, N. Shrivastava, K. Akhtar, Y. Javed, J. Coaquira, and S. Sharma, “Liquid-phase synthesis of multifunctional nanomaterials: A recent update,” in *Magnetic Nanoheterostructures*, pp. 1–56, Springer, 2020.

- [12] T. Trindade, P. O'Brien, and N. L. Pickett, "Nanocrystalline semiconductors: synthesis, properties, and perspectives," *Chem. Mater.*, vol. 13, no. 11, pp. 3843–3858, 2001.
- [13] N. Salah, S. S. Habib, Z. H. Khan, A. Memic, A. Azam, E. Alarfaj, N. Zahed, and S. Al-Hamedi, "High-energy ball milling technique for zno nanoparticles as antibacterial material," *Int. J. Nanomedicine*, vol. 6, p. 863, 2011.
- [14] S. Indris, R. Amade, P. Heitjans, M. Finger, A. Haeger, D. Hesse, W. Grünert, A. Börger, and K. D. Becker, "Preparation by high-energy milling, characterization, and catalytic properties of nanocrystalline tio₂," *J. Phys. Chem. B*, vol. 109, no. 49, pp. 23274–23278, 2005.
- [15] F. Kunze, S. Kuns, M. Spree, T. Hülser, C. Schulz, H. Wiggers, and S. M. Schnurre, "Synthesis of silicon nanoparticles in a pilot-plant-scale microwave plasma reactor: Impact of flow rates and precursor concentration on the nanoparticle size and aggregation," *Powder Technol.*, vol. 342, pp. 880–886, 2019.
- [16] M. Dasgupta, P. Fortugno, and H. Wiggers, "Plasma-assisted gas-phase synthesis and in-line coating of silicon nanoparticles," *Plasma Processes and Polymers*, vol. 17, no. 5, p. 1900245, 2020.
- [17] A. Gutsch, H. Mühlenweg, and M. Krämer, "Tailor-made nanoparticles via gas-phase synthesis," *Small*, vol. 1, no. 1, pp. 30–46, 2005.
- [18] C. Schulz, T. Dreier, M. Fikri, and H. Wiggers, "Gas-phase synthesis of functional nanomaterials: challenges to kinetics, diagnostics, and process development," *Proc. Combust. Inst.*, vol. 37, no. 1, pp. 83–108, 2019.
- [19] H. K. Kammler, L. Mädler, and S. E. Pratsinis, "Flame synthesis of nanoparticles," *Chem Eng Technol: Industrial Chemistry-Plant Equipment-Process Engineering-Biotechnology*, vol. 24, no. 6, pp. 583–596, 2001.
- [20] P. Roth, "Particle synthesis in flames," *Proc. Combust. inst.*, vol. 31, no. 2, pp. 1773–1788, 2007.
- [21] K. Wegner and S. E. Pratsinis, "Gas-phase synthesis of nanoparticles: scale-up and design of flame reactors," *Powder Technol.*, vol. 150, no. 2, pp. 117–122, 2005.
- [22] S. E. Pratsinis, W. Zhu, and S. Vemury, "The role of gas mixing in flame synthesis of titania powders," *Powder Technology*, vol. 86, no. 1, pp. 87–93, 1996.
- [23] R. K. Cheng, B. Bédard, and L. W. Kostiuk, "Effects of buoyancy on lean premixed v-flames part i: laminar and turbulent flame structures," *Combust. Flame*, vol. 116, no. 3, pp. 360–375, 1999.
- [24] S. Kluge, L. Deng, O. Feroughi, F. Schneider, M. Poliak, A. Fomin, V. Tsionsky, S. Cheskis, I. Wlokas, I. Rahinov, *et al.*, "Initial reaction steps during flame synthesis of iron-oxide nanoparticles," *CrystEngComm*, vol. 17, no. 36, pp. 6930–6939, 2015.
- [25] O. Korobeinichev, V. Shvartsberg, A. Shmakov, D. Knyazkov, and I. Rybitskaya, "Inhibition of atmospheric lean and rich ch₄/o₂/ar flames by phosphorus-containing compound," *Proc. Combust. inst.*, vol. 31, no. 2, pp. 2741–2748, 2007.

- [26] A. Hayhurst, "Mass spectrometric sampling of a flame," *Combust. Explos. Shock Waves*, vol. 48, no. 5, pp. 516–525, 2012.
- [27] A. D. Abid, J. Camacho, D. A. Sheen, and H. Wang, "Evolution of soot particle size distribution function in burner-stabilized stagnation n-dodecane- oxygen- argon flames," *Energy & Fuels*, vol. 23, no. 9, pp. 4286–4294, 2009.
- [28] M. Zachariah and H. Semerjian, "Experimental and numerical studies on refractory particle formation in flames: Application to silica growth," *High. Temp. Sci.*, vol. 28, pp. 113–125, 1990.
- [29] S. Ehrman, S. Friedlander, and M. Zachariah, "Characteristics of $\text{SiO}_2/\text{TiO}_2$ nanocomposite particles formed in a premixed flat flame," *Journal of Aerosol Science*, vol. 29, no. 5-6, pp. 687–706, 1998.
- [30] J. Herzler, J. A. Manion, and W. Tsang, "Single-pulse shock tube study of the decomposition of tetraethoxysilane and related compounds," *J. Phys. Chem. A*, vol. 101, no. 30, pp. 5500–5508, 1997.
- [31] S. Shekar, M. Sander, R. C. Riehl, A. J. Smith, A. Braumann, and M. Kraft, "Modelling the flame synthesis of silica nanoparticles from tetraethoxysilane," *Chem. Eng. Sci.*, vol. 70, pp. 54–66, 2012.
- [32] J. Chu, R. Soller, M.-C. Lin, and C. Melius, "Thermal decomposition of tetramethyl orthosilicate in the gas phase: An experimental and theoretical study of the initiation process," *J. Phys. Chem.*, vol. 99, no. 2, pp. 663–672, 1995.
- [33] D. Nurkowski, P. Buerger, J. Akroyd, and M. Kraft, "A detailed kinetic study of the thermal decomposition of tetraethoxysilane," *Proc. Combust. Inst.*, vol. 35, no. 2, pp. 2291–2298, 2015.
- [34] D. Nurkowski, P. Buerger, J. Akroyd, S. Mosbach, and M. Kraft, "Skeletal chemical mechanism of high-temperature TEOS oxidation in hydrogen–oxygen environment," *Combust. Flame*, vol. 166, pp. 243–254, 2016.
- [35] M. S. Wooldridge, "Gas-phase combustion synthesis of particles," *Prog. Energy Combust. Sci.*, vol. 24, no. 1, pp. 63–87, 1998.
- [36] M.-S. Chen, J.-S. Chou, and S.-C. Lee, "Planarization of amorphous silicon thin film transistors by liquid phase deposition of silicon dioxide," *IEEE Transactions on Electron Devices*, vol. 42, no. 11, pp. 1918–1923, 1995.
- [37] J. L. Vossen, W. Kern, W. Kern, *et al.*, *Thin film processes II*, vol. 2. Gulf Professional Publishing, 1991.
- [38] S. M. Sze and K. K. Ng, *Physics of semiconductor devices*. John Wiley & sons, 2006.
- [39] T. Horiuchi, K. Kanba, T. Homma, Y. Murao, and K. Okumura, "A 7-mask cmos process with selective oxide deposition," *IEEE transactions on electron devices*, vol. 40, no. 8, pp. 1455–1460, 1993.

- [40] T. Homma, T. Katoh, Y. Yamada, and Y. Murao, "A selective SiO_2 film-formation technology using liquid-phase deposition for fully planarized multilevel interconnections," *Journal of the Electrochemical Society*, vol. 140, no. 8, p. 2410, 1993.
- [41] N. Benissad, C. Boisse-Laporte, C. Vallée, A. Granier, and A. Goulet, "Silicon dioxide deposition in a microwave plasma reactor," *Surface and Coatings Technology*, vol. 116, pp. 868–873, 1999.
- [42] M. Benelmekki and A. Erbe, "Nanostructured thin films—background, preparation and relation to the technological revolution of the 21st century," in *Frontiers of Nanoscience*, vol. 14, pp. 1–34, Elsevier, 2019.
- [43] P. Post, L. Wurlitzer, W. Maus-Friedrichs, and A. P. Weber, "Characterization and applications of nanoparticles modified in-flight with silica or silica-organic coatings," *Nanomaterials*, vol. 8, no. 7, p. 530, 2018.
- [44] G. A. Silva, "Introduction to nanotechnology and its applications to medicine," *Surgical neurology*, vol. 61, no. 3, pp. 216–220, 2004.
- [45] E. F. Vansant, P. Van Der Voort, and K. C. Vrancken, *Characterization and chemical modification of the silica surface*. Elsevier, 1995.
- [46] M. Sokolowski, A. Sokolowska, A. Michalski, and B. Gokieli, "The "in-flame-reaction" method for Al_2O_3 aerosol formation," *Journal of Aerosol Science*, vol. 8, no. 4, pp. 219–230, 1977.
- [47] B. Marshall, I. Telford, and R. Wood, "A field method for the determination of zinc oxide fume in air," *Analyst*, vol. 96, no. 1145, pp. 569–578, 1971.
- [48] R. Mueller, L. Mädler, and S. E. Pratsinis, "Nanoparticle synthesis at high production rates by flame spray pyrolysis," *Chem. Eng. Sci.*, vol. 58, no. 10, pp. 1969–1976, 2003.
- [49] K. Wegner and S. E. Pratsinis, "Scale-up of nanoparticle synthesis in diffusion flame reactors," *Chem. Eng. Sci.*, vol. 58, no. 20, pp. 4581–4589, 2003.
- [50] A. Rittler, L. Deng, I. Wlokas, and A. Kempf, "Large eddy simulations of nanoparticle synthesis from flame spray pyrolysis," *Proc. Combust. inst.*, vol. 36, no. 1, pp. 1077–1087, 2017.
- [51] D. Dasgupta, P. Pal, R. Torelli, and S. Som, "Computational fluid dynamics modeling of flame spray pyrolysis for nanoparticle synthesis," in *Spring Technical Meeting Central States Section of The Combustion Institute*, 2020.
- [52] F. Schneider, S. Suleiman, J. Menser, E. Borukhovich, I. Wlokas, A. Kempf, H. Wiggers, and C. Schulz, "Spraysyn—a standardized burner configuration for nanoparticle synthesis in spray flames," *Review of Scientific Instruments*, vol. 90, no. 8, p. 085108, 2019.
- [53] W. J. Stark and S. E. Pratsinis, "Aerosol flame reactors for manufacture of nanoparticles," *Powder Technol.*, vol. 126, no. 2, pp. 103–108, 2002.

- [54] J. Rowell, "Photonic materials," *Scientific American*, vol. 255, no. 4, pp. 146–157, 1986.
- [55] J. Hwang, Y. Gil, J. Kim, M. Choi, and S. Chung, "Measurements of temperature and OH radical distributions in a silica generating flame using LIF and PLIF," *Journal of Aerosol Science*, vol. 32, no. 5, pp. 601–613, 2001.
- [56] D. Powers, "Kinetics of SiCl₄ oxidation," *Journal of the American Ceramic Society*, vol. 61, no. 7-8, pp. 295–297, 1978.
- [57] B. Lee, S. Oh, and M. Choi, "Simulation of growth of nonspherical silica nanoparticles in a premixed flat flame," *Aerosol Science & Technology*, vol. 35, no. 6, pp. 978–989, 2001.
- [58] H. Kim, J. Jeong, Y. Park, Y. Yoon, and M. Choi, "Modeling of generation and growth of non-spherical nanoparticles in a co-flow flame," *Journal of Nanoparticle Research*, vol. 5, no. 3-4, pp. 237–246, 2003.
- [59] N. Morgan, C. Wells, M. Kraft, and W. Wagner, "Modelling nanoparticle dynamics: coagulation, sintering, particle inception and surface growth," *Combustion Theory and Modelling*, vol. 9, no. 3, pp. 449–461, 2005.
- [60] K.-S. So, H. Lee, T.-H. Kim, S. Choi, and D.-W. Park, "Synthesis of silicon nanopowder from silane gas by rf thermal plasma," *physica status solidi (a)*, vol. 211, no. 2, pp. 310–315, 2014.
- [61] S. Tamir and S. Berger, "Correlation between microstructure and photoluminescence of nanocrystalline silicon powder prepared by laser-induced CVD," *Thin Solid Films*, vol. 276, no. 1-2, pp. 108–111, 1996.
- [62] E. Khokhlov, D. Kolmykov, N. Kononov, G. Kuz'min, S. Polyakov, A. Prokhorov, N. Sulimov, and O. Tikhonovitch, "The synthesis and structure of ultradispersed silicon powders," *Laser physics*, vol. 8, no. 5, pp. 1070–1073, 1998.
- [63] K. Kim, D. Woo, J.-H. Park, S.-G. Doo, and T. Kim, "Formation of silicon nanoparticles using SiH₄ pyrolysis at atmospheric- and low-pressure," *J. Korean Phys. Soc.*, vol. 54, pp. 1021–1026, 2009.
- [64] A. Kharchenko, K. Ouaras, V. Suendo, J. Ebothé, and P. Roca i Cabarrocas, "Influence of p- and n-type doping gases on nanoparticle formation in SiH₄/H₂ radiofrequency plasma discharges used for polymorphous silicon thin film deposition," *Journal of Applied Physics*, vol. 125, no. 16, p. 163307, 2019.
- [65] A. Abdali, M. Fikri, H. Wiggers, and C. Schulz, "Shock-tube study of the ignition delay time of tetraethoxysilane (TEOS)," in *Shock Waves*, pp. 781–785, Springer, 2009.
- [66] A. Abdali, M. Fikri, H. Orthner, H. Wiggers, and C. Schulz, "Ignition delay times of shock-heated tetraethoxysilane, hexamethyldisiloxane, and titanium tetrakisopropoxide," *Chemical Physics Letters*, vol. 601, pp. 54–58, 2014.
- [67] N. M. Marinov, "A detailed chemical kinetic model for high temperature ethanol oxidation," *Int. J. Chem. Kinet.*, vol. 31, no. 3, pp. 183–220, 1999.

- [68] H. Chagger, D. Hainsworth, P. Patterson, M. Pourkashanian, and A. Williams, "The formation of SiO₂ from hexamethyldisiloxane combustion in counterflow methane-air flames," *Symp. Int. Comb.*, vol. 26, no. 2, pp. 1859–1865, 1996.
- [69] O. M. Feroughi, L. Deng, S. Kluge, T. Dreier, H. Wiggers, I. Wlokas, and C. Schulz, "Experimental and numerical study of a HMDSO-seeded premixed laminar low-pressure flame for SiO₂ nanoparticle synthesis," *Proc. Combust. Inst.*, vol. 36, no. 1, pp. 1045–1053, 2017.
- [70] M. R. Zachariah and D. R. Burgess Jr, "Strategies for laser excited fluorescence spectroscopy. measurements of gas phase species during particle formation," *J. Aerosol Sci.*, vol. 25, no. 3, pp. 487–497, 1994.
- [71] N. G. Glumac, "Formation and consumption of SiO in powder synthesis flames," *Combust. Flame*, vol. 124, no. 4, pp. 702–711, 2001.
- [72] R. S. Chrystie, H. Janbazi, T. Dreier, H. Wiggers, I. Wlokas, and C. Schulz, "Comparative study of flame-based SiO₂ nanoparticle synthesis from TMS and HMDSO: SiO-LIF concentration measurement and detailed simulation," *Proc. Combust. Inst.*, vol. 37, no. 1, pp. 1221–1229, 2019.
- [73] R. S. Chrystie, F. L. Ebertz, T. Dreier, and C. Schulz, "Absolute SiO concentration imaging in low-pressure nanoparticle-synthesis flames via laser-induced fluorescence," *Appl. Phys. B*, vol. 125, no. 2, p. 29, 2019.
- [74] D. Chaussende, M. Ucar, L. Auvray, F. Baillet, M. Pons, and R. Madar, "Control of the supersaturation in the CF-PVT process for the growth of silicon carbide crystals: research and applications," *Cryst. Growth. Des.*, vol. 5, no. 4, pp. 1539–1544, 2005.
- [75] P. Sela, S. Peukert, J. Herzler, M. Fikri, and C. Schulz, "Shock-tube study of the decomposition of tetramethylsilane using gas chromatography and high-repetition-rate time-of-flight mass spectrometry," *Phys. Chem. Chem. Phys.*, vol. 20, no. 16, pp. 10686–10696, 2018.
- [76] P. Sela, S. Peukert, J. Herzler, Y. Sakai, M. Fikri, and C. Schulz, "High-temperature gas-phase kinetics of the thermal decomposition of tetramethoxysilane," *Proc. Combust. Inst.*, vol. 37, no. 1, pp. 1133–1141, 2019.
- [77] M. A. Reed, *The thermal reaction between tetramethylsilane and oxygen in the gas phase*. Thesis, University of Leicester, 1973.
- [78] A. C. Baldwin, I. M. Davidson, and M. D. Reed, "Mechanism of thermolysis of tetramethylsilane and trimethylsilane," *J. Chem. Soc., Faraday Trans 1*, vol. 74, pp. 2171–2178, 1978.
- [79] R. Clifford, B. Gowenlock, C. Johnson, and J. Stevenson, "The pyrolysis of organometallic compounds iv. kinetic studies of the decomposition of tetramethylsilane," *J. Organomet. Chem.*, vol. 34, no. 1, pp. 53–61, 1972.
- [80] J. E. Taylor and T. S. Milazzo, "A comparative study of the pyrolyses of the tetramethyl derivatives of silicon, germanium, and tin using a wall-less reactor," *J. Phys. Chem.*, vol. 82, no. 8, pp. 847–852, 1978.

- [81] Y. Karakaya, S. Peukert, and T. Kasper, "Mass spectrometric study on the combustion of tetramethylsilane and the formation of silicon oxide clusters in premixed laminar low-pressure synthesis flames," *J. Phys. Chem. A*, vol. 122, no. 36, pp. 7131–7141, 2018.
- [82] R. J. Kee, M. E. Coltrin, P. Glarborg, and H. Zhu, *Chemically Reacting Flow: Theory, Modeling, and Simulation*. John Wiley & Sons, 2017.
- [83] L. Deng, A. Kempf, O. Hasemann, O. P. Korobeinichev, and I. Wlokas, "Investigation of the sampling nozzle effect on laminar flat flames," *Combust. Flame*, vol. 162, no. 5, pp. 1737–1747, 2015.
- [84] G. Skandan, Y. Chen, N. Glumac, and B. Kear, "Synthesis of oxide nanoparticles in low pressure flames," *Nanostructured materials*, vol. 11, no. 2, pp. 149–158, 1999.
- [85] N. G. Glumac, Y. Chen, and G. Skandan, "Diagnostics and modeling of nanopowder synthesis in low pressure flames," *J. Mater. Res.*, vol. 13, no. 9, pp. 2572–2579, 1998.
- [86] M. D. Smooke, "Solution of burner-stabilized premixed laminar flames by boundary value methods," *Journal of Computational Physics*, vol. 48, no. 1, pp. 72–105, 1982.
- [87] R. B. Bird, "Transport phenomena," *Appl. Mech. Rev.*, vol. 55, no. 1, pp. R1–R4, 2002.
- [88] J. O. Hirschfelder, C. F. Curtiss, R. B. Bird, and M. G. Mayer, *Molecular theory of gases and liquids*, vol. 165. Wiley New York, 1964.
- [89] C. Wilke, "A viscosity equation for gas mixtures," *J. Chem. Phys.*, vol. 18, no. 4, pp. 517–519, 1950.
- [90] S. Mathur and S. Saxena, "Methods of calculating thermal conductivity of binary mixtures involving polyatomic gases," *Applied Scientific Research*, vol. 17, no. 2, pp. 155–168, 1967.
- [91] J. Warnatz, U. Maas, and R. W. Dibble, "Physical and chemical fundamentals, modeling and simulation, experiments, pollutant formation," 1990.
- [92] D. Ben-Amotz and K. G. Willis, "Molecular hard-sphere volume increments," *J. Phys. Chem.*, vol. 97, no. 29, pp. 7736–7742, 1993.
- [93] R. Kee, F. Rupley, J. Miller, M. Coltrin, J. Grcar, E. Meeks, H. Moffat, A. Lutz, G. Dixon-Lewis, and M. Smooke, "Chemkin collection, release 3.6, reaction design," *Inc., San Diego, CA*, vol. 20, no. 0, p. 0, 2000.
- [94] T. Turányi and A. S. Tomlin, *Analysis of kinetic reaction mechanisms*. Springer, 2014.
- [95] S. Arrhenius, "Über die reaktionsgeschwindigkeit bei der inversion von rohrzucker durch säuren," *Zeitschrift für physikalische Chemie*, vol. 4, no. 1, pp. 226–248, 1889.
- [96] F. A. Lindemann, S. Arrhenius, I. Langmuir, N. Dhar, J. Perrin, and W. M. Lewis, "Discussion on "the radiation theory of chemical action"," *Transactions of the Faraday Society*, vol. 17, pp. 598–606, 1922.

- [97] M. J. Pilling and P. W. Seakins, *Reaction kinetics*. Oxford University Press, 1995.
- [98] P. Atkins, J. De Paula, and J. Keeler, *Atkins' physical chemistry*. Oxford University Press, Oxford, U.K., 2018.
- [99] R. Gilbert, K. Luther, and J. Troe, "Theory of thermal unimolecular reactions in the fall-off range. ii. weak collision rate constants," *Berichte der Bunsengesellschaft für physikalische Chemie*, vol. 87, no. 2, pp. 169–177, 1983.
- [100] J. Troe, "Predictive possibilities of unimolecular rate theory," *J. Phys. Chem.*, vol. 83, no. 1, pp. 114–126, 1979.
- [101] J. Troe, "Theory of thermal unimolecular reactions in the fall-off range. i. strong collision rate constants," *Berichte der Bunsengesellschaft für physikalische Chemie*, vol. 87, no. 2, pp. 161–169, 1983.
- [102] R. G. Gilbert and S. C. Smith, "Theory of unimolecular and recombination reactions," *Blackwell Scientific*, 1990.
- [103] C. K. Law, "Combustion at a crossroads: Status and prospects," *Proc. Combust. inst.*, vol. 31, no. 1, pp. 1–29, 2007.
- [104] A. S. Tomlin, M. J. Pilling, T. Turányi, J. H. Merkin, and J. Brindley, "Mechanism reduction for the oscillatory oxidation of hydrogen: sensitivity and quasi-steady-state analyses," *Combust. Flame*, vol. 91, no. 2, pp. 107–130, 1992.
- [105] N. J. Brown, G. Li, and M. L. Koszykowski, "Mechanism reduction via principal component analysis," *Int. J. Chem. Kinet.*, vol. 29, no. 6, pp. 393–414, 1997.
- [106] T. Lu and C. K. Law, "On the applicability of directed relation graphs to the reduction of reaction mechanisms," *Combust. Flame*, vol. 146, no. 3, pp. 472–483, 2006.
- [107] P. Pepiot-Desjardins and H. Pitsch, "An efficient error-propagation-based reduction method for large chemical kinetic mechanisms," *Combust. Flame*, vol. 154, no. 1-2, pp. 67–81, 2008.
- [108] M. Chase Jr, "Nist-janaf thermochemical tables, 4th edn, part ii, cr–zr," *J. Phys. Chem. reference data, Monograph*, vol. 4, no. 9, 1998.
- [109] P. Linstrom and W. Mallard, "Nist chemistry webbook, nist standard reference database number 69," *National Institute of Standards and Technology, Gaithersburg MD*, vol. 20899, 2020.
- [110] B. Ruscic and D. Bross, "Active thermochemical tables (atct) values based on ver. 1.122 e of the thermochemical network, argonne national laboratory, 2019," 2019.
- [111] A. Burcat, B. Ruscic, *et al.*, "Third millenium ideal gas and condensed phase thermochemical database for combustion (with update from active thermochemical tables).," tech. rep., Argonne National Lab.(ANL), Argonne, IL (United States), 2005.
- [112] E. R. Ritter and J. W. Bozzelli, "Therm: Thermodynamic property estimation for gas phase radicals and molecules," *Int. J. Chem. Kinet.*, vol. 23, no. 9, pp. 767–778, 1991.

- [113] C. Muller, V. Michel, G. Scacchi, and G.-M. Côme, “Thergas: a computer program for the evaluation of thermochemical data of molecules and free radicals in the gas phase,” *J. Chim. Phys., Phys.-Chim. Biol.*, vol. 92, pp. 1154–1178, 1995.
- [114] E. S. Blurock, V. Warth, X. Grandmougin, R. Bounaceur, P.-A. Glaude, and F. Battin-Leclerc, “Thergas: Thermodynamic estimation from 2d graphical representations of molecules,” *Energy*, vol. 43, no. 1, pp. 161–171, 2012.
- [115] T. Varga, C. Olm, A. Busai, and I. G. Zsély, “Respecth kinetics data format specification v2.2,” *ELTE Eötvös Loránd University, Institute of Chemistry Chemical Kinetics Laboratory*, vol. 2.2, 2019.
- [116] T. Faravelli, E. Ranzi, A. Frassoldati, A. Cuoci, M. Mehl, M. Pelucchi, A. Stagni, P. Debiagi, G. Bagheri, A. Bodor, *et al.*, “The creck modeling group,” 2020.
- [117] H. Curran, “Combustion chemistry centre,” *National University of Ireland Galway, University Road, Galway, Ireland*, 2020.
- [118] S. Peukert, P. Sela, D. Nativel, J. Herzler, M. Fikri, and C. Schulz, “Direct measurement of high-temperature rate constants of the thermal decomposition of dimethoxymethane, a shock tube and modeling study,” *J. Phys. Chem. A*, vol. 122, no. 38, pp. 7559–7571, 2018.
- [119] W. C. M. Lewis, *A System of Physical Chemistry: Kinetic Theory*, vol. 1. Longmans, Green and Company, 1918.
- [120] M. Trautz, “Das gesetz der reaktionsgeschwindigkeit und der gleichgewichte in gasen. bestätigung der additivität von $cv^{-3/2}$. neue bestimmung der integrationskonstanten und der moleküldurchmesser,” *Zeitschrift für anorganische und allgemeine Chemie*, vol. 96, no. 1, pp. 1–28, 1916.
- [121] C. Vallance, *An Introduction to Chemical Kinetics*. Morgan & Claypool Publishers, 2017.
- [122] M. Evans and M. Polanyi, “Further considerations on the thermodynamics of chemical equilibria and reaction rates,” *Trans. Faraday Soc.*, vol. 32, pp. 1333–1360, 1936.
- [123] H. Eyring, “The activated complex in chemical reactions,” *J. Chem. Phys.*, vol. 3, no. 2, pp. 107–115, 1935.
- [124] H. Eyring, “The activated complex and the absolute rate of chemical reactions.,” *Chemical Reviews*, vol. 17, no. 1, pp. 65–77, 1935.
- [125] S. Glasstone, K. J. Laidler, and H. Eyring, “The theory of rate processes; the kinetics of chemical reactions, viscosity, diffusion and electrochemical phenomena,” tech. rep., McGraw-Hill Book Company,, 1941.
- [126] D. McQuarrie, “Statistical mechanics,” 1976.
- [127] H. Avery, “Theory of unimolecular reactions,” in *Basic Reaction Kinetics and Mechanisms*, pp. 71–79, Springer, 1974.

- [128] C. N. Hinshelwood, "On the theory of unimolecular reactions," *Proceedings of the Royal Society of London. Series A, Containing Papers of a Mathematical and Physical Character*, vol. 113, no. 763, pp. 230–233, 1926.
- [129] O. K. Rice and H. C. Ramsperger, "Theories of unimolecular gas reactions at low pressures," *Journal of the American Chemical Society*, vol. 49, no. 7, pp. 1617–1629, 1927.
- [130] O. K. Rice and H. C. Ramsperger, "Theories of unimolecular gas reactions at low pressures. ii," *Journal of the American Chemical Society*, vol. 50, no. 3, pp. 617–620, 1928.
- [131] L. S. Kassel, "Studies in homogeneous gas reactions. i," *J. Phys. Chem.*, vol. 32, no. 2, pp. 225–242, 1928.
- [132] L. S. Kassel, "Studies in homogeneous gas reactions. ii. introduction of quantum theory," *J. Phys. Chem.*, vol. 32, no. 7, pp. 1065–1079, 1928.
- [133] R. A. Marcus, "Unimolecular dissociations and free radical recombination reactions," *J. Chem. Phys.*, vol. 20, no. 3, pp. 359–364, 1952.
- [134] S. Canneaux, F. Bohr, and E. Henon, "Kisthelp: a program to predict thermodynamic properties and rate constants from quantum chemistry results," *J. Comput. Chem.*, vol. 35, no. 1, pp. 82–93, 2014.
- [135] F. A. Berezin and M. Shubin, *The Schrödinger Equation*, vol. 66. Springer Science & Business Media, 2012.
- [136] M. Frisch, G. Trucks, H. B. Schlegel, G. Scuseria, M. Robb, J. Cheeseman, G. Scalmani, V. Barone, B. Mennucci, G. Petersson, *et al.*, "Gaussian 09, revision a. 02, gaussian," *Inc., Wallingford, CT*, vol. 200, p. 28, 2009.
- [137] J. W. Ochterski, "Thermochemistry in gaussian," *Gaussian Inc*, pp. 1–19, 2000.
- [138] W. J. Hehre, R. Ditchfield, L. Radom, and J. A. Pople, "Molecular orbital theory of the electronic structure of organic compounds. v. molecular theory of bond separation," *Journal of the American Chemical Society*, vol. 92, no. 16, pp. 4796–4801, 1970.
- [139] S. W. Benson, *Thermochemical kinetics*. Wiley, New York, 1976.
- [140] R. Van de Vijver, N. M. Vandewiele, P. L. Bhoorasingh, B. L. Slakman, F. Seyedzadeh Khanshan, H.-H. Carstensen, M.-F. Reyniers, G. B. Marin, R. H. West, and K. M. Van Geem, "Automatic mechanism and kinetic model generation for gas-and solution-phase processes: a perspective on best practices, recent advances, and future challenges," *Int. J. Chem. Kinet.*, vol. 47, no. 4, pp. 199–231, 2015.
- [141] A. G. Vandeputte, M. K. Sabbe, M. Reyniers, and G. B. Marin, "Modeling the gas-phase thermochemistry of organosulfur compounds," *Chem – Eur J*, vol. 17, no. 27, pp. 7656–7673, 2011.

- [142] M. K. Sabbe, M. Saeys, M.-F. Reyniers, G. B. Marin, V. Van Speybroeck, and M. Waroquier, "Group additive values for the gas phase standard enthalpy of formation of hydrocarbons and hydrocarbon radicals," *J. Phys. Chem. A*, vol. 109, no. 33, pp. 7466–7480, 2005.
- [143] N. Cohen and S. Benson, "Estimation of heats of formation of organic compounds by additivity methods," *Chem. Rev.*, vol. 93, no. 7, pp. 2419–2438, 1993.
- [144] P. D. Paraskevas, M. K. Sabbe, M. Reyniers, N. Papayannakos, and G. B. Marin, "Group additive values for the gas-phase standard enthalpy of formation, entropy and heat capacity of oxygenates," *Chem. Eur. J.*, vol. 19, no. 48, pp. 16431–16452, 2013.
- [145] M. K. Sabbe, F. De Vleeschouwer, M.-F. Reyniers, M. Waroquier, and G. B. Marin, "First principles based group additive values for the gas phase standard entropy and heat capacity of hydrocarbons and hydrocarbon radicals," *J. Phys. Chem. A*, vol. 112, no. 47, pp. 12235–12251, 2008.
- [146] K. R. Bjorkman, C.-Y. Sung, E. Mondor, J. C. Cheng, D.-Y. Jan, and L. J. Broadbelt, "Group additivity determination for enthalpies of formation of carbenium ions," *Ind Eng Chem Res*, vol. 53, no. 50, pp. 19446–19452, 2014.
- [147] C. W. Gao, J. W. Allen, W. H. Green, and R. H. West, "Reaction mechanism generator: Automatic construction of chemical kinetic mechanisms," *Comput. Phys. Commun.*, vol. 203, pp. 212–225, 2016.
- [148] R. H. West, J. W. Allen, and W. H. Green, "Automatic reaction mechanism generation with group additive kinetics," *ChemInform*, vol. 43, no. 36, p. no, 2012.
- [149] G. E. P. Box and K. B. Wilson, "On the experimental attainment of optimum conditions," *J. R. Stat. Soc. B*, vol. 13, no. 1, pp. 1–45, 1951.
- [150] N. Sikalo, O. Hasemann, C. Schulz, A. Kempf, and I. Wlokas, "A genetic algorithm-based method for the optimization of reduced kinetics mechanisms," *Int. J. Chem. Kinet.*, vol. 47, no. 11, pp. 695–723, 2015.
- [151] D. E. Goldberg and K. Deb, "A comparative analysis of selection schemes used in genetic algorithms," in *Foundations of genetic algorithms*, vol. 1, pp. 69–93, Elsevier, 1991.
- [152] T. Blickle and L. Thiele, "A comparison of selection schemes used in evolutionary algorithms," *Evolutionary Computation*, vol. 4, no. 4, pp. 361–394, 1996.
- [153] K. A. De Jong, "Analysis of the behavior of a class of genetic adaptive systems," tech. rep., The University of Michigan, 1975.
- [154] Z. Michalewicz, *Genetic algorithms+ data structures= evolution programs*. Springer Science & Business Media, 2013.
- [155] W. M. Spears and K. D. De Jong, "On the virtues of parameterized uniform crossover," tech. rep., Naval Research Lab Washington DC, 1995.

- [156] U. Bhowan, M. Johnston, and M. Zhang, "Developing new fitness functions in genetic programming for classification with unbalanced data," *IEEE Transactions on Systems, Man, and Cybernetics, Part B (Cybernetics)*, vol. 42, no. 2, pp. 406–421, 2011.
- [157] I. Wlokas, A. Faccinetto, B. Tribalet, C. Schulz, and A. Kempf, "Mechanism of iron oxide formation from iron pentacarbonyl-doped low-pressure hydrogen/oxygen flames," *Int. J. Chem. Kinet.*, vol. 45, no. 8, pp. 487–498, 2013.
- [158] A. T. Balaban, "Applications of graph theory in chemistry," *Journal of chemical information and computer sciences*, vol. 25, no. 3, pp. 334–343, 1985.
- [159] S. A. Vázquez, X. L. Otero, and E. Martínez-Núñez, "A trajectory-based method to explore reaction mechanisms," *Molecules*, vol. 23, no. 12, p. 3156, 2018.
- [160] T. Lu and C. K. Law, "A directed relation graph method for mechanism reduction," *Proc. Combust. Inst.*, vol. 30, no. 1, pp. 1333–1341, 2005.
- [161] T. Umeda, T. Kuriyama, E. Oshima, and H. Matsuyama, "A graphical approach to cause and effect analysis of chemical processing systems," *Chem. Eng. Sci.*, vol. 35, no. 12, pp. 2379–2388, 1980.
- [162] M. Bastian, S. Heymann, and M. Jacomy, "Gephi: an open source software for exploring and manipulating networks," in *Third international AAAI conference on weblogs and social media*, 2009.
- [163] D. Goodwin, H. K. Moffat, and R. L. Speth, "Cantera: An object-oriented software toolkit for chemical kinetics, thermodynamics, and transport processes," *Caltech, Pasadena, CA*, 2009.
- [164] R. J. Kee, F. M. Rupley, and J. A. Miller, "Chemkin-ii: A fortran chemical kinetics package for the analysis of gas-phase chemical kinetics," tech. rep., Sandia National Labs., Livermore, CA (USA), 1989.
- [165] T. Hülser, S. M. Schnurre, H. Wiggers, and C. Schulz, "Gas-phase synthesis of nanoscale silicon as an economical route towards sustainable energy technology," *KONA Powder Part J*, vol. 29, pp. 191–207, 2011.
- [166] N. Petermann, N. Stein, G. Schierning, R. Theissmann, B. Stoib, M. S. Brandt, C. Hecht, C. Schulz, and H. Wiggers, "Plasma synthesis of nanostructures for improved thermoelectric properties," *J. Phys. D: Appl. Phys.*, vol. 44, no. 17, p. 174034, 2011.
- [167] T. Miller, M. Wooldridge, and J. Bozzelli, "Computational modeling of the $\text{SiH}_3 + \text{O}_2$ reaction and silane combustion," *Combust. Flame.*, vol. 137, no. 1-2, pp. 73–92, 2004.
- [168] J. A. Britten, J. Tong, and C. K. Westbrook, "A numerical study of silane combustion," *Proc. Combust. Inst.*, vol. 23, no. 1, pp. 195–202, 1991.
- [169] L. A. Curtiss, P. C. Redfern, and K. Raghavachari, "Gaussian-4 theory," *J. Phys. Chem.*, vol. 126, no. 8, pp. 084–108, 2007.
- [170] A. Miyoshi, "Gpop software, rev. 2013.07. 15m7," available from the author, 2013.

- [171] S. R. Gunn and L. G. Green, "The heats of formation of some unstable gaseous hydrides," *J. Phys. Chem.*, vol. 65, no. 5, pp. 779–783, 1961.
- [172] S. R. Gunn and L. G. Green, "The heats of formation of trisilane and trigermane," *J. Phys. Chem.*, vol. 68, no. 4, pp. 946–949, 1964.
- [173] A. M. Doncaster and R. Walsh, "Thermochemistry of silicon-containing compounds. part 2. the enthalpies of formation of the methylsilanes, an experimental study and review," *J. Chem. Soc., Faraday Trans. 2*, vol. 82, no. 4, pp. 707–717, 1986.
- [174] W. Steele, "The standard molar enthalpies of formation of organosilicon compounds and related bond-dissociation enthalpies ii. tetramethylsilane," *J. Chem. Thermodyn*, vol. 15, no. 6, pp. 595–601, 1983.
- [175] R. Becerra and R. Walsh, "Some hazards of electronegativity correlations," *J. Phys. Chem. A*, vol. 101, no. 47, pp. 8959–8963, 1997.
- [176] D. Feller and D. A. Dixon, "Theoretical study of the heats of formation of small silicon-containing compounds," *J. Phys. Chem. A*, vol. 103, no. 32, pp. 6413–6419, 1999.
- [177] J. A. Montgomery Jr, M. J. Frisch, J. W. Ochterski, and G. A. Petersson, "A complete basis set model chemistry. vii. use of the minimum population localization method," *J Chem Phys*, vol. 112, no. 15, pp. 6532–6542, 2000.
- [178] J. M. Martin and G. de Oliveira, "Towards standard methods for benchmark quality ab initio thermochemistry—w1 and w2 theory," *J Chem Phys*, vol. 111, no. 5, pp. 1843–1856, 1999.
- [179] M. D. Allendorf and C. F. Melius, "Theoretical study of the thermochemistry of molecules in the silicon-carbon-hydrogen system," *J. Phys. Chem.*, vol. 96, no. 1, pp. 428–437, 1992.
- [180] P. Ho and C. F. Melius, "Theoretical study of the thermochemistry of molecules in the Si-OHC system," *J. Phys. Chem.*, vol. 99, no. 7, pp. 2166–2176, 1995.
- [181] J. M. Simmie and K. P. Somers, "Benchmarking compound methods (cbs-qb3, cbs-apno, g3, g4, w1bd) against the active thermochemical tables: A litmus test for cost-effective molecular formation enthalpies," *J. Phys. Chem. A*, vol. 119, no. 28, pp. 7235–7246, 2015.
- [182] K. P. Somers and J. M. Simmie, "Benchmarking compound methods (cbs-qb3, cbs-apno, g3, g4, w1bd) against the active thermochemical tables: Formation enthalpies of radicals," *J. Phys. Chem. A*, vol. 119, no. 33, pp. 8922–8933, 2015.
- [183] G. Lewis and M. Randall, "Thermodynamics and the free energy of chemical substances," *Thermodynamics*, 1923.
- [184] F. J. Zeleznik and S. Gordon, "Simultaneous least-squares approximation of a function and its first integrals with application to thermodynamic data," *NASA Technical Note D-767*, 1961., 1961.

- [185] R. Wilhoit, *Thermodynamics research center current data news*, vol. 3. NIST, 1975.
- [186] H. Janbazi, Y. Karakaya, T. Kasper, C. Schulz, I. Wlokas, and S. Peukert, "Development and evaluation of a chemical kinetics reaction mechanism for tetramethylsilane-doped flames," *Chem. Eng. Sci.*, vol. 209, p. 115209, 2019.
- [187] N. Cohen, "Revised group additivity values for enthalpies of formation (at 298 k) of carbon–hydrogen and carbon–hydrogen–oxygen compounds," *J. Phys. Chem. Ref. Data*, vol. 25, no. 6, pp. 1411–1481, 1996.
- [188] L. A. Curtiss, P. C. Redfern, and K. Raghavachari, "Gaussian-4 theory using reduced order perturbation theory," *J. Chem. Phys.*, vol. 127, no. 12, p. 124105, 2007.
- [189] S. K. Shin, K. K. Irikura, J. Beauchamp, and W. A. Goddard, "Thermochemistry of silaethylene and methylsilylene from experiment and theory," *J. Am. Chem. Soc.*, vol. 110, no. 1, pp. 24–30, 1988.
- [190] W. G. K.S. Pitzer, "Energy levels and thermodynamic functions for molecules with internal rotation i. rigid frame with attached tops," *J. Chem. Phys.*, vol. 10, no. 7, pp. 428–440, 1942.
- [191] N. R. Draper and H. Smith, *Applied regression analysis*, vol. 326. New York: John Wiley & Sons, 1998.
- [192] G. Pilcher, M. L. P. Leitão, Y. Meng-Yan, and R. Walsh, "Standard enthalpy of formation of hexamethyldisilane," *Journal of the Chemical Society, Faraday Transactions*, vol. 87, no. 6, pp. 841–845, 1991.
- [193] J. A. Boatz and M. S. Gordon, "Predicted enthalpies of formation for methyl-substituted disilanes," *J. Phys. Chem.*, vol. 94, no. 10, pp. 3874–3876, 1990.
- [194] J. Z. Dávalos and T. Baer, "Thermochemistry and dissociative photoionization of $\text{si}(\text{ch}_3)_4$, $\text{brsi}(\text{ch}_3)_3$, $\text{isi}(\text{ch}_3)_3$, and $\text{si}_2(\text{ch}_3)_6$ studied by threshold photoelectron-photoion coincidence spectroscopy," *J. Phys. Chem. A*, vol. 110, no. 27, pp. 8572–8579, 2006.
- [195] T. Brix, N. Arthur, and P. Potzinger, "Stationary and pulsed photolysis and pyrolysis of 1, 1-dimethylsilacyclobutane," *J. Phys. Chem.*, vol. 93, no. 25, pp. 8193–8197, 1989.
- [196] M. Frenklach, L. Ting, H. Wang, and M. J. Rabinowitz, "Silicon particle formation in pyrolysis of silane and disilane," *Israel Journal of Chemistry*, vol. 36, no. 3, pp. 293–303, 1996.
- [197] T. Yamada, T. H. Lay, and J. W. Bozzelli, "Ab initio calculations and internal rotor: contribution for thermodynamic properties s 298 and c p (t)'s (300< t/k< 1500): group additivity for fluoroethanes," *J. Phys. Chem. A*, vol. 102, no. 37, pp. 7286–7293, 1998.
- [198] L. D. Dellon, C.-Y. Sung, D. J. Robichaud, and L. J. Broadbelt, "Group additivity determination for oxygenates, oxonium ions, and oxygen-containing carbenium ions," *Ind. Eng. Chem. Res.*, vol. 56, no. 37, pp. 10259–10270, 2017.

- [199] J. A. Montgomery Jr, M. J. Frisch, J. W. Ochterski, and G. A. Petersson, "A complete basis set model chemistry. vi. use of density functional geometries and frequencies," *J. Chem. Phys.*, vol. 110, no. 6, pp. 2822–2827, 1999.
- [200] B. Ruscic, R. E. Pinzon, M. L. Morton, G. von Laszewski, S. J. Bittner, S. G. Nijssure, K. A. Amin, M. Minkoff, and A. F. Wagner, "Introduction to active thermochemical tables: Several "key" enthalpies of formation revisited," *J. Phys. Chem. A*, vol. 108, no. 45, pp. 9979–9997, 2004.
- [201] B. Ruscic, "Uncertainty quantification in thermochemistry, benchmarking electronic structure computations, and active thermochemical tables," *International Journal of Quantum Chemistry*, vol. 114, no. 17, pp. 1097–1101, 2014.
- [202] B. Ruscic, R. E. Pinzon, G. Von Laszewski, D. Kodeboyina, A. Burcat, D. Leahy, D. Montoy, and A. F. Wagner, "Active thermochemical tables: thermochemistry for the 21st century," in *Journal of Physics: Conference Series*, vol. 16, p. 561, IOP Publishing, 2005.
- [203] H. Janbazi, C. Schulz, I. Wlokas, H. Wang, and S. Peukert, "Thermochemistry of organosilane compounds and organosilyl radicals," *Proc. Combust. inst.*, vol. 38, 2020.
- [204] M. D. Allendorf, C. F. Melius, P. Ho, and M. R. Zachariah, "Theoretical study of the thermochemistry of molecules in the Si-OH system," *J. Phys. Chem.*, vol. 99, no. 41, pp. 15285–15293, 1995.
- [205] H. Krieg and S. Grimme, "Thermochemical benchmarking of hydrocarbon bond separation reaction energies: Jacob's ladder is not reversed!," *Molecular Physics*, vol. 108, no. 19-20, pp. 2655–2666, 2010.
- [206] I. M. Davidson, C. E. Dean, and F. T. Lawrence, "Kinetics of addition of 2-methyl-2-silapropene to hydrogen chloride, hydrogen bromide, and oxygen," *J. Chem. Soc. Chem. Comm.*, vol. 2, pp. 52–53, 1981.
- [207] R. Alleni, P. Kochs, and G. Chandra, "Industrial organosilicon materials, their environmental entry and predicted fate," in *Organosilicon materials*, pp. 1–25, Springer, 1997.
- [208] Y. Qi, Z. Xiao, and T. Mantei, "Comparison of silicon dioxide layers grown from three polymethylsiloxane precursors in a high-density oxygen plasma," *Journal of Vacuum Science & Technology A: Vacuum, Surfaces, and Films*, vol. 21, no. 4, pp. 1064–1068, 2003.
- [209] M. Voronkov, V. Klyuchnikov, E. Mironenko, G. Shvets, T. Danilova, and Y. I. Khudobin, "Thermochemistry of organosilicon compounds: V. thermochemical properties of perorganyloligocyclosiloxanes," *Journal of organometallic chemistry*, vol. 406, no. 1-2, pp. 91–97, 1991.
- [210] T. Tanaka, "Heats of formation of lower members of dimethyl- and methylisopropoxy-cyclopolysiloxanes," *Bulletin of the Chemical Society of Japan*, vol. 33, no. 3, pp. 282–286, 1960.

- [211] T. Tanaka, U. Takahashi, R. Okawara, and T. Watase, "Heats of combustion and formation of some organosilicon compounds," *J. Chem. Phys.*, vol. 19, no. 10, pp. 1330–1330, 1951.
- [212] T. Tanaka, U. Takahashi, R. Okawara, and T. Watase, "Erratum: Heats of combustion and formation of some organosilicon compounds," *J. Chem. Phys.*, vol. 22, no. 5, pp. 957–957, 1954.
- [213] J. Tamas, Á. Gömöry, I. Besenyei, O. Nefedov, V. Khabashesku, Z. Kerzina, N. Kagramanov, and A. Maltsev, "Mass spectrometric evidences for the formation of unstable 1, 1, 3, 3-tetramethyl-1, 3-cyclodisiloxane in the gas phase," *Journal of organometallic chemistry*, vol. 349, no. 1-2, pp. 37–41, 1988.
- [214] C. R. A. Catlow, S. T. Bromley, S. Hamad, M. Mora-Fonz, A. A. Sokol, and S. M. Woodley, "Modelling nano-clusters and nucleation," *Phys. Chem. Chem. Phys.*, vol. 12, no. 4, pp. 786–811, 2010.
- [215] P. Buerger, J. Akroyd, S. Mosbach, and M. Kraft, "A systematic method to estimate and validate enthalpies of formation using error-cancelling balanced reactions," *Combust. Flame*, vol. 187, pp. 105–121, 2018.
- [216] S. E. Pratsinis, "Flame aerosol synthesis of ceramic powders," *Prog. Energy Combust. Sci.*, vol. 24, no. 3, pp. 197–219, 1998.
- [217] D. Lindackers, M. Strecker, P. Roth, C. Janzen, and S. E. Pratsinis, "Formation and growth of SiO₂ particles in low pressure H₂/O₂/Ar flames doped with SiH₄," *Combust. Sci. Technol.*, vol. 123, no. 1-6, pp. 287–315, 1997.
- [218] J. Chen, Z. Huang, and L. Zheng, "Detailed OMCTS/H₂/O₂ chemical kinetics mechanism and its application in the fused silica glass synthesis," *J. Non-Cryst. Solids*, vol. 481, pp. 33–40, 2018.
- [219] N. Bahlawane, U. Struckmeier, T. S. Kasper, and P. Oßwald, "Noncatalytic thermocouple coatings produced with chemical vapor deposition for flame temperature measurements," *Rev. Sci. Instrum.*, vol. 78, no. 1, p. 013905, 2007.
- [220] T. A. Cool, K. Nakajima, C. A. Taatjes, A. McIlroy, P. R. Westmoreland, M. E. Law, and A. Morel, "Studies of a fuel-rich propane flame with photoionization mass spectrometry," *Proc. Combust. Inst.*, vol. 30, no. 1, pp. 1681–1688, 2005.
- [221] U. Struckmeier, P. Oßwald, T. Kasper, L. Böhling, M. Heusing, M. Köhler, A. Brockhinke, and K. Kohse-Höinghaus, "Sampling probe influences on temperature and species concentrations in molecular beam mass spectroscopic investigations of flat premixed low-pressure flames," *Z. Phys. Chem.*, vol. 223, no. 4-5, pp. 503–537, 2009.
- [222] J. Simmie and J. Sheahan, "Validation of a database of formation enthalpies and of mid-level model chemistries," *J. Phys. Chem. A*, vol. 120, no. 37, pp. 7370–7384, 2016.
- [223] L. Gusel'nikov and N. Nametkin, "1, 1-dimethyl-1-silaethylene: Heat of formation, ionization potential and the energy of the silicon-carbon π -bond," *Journal of Organometallic Chemistry*, vol. 169, no. 2, pp. 155–164, 1979.

- [224] M. Ó Conaire, H. J. Curran, J. M. Simmie, W. J. Pitz, and C. K. Westbrook, "A comprehensive modeling study of hydrogen oxidation," *Int. J. Chem. Kinet.*, vol. 36, no. 11, pp. 603–622, 2004.
- [225] T. Varga, C. Olm, T. Nagy, I. G. Zsély, E. Valkó, R. Pálvölgyi, H. J. Curran, and T. Turányi, "Development of a joint hydrogen and syngas combustion mechanism based on an optimization approach," *Int. J. Chem. Kinet.*, vol. 48, no. 8, pp. 407–422, 2016.
- [226] S. Peukert, J. Herzler, M. Fikri, and C. Schulz, "High-temperature rate constants for H + tetramethylsilane and H + silane and implications about structure–activity relationships for silanes," *Int. J. Chem. Kinet.*, vol. 50, no. 1, pp. 57–72, 2018.
- [227] A. T. Hartlieb, B. Atakan, and K. Kohse-Höinghaus, "Effects of a sampling quartz nozzle on the flame structure of a fuel-rich low-pressure propene flame," *Combust. Flame*, vol. 121, no. 4, pp. 610–624, 2000.
- [228] R. Sivaramakrishnan, N. Srinivasan, M.-C. Su, and J. Michael, "High temperature rate constants for OH + alkanes," *Proc. Combust. Inst.*, vol. 32, no. 1, pp. 107–114, 2009.
- [229] N. Cohen and K. Westberg, "Chemical kinetic data sheets for high-temperature reactions. part ii," *J. Phys. Chem. Ref. Data*, vol. 20, no. 6, pp. 1211–1311, 1991.
- [230] H. J. Curran, "Rate constant estimation for C1 to C4 alkyl and alkoxy radical decomposition," *Int. J. Chem. Kinet.*, vol. 38, no. 4, pp. 250–275, 2006.
- [231] I. M. Davidson and J. F. Thompson, "Kinetics of the oxidation of octamethylcyclotetrasiloxane in the gas phase," *J. Chem. Soc., Faraday Trans. I*, vol. 72, pp. 1088–1095, 1976.
- [232] G. Smith and D. Golden, "Application of RRKM theory to the reactions $\text{OH} + \text{NO}_2 + \text{N}_2 \rightarrow \text{HONO}_2 + \text{N}_2$ (1) and $\text{ClO} + \text{NO}_2 + \text{N}_2 \rightarrow \text{ClONO}_2 + \text{N}_2$ (2); a modified gorin model transition state," *Int. J. Chem. Kinet.*, vol. 10, no. 5, pp. 489–501, 1978.
- [233] N. Srinivasan, J. Kiefer, and R. Tranter, "Dissociation, relaxation, and incubation in the pyrolysis of neopentane: heat of formation for tert-butyl radical," *J. Phys. Chem. A*, vol. 107, no. 10, pp. 1532–1539, 2003.
- [234] V. Khabashesku, Z. Kerzina, E. Baskir, A. Maltsev, and O. Nefedov, "Direct spectroscopic study of unstable molecules with silicon oxygen multiple bonds: low temperature matrix stabilization of $(\text{CH}_3)_2\text{SiO}$ and $(\text{CD}_3)_2\text{SiO}$ in the gas phase," *J. Organomet. Chem.*, vol. 347, no. 3, pp. 277–293, 1988.
- [235] C. Yeh, E. Zhao, and H. Ma, "Combustion synthesis of SiO_2 on the aluminum plate," *J. Therm. Sci.*, vol. 10, no. 1, pp. 92–96, 2001.
- [236] H. Ma, E. Zhao, C. Yeh, and K. Chung, "The formation of nano-size SiO_2 thin film on an aluminum plate with hexamethyldisilazane (HMDSA) and hexamethyldisiloxane (HMDSO)," *J. Therm. Sci.*, vol. 12, no. 1, pp. 89–96, 2003.

-
- [237] M. R. Zachariah and W. Tsang, "Theoretical calculation of thermochemistry, energetics, and kinetics of high-temperature $\text{Si}_x\text{H}_y\text{O}_z$ reactions," *J. Phys. Chem.*, vol. 99, no. 15, pp. 5308–5318, 1995.
- [238] O. M. Feroughi, S. Hardt, I. Wlokas, T. Hülser, H. Wiggers, T. Dreier, and C. Schulz, "Laser-based in situ measurement and simulation of gas-phase temperature and iron atom concentration in a pilot-plant nanoparticle synthesis reactor," *Proc. Combust. Inst.*, vol. 35, no. 2, pp. 2299–2306, 2015.
- [239] J. M. Plane, J. C. Gómez-Martín, W. Feng, and D. Janches, "Silicon chemistry in the mesosphere and lower thermosphere," *J. Geophys. Res. Atmos.*, vol. 121, no. 7, pp. 3718–3728, 2016.
- [240] C. Xu, W. Wang, W. Zhang, J. Zhuang, L. Liu, Q. Kong, L. Zhao, Y. Long, K. Fan, and S. Qian, "Magic numbers in silicon dioxide-based clusters," *J. Phys. Chem. A*, vol. 104, no. 42, pp. 9518–9524, 2000.
- [241] A. Y. Timoshkin, "Gas phase generation of Si-OH clusters: an ab initio study of structural and thermodynamic properties," in *High Temperature Corrosion and Materials Chemistry III: Proceedings of the International Symposium*, p. 262, Proc. Electrochem. Soc., 2001.
- [242] S.-M. Suh, M. Zachariah, and S. Girshick, "Modeling particle formation during low-pressure silane oxidation: Detailed chemical kinetics and aerosol dynamics," *J. Vac. Sci. Technol. A*, vol. 19, no. 3, pp. 940–951, 2001.
- [243] H. Janbazi, C. Schulz, I. Wlokas, and S. Peukert, "Thermochemistry of oxygen-containing organosilane radicals and uncertainty estimations of organosilane group-additivity values," *The Journal of Physical Chemistry A*, 2021.

Appendix A

The author's other publications

This chapter gives a brief overview of the papers that the author of this thesis contributed which are not directly related to this thesis but helped the author to be able to finish this thesis.

A.1 Thermochemistry of Oxygen-Containing Organosilane Radicals and Uncertainty Estimations of Organosilane Group-Additivity Values

Authors: H. Janbazi, C. Schulz, I. Wlokas, S. Peukert

The paper is published in 'The Journal of Physical Chemistry A' [243]. The abstract is reprinted with permission from American Chemical Society. This paper is published after the original submission date of this dissertation. It is not considered in the examination process of this dissertation.

Abstract

Si–C–H–O-containing radicals are important intermediates during the combustion and pyrolysis of precursors applied for the gas-phase synthesis of silica nanoparticles. Despite the industrial importance of silica nanoparticles, a comprehensive thermodynamics database of organosilane species is still missing. This work presents thermochemical data of 91 Si–C–H–O radical species. Quantum-chemical calculations and isodesmic reaction schemes are used to determine the standard enthalpy of formation, entropy, and heat capacities covering the 298–2000 K temperature range. In addition, 90 group-additivity values (GAVs) are calculated, which cover all relevant group increments. A combinatorial approach is used

to ensure that all possible group increments are considered. The theoretically calculated species are used as a training set to derive 90 GAVs of Si–C–H–O radical species for the first time. In addition, uncertainty contributions of GAVs were estimated. These uncertainty estimates also comprise GAVs that were previously derived to compute thermochemical data of stable Si–C–H species and radicals as well as stable Si–C–H–O compounds. Therefore, uncertainty contributions of GAVs for a whole set of 243 group increments used to predict thermochemical data of Si-organic species are reported.

A.2 Experimental and numerical study on the influence of equivalence ratio on key intermediates and silica nanoparticles in flame synthesis

Authors: Y. Karakaya, H. Janbazi, I. Wlokas, A. Levish, M. Winterer, T. Kasper

The paper is published in 'Proceedings of the Combustion Institute 38 (2021) 1375-1383'.

The abstract and the contribution of the author of this work to this paper are reprinted with permission from Elsevier.

Abstract

Tetramethylsilane is a precursor often used for the production of flame-synthesized silica nanoparticles or coatings. This study investigates the chemical reaction mechanism of tetramethylsilane in a series of H₂/O₂/Ar low-pressure (p=30 mbar) flames from fuel-lean to slightly fuel-rich flame conditions ($\phi = 0.8, 1.0$ and 1.2). Mole fraction profiles are obtained by molecular-beam mass spectrometry. The experimental data are compared to simulations using a recently published reaction mechanism. The present study reveals the influence of the flame composition on the depletion of the precursor TMS, the formation of its main carbon-containing products (e.g. CO₂ and CO) and the main silicon-containing intermediates (e.g. Si(CH₃)₃(CH₂)OO), Si(OH)₄, SiO₂, Si₄O₁₀H₄) appearing along the routes of particle formation. TEM images of synthesized particles reveal that the nanoparticles obtained from the gas-phase synthesis are spheres with a low degree of agglomeration. The particle size distribution appears to be dependent on the equivalence ratio of the synthesis flames and the changes can tentatively be traced to different particle formation pathways. The data set provided in this work can serve a basis for improvements to the reaction mechanisms of the Si–O–C–H system that are urgently needed to improve particle synthesis processes.

Validation of developed mechanism for constant load of TMS at different equivalence ratios

Figure A.1a compares the temperature profiles of the doped and the undoped flames with different equivalence ratios. The maximum temperature is almost identical in the neat and doped flames of identical equivalence ratio, but the temperatures in the reaction zone are about 100 K higher. The temperature decrease in the exhaust gas is less pronounced in the doped flames. Both observations, can be explained by exothermic reactions of TMS oxidation close to the burner and exothermic hydrolysis reactions of silicon-containing intermediates in the exhaust gas. Figure A.1 shows measured and simulated main species profiles for the systematic change of equivalence ratios (ϕ) between $\phi = 0.6, 0.8, 1.0, 1.2$. For sake of comparison, the equivalence ratio $\phi = 0.6$ from the previous work of Karakaya et al. [81] is included.

The simulated and measured mole fraction profiles of the main species H_2 , O_2 , H_2O are in a very good agreement. Small deviations occur close to the burner surface. These can be traced for all species to the influence of the burner surface and the quartz-probe on the flame structure as discussed before, e.g. in a study of Deng et al. [83]. The hydrogen and oxygen are consumed in the reaction zone of the flame and reach equilibrium values around $HAB = 15$ mm in all flames. Water also reaches an equilibrium value at the same HAB . TMS is consumed completely at $HAB = 10$ mm (see Fig. A.1f). As a consequence, the TMS consumption occurs at very different flame conditions for the flames of different equivalence ratios. The oxygen mole fraction is approximately 50% higher, the hydrogen mole fraction is 30% lower, and the water mole fraction differs by 40% between the flames with $\phi = 0.6$ and $\phi = 1.2$ in the TMS destruction region. The profiles of the other equivalence ratios fall between the profiles of the flames with the largest and smallest equivalence ratio. The flame temperatures rise at $HAB = 10$ mm to 1000 K for all doped flames. It can be observed that the addition of TMS shifts all main species profiles closer to the burner surface as a result of the temperature rise in the reaction zone.

The comparison of measured and simulated TMS profiles in Figure A.1f reveals significant deviations. The simulated mole fraction profiles show a convex-down behavior and the experiments a convex-up behavior, for all equivalence ratios. The difference in profile shape can be explained by the effect of the sampling-probe on the flow- and temperature field of the flame. In addition, the simulations predict a much faster TMS destruction than observed in the experiments, that was also observed in the original reaction mechanism development work [11]. TMS destruction is dominated by hydrogen abstraction reactions from TMS by O, H and OH radicals. The rate coefficient for the hydrogen abstraction from TMS by H

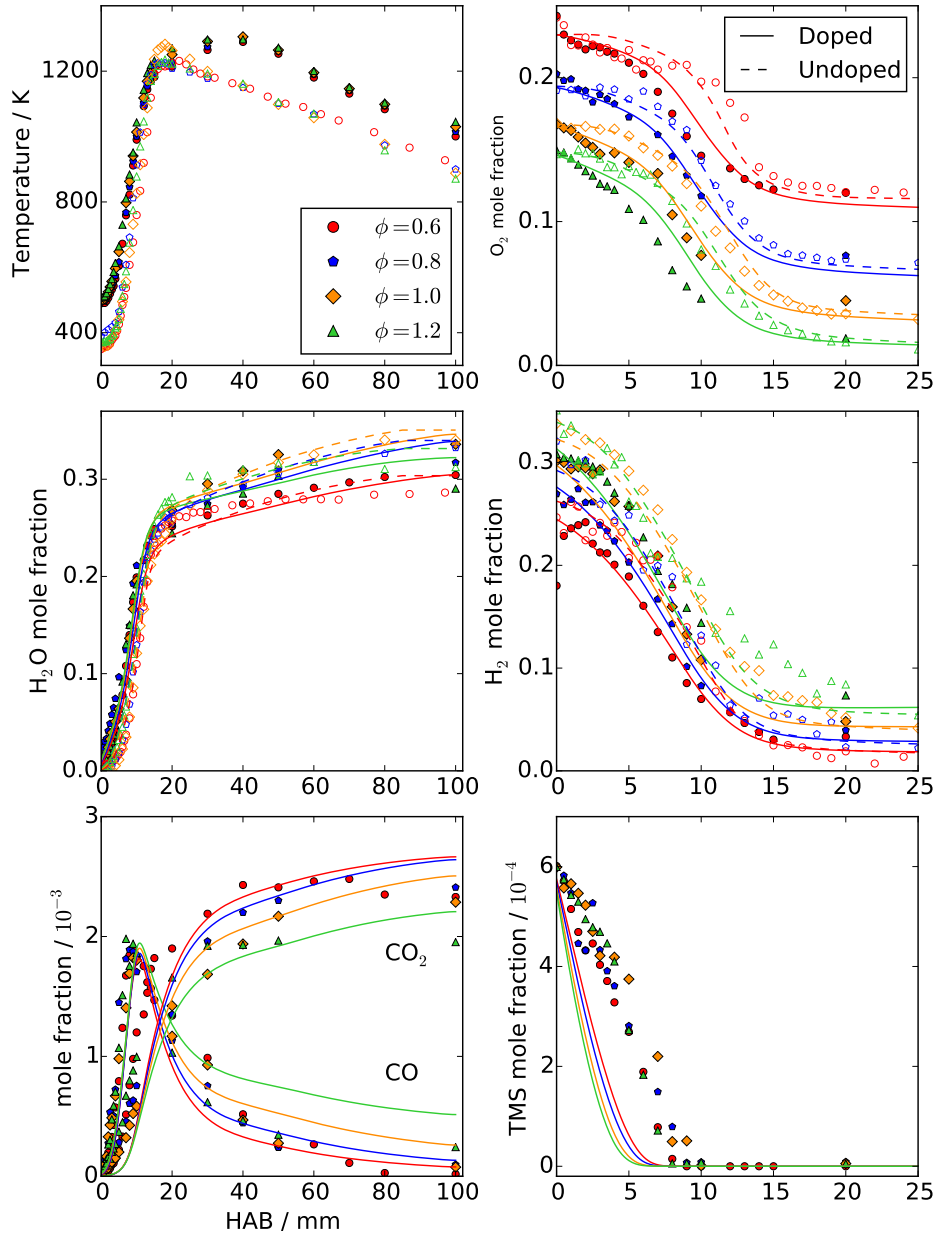


Fig. A.1 Measured (symbols) and simulated (lines) mole fraction profiles of main species (e.g. H_2 , H_2O , TMS , O_2 , CO , CO_2) and temperature profiles in neat (open symbols) and doped (closed symbols) $\text{H}_2/\text{O}_2/\text{Ar}/\text{TMS}$ -flames. Error bars show the uncertainties of measured temperature and mole fractions.

radicals is among the few rate coefficients in the Si/C/H/O system that has been accurately measured by Peukert et al. [226].

The rate coefficients for the hydrogen abstraction by other radicals have been estimated with reasonable accuracy based on analogies of H-abstraction from neopentane. These

reaction rates were not changed in the reaction mechanism optimization. The reactions with OH and H radicals contribute strongly to the decomposition of TMS for equivalence ratios investigated here, while the reaction with O radicals plays only a minor role. The importance of the H-abstraction by H radicals increases with increasing equivalence ratios in agreement with the larger H radical mole fractions, while importance of the reaction with OH radicals is unaffected. The fact that the overestimation of the reaction rate of TMS in the experiments is also independent of the flame conditions, e.g. independent of mole fractions of O, H and OH radicals, suggests that the discrepancies in the TMS consumption rate are most likely linked to the H-abstraction reaction by OH radicals.

Figure A.1e presents measured and simulated mole fraction profiles of the CO₂ and CO formed during oxidation of the TMS. The carbon monoxide profiles peak around HAB= 10 mm, so at the same HAB where all TMS is consumed. In all flames, the CO is further oxidized to CO₂ reaching equilibrium values close to 2400 ppm. Carbon is only introduced into the gas mixture by the TMS addition (2400 ppm). From the carbon balance, it is evident that all carbon is converted to CO and subsequently CO₂ at high HAB, which is desirable in the synthesis of ultrapure silicon-oxide particles. The simulation reproduces the measured CO₂ and CO mole fraction profiles quite well, but deviations appear close to the burner due to probe perturbations. Deviations between measured and simulated CO₂ mole fractions at higher distances are slightly larger than the expected error limit of 15%. They can be explained by a stream stall of the one-dimensional flow field leading to a source for further perturbations.

The comparison of the experimental and simulated mole fraction values demonstrates that the reaction mechanism reproduces the overall flame chemistry with and without addition of TMS well. This is a prerequisite for further analysis and interpretation of observations using the simulations.

Figure A.2a reports measured and simulated mole fraction profiles of SiO₂, Si(OH)₄, Si₄O₁₀H₄ that are important intermediates of particle formation pathway. These species are formed from the initial intermediates and peak at HAB ≥ 10 mm. According to the reaction mechanism, two distinct pathways lead to the formation of silica nanoparticles. The first pathway forms SiO, which condenses to SiO₂ nanoparticles. Condensation of Si(OH)₄ to larger clusters such as Si₄O₁₀H₄ which in turn form silica nanoparticles constitutes the second pathway.

The measured and simulated mole fraction profiles of SiO₂ in Figure A.2a have their maxima near HAB= 10 mm at 1000 K. SiO₂ is consumed slowly in the exhaust gas. The maximum mole fraction of SiO₂ decreases with increasing equivalence ratio and reach the detection limit in the richest flame H. The simulations predict the measured profiles within

the accuracy of the data. According to the reaction path analysis at $\phi = 1$ and HAB= 10 mm SiO_2 is mainly formed by the reaction $\text{SiO} + \text{O}_2 = \text{SiO}_2 + \text{O}$, so consequently less SiO_2 is formed with increasing equivalence ratio because less oxygen is available in the exhaust. It is conceivable that as a consequence more SiO could react to nanoparticles. Figure A.2

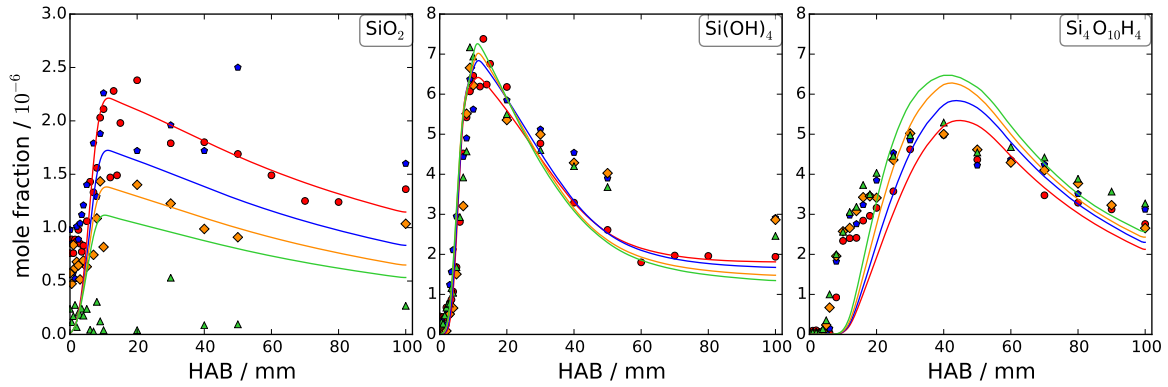


Fig. A.2 Measured (symbols) and simulated (lines) mole fraction profiles of SiO_2 , Si(OH)_4 , and $\text{Si}_4\text{O}_{10}\text{H}_4$ in TMS-doped $\text{H}_2/\text{O}_2/\text{Ar}$ -flames.

presents measured and simulated mole fraction profiles of Si(OH)_4 . The simulation captures the measurements within the absolute uncertainties of the data. Species like Si(OH)_4 are quantified using estimated ionization efficiencies and have large absolute uncertainties of a factor of two. In addition, the model was optimized in the work of Janbazi et al. [186], to fit the absolute mole fractions in flame B, so that a good match of experiment and simulation is expected. When comparing profiles from different equivalence ratios, the uncertainties in the ionization efficiency can be neglected because they will shift the mole fraction values in the same direction.

Figure A.2 shows measured and simulated mole fraction profiles of $\text{Si}_4\text{O}_{10}\text{H}_4$. According to the reaction pathways for HAB= 10 mm and HAB= 20 mm, the first cluster $\text{Si}_4\text{O}_{10}\text{H}_4$ is formed through $\text{Si(OH)}_3 + \text{OH} = 0.5\text{Si}_2(\text{OH})_8$, followed by a dehydration sequence $\text{Si}_2(\text{OH})_8 = 0.5\text{Si}_4\text{O}_{10}\text{H}_4 + 3.0\text{H}_2\text{O}$ or by $\text{Si(OH)}_4 = 0.25\text{Si}_4\text{O}_{10}\text{H}_4 + 1.5\text{H}_2\text{O}$.

At the maximum of the Si(OH)_4 profiles at approximately HAB= 10 mm, the experimental mole fractions of the cluster $\text{Si}_4\text{O}_{10}\text{H}_4$ are about 40% lower in flame B ($\phi = 0.6$) compared to flame H ($\phi = 1.2$), reflecting the decrease in the respective Si(OH)_4 profiles quantitatively. This observation confirms, that independent of the equivalence ratio of the flame the formation of $\text{Si}_4\text{O}_{10}\text{H}_4$ is linked directly to Si(OH)_4 .

In conclusion, the model describes the effect of equivalence ratio on important species in the particle formation path correctly and can be used to estimate the relative importance of both pathways as a function of equivalence ratio. The nanoparticles can be formed either via

the SiO or via the Si₄H₁₀O₄-cluster route. According to a rate of production analysis at $\phi = 1$ at HAB= 10 mm, the ROP of nanoparticles by the SiO pathway is 105 times higher than the ROP by the cluster pathway. At HAB= 20 mm the cluster pathway is more important with a 104 times higher ROP. This observation indicates that the pathway for the formation of nanoparticles changes within the flame with increasing HAB. The relative importance of both pathways in the complete synthesis process is estimated by comparison of the integrated ROP for both routes over all HAB. This analysis shows that 97% of the particles are formed via the SiO route and 3% are formed via the Si₄O₁₀H₄ cluster route.

A.3 Comparative study of flame-based SiO₂ nanoparticle synthesis from TMS and HMDSO: SiO-LIF concentration measurement and detailed simulation

Authors: R.S.M. Chrystie, H. Janbazi, T. Dreier, H. Wiggers, I. Wlokas, C. Schulz

The paper is published in 'Proceedings of the Combustion Institute 37 (2019) 1221-1229'.

The abstract is reprinted with permission from Elsevier.

Abstract

Depending on the chemical nature of precursor species, the flame-based synthesis of silicon dioxide nanoparticles in lean hydrogen/oxygen flames proceeds via different chemical routes, which affects the generated particle characteristics. Modeling the flame chemistry and particle formation therefore can provide valuable understanding of the underlying gas-phase and particle-formation pathways. In the present study we compare experimentally obtained temperature and semi-quantified SiO-concentration profiles in low-pressure (3 kPa), lean ($\phi < 0.6$), inert-gas diluted H₂/O₂/Ar burner-stabilized flat flames doped with 200-4000 ppm hexamethyldisiloxane (HMDSO) or tetramethylsilane (TMS) with results from kinetics modeling. Temperature fields in the flames were determined via multi-line laser-induced fluorescence (LIF) imaging using both added NO and native SiO as target species. Gas-phase silicon monoxide (SiO) was detected via LIF by exciting the rovibrational Q(42) transition in the A¹ Π - X¹ Σ + (1,0) vibronic band system at 230.998 nm that provides a weak temperature dependence when analyzing relative SiO mole fractions. Semi-quantitative SiO mole-fraction profiles as a function of height-above-burner (HAB) were obtained for all flames from the measured SiO-LIF intensities corrected for variations of the temperature-dependent ground-state population and the collisional quenching using measured temperatures and effective

fluorescence lifetimes, respectively. The experimental data were compared with results of appropriate chemical kinetics mechanisms from the literature with suitable modifications to best reproduce measured SiO mole-fraction profiles. Modeling initial cluster formation is important in this study to unravel the observed ‘double-peak’-structure of the SiO concentration profiles assumed to originate from resublimed SiO from early-formed SiO₂ nanoparticles in the rising temperature gradient during initial particle nucleation, and which may be altered by the availability of oxygen in the precursor species.

A.4 Investigation of a high Karlovitz, high Pressure premixed jet flame with heat losses by LES

Authors: P. Gruhlke, H. Janbazi, I. Wlokas, C. Beck, A. Kempf

The paper is published in 'Combustion Science and Technology 192 (2020) 2138-2170'. The abstract is reprinted with permission from Taylor&Francis.

Abstract

A second, smaller mechanism (denoted as UDE mechanism) was generated for the specific conditions of the present test case including NO_x reaction paths. The starting point of the reduction/optimization procedure was the CH₄/O₂ branch of the methane combustion mechanism proposed by Cremer (1972), the H₂/O₂ branch of the C1 mechanism by Li et al. (2007) and the CO and NO_x reaction paths of the GRI-3.0. The latter is known to over-predict NO_x species which could be possibly avoided by reverting to the obsolete GRI 2.11 mechanism (Barlow et al., 2001). The transport and thermodynamic properties of the gas components were taken from the GRI-3.0. The resulting mechanism was reduced and optimized by a genetic-algorithm based method developed by Sikalo et al. (2014, 2015) to match the laminar flame speed, the temperature profile and the mass fractions of CO and NO_x in a laminar flame calculated with the GRI-3.0 as a reference at the equivalence ratio of the DLR flame. The resulting reaction mechanism consists of 20 species (7 N-containing species) and 35 reversible reactions (18 from the C/N/O branch). For the validation of the reaction mechanism, one-dimensional laminar premixed freely propagating flames, 0D reactors and premixed counter flow flames have been used and tested against the GRI-3.0 and DRM19 mechanisms, investigating laminar flame speeds, adiabatic temperatures, ignition delay times, extinction strain rates, and spatial evolutions of Y_{CO}, Y_{NO} and temperature. In comparison to the reference GRI-3.0, a very good agreement in the laminar flame speed, temperature and spatial evolutions of Y_{CO} and Y_{NO} is achieved. The sensitivity to strain

is in good agreement with GRI 3.0 up to around 10^3 s^{-1} while the extinction strain rate is underpredicted. Significant deviations are identified for the ignition delay time τ which are attributed to the non-consideration of τ as an optimization target during mechanism development. In general, it should be noted that the UDE mechanism is purpose-made for the present conditions and application and may not be satisfactory for different conditions. The validation of the mechanism and the mechanism itself is available in appendices A and B.

A.5 Large-Eddy Simulation of a Lifted High-Pressure Jet-Flame with Direct Chemistry

Authors: P. Gruhlke, H. Janbazi, P. Wollny, I. Wlokas, C. Beck, B. Janus, A. Kempf

The paper is published in 'Combustion Science and Technology'. The abstract is reprinted with permission from Taylor & Francis.

Abstract

A reaction scheme is developed for lifted lean premixed high pressure methane jet flames, and tested by three-dimensional large-eddy simulation of an experiment, for which very detailed data is available. Auto-ignition-delay times of different mixtures of fresh gas and products have been introduced as a novel optimization criterion for the mechanism development. The new mechanism has been developed by a genetic algorithm based reduction and optimization, and consists of 15 species and 18 reactions. The large-eddy simulations are performed using a finite rate chemistry (FRC) approach and the dynamic thickened flame (DTF) model to investigate the flame stabilization of a lifted jet flame at high pressure in a gas turbine model combustor. In the simulations, the novel mechanism is compared to a similar mechanism that was generated without this criterion, and a further well-established mechanism. With the new mechanism, the LES predicts the flame as accurately as with the best reference mechanism, at a significantly lower cost. Further post processing with Lagrangian tracer particles confirmed that ignition events occur in the region corresponding to the lift-off height estimated in the experiment, which is corroborated by a chemical explosive mode analysis (CEMA). Overall, the newly developed mechanism with the novel optimization criterion was found to provide a better agreement with the experiments than previous mechanisms of similar cost, or a comparable agreement to a mechanism of significantly higher cost.

A.6 Kinetics of the thermal decomposition of ethylsilane: shock-tube and modeling study

Authors: P. Sela, S. Peukert, H. Somnitz, H. Janbazi, I. Wlokas, J. Herzler, M. Fikri, C. Schulz. The paper is published in 'Energy & Fuels'. The abstract is reprinted with permission from American Chemical Society.

Abstract

The thermal decomposition of ethylsilane ($\text{H}_3\text{SiC}_2\text{H}_5$, EtSiH_3) is investigated behind reflected shock waves and the gas composition is analyzed by gas chromatography/mass spectrometry (GC/MS) and high-repetition-rate time-of-flight mass spectrometry (HRR-TOF-MS) in a temperature range of 990–1330 K and pressure range of 1–2.5 bar. The unimolecular decomposition of EtSiH_3 is considered to be initiated via a molecular elimination of H_2 ($\text{H}_3\text{SiC}_2\text{H}_5 \rightarrow \text{H}_2 + \text{HSiC}_2\text{H}_5$) followed by reactions of cyclic silicon-containing species. The main observed stable products were ethylene (C_2H_4) and silane (SiH_4). Measurements are performed with a large excess of a silylene scavenger (C_2H_2) to suppress bimolecular reactions caused by silylene (SiH_2) and to extract unimolecular rate constants. A kinetics mechanism accounting for the gas-phase chemistry of EtSiH_3 is developed, which consists of 24 Si-containing species, 31 reactions of Si-containing species, and a set of new thermochemical data. The derived unimolecular rate constant is represented by the Arrhenius expression $k_{uni}(T) = 1.96 \times 10^{12} \text{ s}^{-1} \exp(-205 \text{ kJ mol}^{-1}/RT)$. The experimental data is very well reproduced by simulations based on the mechanism of this work and is in very good agreement with literature values. It is shown that EtSiH_3 is a promising precursor for the synthesis of SiC nanoparticles.

DuEPublico

Duisburg-Essen Publications online

UNIVERSITÄT
DUISBURG
ESSEN

Offen im Denken

ub | universitäts
bibliothek

Diese Dissertation wird via DuEPublico, dem Dokumenten- und Publikationsserver der Universität Duisburg-Essen, zur Verfügung gestellt und liegt auch als Print-Version vor.

DOI: 10.17185/duepublico/74931

URN: urn:nbn:de:hbz:464-20211111-085433-4

Alle Rechte vorbehalten.